β-Cyanoporphyrins

Their Synthesis and Applications in Molecular Systems for Artificial Photosynthesis

by

Antaeres' Dawn Antoniuk-Pablant

A Dissertation Presented in Partial Fulfillment
of the Requirements for the Degree
Doctor of Philosophy

Approved April 2015 by the
Graduate Supervisory Committee

Devens Gust, Chair
Ana Moore
Giovanna Ghirlanda

ARIZONA STATE UNIVERSITY

May 2015

ABSTRACT

As sunlight is an ideal source of energy on a global scale, there are several approaches being developed to harvest it and convert it to a form that can be used. One of these is though mimicking the processes in natural photosynthesis. Artificial photosynthetic systems include dye sensitized solar cells for the conversion of sunlight to electricity, and photoelectrosynthetic cells which use sunlight to drive water oxidation and hydrogen production to convert sunlight to energy stored in fuel. Both of these approaches include the process of the conversion of light energy into chemical potential in the form of a charge-separated state via molecular compounds. Porphyrins are commonly used as sensitizers as they have well suited properties for these applications. A high potential porphyrin with four nitrile groups at the beta positions, a β-cyanoporphyrin (CyP), was investigated and found to be an excellent electron acceptor, as well as have the necessary properties to be used as a sensitizer for photoelectrosynthetic cells for water oxidation. A new synthetic method was developed which allowed for the CyP to be used in a number of studies in artificial photosynthetic systems. This dissertation reports the theories behind, and the results of four studies utilizing a CyP for the first time; as a sensitizer in a DSSC for an investigation of its use in light driven water oxidation photoelectrosynthetic cells, as an electron acceptor in a proton coupled electron transfer system, in a carotene-CyP dyad to study energy and electron transfer processes between these moieties, and in a molecular triad to study a unique electron transfer process from a C_{60} radical anion to the CyP. It has been found that CyPs can be used as powerful electron acceptors in molecular systems to provide a large driving force for electron transfer that can aid in the process of the conversion of light to electrochemical potential. The results from these

studies have led to a better understanding of the properties of CyPs, and have provided new insight into several electron transfer reactions.

Dedicated to my Mother,

Viera I. Pablant Ph.D.

Peace and Friendship be with You

ACKNOWLEDGMENTS

I would first like to thank my advisor Professor Devens Gust, for providing me the opportunity to work with him. I would also like to express my gratitude towards his encouragement for creativity by giving me the opportunity and the support to explore my ideas. I would like to also thank him for the time he made and effort he spent contributing to my knowledge and skills.

I want to sincerely thank Dr. Yuichi Terazono for taking me under his wing and taking the time to guide me, while sharing his expertise, and teaching me an immeasurable amount about organic synthesis. I would not be here without his knowledge, guidance, patience, and kindness.

I would like to thank Professor Ana Moore for also giving me the opportunity to work with her and the time she took to guide me in my research, and to be another advisor to me.

I also want to thank Professor Thomas Moore, for also taking the time to guide me, and for making me think about the bigger picture of what I was doing often.

Thank you to Dr. Gerdenis Kodis, for all the work he did on the compounds I synthesized. I also thank him for his patience with my questions and the time he took to answer them several times, in several ways, until I at least partially understood the answer.

I would like to thank Dr. Paul Liddell for being patient with me and sharing his limitless knowledge of organic synthesis with me.

A very special thanks to my brother Dr. Novimir Antoniuk Pablant for being the best brother and friend there is. For always supporting me, believing in me even when I was afraid of failing, giving me confidence and somehow convincing me I would succeed.

I would probably not be in one piece if it weren't for James Klemaszewski. I can't thank him enough for his help, support, and (to name a few) for bringing me food when I forgot to eat and taking midnight walks when I could no longer focus.

I would like to thank my mother Viera I. Pablant for giving me infinite possibilities in life, supporting me, teaching me everything I know, and for making me want to be the best person I can be.

TABLE OF CONTENTS

Page

CHAPTER Page

APPENDIX

LIST OF TABLES

Table Page

LIST OF FIGURES

Figure Page

LIST OF FIGURES

Figure Page

Figure Page

Figure Page

Chapter 1 Renewable Energy and Artificial Photosynthesis

Energy production is one of the most important issues currently facing humanity.[1] Globally, energy demands continue to increase in both developed and developing countries. The development of clean, renewable energy sources is crucial in sustaining our energy-dependent economy, especially in light of the limitations and effects of using fossil fuels.[1,2] Alternative energy sources seek to maintain or increase energy production while reducing greenhouse-gas emissions and atmospheric pollutants. To these ends, this dissertation focuses on the development of organic compounds that are directed toward developing artificial photosynthetic systems for the conversion of sunlight to useful energy, which may eventually play an important part in meeting our future energy needs.

This dissertation reports on the research I have conducted related to the field of alternative energy, particularly solar energy via artificial photosynthetic systems. My research has focused on the synthesis and study of organic compounds that have applications directed toward these systems. Specifically, my major contributions include the development and implementation of synthetic methods to produce a variety of organic compounds as well as investigating them with respect to their electrochemical and photophysical properties. These compounds were designed specifically to study energy and electron transfer processes, building upon a better understanding of natural photosynthesis, and to develop efficient artificial photosynthetic systems for the conversion of solar energy to more useful forms. The research described in this dissertation is reported, in part, in the following published and in-preparation articles:

1. Antoniuk-Pablant, A., Kodis, G., Moore, A. L., Moore, T. A., and Gust, D. Photoinduced electron and energy transfer in a molecular triad featuring a fullerene redox mediator. *In Preparation*. **2015**

2. Antoniuk-Pablant, A., Terazono, Y., Megiatto, J. D., Sherman, B. D., Moore, A. L., Moore, T. A., and Gust, D. New Synthetic Method for beta-Cyano Substituted Porphyrins. *Submitted, Tetrahedron*. **2015**

3. Antoniuk-Pablant, A., Brennan, B. J., Sherman, B. D., Brudvig, G. W., Moore, A. L., Moore, T. A., and Gust, D. β-Cyano substituted porphyrins as sensitizers in photoelectrochemical devices. *In Preparation*. **2015**

4. Pillai, S., Ravensbergen, J., Antoniuk-Pablant, A., Sherman, B. D., van Grondelle, R., Frese, R. N., Moore, T. A., Gust, D., Moore, A. L., and Kennis, J. T. M. Carotenoids as electron or excited-state energy donors in artificial photosynthesis: an ultrafast investigation of a carotenoporphyrin and a carotenofullerene dyad. *Phys. Chem. Chem. Phys.* **2013,** *15*, 4775–84.

5. Megiatto, J. D., Antoniuk-Pablant, A., Sherman, B. D., Kodis, G., Gervaldo, M., Moore, T. A., Moore, A. L., and Gust, D. Mimicking the electron transfer chain in photosystem II with a molecular triad thermodynamically capable of water oxidation. *Proc. Natl. Acad. Sci. U. S. A.* **2012,** 1–6.

1.1 Global Energy Demands and the Need for Alternative Energy Sources

Global energy demands continue to increase, and at the same time, fossil-fuel reserves decrease. The burning of fossil fuels results in the increase of air pollution and related health issues along with the production of greenhouse gasses contributing to climate change. These negative impacts make research and development of alternative energy sources beneficial, if not vital.[1,3] The search for alternative energy sources has been driven, in part, by climate change. Climate change has been a significant area of discussion and research over the past several decades, due to the evidence that human activity, specifically the burning of fossil fuels, has negatively impacted important systems on the planet.[4,5] The Intergovernmental Panel on Climate Change and climate experts, M. Mastrandrea, and S. Schneider, suggest that a rise of global temperature by 2 degrees above pre-industrial global temperatures may be dangerous, causing not only the

loss of glaciers and ice sheets, but also irreversible species loss.[4,6] These losses, a result of higher temperatures, are related to an increase in atmospheric greenhouse gasses. These greenhouse gasses include CO_2, CH_4, N_2O, CFCs (chlorofluorocarbons), and other traces gasses, which contribute to higher temperatures and climate change by absorbing solar radiation.[7] The increase in long-lived human-produced atmospheric greenhouse gasses has been linked to the burning of fossil fuels.[4,6] One of the most abundant fossil fuels is coal. The burning of coal is used for electricity production, and is especially harmful in countries with poor emission regulations, such as in under-developed countries. In developed countries, crude oil is also in high demand, due to its widespread use, versatility, and ease of extraction and transportation. The demand for oil has increased steadily since the beginning of the 20th century and continues to increase. The ability to meet that demand is expected to become more and more challenging.[1]

The challenges associated with reducing our dependence on fossil fuels in the face of increasing global energy demands have spurred the investigation of alternative energy sources. Some of these energy sources include solar, hydroelectric, geothermal, wind, biofuel and nuclear energy.[1] Each of these energy sources likely has a place in the future global energy landscape. Nuclear energy is a possible alternative energy source through fission or fusion, although the technology of the latter is not advanced enough for civil purposes as of yet.[8] Energy from fission has a number of drawbacks, such as the safe disposal of nuclear waste materials and the potential for nuclear proliferation.[9] Nuclear waste would increase dramatically if nuclear fission became the sole or primary energy source utilizing today's technology, and the uranium resource base would be severely

depleted within 10 years. This would necessitate sophisticated nuclear recycling processes with respect to technology, and potentially stormy politics.[1]

Wind is an attractive, clean energy resource due to its zero emissions, simple harvesting technology and the relatively short construction times for apparatuses. However, major drawbacks include wind variability, ecological impact, the distance from wind farms to cities or towns, noise, and negative aesthetic perceptions.[1] Wind energy is being produced locally in some regions, but cannot produce the energy needed on a global scale. Similarly, geothermal energy is successful locally (e.g., Iceland), but requires significant geothermal gradients that are not present worldwide. In other parts of the world, hydroelectric power is an inexpensive alternative energy, but results in local flooding behind the dam forcing displacement of people and impacting river ecosystems.[1] Each of the aforementioned alternative energy sources has local applications, but they also have limitations for development on a global scale.

In order for any alternative energy source to be viable, it must be able to compete with or replace energy generation via the burning of fossil fuels, not strain or deplete local or global resources, and meet society's energy demands. For example, a feasible system or method would approach or exceed the energy needs of a region or society, but not displace or disrupt ecosystems or other important resources.[1,5] Ideally, such a system would occupy a surface area that has already been altered and utilized by society, and not compete for land or sunlight used currently for food production.[5] For these reasons, of the alternative energy options mentioned above, the most attractive is energy from sunlight. In the following sections more detail will be given to this energy source leading to a

detailed discussion of the methods of artificial synthesis that make up the topic of this thesis.

1.2 Solar Energy

Sunlight is globally available and delivers enough energy to the earth's surface to not only exceed current global energy demands, but to potentially meet the energy demands for the foreseeable future. For example, the sun delivers enough electromagnetic radiation so that solar conversion systems with a 10% energy conversion covering 0.16% of land surfaces would produce 20 TW of power. This value exceeds the 17 TW of power representing the world's current energy consumption via fossil fuels.[1,5] Consequently, the development of methods to convert sunlight to useful forms of energy is an important and active area of research.[1,4,5] Many methods have been developed and are currently being studied for solar-energy capture and conversion, including direct conversion to electricity and conversion to fuels,[1] which allows the storage of solar energy as chemical energy, and separates energy generation and utilization in both time and space.[5]

The conversion of sunlight to electric power through photovoltaics has been a heavily researched area since the photovoltaic effect was discovered in 1839. The 1973 oil crisis, problems associated with the burning of fossil fuels, and rising crude-oil prices have further contributed to the drive for improved photovoltaics.[9,10] In photovoltaic cells, the direct conversion of sunlight to electricity is done in a regenerative cell, where light is converted to electric power with no net chemical change.[10] These systems generally consist of a semiconductor diode that absorbs light and converts it into electron-hole pairs.[9] A majority of the devices designed in this fashion are classical solid-state junction

devices using crystalline or amorphous silicon, but recently, compound semiconductors are used in photovoltaics and solar cells.[9,10] Some drawbacks associated with solar cells and photovoltaics are high manufacturing costs, considerable amounts of energy needed to manufacture these devices, and the generation of pollutants.[9,11] In order to minimize these drawbacks, new methods are being developed for the direct conversion of solar energy to electric energy.

A recent method developed for the direct conversion of solar energy to electric energy involves the design and construction of dye sensitized solar cells (**DSSC**).[11–13] These DSSC are an attractive alternative to silicon-based solar cells, due to their relatively low production costs, lighter weight, and the flexibility of their shape and color.[10,11,14,15] DSSC consist of a nanoporous, nanocrystalline, non-light-absorbing photoanode (e.g., TiO_2 or SnO_2) sensitized with an organic dye known as a sensitizer, a counter electrode, and an electrolyte with a redox mediator, see Figure 1.[13,14] The sensitizers function by absorbing sunlight and converting it into electrochemical potential in the form of electron-hole pairs. They do this through the injection of an electron into the conduction band of the photoanode after excitation. The then-oxidized dye is reduced by the redox mediator, and the dye is regenerated as the electrons move through the external circuit to the counter electrode.[14] While the development of photovoltaic solar cells has been a great success and is already starting to change our energy landscape, there is still a need for an energy dense transportable fuel source. One method to achieve this is through the modification of the photovoltaic energy-conversion systems for the direct conversion of sunlight into chemical fuels.

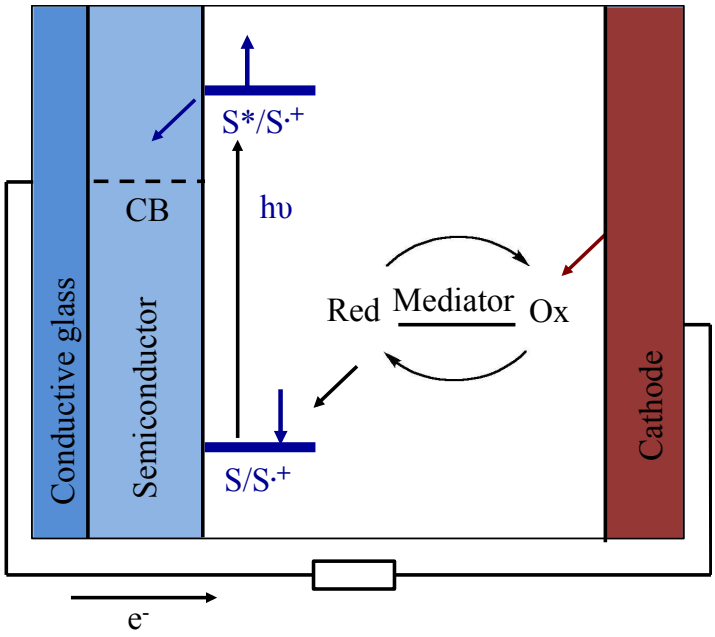

Figure 1. General schematic of the set up of a dye sensitized solar cell. The sensitizer (S) represents the dye that is sensitizing the semiconductor. CB represents the energy level of the conduction band of the semiconductor.

A system that can directly convert sunlight into chemical fuels is advantageous because it provides a practical energy source that can be stored and transported.[1] Hydrogen gas is a particularly attractive energy source, as its reaction with oxygen is highly exothermic, and water is the only the by-product.[16,17] In order to use hydrogen gas for our energy needs, a sustainable method to generate it must be found. One promising route is through photochemical water oxidation and the conversion of the products, namely protons and electrons, into hydrogen. While promising, this method has proven to be difficult to develop as it requires single-photon excitation with multiple electron and proton transfer events to drive the half reactions.[4,16,18–20] One of the more difficult steps of this process is the oxidation of water.

Equation 1 describes the reduction of protons to hydrogen[4]

$$2H^+ + 2e^- \longrightarrow H_2 \quad (1)$$

$E^{o'} = (0.00 - 0.0591*pH)$ V vs. NHE

Equation 2 describes the interconversion between water and oxygen[4]

$$O_2 + 4H^+ + 4e^- \longrightarrow 2H_2O \quad (2)$$

$E^{o'} = (1.23 - 0.0591*pH)$ V vs. NHE

Equation 3 describes the combination of both reactions above for an overall reaction, [4]

$$2H_2O \longrightarrow 2H_2 + O_2 \quad (3)$$

$\Delta E^{o'} = -1.23$ V

$\Delta G^{o'} = 474$ KJ mol^{-1}

where $E^{o'}$ is the formal potential of the respective reaction under standard conditions, $\Delta G^{o'}$ is the free energy change of the reaction under standard conditions, $\Delta E^{o'}$ is the cell voltage under standard conditions, and NHE stands for normal hydrogen electrode.

One approach to achieve photochemical water oxidation is through the design of dye-sensitized photoelectrosynthetic cells. These systems include the use of photoelectrochemical regenerative-type cells and couple them to catalysts for water oxidation and hydrogen reduction. In these systems the sensitizers or molecular reaction centers, upon photoexcitation, provides the driving force for the respective catalysis.[20] Photosynthesis has been achieving solar energy conversion for centuries, using light energy to overcome the kinetic and theromodynamic barriers of water oxidation.[4] Although the efficiency of photosynthesis in green plants, in terms of its biomass production, is relatively inefficient, around 1%, the overall, the basic processes can provide us with invaluable information for harnessing solar energy.[20] By using the

processes of natural photosynthesis as a blueprint, it is theoretically possible to develop artificial systems that are tailored to generating fuels that can be used for our energy needs. [1,2,4,5,17] In order to mimic the intricate energy and electron transfer processes in photosynthesis, the overall general mechanism as well as the individual electron and energy transfer processes between the components needs to be well understood.

1.3 Natural Photosynthesis

Photosynthesis is the largest-scale system for solar energy harvesting and conversion on the planet. Photosynthesis is responsible for the energy stored in coal, petroleum, and natural gas on which our current energy economy is based.[2] Oxygenic photosynthetic organisms use solar energy to oxidize water and utilize the electrons from this process for fuel generation, through the coupling of several subsystems. In natural photosynthesis, as well as in artificial systems for solar energy conversion, the first step is the absorption of light, leading to energy transfer in the antenna systems where electronic excited states migrate from one molecule to another.[21] After the absorption of light and energy transfer processes, photoinduced electron transfer from the singlet excited state of an electron donor to an acceptor takes place.[22] This electron transfer results in a cascade of electron transfer processes which lead to conversion of excitation energy to electrochemical potential energy stored in oxidizing and reducing equivalents in a charge-separated state across the photosynthetic membrane.[4,23–25]

In oxygenic photosynthesis, harvested solar energy is transported to catalytic sites by a series of electron-transfer steps and is then used to oxidize water and produce fuels.[1,2,4] The absorbed solar energy is stored as both redox potential and PMF that are used to

produce sugar from CO_2 and ATP. A simplified overview of the overall electron transport processes in oxygenic photosynthesis is depicted in a 'Z-scheme'. Two photons are needed to transport one electron from PSII through the cytochrome b6f complex, and then through PSI. From the luminal side of PSII, a hole is transported from the P680+ electron donor to the oxygen-evolving complex (OEC), a Mn_4O_4Ca cluster. This complex accumulates four oxidizing equivalents and catalyzes the oxidation of water to form molecular oxygen and protons. The electrons from water oxidation are increased in reducing potential by PSI are later used to produce NADPH from $NADP^+$.[4] Ultimately in photosynthesis, four photoexcitations of photosystem I (PSI) and photosystem II (PSII) results in the production of one O_2, two NADPH, and three ATP molecules, converting light energy into chemical energy in the bonds of biomass.[4]

Purple photosynthetic bacteria have been studied in detail both structurally and spectroscopically and share many fundamental steps with oxygenic photosynthesis. In purple photosynthetic bacteria, light is harvested and the electronic excitation energy migrates in the antenna pigments and is eventually funneled to a reaction center, the special pair, a bacteriochlorophyll dimer $(Bchl)_2$, where it undergoes a multistep electron transfer process through a series of compounds until it gets stored as electrochemical potential in the form of a charge-separated state.[26] This multistep electron transfer has a quantum yield approaching unity, and a long-lived charge-separated state due to stabilization of the charges across a bilayer. [27] Sequentially, electron transfer from the singlet excited state of the $(Bchl)_2$, via a two-step or a one-step superexchange mechanism, occurs within about 3 ps to the bacteriopheophytin (Bphe) which is located about 9 Å distant, edge to edge.[28] This initial electron transfer generates a charge-

separated state, with the radical cation on the bacteriochlorophyll $(Bchl)_2^{\cdot+}$, and the radical anion on the bacteriopheophytin $Bphe^{\cdot-}$; the energy of the charge-separated state is lowered by about 0.2 eV from the excited state. This amount of energy matches the reorganization energy of electron transfer, but places the charge recombination process into the Marcus inverted region, which hinders back electron transfer and favors forward electron transfer.[23,28] The charge-separated state then undergoes a charge-shift step, where the electron is transferred to the primary quinone (Q_A). This step happens in about 200 ps over a distance (edge-to-edge) of about 9 Å. One final electron transfer from the quinone Q_A to quinone Q_B, occurs in about 100 μs.

This electron-transfer system is efficient due to the low reorganization energy, the electronic coupling between the donor and acceptors, and the arrangement of each donor and acceptor couple. The arrangement in this system is aided by the non-covalent incorporation into well-defined transmembrane proteins.[29] These properties and arrangements allow the natural system to generate a long-lived charge-separated state through small reorganization energies, and by spatially separating the charges through a multi-step electron transfer process.

In order to mimic natural photosynthetic systems, it is important to understand, in detail, the molecular basis of the process.[1] Therefore, many aspects of photosynthesis are being studied, one of which is the absorption and conversion of light into energy. The function of PSII and its ability to combine single photon excitation with the multi-electron process of water oxidation is a key area of interest, by mimicking these processes, artificial systems are being designed to harness solar energy for societal

energy needs. One key process within the conversion of light-to-energy in the natural system is the series of events that involve the initial charge-separation that generates the electron hole pair, which then drives water oxidation. This process involves a proton-coupled electron transfer relay between the chlorophyll complex P680 and the oxygen-evolving complex. This proton-coupled electron transfer process is covered in more detail in Chapter 4, along with a reported study on this subject.

In addition to charge separation, another key process in photosynthesis is the gathering of light energy. Natural systems utilize antenna systems consisting of various chroromphores that absorb a wide range of the solar spectrum and transfer the energy first from auxiliary chromophores to the chlorophyll molecules which then undergo energy transfer to the RC via singlet-singlet energy transfer.[17] These auxiliary chromophores consist of compounds that absorb the part of the solar spectrum that the chlorophylls do not, including carotenoid polyenes, phycoerythrins, and phycocyanins.[17,25,30] Carotenoids are an important component in antenna systems; they are found in all known native photosynthetic organisms. Carotenoids are extended molecules with delocalized pi-electron systems, and in oxygenic organisms usually have ring structures at each end.[21] Carotenoids have several functions in photosynthesis, including light absorption and subsequent energy transfer to a chlorophyll-type pigment, and photoprotection. Energy transfer from carotenoids, coupled with the role their structure and thermodynamics play in controlling this process, is an important aspect light harvesting systems.[21]

1.4 Artificial Photosynthesis

Artificial photosynthetic systems could, in theory, provide energy to satisfy the global energy demand, utilizing abundant and inexpensive materials, and without competing for land necessary for food production, natural systems and/or animals. Artificial photosynthetic systems are being studied and designed by utilizing and adapting the processes and structures of natural photosynthesis, with the goal to meet society's needs by developing systems that convert light energy into chemical energy stored as a dense and transportable fuel by means of an efficient, clean, and inexpensive method.[1,2,4,5,17] In order for artificial photosynthetic systems to be viable, the efficiency of solar-energy conversion would need to be higher than in the natural system.[1] Artificial systems include dye sensitized solar cells, which are being designed for the conversion of sunlight to electricity, as well as photoelectrosynthetic cells for conversion of solar energy to fuel.[10,17,19,31–33] Some photoelectrosynthetic cells are designed to use solar energy to oxidize water, using the products of this reaction to cleanly and efficiently produce hydrogen gas with materials that are abundant and relatively inexpensive.[5,17]

These photoelectrosynthetic cells employ an extension of dye-sensitized nanoparticulate wide band gap semiconductor electrodes, with the addition of suitable catalysts for water oxidation or fuel production.[10] The potential energy of the holes generated after electron injection into the semiconductor is used to drive electron transfer from a catalyst instead of from a mediator.[19,31–33] These systems can use organic compounds as sensitizers that can absorb in the visible range of the spectrum. The sensitizers have energy levels that are tailored to inject efficiently an electron into the

semiconductor, and in their oxidized form accept an electron from the catalyst with sufficient potential to drive the desired reaction.[10] Systems with higher complexity have been designed with two photosynthetic cells used in tandem, one for water oxidation and the other for hydrogen reduction. For example, one cell absorbs blue photons and the generated holes can drive water oxidation, whereas the other cell absorbs in the green and red parts of the spectrum utilizing the generated photovoltage along with the protons and electrons from water oxidation to generate hydrogen.[10] These cells are physically separated so H_2–O_2 recombination cannot occur.[19] This system is comparable to the "Z-scheme" of electron transfer for water splitting in natural photosynthesis, but makes better use of the available solar spectrum.[10]

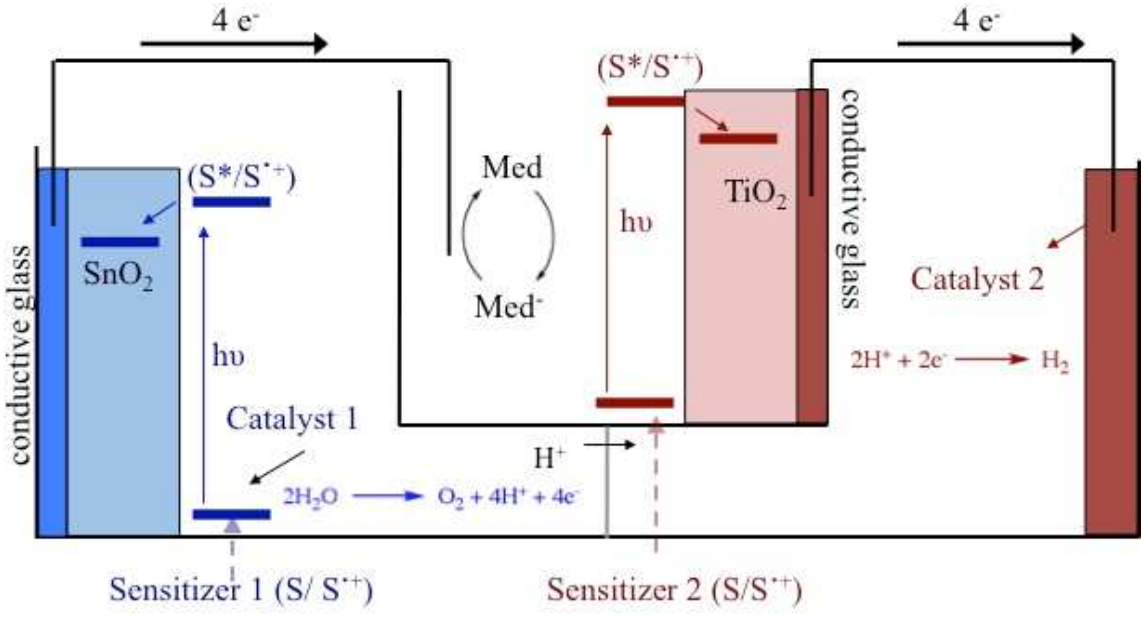

Figure 2. An example of a general set up schematic of a dual-threshold photoelectrochemical water splitting cell. A high potential sensitizer (S 1) drives water oxidation by Catalyst 1. Med represents a mediator such as iodine/triiodide. Sensitizer 2 represents a low potential sensitizer for the reduction of protons by Catalyst 2. The figure is an adaptation of a diagram made by Benjamin Sherman.

Generally, photoelectrosynthetic cells have four major components, 1) a water oxidation catalyst 2) a fuel production catalyst 3) light harvesting antenna systems, 4) sensitizers or reaction centers (RC).[17,18] A general schematic of a photoelectrochemical water splitting cell modeled after natural photosynthesis is shown in Figure 2.

The sensitizers, which can include more complex molecular systems that generate a charge-separated state before electron injection, will be referred to as reaction centers herein. The RC are bound to a nanoporous transparent semiconductor and linked to the water oxidation catalyst or the proton reduction catalyst. In water oxidation, irradiation of the RC will result in an excited state, followed by electron injection into the appropriate semiconductor, which is then followed by the reduction of the oxidized RC by the water oxidation catalyst regenerate the RC and transfer a hole to the catalyst.[2] The excited state redox potentials of the RC must have the thermodynamic driving force necessary to inject an electron into the conduction band of a semiconductor such as TiO_2 or SnO_2, as well as accept an electron from the water oxidation catalyst. Proton reduction can be achieved by utilizing the electrons from water oxidation that, through excitation by the sensitizers and the CB of the semiconductors, are given sufficient potential to drive a suitable catalyst.

Water oxidation and hydrogen reduction catalysts are key elements in this system. Water oxidation being a four-electron process, is a slow reaction even with good catalysts.[11] Therefore the development of an efficient water oxidation catalyst has been a focus of research.[17,19,34] Transition metal oxides (e.g., $IrO_2 \bullet nH_2O$, RuO_2, Co_3O_4,) and more recently oxynitride semiconductor particles are known to be good catalysts for water oxidation.[11,31] IrO_2 has been shown to be stable and active, and $IrO_2 \bullet nH_2O$

nanoparticles have been studied as a water oxidation catalyst in electrochemical and photochemical systems.[31] To catalyze hydrogen reduction, platinum has been frequently used. However platinum is expensive and has limited availability. Improved catalysts based on earth-abundant elements are being developed. One approach involves optimizing hydrogenases, which catalyze proton reduction in nature, although most hydrogenases lack oxygen stability.[2,19]

Efficient absorption of solar electromagnetic radiation is an essential process in photosynthetic systems, and is accomplished by light-harvesting antenna systems. Antenna systems absorb solar energy which then undergoes a rapid singlet excited-state energy migration to the reaction centers.[35] Approximately half of the energy in sunlight occurs at wavelengths below 700 nm,[36] so antenna systems ideally contain chromophores that absorb a wide range of solar radiation including ultraviolet, and visible but also into the near infrared. Some of these chromophores also provide photoprotection and photoregulation.[17,36] For efficient light harvesting the theoretical optimum band gap is at about 1100 nm, but absorption at longer wavelengths allows harvesting over a larger portion of the solar spectrum.[36] Light-harvesting arrays are designed to absorb light over a large area and transfer the excitation energy over a long distance to a single reaction center.[2] In general, photosynthetic organisms use chlorophylls as the primary excited-state electron donors; chlorophylls absorb around 430 and 660 nm.[2] Many organisms employ an array of other chromophores to absorb sunlight where chlorophyll does not, including carotenoid polyenes, phycoerythrins, tetrapyrrole macrocycles, and phycocyanins.[2,17] In order to improve efficient energy-absorption and energy-transfer systems, the process by which excitation energy is transferred to the reaction centers and

proceeds to undergo electron transfer that converts it to electrochemical potential, is important to understand. Artificial systems that mimic this process are designed and studied, including carotenoid polyenes linked to porphyrins. In these dyads, the carotenoid polyene absorbs light in spectral regions where the porphyrin absorbs weakly, and then transfers the singlet excitation energy to the porphyrin, mimicking the antenna function of carotenoids. Because carotenoid polyenes are able to quench chlorophyll triplet states before they can interact with oxygen and deactivate singlet oxygen itself, [30] dyads of this kind can also be designed to study the role that the carotenoids have in photoprotection from singlet oxygen damage. Energy and electron transfer from carotenoids are covered in greater detail in Chapter 5, along with the results from a study of energy and electron transfer within a porphyrin carotene dyad.

The primary function of the RC is the conversion of light energy, either directly or from excitation energy received from light harvesting antennas, into chemical potential. RCs convert light into a chemical potential through rapid electron transfer forming a charge-separated state (CS) that resists recombination long enough for the stored electrochemical energy to be utilized to drive a given process (e.g., water oxidation) and fuel production (e.g., hydrogen gas).[2,5,13,17,37] In reaction centers electron transfer occurs between donor and acceptor components. Studies of organic RCs used in energy-harvesting systems include DSSC, light-driven water oxidation, organic photovoltaic cells, and basic studies on electron transfer between organic compounds. In all of these systems it is necessary that, upon photo-excitation and generation of a charge-separated state, rapid forward electron transfer out-competes charge recombination (CR), thereby avoiding energy loss.[5,11,14,17,19,38] In photosynthetic water-splitting cells, CR is a major

factor for the observed low quantum yield. In one recently studied system, the electron transfer from TiO_2 to the oxidized dye occurs about 1 order of magnitude more rapidly than electron transfer from the water oxidation catalyst to the dye.[2,19] Rapid forward electron transfer and slow charge recombination in molecular systems depend on many variables including the component interactions. In a photosynthetic cell, these include the RCs anchoring and spatial orientation to the photoanode and catalyst.

Designing and studying molecular systems that emulate the electron-transfer processes in natural photosynthesis aids in the design of efficient artificial systems for solar-energy conversion. Much of the research of the Gust, Moore, and Moore group has focused on this topic. Approaches to designing molecule-based reaction centers include molecular dyads and triads that, as discussed later, involve a multistep electron transfer processes. By using the compounds that function similarly to the ones in the natural systems such as chlorophylls, carotenoids, pheophytins, and quinones, artificial systems aim to increase the efficiency of the energy conversion process. Several classes of compounds have been studied, including fullerenes, naphthalocyanines, porphyrins, and perylenes.

The research herein focuses on designing RCs for artificial photosynthetic systems directed toward solar energy conversion. Before going into more detail on the design of these systems, a brief overview of related processes is given. The basic theories of photoinduced energy and electron transfer between donors and acceptors are reviewed, followed by a review of select studies on porphyrin-fullerene systems that lead into the research reported.

1.5 Introduction to Energy and Electron Transfer

There are several processes that can occur between chromophores when excited states are involved, including both energy and electron transfer.[39] Herein the focus will be on interactions between complexes that consist of at least two components, a donor (D) and an acceptor (A).

The first step in photoinduced reactions is resonance absorption. Resonance absorption occurs when a molecule absorbs a photon with energy equal to the energy spacing between two molecular quantum levels, placing the molecule into an excited state.

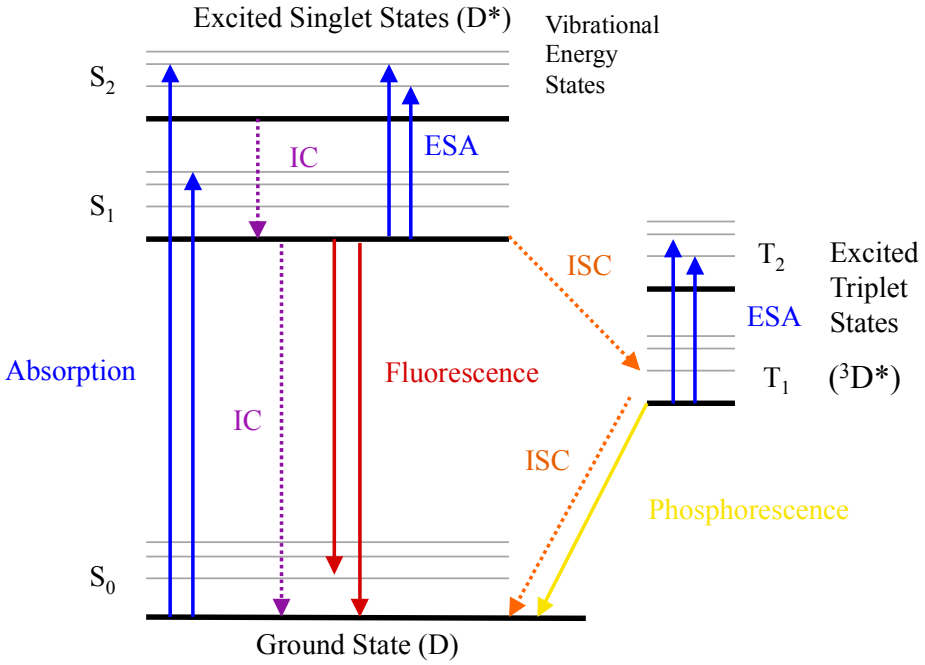

Figure 3. Jablonski diagram for organic dyes.[40,41] ESA-excited state absorption, ISC-intersystem crossing, and IC-internal conversion.

Fluorescence is a downward transition of the molecular energy, where a photon is emitted with an energy correspondent with the spacing between molecular quantum

states. Molecular energy levels can be divided into four classes: electronic, vibrational, rotational and translational. The Jablonski diagram[40] (Figure 3) is a convenient scheme to describe the intra- and intermolecular electronic transitions.

The electronic and vibrational energy levels have the largest effect on the spectra of molecular systems.[21] Within a particular electronic state of a molecule there are multiple associated vibrational energy levels. These vibrational energy levels can be described in terms of a quantum-mechanical harmonic oscillator. Transition between energy levels can occur when the frequency of an absorbed or emitted photon is equal to the energy in a particular molecular vibrational mode in a certain electronic level.[21] Molecules can exist in several electronic states and each has its own potential energy function for the nuclear motion. The ground state of a molecule is the lowest energy electronic state of the molecule; higher electronic states are high-energy excited states. These states follow the Pauli exclusion principle where each orbital can only hold two electrons that must have opposite spins. In an excited state an electron is promoted to the lowest unoccupied molecular orbital (LUMO). In this configuration the electron is no longer constrained to have the opposite spin as the electron remaining in the highest occupied molecular orbital (HOMO), and when it doesn't it is called the triplet state. The energy of the triplet state is lower than the singlet state (when the electrons retain the opposite spin).

When a photon is absorbed and the molecule is promoted to an excited state, the distribution of electrons in this state defines a new potential energy function. The distribution of electrons changes instantaneously, whereas the nuclear configuration change is much slower. Consequently the vibrational level of the excited state to which

the transition occurs is usually not the lowest energy vibrational level of the excited states, due to the horizontal displacement of the two electronic states. The decay process through fluorescence is similar, where the final state that is initially populated is usually an excited vibrational state of the ground electronic state. This energy difference is seen in a spectral shift, called the Stokes shift, which is a measure of how much the excited state potential energy curve differs from the ground-state potential energy curve.[21] Decay from the excited state can also occur by nonradiative processes including intersystem crossing and internal conversion, and by energy transfer or photochemistry. The direct conversion to the triplet state is intersystem crossing.[21]

1.6 Energy Transfer

In a donor acceptor system, after the excitation of a donor chromophore (D), energy transfer with another chromophore, an acceptor (A), can occur to produce an electronically excited state A*. This energy transfer can take place via two main mechanisms, Dexter, and Förster.[39]

1.6.1 Dexter

A Dexter electron exchange mechanism of energy transfer is through a direct interaction of the wave functions of D* and A.[39] In this mechanism the excited state of D causes an electron exchange from the LUMO orbitals, going from D to A, and concurrently an electron exchange from the HOMO orbitals from A to D, generating A*, while conserving the spin of the electron.[39] Due the conservation of spin, this energy transfer mechanism allows a triplet state of ^{3}D* to produce a triplet state of ^{3}A*, see Figure 4.[39] The rate of the electron transfer k_{ee} is related to the specific orbital interaction,

and in the simplest case depends inversely and exponentially on the distance between D and A, see Equation 4. Therefore, this mechanism of energy exchange occurs between compounds over only fairly short distances on the order of 5-10 Å.[39]

$$k_{ee} = KJe^{\frac{-2r_{DA}}{L}} \quad (4)$$

Where K is related to the magnitude of a specific orbital interaction of electron exchange, J is a spectral overlap integral describing the overlap of the absorption spectrum of the donor and acceptor, L is the sum of the van der Waals radii, and r_{DA} is the distance between D and A.[39]

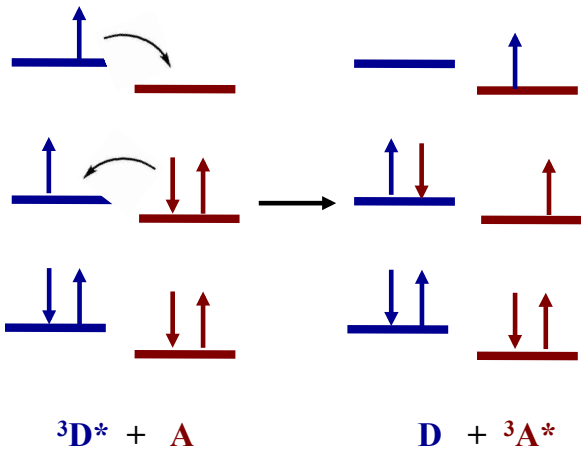

Figure 4. Schematic diagram of Dexter energy transfer involving the triplet state of D. Adapted from Anslyn, E., Dougherty, D.[39]

1.6.2 Förster

The Förster mechanism of energy transfer is a non-radiative transfer that can occur over long distances, up to around 80 Å. It is typically associated with singlet states. This mechanism requires a coupling of two transitions, D*→D and A → A*, and because the transition probability is proportional to the transition dipole, this type of energy transfer is

proportional to the interaction of transition dipoles, a dipole-dipole coupling. For this energy transfer to occur the energy between the two states D* and A need to match, therefore, some overlap between the emission spectrum of D* and the absorption spectrum of A is necessary for this energy transfer to occur.[21,39] The rate constant, *k*, of the energy transfer is given in Equation 5,

$$k \propto E^2 \propto \frac{{D_D}^2 {D_A}^2}{r_{DA}^6} \quad (5)$$

where *k* is proportional to E^2 where E is the interaction energy of the dipoles, D is the dipole of each chromophores, and r is the distance between the chromophores.[39]

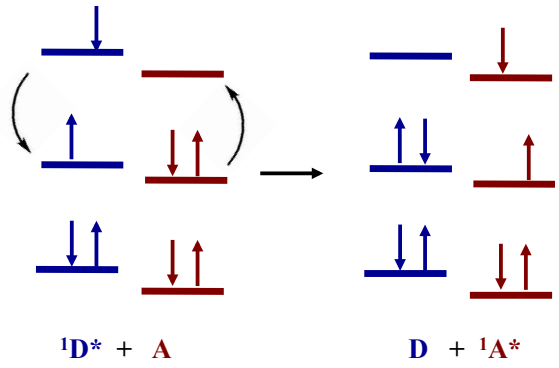

Figure 5. Schematic diagram of the Förster energy transfer mechanism. Note the transitions occur simultaneously. Adapted from Anslyn, E., Dougherty, D.[39]

1.7 Electron Transfer

Intramolecular electron transfer in systems where the donor and acceptor are separated by rigid bonds is of interest for studying artificial photosynthetic systems because the molecular geometry can be well defined.[42] This process is a nonradiative relaxation process that generally occurs between a donor molecule that has a high-energy filled

orbital and an acceptor molecule that has a low-energy empty orbital, a donor acceptor complex D-A.[39] We can begin to describe this process with simple reduction and oxidation reactions, where an electron transfer occurs from a compound with the donor reduced and the acceptor oxidized to a state where the donor is oxidized and the acceptor is reduced.[21]

$$D_{red} \rightleftharpoons D_{ox} + e^-$$

$$A_{ox} + e^- \rightleftharpoons A_{red}$$

$$D_{red} + A_{ox} \rightleftharpoons D_{ox} + A_{red}$$

Figure 6. General redox processes.

The free energy changes (ΔG) of these reactions can be estimated by using electrical measurements, and the conversion between Joules and measured volts is given by Equation 6; ΔE is the electrical potential (V), F is the Faraday constant, and n is the number of electrons in the reaction.[21]

$$\Delta G = -nF\Delta E \tag{6}$$

Using the free-energy change of a chemical reaction and Equation 4, the basic equation for describing electrochemical processes, the Nernst equation is obtained (See equation 7),[21]

$$\Delta E = \Delta E^o - \frac{RT}{nF}\ln\left(\frac{[A]_{red}[B]_{ox}}{[A]_{ox}[B]_{red}}\right) \tag{7}$$

where ΔE^o is the standard state potential, R is the gas constant, and T is absolute temperature.[21]

As mentioned, electron transfer also occurs to and from the excited states of compounds. These processes are important in many chemical and physical processes, including photosynthesis and have been a heavily researched subject for many years.[43] Photoinduced electron transfer is the process by which absorption of light excites a molecule to an electronically excited state, and this excitation causes electron transfer between moieties [39] Many of the theories developed to describe this process follow the original theories developed by Marcus[44,45], Hush[46], and Levich.[47] These theories describe the rates of photoinduced electron transfer as functions of electronic coupling between the initial and final states, thermodynamic driving force, temperature, and solvent and internal reorganization energies.[17]

Photoinduced electron transfer can occur in these D-A complexes, which can generate a charge-separated state, an important process in natural and artificial photosynthetic systems (see Figure 7). When a compound undergoes an electron transfer process in its excited state, the transfer occurs at a potential which reflects its excited state energy levels, where it can be both a reducing and an oxidizing agent.[21]

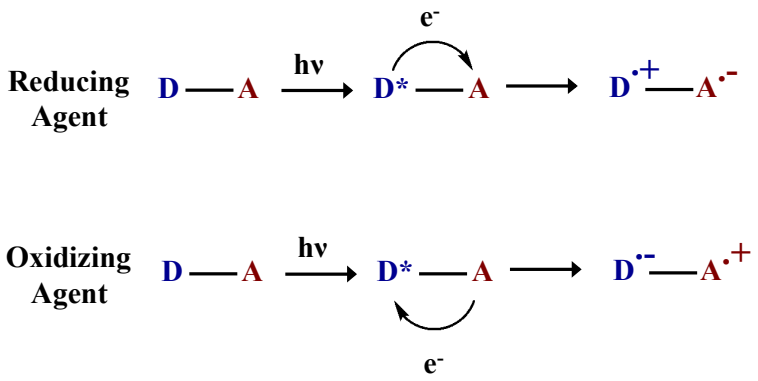

Figure 7. Electron transfer from the excited state of D. Where D is acting as a reducing or oxidizing agent.

This process begins with an initial excitation that promotes an electron into an antibonding orbital of the D molecule, commonly the LUMO orbital. The occupied LUMO orbital has an oxidation potential that is significantly different than the ground state orbital, which results in the excited state of the molecule being easier to oxidize than the ground state. The excitation of an electron into the LUMO orbital leaves a vacancy in the HOMO orbital, a hole, which can then accept an electron.[39] From this excited state, the electron in the LUMO of the D molecule can be donated to the electron acceptor A, which needs to have a LUMO orbital energetically downhill with respect to the LUMO of the D molecule. This electron transfer leaves a positive charge on the donor, $D^{\cdot+}$, and a negative charge on the acceptor, $A^{\cdot-}$, giving a charge separated state, $D^{\cdot+}$-$A^{\cdot-}$, see Figure 8.

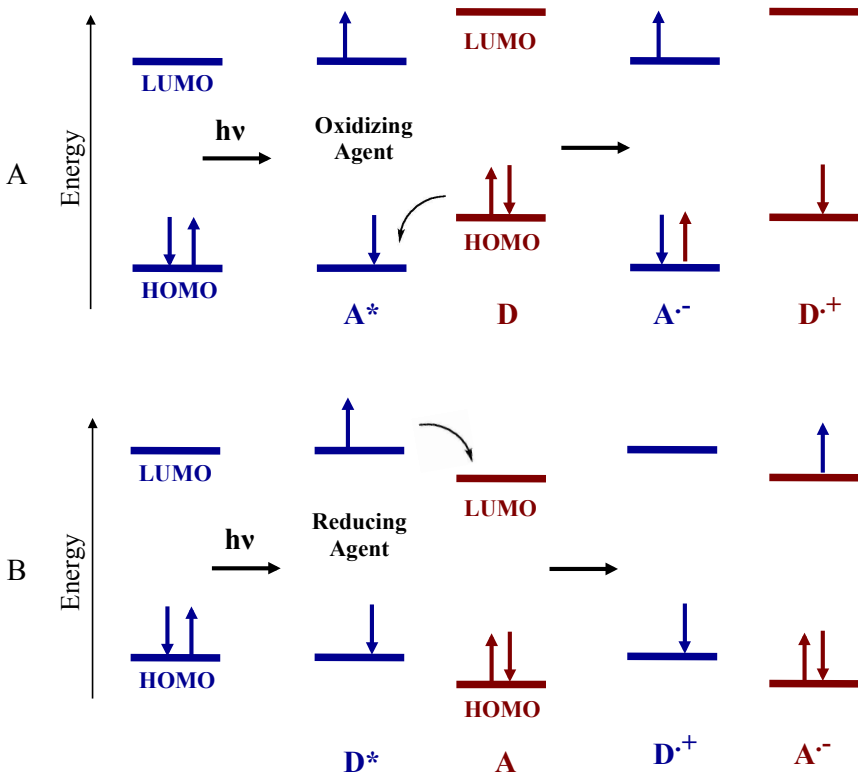

Figure 8. Photoinduced electron transfer. A) Excited state D* acting as an oxidizing agent B) Excited state D* acting as a reducing agent. Adapted from Anslyn, E., Dougherty, D.[39]

Charge recombination, or back electron transfer, describes the process of relaxation that is electron transfer from the acceptor back to the original donor, which returns the complex to the original ground state.[39] The quantum yield of a photochemical process is an indicator of how efficient a process is, as it is equal to the number of photons emitted divided by the number of photons absorbed.[39]

Photoinduced electron transfer occurring in donor-acceptor molecules can be described using Marcus theory. This theory uses parabolic models of potential energy and reaction coordinates to describe chemical reactions, [42,43,48,49] and was developed and used to make predictions of structural and environmental effects on kinetics of electron transfer reactions.[39,50] This theory best describes one-step electron transfer reactions, but can still

give insight into more complex multi-step electron transfer reactions.[49] The complex potential energy surfaces in Marcus theory can be simplified to one dimension, described by parabolas of Gibbs free energy vs. the reaction coordinate of the potential energy surfaces of the reactant and product states, see Figure 9.[49] These parabolas represent the approximation of the free energy change ($-\Delta G$) during a change in the nuclear coordinates of the donor-acceptor molecule as well as the surrounding solvent near the energy minima.[49] Electron transfer is described as the transition between two potential-energy surfaces, which requires a change in free energy, $-\Delta G^{o}$ and reorganization energy, λ.[43] The intersection of the two parabolic curves, where the initial and final state have the same configuration in terms of the nuclear coordinates, describes the transition state of the reaction where electron transfer occurs.[39,49] The activation energy $\Delta G^{\ddagger}$ is the amount the reactant must shift from equilibrium for electron transfer to take place.[49] The free energy change ΔG is the energy displacement of the two parabolas, and the reorganization energy λ is the potential energy difference in nuclear and solvent configuration between the states.[43,49]

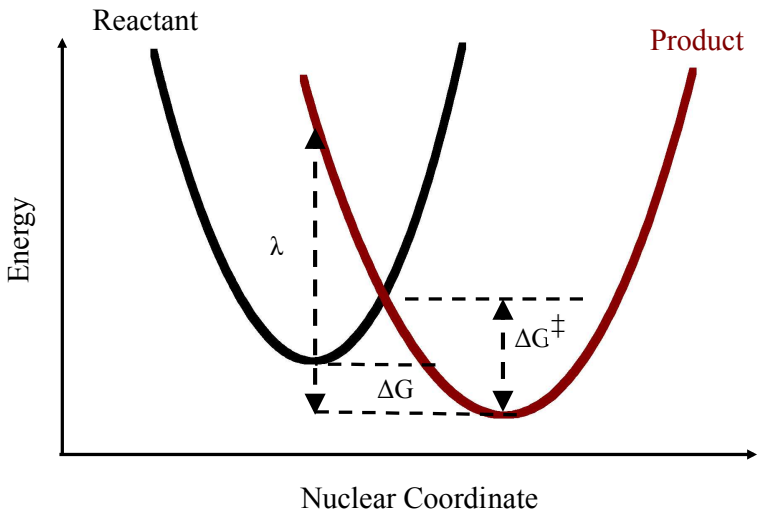

Figure 9. Representation of intersecting parabolic potential energy surfaces of an electron transfer reaction.

The reorganization energy is the sum of the energy required to reorganize the internal structure of the compound and of the outer solvation sphere to bring the donor and acceptor orbitals to the same energy for electron transfer.[39] The internal reorganization term is solvent independent and is determined by the difference in structure of the product and the reactant states. The solvent reorganization energy is due to the energy required to change surrounding solvent molecules and their orientation and polarization.[39,49] The internal nuclear movements and solvent motions cause the donor and acceptor energy levels in both the reactant and product to be in continual flux. For electron transfer to occur the donor and acceptor must reach a configuration where the energy levels match, which requires that the geometries and solvation arrangements of the molecules match.[39] During electron transfer the nuclei do not change position, and the energy of the electron does not change, which means that for the electron transfer to occur the energy of the donor and acceptor orbitals must be the same.[39] The free energy

change and the intrinsic barrier determine the shapes and intersections of the parabolas and these values can be calculated using the Marcus theory.[50]

The nonadiabatic electron transfer rate constant k_{ET} is given in Equation 8, where V is the electronic coupling, $-\Delta G^o$ is the free energy gap between the equilibrium nuclear configuration of the reactants and the products, λ represents the reorganization energy, T is the absolute temperature, h is Planck's constant, and k_B is Bolzmann's constant.[22,23]

$$k_{ET} = \left(\frac{4\pi^3}{h^2 \lambda k_B T}\right)^{1/2} V^2 \exp\left[-\frac{(\Delta G^o + \lambda)^2}{4\lambda k_B T}\right] \quad (8)$$

In this equation, the electron transfer driving force between electron donors and acceptors ($-\Delta G^o$) is related to the logarithm of the electron transfer rate constant ($\log k_{ET}$), and the reorganization energy required in the electron transfer reaction.[22] The rate of electron transfer will increase as the free energy change becomes larger until it reaches a maximum rate where $-\Delta G^o = \lambda$. If the free energy change becomes even larger $-\Delta G^o > \lambda$ positive, the electron transfer rate will decrease with increasing driving force. This is what is called the Marcus inverted region.[22,23,39,42] See Figure 9 for a representation of the potential energy surfaces, and Figure 10 for a representation of the free energy change at different reorganization energies.

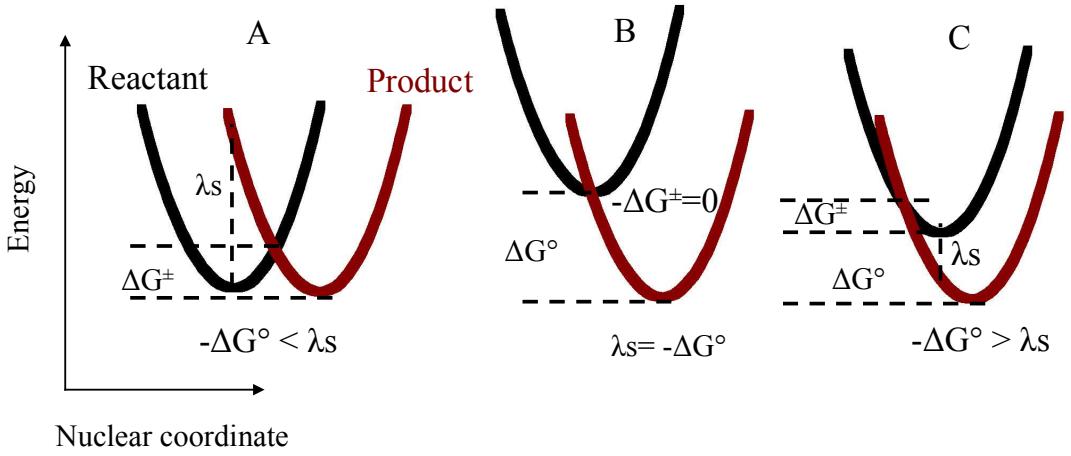

Figure 10. Representation of intersecting parabolic potential energy surfaces of three different electron transfer reactions. A) Normal region, $-\Delta G^{o} < \lambda$ where an increase of $-\Delta G^{o}$ increases the rate of the reaction. B) Activationless region and maximum rate where $-\Delta G = \lambda$ C) Inverted region $-\Delta G^{o} < \lambda$ where an increase of$-\Delta G^{o}$ decreases the rate of the reaction

It has been thought that the Marcus inverted region could be a major reason why the recombination reactions in the natural systems are slow. The reorganization energy of a donor-acceptor system is an important factor in slowing down charge recombination. When the driving force becomes larger than the reorganization energy, an increase in driving force results in a decrease in rate constant due to the vibrational overlap of the product and reactant wave functions lessening. This region is important for the generation of long lived charge separated sates.[22] See Figure 11.

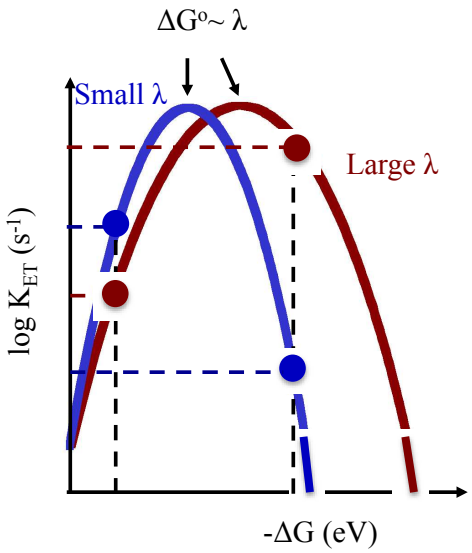

Figure 11. Representation of the dependence of the rate of electron transfer on free energy change of donor-acceptor linked compounds with small and large reorganization energies.

1.8 Energy and Electron Transfer in Organic Molecular Systems

Understanding and optimizing both energy and electron transfer in molecular constructs is an important aspect of solar energy conversion. Model systems using donor-acceptor molecules have been constructed and studied in order to understand the processes of photoinduced energy and electron transfer as well as to aid in the design of systems for solar energy conversion.[17,25,27,51] Using the information we have learned from the natural systems, along with the basic theories describing energy and electron transfer, systems are being designed to optimize the electron transfer process. There are several routes to do this, including the design and utilization of compounds that are not found in the natural system to develop molecular constructs that harvest solar energy and convert it to electrochemical potential more efficiently. To improve energy conversion, some of these systems incorporate arrays that are designed to have a large number of antenna pigments as well as incorporate a variation of pigments which allow for a wider range of

the solar spectrum to be absorbed.[25] Therefore the design of molecular systems that incorporate both antenna systems as well as reaction centers can give us valuable insight into designing efficient solar energy conversion systems.[25,26,52] Using the theories described above for energy and electron transfer processes and important factors for efficient light-energy conversion systems, many molecular models have been designed and studied to investigate the effect of distance, orientation, and molecular topology on the photoinduced charge separation and charge recombination.[49,53] These systems consist of reaction centers[25] which are constructed from various compounds such as porphyrins that are covalently linked to electron acceptors and/or donors such as quinones, aromatic imides, fullerenes, other porphyrins, amines, or carotenoid polyenes.[25] Dyads and supermolecules that consist of two or more electron donor and acceptor units are effective at producing highly energetic charge-separated states, enhancing the rate of charge separation, and retarding charge recombination. Therefore, these are good models to study and work on with the goal of optimizing photoinduced electron transfer.[54]

When designing these systems two important processes are kept in mind, forward electron and charge recombination. Charge recombination is a major cause of inefficiency in these artificial systems. This process occurs when the electron transfer processes proceeding from the initial charge separated state are not fast enough to compete with the decay of the charge separated state back to ground state.[17] Electron transfer is dependent on several factors which include the energies of the ground, excited, and charge separated states, solvent and internal reorganization energy, temperature and the electronic coupling between the initial and final states.[17] In a covalently bonded pair, the electronic interactions are through the bonds, and the separation between the donor

and acceptor is an important factor as it governs the orbital overlap between the donor and acceptor which is directly related to the electronic coupling.[17] Therefore, these factors are important when designing donor acceptor molecules for energy conversion.[17,26]

For efficient electron or energy transfer is it important to choose donor acceptor pairs that have redox potentials and excitation energies that are suitable for forward electron transfer. [28] The energy level of the acceptor must be thermodynamically poised to be lower than that of the donor, driving the electron to a more favorable and stable energy level, and thereby stabilizing the negative charge. Compounds such as quinones and C_{60} are examples of compounds that are used as acceptors as they thermodynamically can provide a driving force for electron transfer and can accept an electron from a number of donor compounds.

The reorganization energy of the electron transfer step has a large effect on the rate of electron transfer both forward and in charge recombination.[28] It is important to use donor-acceptor pairs with small reorganization energies in order to accelerate charge separation and hinder charge recombination.[28] As mentioned above, the reorganization energy is a combination of the internal (vibrational energy changes) and solvent reorganization energy. It is possible to control the reorganization energy through the intrinsic properties of the compounds such as size, shape, heterogeneity, and molecular orbitals.[23] In photosynthetic models the surrounding solvent is a large contributor to the reorganization energy, which has proven to be difficult to control. The solvent reorganization energy is a function of the separation distance between the donor and acceptor, the radius of the

complex, as well as solvent polarity.[23,28] It is important to note that with decreasing distance between the donor and acceptor a decrease in reorganization energy occurs.[28] Marcus theory also predicts that with short distances between donor and acceptor and strong electronic coupling, the CS process would be pushed to where $-\Delta G_{CS} = \lambda$, and the CR process will be shifted into the Marcus region where $-\Delta G_{CS} >> \lambda$.[28] The electronic interaction between the donor and acceptor is an important aspect for efficient electron and energy transfer processes. A covalent linkage between the donor and acceptor allows electronic coupling interactions occur through the chemical bonds instead of through space that allows these compounds to be designed with more control over the properties of the electronic interaction between compounds.[17] Having electron transfer occur between a strongly coupled donor-acceptor has the advantage of minimizing the loss of photon energy, as well as allowing for fast forward electron transfer.[17,22,28] Unfortunately, strong electronic coupling also leads to fast charge recombination. To get around this problem and retain the fast forward electron transfer, the natural photosynthetic system uses a multi-step electron transfer process. This process uses multiple molecules to drive electron transfer and charge-shift reactions resulting in a spatially separated final charge-separated state, which reduces the electronic coupling of the state resulting in longer lived charge-separated states.[22,28] A consequence of multistep electron transfer systems is that some amount of the input photon energy will be lost in the process with each electron transfer step.[22,28]

Systems that can achieve long-lived charge separated states while maintaining strong coupling and minimizing the number of electron transfer steps, are ideal for use in solar energy conversion systems. To achieve this, it is necessary to focus on slowing down the

rate of charge recombination.[22] Besides compounds that can efficiently spatially separate the charges, methods to slow down back electron transfer between relatively close D-A pairs would be ideal. Systems which undergo charge recombination in the Marcus inverted region can be used for this purpose.[22] In particular, molecules containing covalently linked porphyrins and fullerenes (C_{60}) due to their redox, optical, and photochemical properties have often been investigated with respect to these considerations.[23,53–55]

1.9 Fullerenes (C_{60})

C_{60}s have been used extensively in many applications such as superconductors, photoconductors, nonlinear optical materials, catalysts, luminescence devices, molecular optical and electronic devices. They have unique electrochemical and photophysical properties, and can be used as both an electron acceptor and a sensitizer as they weakly absorb over most of the visible region.[53,56] There are a number of reports of utilizing C_{60} in intermolecular photoinduced electron transfer in heterogeneous and homogeneous systems. They have also been extensively used to design systems that are aimed at studying electron transfer in artificial photosynthetic systems.[5,56] Many donor-fullerene systems have been synthesized and studied, where the donor has varied from amines, polycondensed aromatics, transition metal complexes, carotenoids, ferrocenes, phthalocyanies, and porphyrins. [22,49,53,54,56–58]

The C_{60} is a spherical molecule made of 60 carbon atoms. It is 8.8 Å in diameter and consists of carbon atoms making up 20 hexagons and 12 pentagons in a structure where no two pentagons are adjacent and each pentagon is surrounded by six-membered

rings.[39,59] It has a closed-shell configuration consisting of 60 π-electrons in 30 π-bonding molecular orbitals, that are suitable for electron transfer.[60]

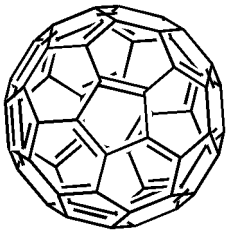

Figure 12. C_{60}; also known as a fullerene molecule or a Bucky Ball.

There are two types of bonds in C_{60}, one being at the junction between two six-membered rings, a 6-6 bond, and one which lies at the junctions of the six and five membered rings, a 5-6 bond.[39] It has been found that the 6-6 bond has more double bond character than the 5-6, and reacts like a strained electron-deficient alkene.[39] Fullerenes are well known electron acceptors that can accept up to six electrons and have first reduction potentials of -0.3 to -0.4 V vs. SCE. The UV/Vis spectrum of C_{60} shows absorption in the visible and near-IR regions and consists of multiple absorption bands corresponding to $S_0 \rightarrow S_n$ electronic transitions, with its longest wavelength absorption maximum at 620nm. In its first excited singlet state, $^1C_{60}$'s energy levels are comparable to those of the larger π-systems such as porphyrins, being about 2 eV above the ground state, and its triplet states, $^3C_{60}$*, lie at 1.58 eV above the ground state. [55,61] The extinction coefficient of the absorption spectrum between 492 and 620 nm is lower than or equal to 750 M^{-1} cm^{-1}, and at 480 nm is 2.4 X 10^3 $M^{-1}cm^{-1}$.[62] The fluoresce emission spectrum of C_{60} consists of multiple peaks in the 686-762 nm region and three spectral shoulders in

the 620-677 nm region.[63] $^1C_{60}$* is converted to $^3C_{60}$* with a high yield through intersystem crossing. The triplet-triplet absorption spectrum of C_{60} has a λ_{max} at 740 nm with an extinction coefficient of 18,000 $M^{-1}cm^{-1}$.[64] The π-radical anion of C_{60} absorbs in the near-IR region at around 1080 nm.[64]

The large three dimensional structure of C_{60} gives it unique properties, compared to smaller electron acceptors. C_{60} has a smaller reorganization energy, which causes the rate of photoinduced charge separation in many donor-acceptor constructs to be in the normal region of the Marcus parabolic curve. Concurrently the charge recombination rate is pushed into the inverted region of the Marcus curve.[53,56,59] This can increase the rate of charge separation and decrease the rate of charge recombination, both of which are key for generating longer lived charge-separated states. It has been hypothesized that the large size, symmetry, and rigidity of the C_{60} causes the actual reorganization energy of the C_{60} to be small. The size and symmetry allow the radical anion to be spread over a larger area which decreases the solvent reorganization energy, and the internal reorganization energy is lowered by the rigidity.[5,23,53,56,59,65] This effect was studied comparing the electron transfer properties in complex with a C_{60} as the electron acceptor to a similar complex with a quinone as the electron acceptor. A porphyrin-linked quinone (P-Q), and a similarly linked porphyrin-C_{60} (P-C_{60}), were synthesized and studied to gain further insight into the difference of electron transfer properties between a small flat electron acceptor and a larger three dimensional C_{60} acceptor. It was noted that the porphyrin-linked C_{60} had a forward electron transfer rate that was larger than the porphyrin-linked quinone by a factor of 6 and a charge recombination rate that was lower by a factor of <1/25 (in THF).[5,23,56,59] These rate differences are hypothesized to be due to

the smaller solvent and internal reorganization energy associated with the C_{60} as stated above, see Figure 13.[23]

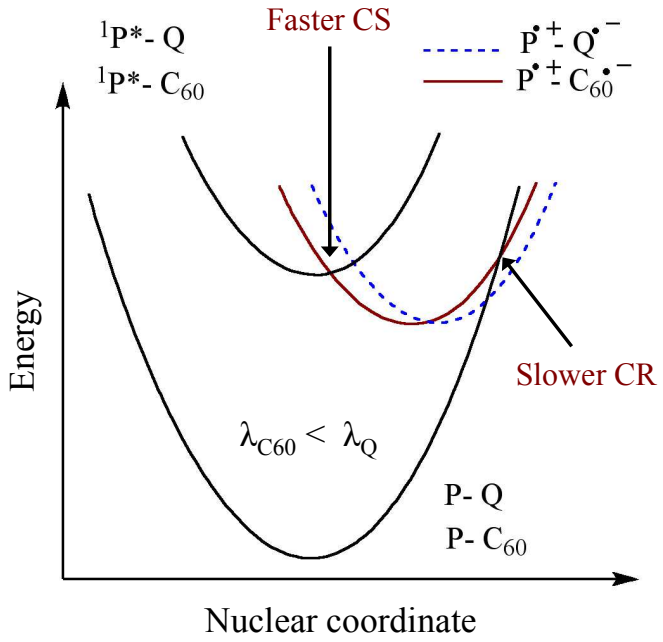

Figure 13. Potential energy surface schematic for photoinduced electron transfer of the compounds P-Q and P-C_{60}.

The solvent reorganization is smaller in the $C_{60}^{\bullet-}$ due to the charge being spread over the framework causing the individual charge densities on each carbon to be small. In the case of the Q, the reorganization energy is large as the charge of the $Q^{\bullet-}$ is localized on the oxygens, causing the solvent reorganization energy to be large, along with the larger internal reorganization energy.[59] This study showed the benefits of C_{60} used as the electron acceptor in artificial photosynthetic systems.[23,56,59]

The C_{60} in terms of chemical reactivity is that of a typical electron deficient olefin. The functionalization of fullerenes has been a widely studied area; many of the approaches

follow the work of Wudl with diazomethanes.[66] One of the most common reactions to functionalize a C_{60} is the cycloaddition of azomethine ylides, leading to fulleropyrrolidines - the Prato reaction developed by Maggini et al. [66,67] Azomethine ylides are a class of 1,3-dipoles which react readily with dipolarophiles to form substituted pyrrolidines.[67] These reactions take place on the 6,6 ring junction of fullerenes. Azomethine ylides can be generated through the decarboxylation of immonium salts which are derived from the condensation of an alpha amino acid with an aldehyde.[67,68] When the Prato reaction takes place in the presence of C_{60} in refluxing toluene, the C_{60} is functionalized with about an 82% yield.[67,68] The pyrrolidine products are also suited for further functionalization, making this reaction a good candidate for synthesizing highly functionalized C_{60}s.[67] The pyrrolidine substituent has little effect on the properties of the C_{60} except that it causes a partial loss of conjugation by the saturation of one of the double bonds, causing the reduction potentials to be more negative than those of an unsubstituted C_{60}.[68] The absorption spectra of fulleropyrrolidines have a broader range than C_{60}, with a peak at 430 nm and a broader band at around 700 nm. This method of C_{60} functionalization is widely used due to the ease of obtaining a variety of azomethine ylides, the fact that only a single monoaddition compound is synthesized, and the possibility of introducing two functional chains simultaneously, which allows the synthesis of a variety of substituted fullerenes.[66,68]

1.10 Porphyrins

Porphyrins have been used extensively as light absorbers and electron donors in artificial photosynthetic molecules as they are generally similar to their natural

chlorophyll relatives.[2,11,13,17,36,69–77] They have been used in numerous other model systems including in biomimetic and materials chemistry such as enzyme models, chiral catalysts, chiral sensors, synthetic receptors, optoelectronic devices, and potential sensitizers for photodynamic cancer therapy.[64,78] It has been shown that porphyrins over other chromophores are ideal components for these systems as they have generally smaller reorganization energies, and they absorb with in the UV/Vis region, and their high electronic excitation energy allows for exergonic electron transfer.[29] They have proved to be an asset to photovoltaic cells, photoelectrochemical cells, and in molecular systems to study photoinduced electron transfer and charge separation. In these applications porphyrins can act as both antennas and reaction centers wherein they absorb light and transfer singlet excitation energy to other chromophores, or use excitation energy to initiate electron transfer to or from acceptor or donor moieties to generate charge-separated states. They have been used to sensitize wide bandgap semiconductors such as NiO, ZnO, SnO_2, and TiO_2,[13] and recently they have been become some of the most efficient sensitizers in DSSC having a power conversion efficiency of up to 13%.[11,14,15] Porphyrins also have been studied successfully as RCs in light driven water oxidation systems.[31] They are particularly useful in these systems because of the properties described and the relative ease that their redox potentials can be modified to be thermodynamically poised to drive reactions, such as water oxidation.[4,11,79]

Porphyrins are tetrapyrrole molecules; their simplest form is called porphine. The porphyrin consist of four pyrrole compounds linked together between their α-positions through methine bridges, denoted as *meso* carbons. Porphyrins are more elaborate structures that have added on functional groups to various positions on the parent

porphine structure. Porphyrins have a large π-aromatic system conisisting of 24 π-electrons, and in the free base porphyrin macrocycle, 18 π-electron contribute to a conjugation pathway. This conjugated system consists of two equilibrating 18-π annulene aromatic delocalization pathway tautomers, each with two localized β-β'pyrrolic bonds at the antipodal 7,8,12,13-positions of the β-pyrrole carbons.[80,81] The macrocycle is a tetradentate chelating ligand in its deprotonated form, which can bind various metal ions with an in-plane and out of plane coordination modes. These metalloporphyrins do not retain this 18-pi electron pathway, and do not consist of a mixture of tautomers.

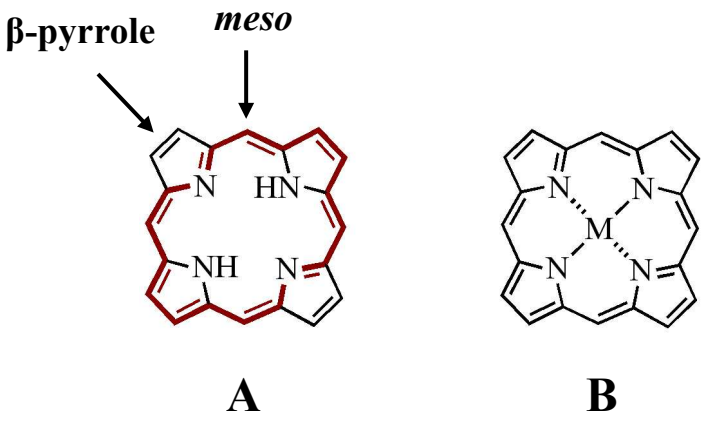

Figure 14. Chemical structure and nomenclature for the different carbon atoms of free base porphyrins, with the 18 π-electron system highlighted.

Porphyrins absorb in the UV/vis region of the solar spectrum with several distinctive bands typically from 400 to 650 nm which arise from π-π* transitions. [11,82] They feature an intense band, with an extinction coefficient >200,000, at around 400 nm, the Soret band, and weaker bands from about 450 to 750 nm (Q bands).[64] The optical spectrum of porphyrins can be described by Gouterman's 4-orbital model. This model is based on a linear combination of atomic orbitals, which was the first to describe the relative

intensities of the two lowest energy pi to pi* electronic transitions.[83] These bands arise from the transitions from the HOMO and $HOMO^{-1}$ pi orbitals labeled a1u and a_2u and the LUMO and $LUMO^{+1}$ pi* orbitals labeled egx and egy. Metalloporphyrins have a D_{4h} symmetry and the a1u and a2u orbitals lie close enough in energy to be degenerate, and the eg orbitals are doubly degenerate. [11] This model describes the excited states in terms of the transitions between the transitions from a1u →eg ^{1}(a1u,eg) and a2u → eg ^{1}(a2u, eg), in which the latter is a forbidden transition.[82] These transitions are of E_u symmetry, in which they consist of equivalent dipole transitions in the x and y directions, where the egy and a2u to egx orbitals have x-polarization, and the a1u to egx and a2u to egy orbitals are y polarized. These excited state configurations are nearly degenerate, and there is a strong electron interaction between them resulting in resonances which leads two transitions. The low intensity and low energy (Qx and Qy) bands are a result of the transition dipoles of the two configurations nearly canceling, and the high energy and high intensity (Bx and By) Soret bands, are a result of the transition dipoles of the configuration adding. [84] Certain bands of the spectra have been shown to be from vibrations of the Q and B electronic states.[85] The asymmetrically substituted free base porphyrins have D_{2h} symmetry, resulting in nondegeneracy of the eg orbitals which results in splitting Q (0,0) bands into the x and y components, Qx(0,0) and Qy(0,0) resulting in four Q bands labeled Qy(1,0), Qy(0,0), Qx(1,0) and Qx(0,0), and two Bx, and By transitions.[11,86]

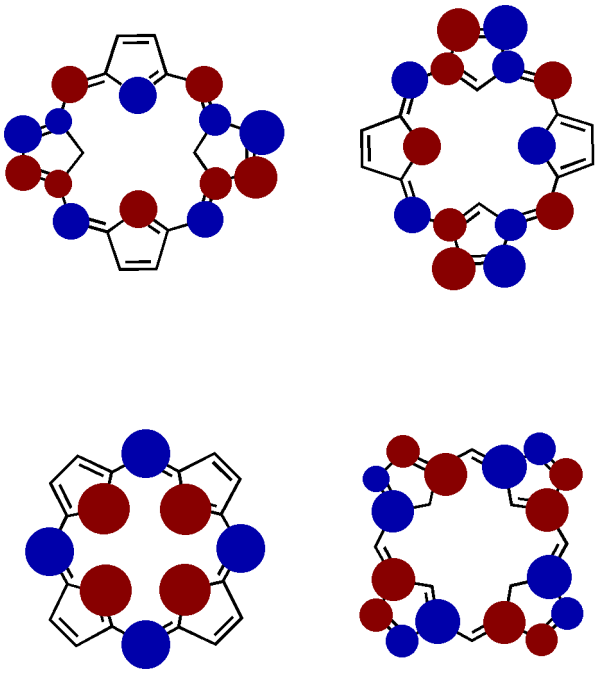

Figure 15. Gouterman's four orbital theory representation of porphine's molecular orbitals. Coefficients are proportional to the size of the circle and the color indicates the sign.[82]

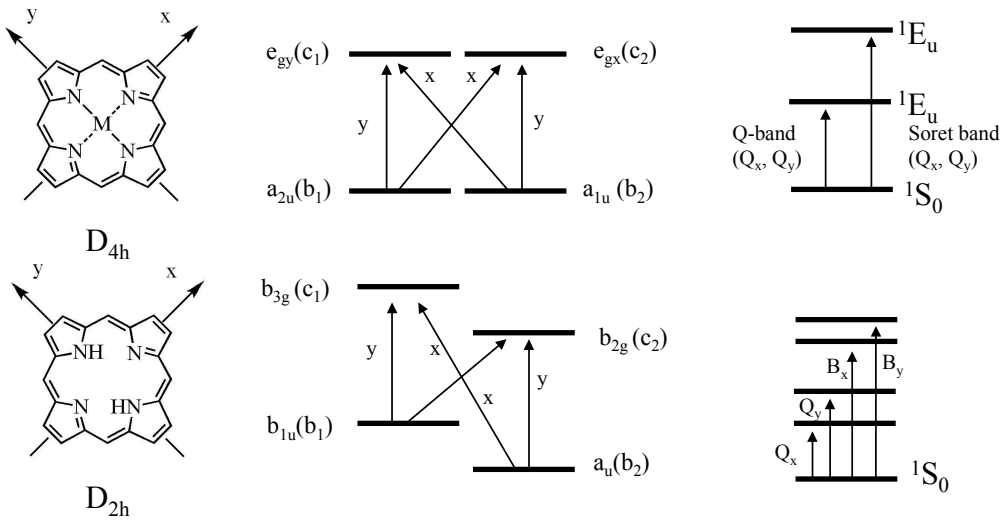

Figure 16. Goutermans four-orbital model for free base porphyrins (bottom) and transition metal porphyrins. A simplified explanation for the UV/Vis spectra of porphyrins. Adapted from Nemykin, V. et al.[82,86]

Porphyrins have a relatively high molar extinction coefficient and also have singlet and triplet excited states that live long enough that they have a high probability of undergoing energy or electron transfer before deactivation.[64,87] The fluorescence emission spectrum of typical porphyrins consist of two strong emission bands at wavelengths greater than the long wavelength band, from Qx(0,0).[88]

Porphyrins are electroactive and can undergo multiple redox processes. The half wave potentials at which these processes occur depend on several factors including the substituents, the planarity of the macrocycle, and the type and oxidation state of the central metal ion.[89] In a typical cyclic voltammogram of a porphyrin these are seen as two reversible one electron reductions showing the sequential formation of the π -anion radical and dianion, and two reversible oxidations from the sequential formation of the π -cation and dication.[90] Unsubstituted metalloporphyrins generally have a HOMO-LUMO gap of 2.25 (+/- 0.15) V [90], the potentials have a wide range but for an example a simple Zn(II) 5,10,15,20-tetraphenylporphin metalloporphyrin's first reduction and oxidation potentials are around $E_{red\ 1/2}$ = -1.32 V vs SCE and $E_{ox1/2}$ = 0.82 V vs SCE.[91] Porphyrins are relatively stable compounds. The porphyrin's core is relatively stable in aqueous solutions, atmospheric conditions, and in moderately strong acidic and basic conditions. The protonation/deprotonation of the inner pyrroles occur readily but are easily reversed. Porphyrins are relatively stable upon exposure to oxygen, making them practical molecules for use in solar conversion systems. Their mono- and di-cation π-radical species are relatively stable allowing them to be used in many visible photon-electron conversion processes, and they can undergo numerous photoionization, and electrochemical reactions with little degradation.[64]

There has been an extensive amount of work on the development of methods for the synthesis of symmetric and non-symmetric porphyrins. Two main methods are generally used for their synthesis, the method developed by Lindsey and one developed in the 1940 by Rothemund and then later expanded on in the1960's by Adler and Longo. The Lindsey method is useful for the synthesis of symmetric and asymmetric meso-substituted porphyrins.[92] The use of dipyrromethanes and aldehydes in a McDonald type 2+2 condensation has been also used to synthesize a variety of meso- substituted trans-porphyrins.[78] Numerous methods have been developed to modify and add substituents to the meso and β-pyrrole positions, as well as for coordination of a metal atom to the porphyrin macrocycle and utilization of the metal for further coordination of an axial substituent.

One of the appeals of utilizing porphyrins as sensitizers is because of the relative ease of the modification of their optical, and electrochemical properties. There has been an extensive amount of work done to optimize porphyrins for use in these systems, from adding substituents for anchoring and bonding to surfaces and other compounds, to substituents that affect the electronic structure of the porphyrin. Numerous porphyrins with various substituents have been synthesized that have allowed them to selectively anchor to metal oxides including semiconductors and/or catalysts. These groups include salicylate, carboxylic acid, benzoic acid, cyanoacrylic acid, sulfonic acid, phosphonic acid, and acetylacetonate derivatives.[13,14] Porphyrins can be more intricately modified in ways that tune their optical and electrochemical properties. There have been several studies on modifying the electronic structure of porphyrins in order to design porphyrins or larger porphyrin arrays that absorb beyond 600 nm, as one of the drawbacks of

utilizing porphyrins is their poor light harvesting ability beyond this region.[14] These kinds of modifications can also be used to tailor the ground state redox potential and excited state redox potential energy levels of the porphyrins to be able to drive redox reactions and donate electrons to an acceptor at specific energy levels. Push-pull structures have been incorporated into the porphyrin π-conjugated system which elongates it and enables a porphyrin to absorb light in the near infrared regions, making more efficient use of the solar spectrum in energy conversion applications.[14] Recently, by using the intrinsic properties of the porphyrins and by fine tuning the HOMO and LUMO orbitals a DSSC using a specially designed Zn(II) porphyrin was found to outperform a ruthenium sensitizer, which was previously the highest .[14,15] These porphyrins also exhibit optimization of electron injection due to intramolecular charge transfer character.[14] Another successful way of synthesizing porphyrins that absorb more of the solar spectrum is by the extension of the porphyrin pi-conjugation system. The elongation of the pi conjugation and loss of symmetry causes a broadening and a red shift in the absorption bands, together with an increased intensity of the Q bands relative to the Soret. These changes arise from the splitting in the pi and pi* levels and a decrease in the HOMO-LUMO gap.[11] These kinds of modifications have been shown to enhance the light harvesting ability in the near infrared regions.[14]

In addition, the substitution of electron donating or withdrawing groups on the porphyrin macrocycle can tailor the electronic properties and redox potential energy levels for specific purposes.[14,93,94] There have been numerous studies on the effects on the electronic structure and electrochemical properties of porphyrins from the addition of electron donating groups and electron withdrawing groups to the porphyrin macrocycle,

including the effects of a complexed metal.[87,95–97] It is known that both the number and electronic properties of substituents, as well as the planarity of the macrocycle influence both the electronic structure and electrochemical properties. [89,91,96,97] The position of the substituents influences the amount of coupling to the macrocycle; the higher the coupling the more of an effect they have on the electronic properties of the porphyrin. An example of the effects of electron withdrawing groups on the meso-phenyl positions are porphyrins with bis(pentafluorophenyl) groups on the 10,20-meso positions. Due to the electron withdrawing properties of these bis(pentafluorophenyl) meso substituents, these porphyrins have a significant shift in their redox potentials as well as their absorption spectra. These porphyrins have been utilized as high potential dyes in various studies.[79,98] The $E^{o\text{-}o}$ transition energy of a zincated methyl ester analogue is around 2.12 eV, and the free base methyl ester analogue is around 1.93 eV. One of the appeals of utilizing this porphyrin in light driven water oxidation is that due to the increased driving force for electron transfer between the catalyst and the photooxidized sensitizer, the forward electron transfer may out compete recombination from the semiconductor.[98]

The β-pyrrole positions on the porphyrin are known to have the closest interaction with the conjugated system which causes them to have the greatest effect on the energy levels of the porphyrin.[81,90,95,99] Several studies looked at the effect on the optical and electrochemical properties of free base and metallated porphyrins of both electron withdrawing and electron donating groups added specifically to the β-pyrrole positions.[89,91,95,96] Electron withdrawing groups on the β-positions stabilize both the lowest unoccupied molecular orbitals (LUMOs) and the highest occupied molecular orbitals (HOMOs), with the latter being slightly less affected, and they also affect the

non-planarity of the porphyrin.[89,99,100] The effect of the addition of the substituents is clear in β-bromo porphyrins; the addition of the larger bromine atoms on the β-positions increases the distortion of the porphyrin macrocycle causing a rise in the HOMO energy.[90,101] It was shown that an anodic shift of the reduction potential is at least five times larger for electron withdrawing substituents on the β-pyrroles vs. substituents on the meso phenyl positions. This is thought to be due to the β-substituents being conjugated to the π-bonded ring system.[102]

It has been recently shown that the addition of four cyano substituents on the β-pyrrole positions causes an even greater shift in the redox potentials when compared to substituents on the meso-phenyl, which may be beneficial in efficient artificial photosynthetic solar energy conversion systems. Although there is some data reported on derivatives of this porphyrin, there was no reported use of the CyP in any electron transfer or energy transfer systems, mainly due to the synthetic limitations. To begin studying the CyP in complex systems, it was necessary to do a more thorough study of their relevant properties. A new synthetic method was developed in our laboratory for CyPs, which allowed for a more detailed investigation of their properties, as well as the synthesis of various analogs. This study is reported in Chapter 2.

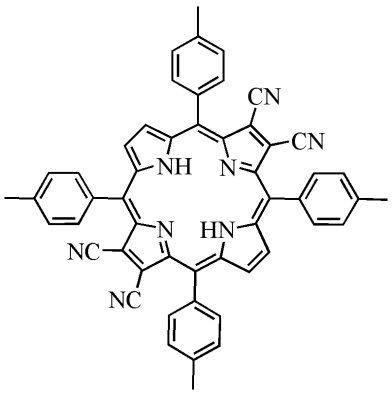

Figure 17. Example of a CyP, 7,8,17,18-tetracyano-5,10,15,20-tetrakis-(4-methylphenyl)porphyrin

From the study reported herein the new data on the properties of the CyP as well as the new synthetic method which allows for a wider variety of CyP with various functional groups to be synthesized, CyPs for the first time could be used in several studies in molecular systems toward solar energy conversion. A CyP was studied as a photosensitizer in a DSSC, to initially study its electron injection properties before utilizing it in a more complex photochemical set up, for water oxidation see Chapter 6. One of the unique properties of the CyP that was re-examined was the low-lying LUMO orbitals which makes them very strong electron acceptors due to the electron withdrawing effects of the cyano groups as well as their position on the porphyrin macrocycle. The electron accepting properties of CyP were recognized and it was used as an acceptor in a proton coupled electron transfer system, and in a porphyrin-carotene dyad to study the electron and energy transfer processes in these types of complexes in artificial and natural systems; see Chapters 4 and 5 respectively. C_{60} is generally used as the electron acceptor in D-A complexes in part due to its reduction potential being one of the highest in compounds suitable for these photoinduced charge separation systems. The CyP

reduction potentials are significantly higher than those of the C_{60}, which make them even better electron acceptors. This instigated the design and synthesis of a novel molecular triad that utilizes a CyP as an ultimate electron acceptor from a C_{60} radical anion. In this triad the CyP allows the C_{60} to act as an electron transfer bridge accepting an electron from a donor and sequentially donating an electron to the CyP.

This particular electron transfer reaction has not been studied until now, although there has been an extensive amount of work on porphyrin-C_{60} compounds in our laboratory, and elsewhere. The more traditional systems study the electron transfer process between the porphyrin and the C_{60} that use the C_{60} as an electron acceptor in a traditional fashion. Many variations of these kinds compounds have been synthesized, including multicomponent systems. These systems are designed with various linkers, orientation, and chromophores, in order to study the electron transfer properties and be able to optimize the forward electron transfer. In fact it was here in our laboratory that the first example of a porphyrin-C_{60} artificial reaction center was reported. These studies have provided us with valuable insight into the design of efficient electron transfer systems. In the next section the results and analysis of a select few studies of these more traditional porphyrin-C_{60} compounds will be discussed to give the reader a broader idea of these types of systems and the information they provide, before describing the design and results of the triad.

1.11 Porphyrin-C_{60} Systems, a Brief Review of Select Studies

The first example of these systems was studied in our laboratory. A porphyrin and a Zn(II) porphyrin linked to a C_{60} through a bicyclic ridge bridge was synthesized by

Liddell, P et al., and the photophysical processes were studied, see Figure 18.[103] The C_{60}-porphyrin dyads took a folded conformation where the C_{60} was over the porphyrin and the center-to-center (R_{CC}) distance from the porphyrin to the C_{60} was 7 A. After photoexcitation these compounds underwent a photoinduced singlet-singlet energy transfer from the porphyrin to the C_{60} followed by a through space intramolecular photochemical electron transfer (both processes with a rate constant of ~2 X 10^{11} s^{-1}) in benzonitrile forming the charge separated states of, $ZnP^{\bullet+}$ - $C_{60}^{\bullet-}$, and $H_2P^{\bullet+}$-$C_{60}^{\bullet-}$. [23,56,103]

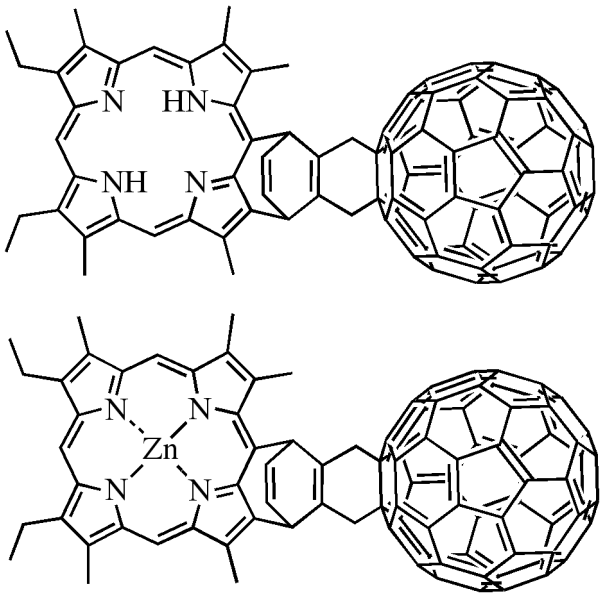

Figure 18. Structure of Zn(II)Porphyrin-C_{60} (P_{Zn}-C_{60}), and Free base porphyrin-C_{60} (P-C_{60}) Dyads synthesized by Liddell, P et al.[103]

Several other dyads with various linkers have been synthesized to test the electron transfer properties of C_{60} linked porphyrins with various linkers and different distances between the porphyrin and C_{60}.[55,56] These studies tested the properties of photoinduced electron transfer between porphyrins and C_{60} when linked through an amido bond in

various positions on the meta, ortho, and para position of a meso-phenyl ring on a porphyrin, see Figure 19.[56]

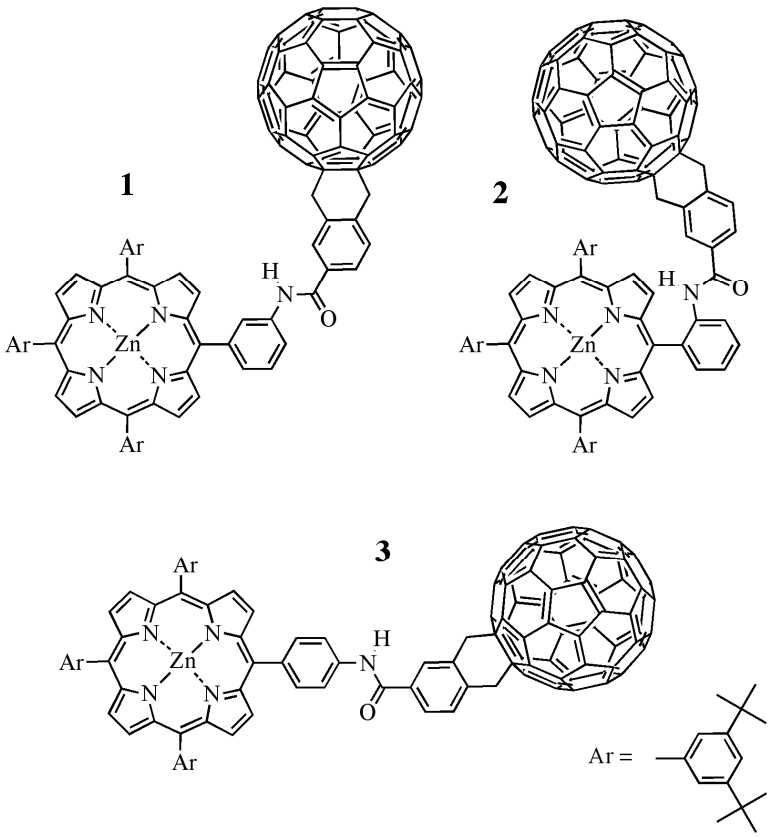

Figure 19. Structures of C_{60} linked to a meso-porphyrin aryl ring at linked to via an amido bond at the 1. meta, 2. ortho, an 3. para positions.[56]

These dyads have a center-to-center distance (R_{CC}) ranging from 18.6 A to 12.5 A, with one of them adopting a folded conformation similar to the dyad synthesized by Liddell, P. in 1994 as described above. These compounds exhibited photoinduced charge separation and subsequent charge recombination. The compound which had the linkage at the meta position of the meso-phenyl ring exhibited rates of charge separation and charge recombination 5 times slower than on the para or ortho positions. In THF the excited singlet state of the porphyrin equilibrates with the excited singlet state of the C_{60} and both

excited states undergo an electron transfer to give the charge-separated state. The difference of the rates between dyads can be explained through the larger electron densities at these positions, vs the meta, which would decrease the electronic coupling between the chromophores. These compounds exhibited photoinduced electron transfer as the main pathway in both benzene and THF, in contrast to the P-C_{60} system by Liddell due to the enhanced electronic coupling of these dyads. [55,56]

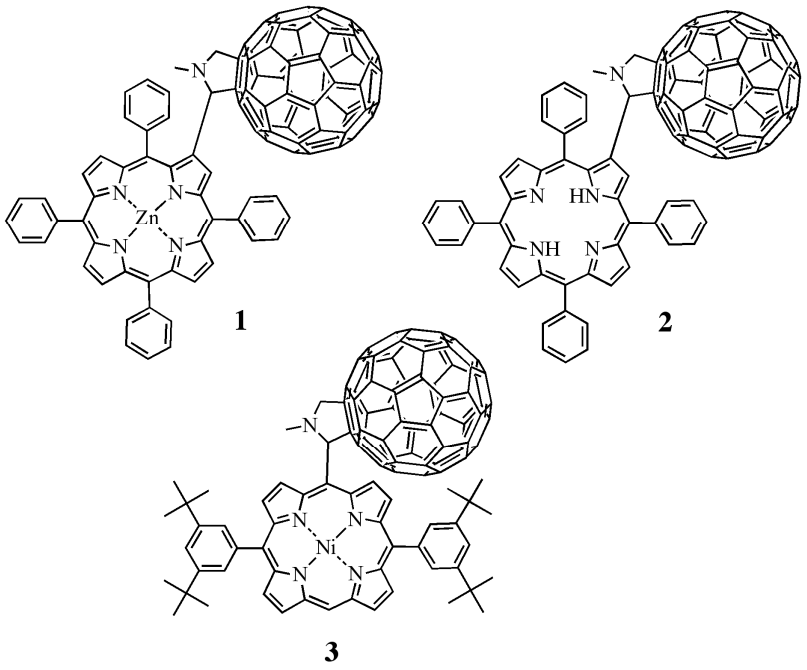

Figure 20. 1. Zn(II) porphyrin and 2. Free base porphyrin linked to C_{60} via a pyrrolidine linker to the beta position, by Gust, D. in collaboration with Reed, C. A.[105] 3. Ni(II) porphyrin linked to C_{60} via a pyrrolidine linker to the meso position.[106]

Compounds of these kinds were further studied by Gust, D. in collaboration with Reed, C. A. by linking the porphyrin to the C_{60} via a pyrrolidine spacer linked to the beta position of a zincated and free base porphyrin.[104,105] A similar dyad with this kind of

linkage was also prepared by Imahori, H where the porphyrin is linked to the C_{60} at a meso position, still via a pyrrolidine spacer.[106]

In the P-C_{60} dyads synthesized by Gust, D., the initial singlet excited state of the porphyrin, in toluene, undergoes singlet singlet energy transfer to the C_{60}, which then undergoes intersystem crossing to the triplet state and is in equilibrium with the porphyrin triplet state. In polar solvents photoinduced electron transfer competes with energy transfer from the porphyrin first excited singlet state to the C_{60}, and the porphyrin can quench the C_{60} excited singlet state by electron transfer. The quantum yield of the resulting charge separated state is near unity, and it has a lifetime of 50 ps with Zn(II) porphyrin and 290 ps with a free base porphyrin. [56] In comparison the meso linked C_{60} exhibited theoretically stronger electronic coupling due to the position of the linkage, but there was no reported charge transfer.[56] This illustrates the importance of the type of linkage between the two chromophores, including the position in respect to the molecular orbitals. Comparing the results of these studies of various porphyrin-C_{60} dyads shows that the magnitude of the electronic coupling plays a significant role in energy vs electron transfer. Many other compounds involving porphyrins and fullerene dyads with various linkers and electron donors have been synthesized and studied since then.[53]

A problem with these systems is that the lifetime of this charge separated state rapidly decays through charge recombination, which doesn't allow for use of this energy.[26,107] As mentioned previously increasing the distance between the charges leads to longer-lived charge separated states. There have been a number of compounds designed and studied since the 1980s that utilize a multistep electron transfer approach to reduce the amount of

charge recombination in donor-bridge-acceptor molecules. [5,17,22,23,51] These systems incorporate a third component thermodynamically able to carry out another electron transfer after the initial charge separated state has been formed.[5] By using this method, charge separated states with lifetimes of hundreds of microseconds to even a few milliseconds have been detected.[17] These compounds are designed so there is rapid electron transfer through a series of intermediate donor acceptor compounds linked together, to form a final charge separated state. This process spatially separates the electron and the hole which causes a longer lived charge separated state.[17]

The Gust, Moore, Moore group designed and studied a carotenene-porphyrin-quinone C-P-Q molecular triad that helped future designs of these multi step electron transfer systems (see Figure 21).[108]

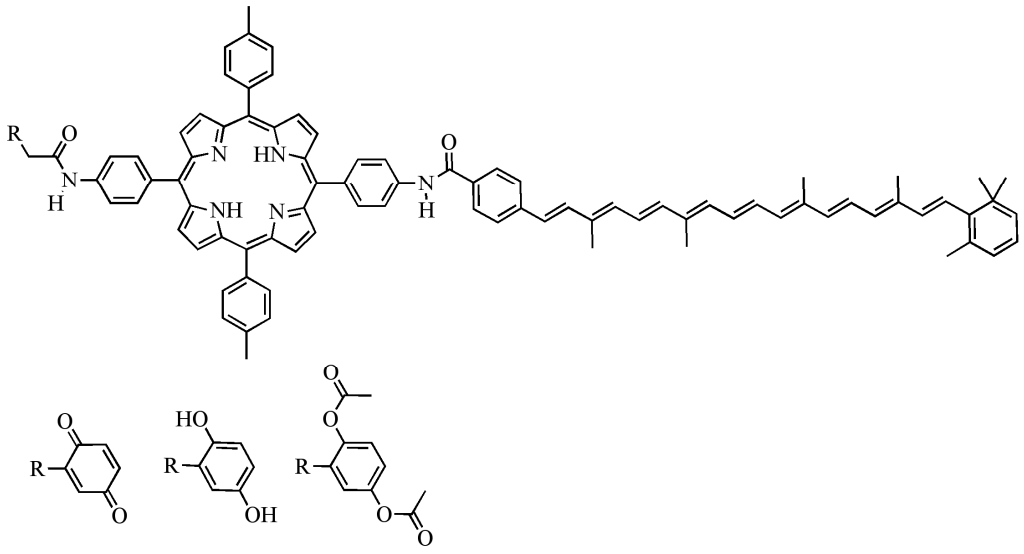

Figure 21. Structure of carotenene-porphyrin-quinone triad.[108]

After excitation of the porphyrin electron transfer occurs from the P* to the quinone generating the charge separated state C-$P^{\cdot+}$-$Q^{\cdot-}$. A second electron transfer occurs thereafter generating the final charge separated state $C^{\cdot+}$-P-$Q^{\cdot-}$. This triad uses the benefits of spatially separating the final charge separated state hindering charge recombination.[5] This compound generated a charge separated state lifetime of 170 ns in dichloromethane, which increased to 2.5 microseconds in electrolyte-saturated solvent. When compared to the fast decay of a simple porphyrin-quinone complex[30,109,110], this result reinforces the advantages of the multistep method.[5] The design of this triad was expanded to developing tetrad and pentad complexes, which successfully carried out multiple electron transfer steps resulting in long lived charge separated states by having an even greater spatial separation.[5] The utilization of fullerenes in these larger systems was recognized and these multicomponent systems using C_{60} as the electron acceptor were later designed and studied with more electron transfer steps.[23,58]

A C_{60} was first used in a carotene porphyrin fullerene Car-P-C_{60}, triad by Liddell et al. in 1997. Excitation of the porphyrin and sequential electron transfers generated a charge separated state with a lifetime of 170 ns, in 2-methyltetrahydrofuran.[5,111] This triad was further expanded utilizing carotenes with a lower potential and various porphyrins such as a dimesitylporphyrin (which affects the electronic coupling and thermodynamic driving force), see Figure 22.[54]

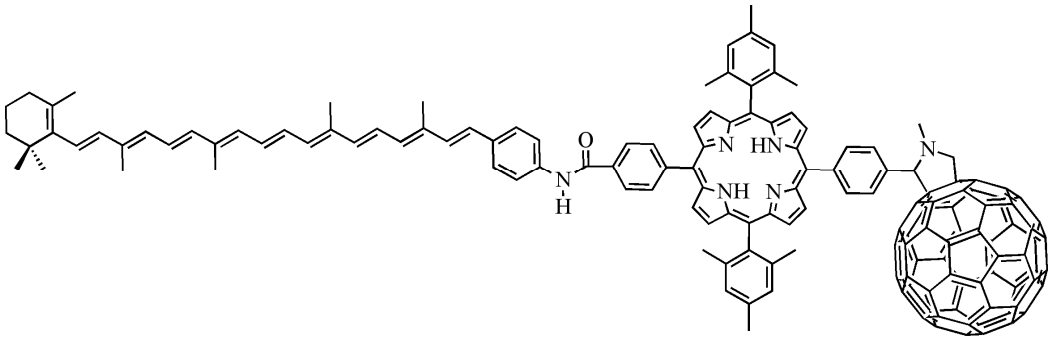

Figure 22. Structure of carotene-porphyrin-fullerene triad synthesized and studied by Liddell et al.[54]

These triad systems are useful models for studying the natural photosynthetic processes.[54] The final charge separated state occurs in three steps; 1) excitation of the porphyrin to produce the porphyrin first excited singlet state. 2) photoinduced electron transfer to give the porphyrin radical cation and $C_{60}^{\cdot -}$. 3) charge shift to give the final charge separated state.[54] The triad shown in Figure 22 was found to generate the final charge separated state with a quantum yield near unity (0.95), storing about 1 eV of the 1.9 eV photon energy as electrochemical potential, with a life time of 57 ns.[5,54,111]

These studies are among many where C_{60} has been shown be invaluable in these systems due to its unique electron transfer properties. Further understanding its electron transfer properties in these types of systems could aid in efficient solar energy conversion. Due to the strong electron accepting properties of C_{60} it is generally used as the final electron acceptor in these electron transfer studies. There are a few studies using it as an electron transfer mediator in an electron transfer process in a self-assembled mono-layer in a photoelectrochemical cell with the functional molecules anchored to a surface of an electrode. [23,65] A C_{60}-porphyrin dyad with a methylthio group to anchor it to a gold electrode, along with only porphyrin anchored to the electrode, was one of the

compounds studied.[23] Photoelectrochemical experiments were conducted using a platinum electrode as the counter electrode and methylviologen as an electron carrier. These experiments compared the photocurrent generated between the two systems where high photocurrent is an indication of forward electron transfer. They demonstrated that the intensity of the photocurrent in the system utilizing the C_{60} as a mediator is about five times larger when compared to a system that has only the free base porphyrin bound to the surface of the electrode. This showed that the C_{60} could be used as an electron transfer mediator. Imahori and Sakata et al. developed a similar system that modified a gold electrode with a ferrocene-porphyrin-fullerene (F-P-C_{60}) triad to study multistep electron transfer, where $C_{60}^{\cdot -}$ donates an electron to a free mediator in solution, to methylviologen. The results of photocurrent generated from photoinduced electron transfer when compared to the photocurrent generated with a similar system not containing the ferrocene or C_{60} moiety, had an intensity of two orders of magnitude larger. This indicated that in this system the C_{60} also acts as an effective electron mediator and that C_{60} in part is responsible for the increase in the efficiency. These experiments show that the use of C_{60} in this kind of system also aids the initial photoinduced electron transfer from the porphyrin to the C_{60} must out compete the deactivation pathway to the gold electrode, or charge recombination to the ground state.

The results from these studies that utilize the reduced C_{60} as an electron donor indicate that it may be beneficial in electron transfer systems to utilize the C_{60} in this way in covalently bound molecular system, where the coupling between the C60 and the donor could be more controlled than in the linkages in the systems described above. Due to the energetics of the C_{60} and of the compounds that have the necessary properties to be used

in artificial photosynthetic systems, there have been no studies that utilized the C_{60} as a mediator for electron transfer in a bound system. The initial investigation into CyP, suggested that it might have the necessary reduction potentials to be able to drive this electron transfer from a C_{60} radical anion. The new synthetic method developed for the CyP, as described in the next chapter, increased synthetic availability of these porphyrins and allowed for them to be studied more thoroughly for use in artificial photosynthetic systems. The results from this study prompted the design of a triad that utilizes C_{60} as an electron transfer mediator with its radical anion donating an electron to a CyP. This would allow for the electron transfer reaction from a C_{60} to be investigated in a covalently bound system.

This system was designed to have three compounds covalently linked, a triad. This triad is a simple model system which is designed to use the C_{60} as an electron transfer bridge, D-C_{60}-A, where D is a sensitizer and can donate an electron from its excited state to C_{60}, and A is a compound which is theromodynamicaly poised to accept an electron from $C_{60}^{\cdot -}$. Theoretically the initial electron transfer would occur from the excited state of D* to the C_{60} generating the first charge separated state $D^{\cdot +}$-$C_{60}^{\cdot -}$-A an known electron transfer processes as described in some of the example systems in the text above. A second electron transfer would generate the final charge separated state $D^{\cdot +}$-C_{60}-$A^{\cdot -}$. In the first electron transfer step the rate from D to C_{60} would be increased, and the rate of the charge recombination process would be hindered when compared to an electron transfer without C_{60}. Having the A compound electronically coupled to C_{60} theoretically would allow a second electron transfer from the $C_{60}^{\cdot -}$ to A generating the final charge separated state $D^{\cdot +}$-C_{60}-$A^{\cdot -}$. This second electron transfer step would both structurally and

energetically further separate the charges while capitalizing on the favorable electron transfer properties due to the C_{60} in the first step. The structural design of this triad ideally would put the donor and acceptor with in close proximity to the C_{60} and would allow for a strong electronic coupling between the them and the C_{60}, as well as low the reorganization energy, as reorganization energy decreases as the separation between donor and acceptor decreases.[28,112] In theory a strong coupling with small reorganization energy would put the CR process in the Marcus inverted region, and push the free energy change ($-\Delta G$) forward electron transfer process to approach the λ.[28]

Chapter 2 New Synthetic Method for β-Cyano Substituted Porphyrins.

A new synthetic method for the synthesis of β-cyano porphyrins was developed in order to be able to design and synthesize these porphyrins with a range of substituents for use in light driven water oxidation studies and in other studies which are directed toward the design of artificial photosynthetic systems. The following chapter is a report of the method that I developed for the synthesis of β-cyano porphyrins.

This chapter has been adapted from a report submitted for publication: Antaeres Antoniuk-Pablant, Yuichi Terazono, Jackson D. Megiatto Jr., Benjamin Sherman, Ana L. Moore, Thomas A. Moore, Devens Gust

2.1 Abstract

A new method has been developed for the synthesis of β-cyano substituted porphyrins. This approach involves reaction of $Zn(CN)_2$ with brominated zinc porphyrins in the presence of tris-(dibenzylideneacetone)dipalladium. The cyanation can be completed under milder conditions than are employed by previous methods and gives improved yields. By using *N*,*N*-dimethylacetamide as the solvent and 1,1'-bis-(diphenylphosphino)ferrocene as the ligand, as well as several reagents to aid the availability of cyanide in the reaction and keep the Pd(0) active, this cyanation reaction has given yields of up to ~50%. The zinc may be removed after cyanation is complete. The procedure allows for the cyanation of porphyrins with relatively sensitive functional groups, permitting the synthesis and study of specialized cyanoporphyrins. Examples of its application to a range of substituted tetra-arylporphyrins are reported, and absorption and electrochemical properties of the compounds prepared are given.

2.2 Introduction

Many of the properties of synthetic porphyrins are generally similar to those of their natural chlorophyll relatives, and for this reason, porphyrins are often used as light absorbers in artificial photosynthetic systems.[1-10] Porphyrins can act as antennas, wherein they absorb light and transfer singlet excitation energy to other chromophores, and as components of artificial reaction centers, where they use excitation energy to initiate electron transfer to or from acceptor or donor moieties to generate charge separated states. These charge separated states preserve some of the photon energy as electrochemical potential energy.

Porphyrins with cyano groups in β-positions are potentially attractive for these purposes because they absorb light at longer wavelengths than most porphyrins lacking such substituents, and thus can in principle make more efficient use of the solar spectrum in energy conversion applications. Furthermore, addition of electron withdrawing groups such as cyano groups at the β-positions of a porphyrin stabilizes both the lowest unoccupied molecular orbitals (LUMOs) and the highest occupied molecular orbitals (HOMOs). As a result, cyanoporphyrins are more easily reduced than their unsubstituted analogs, making them well suited as electron acceptors in photoinduced electron transfer reactions. They can replace more commonly used electron acceptors such as fullerenes or quinones.[11] Their radical cations are very strong oxidants, which could in principle make them useful for driving water oxidation in solar fuel production systems.

In spite of the advantages of β-cyanoporphyrins over other high potential porphyrins there have been no reports of the CyP used thus far in any kind of electron transfer

transfer system and even no reported emission data that is required to determine if the porphyrin is thermodynamically capable of injecting an electron into a semiconductor from an excited state, they have been little explored for such uses, due mainly to the difficulty of producing them synthetically. Therefore, a new route for their synthesis was developed which would allow them to be potentially explored in artificial photosynthetic systems.

The synthesis of the CyP focuses on the chemistry of the β-positions of the porphyrin. These localized β-β'pyrrolic bonds act as aromatic double bonds, and therefore can undergo reactions that are developed for such bonds such as an electrophilic substitution.[81] The bromination by N-bromosuccinimide first brominates the two localized β-β'pyrrolic bonds that have higher electron density than the two other β-pyrroles[113] through an electrophilic aromatic substitution or through a radical mechanism.[80] The first tetrasubstituted β-cyanoporphyrin was reported by Callot in 1973.[12] Bromination of 5,10,15,20-tetraphenylporphyrin with *N*-bromosuccinimide (NBS) yielded a porphyrin with bromine atoms at four β-positions, and treatment of the nickel derivative of this compound with CuCN in pyridine yielded the tetracyano analog. Using the same synthetic method, Callot and coworkers synthesized various cyanoporphyrins.[13-16] In 1991, Crossley and coworkers reported that the tetrabromo-, and consequently the free base tetracyano-tetraarylporphyrins formed in this way have the 7,8,17,18 substituent pattern, wherein substitution occurs only on transannular double bonds, opposite one another on the porphyrin macrocycle.[17] A few additional reports of the synthesis of tetracyanoporphyrins have appeared since that time.[18, 19]

In these previous reports, the same basic method was employed to prepare the porphyrins. The method requires harsh conditions that are unsuitable for some kinds of substituted porphyrins. The cyanation step necessitates a copper catalyst, and if free base porphyrins or porphyrins containing zinc or other easily replaced metals are used in the cyanation step, copper is introduced into the macrocycle during the reaction. Removal of the copper requires the use of concentrated sulfuric acid. Bhyrappa *et al.* avoided the copper insertion by first incorporating nickel into the porphyrin,[19] but removal of the Ni(II) also requires strong acid. This method was attempted several times in our laboratory using $CuTMPBr_4$, and $NiTMPBr_4$, and a small amount of metallated CyP was synthesized. It was observed that the method produced several side products, which complicated the purification as well as resulted in overall low yields for the metallated CyP. The demetallation of both Cu and Ni CyP was also attempted in our laboratory using various strong acids and concentrations but was unsuccessful and resulted in little or no product due to porphyrin degradation, possible nitrile hydrolysis, or no demetallation. As tested in our laboratory Cu(II) insertion would also occur when Zn(II) was used to protect the macrocycle. Overall in the literature methods the demetallation step lowers the overall yield of the porphyrin as well as could limit the functionalization of the porphyrin.

It is known that aromatic halides may be converted to nitriles via palladium-catalyzed cross-coupling reactions,[20-35] and in 2006 Liu and Chen[36] reported synthesis of a β-trifluoromethylated porphyrin from a tetra-β-bromoporphyrin using such a reaction.[36] Based on these reports, we have investigated and developed a method for the preparation

β-cyanoporphyrins via palladium-catalyzed cross coupling. The palladium catalyzed cyanation we have developed gives yields of ca. 50% for simple porphyrins. The conditions of the reaction are relatively mild, employing temperatures up to 110° C. This method eliminates the use of CuCN, which avoids the insertion of Cu into the porphyrin macrocycle, and therefore eliminates the demetallation step which requires harsh conditions. The new approach opens up the synthesis of β-cyanoporphyrins that have relatively sensitive functional groups.

2.3 Results and Discussion

2.3.1 Synthesis of β-Cyanoporphyrins

The overall scheme for preparation of β-tetracyanoporphyrins is shown in Figure 23, and the compounds prepared are depicted in Figure 24. The requisite dipyrromethanes **A** were prepared from the corresponding aromatic aldehyde and pyrrole by addition of trifluoroacetic acid (TFA), and then triethylamine. Condensation of the dipyrromethane with the appropriate aldehydes under the conditions described previously[40-42] yielded the porphyrins **B**. Treatment of the porphyrins with recrystallized *N*-bromosuccinimide (NBS) in chloroform or dichloromethane solution beginning with one addition of 4.5 mol equivalents of NBS per mol of porphyrin in solution, followed by several portions of ~2.5 equivalents of NBS until complete reaction was observed, yielded the 7,8,17,18-tetrabromoporphyrins. Introduction of zinc yielded the zinc 2,3,12,13-tetrabromoporphyrins **C**, which were converted to the corresponding zinc β-cyanoporphyrins **D** as discussed above. In the case of the compounds where the R_1 groups are aryl groups bearing methoxycarbonyl substituents, hydrolysis of **D** with base

as discussed above yielded the corresponding acid derivatives. Finally, removal of the zinc with TFA gave the free base porphyrins **E.**

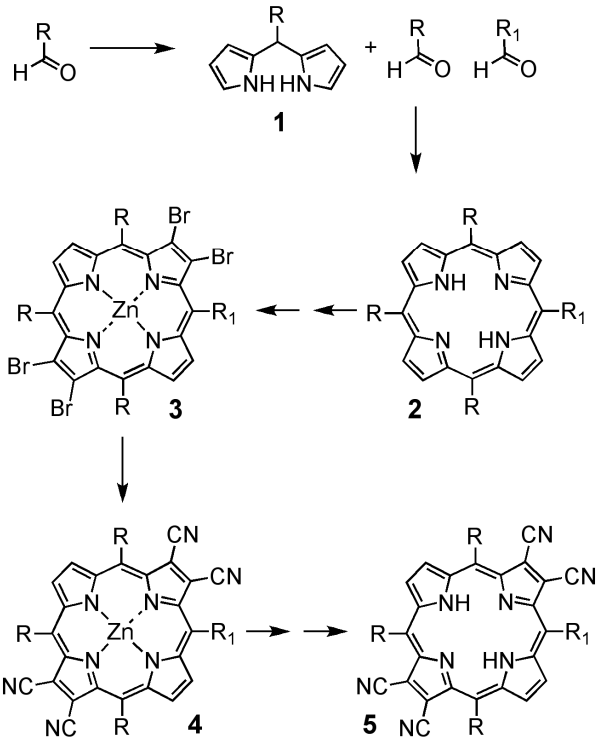

Figure 23. Synthetic scheme for zinc and free base β-cyanoporphyrins. See the text for reagents and conditions.

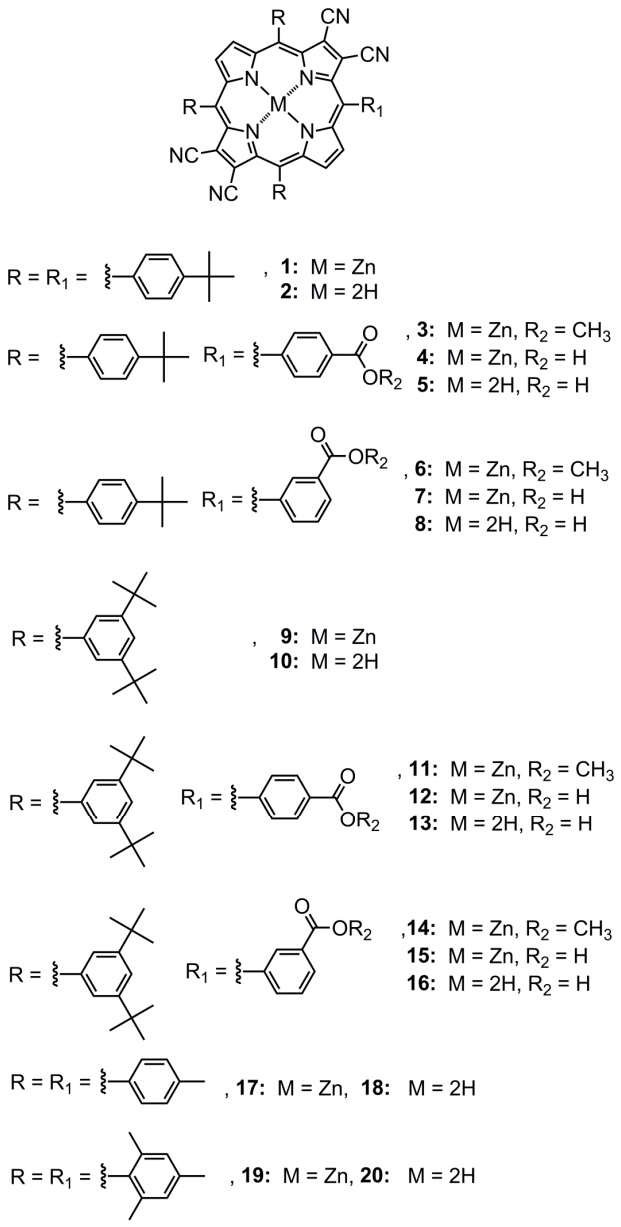

Figure 24. Porphyrins prepared using the cyanation procedure.

2.3.2 Electrochemical and Spectroscopic Properties

We obtained the absorption and emission spectra and selected electrochemical properties of the compounds synthesized, as these properties are relevant for possible

applications of these materials to solar energy conversion and other optoelectronic applications.

The electrochemical properties of the cyanoporphyrins were studied by cyclic voltammetry, and the redox potentials are reported vs. SCE in Table 1. Cyclic voltammetry was performed under an argon atmosphere in purified dichloromethane containing 0.1 M tetrabutylammonium hexafluorophosphate as supporting electrolyte. A Pt disk working electrode, Pt mesh counter electrode, and Ag^{+}/Ag quasi-reference electrode were employed. Potentials were determined using a ferrocene internal reference and the results were converted to SCE by referencing peaks to the first oxidation wave of ferrocene, which is assigned to be 0.45 V vs SCE in this solvent.[43] A typical voltammogram, that for free base compound **20**, is shown in Figure 25.

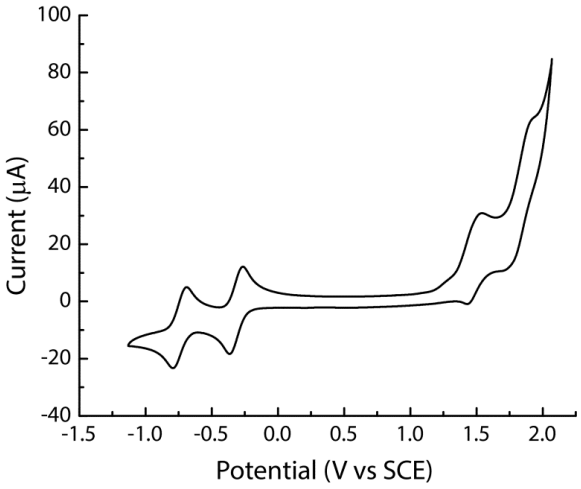

Figure 25. Cyclic voltammogram of free base porphyrin **20** in dichloromethane obtained under the conditions described in the text.

The free base cyanoporphyrins show two reversible reduction waves. The first oxidation wave is reversible and followed by a quasi-reversible second oxidation wave.

The free base cyanoporphyrins have higher oxidation potentials than their zinc containing analogs, and are more easily reduced. It will be noted that the cyanoporphyrins are much more easily reduced than the corresponding porphyrins without β-substituents, and are substantially more difficult to oxidize.

The UV-VIS absorption and emission maxima for the cyanoporphyrins in dichloromethane are given in Table 1.The absorption spectrum of **13** is shown in Figure 26.

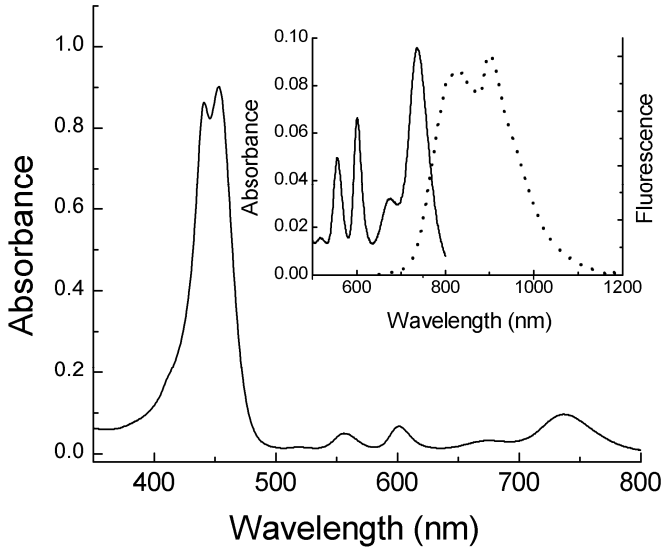

Figure 26. Spectrum of **13** in dichloromethane. The inset shows absorbance (solid line), and fluorescence (dotted line) with excitation at 451 nm.

In general, the UV/VIS maxima of the cyanoporphyrins are shifted to longer wavelengths as compared to porphyrins without β-substituents due to the electron withdrawing properties of the nitrile groups. As can be seen in Figure 25, the Soret band is split into two peaks. In terms of the Gouterman four orbital theory,[44] the Soret band (B) is due to electronic transitions from the b_2 orbital (HOMO) to the c_1 and c_2 LUMO orbitals. These transitions consists of two transition dipole moments in directions along a

set of axes, *x* and *y*, on the porphyrin which pass through the two sets of opposing pyrrole rings. At room temperature these transitions are observed as a single peak in most porphyrins.[44] Due to the electronic effects of the 4 cyano substituents on the antipodal β-pyrrole positions on only one axis, the energies of the c_1 and c_2 orbitals are no longer degenerate in these compounds, and this in turn leads to the observed split in the Soret band. The fluorescence spectrum of **13** is also shown in Figure 26. The spectrum features a relatively large Stokes shift and is not the mirror image of the longest-wavelength Q-bands. This is in contrast to most porphyrins, which show small Stokes shifts, and indicates that the relaxed excited singlet state has significant electronic differences from the ground state. It may indicate some charge-transfer character in the excited state.

Table 1. Spectroscopic and cyclic voltammetric data for the cyanoporphyrins

Cmpd	Soret By[a] λ_{max} (nm)	Soret Bx[a] λ_{max} (nm)	Q bands[a] λ_{max} (nm)	Emission[b] λ_{max} (nm)	Ox_1 ($E_{1/2}$, V vs SCE)	Ox_2 ($E_{1/2}$, V vs SCE)	Red_1 ($E_{1/2}$, V vs SCE)	Red_2 ($E_{1/2}$, V vs SCE)
1	443	459	660, 685	740	1.01	1.42	-0.59	-0.98
2	441	454	556, 600, 670, 738	781	1.22	--	-0.34	-0.61
3	443	454	657, 677	739	1.19	--	-0.38	-0.75
4	443	458	659, 681	--	--	--	--	--
5	445	459	555, 602, 672, 738	781	1.32		-0.31	-0.61
6	443	459	661, 685	737, ~827 (sh)	0.94	--	-0.64	-1.02
7	443	460	662, 689	--	--	--	--	--
8	441	453	556, 601, 668, 735	781	1.27	--	-0.42	-0.69 (E_p)
9	443	458	655, 677	711, ~776 (sh)	1.04	--	-0.62	-1.02
10	440	453	553,599, 667, 730	768	1.41	--	-0.38	-0.67
11	443	458	655, 679	713	1.18	--	-0.45	-0.88
12	443	458	657, 681	--	1.10	--	-0.54	-0.92
13	441	452	554, 599, 667, 729	768	1.38	--	-0.32	-0.62
14	444	456	655, 680	709	1.22	--	-0.72	-1.17
15	445	460	661, 685	712	--	--	--	--
16	443	453	555, 600, 669, 730	767	~1.29[d]	1.47	-0.37	-0.94 (E_p)
17	441	458	659, 680	737	~0.87	1.47	-0.47	-0.88
18	441	453	556, 601, 679, 737	783	1.28	1.51	-0.30	-0.58
19	444	460	662, 686	703, 770	1.22	1.65	-0.49	-0.95
20	439	451	552, 599, 673, 733	742, ~823 (sh)	1.48	1.80	-0.32	-0.75

[a]Spectra were obtained in dichloromethane. For the porphyrins bearing a carboxylic acid, a solution containing 2 % methanol was used to prevent aggregation.
[b]Emission spectra were obtained in dichloromethane, with excitation into the Soret band. For the porphyrins bearing a carboxylic acid, a solution of 2% methanol in dichloromethane was used.

2.3.3 Synthetic Method Development Discussion

The general method of synthesis of the β-cyanoporphyrins from the corresponding β-bromoporphyrins is illustrated in Figure 27.

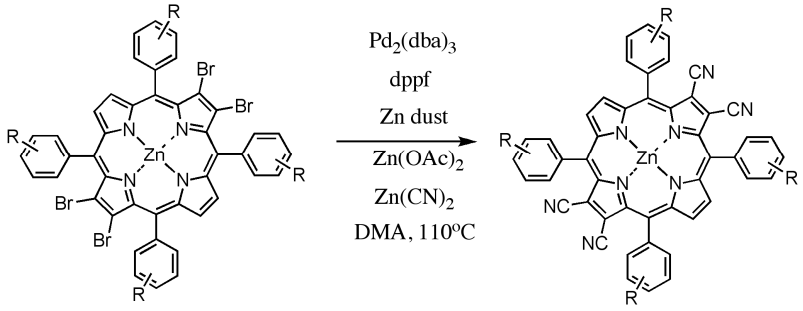

Figure 27. General synthetic scheme for cyanation of β-bromoporphyrins.

The method developed was modeled after a fluoroalkylation reaction which synthesized trifluoromethylated porphyrins.[114] This method used catalytic amounts of $Pd_2(dba)_3$, along with triphenylarsine, CuI, and methyl difluoro(fluorosulfonyl)acetate (FSO_2CF_2COOMe) as the fluoromethylating agent.[114] There are numerous methods studied for the cyanation of aromatic bromides that utilize tris(dibenzylideneacetone)dipalladium(0) as the catalyst along with various ligands and sources of cyanide.[115–130]

The first method developed for the cyanation of a zincated tetra-β-bromoporphyrin replaced the fluoromethylating agent with potassium ferrocyanide as it has been studied in several palladium catalyzed cyanation methods and possible benefits in a palladium catalyzed reaction have been reported. [123] This resulted in the cyanation of the tetra-bromo porphyrin, but with poor yields (<2%) due to a significant amount starting material present, partially cyanated porphyrin, and several side products due to the CuI.

CuI was removed from the reagents which improved the yield of the reaction. It was hypothesized that the low yield of this method is due to a number of problems including, solubility issues, slow reaction rates, catalyst poisoning, and dehalogenation.

Using this developed method as a starting point, several methods from palladium catalyzed cyanation of aryl bromides were then studied and gradually incorporated into the method to increase the yield of the reaction. The final method reproducibly synthesized a CyP with 56% yield for the cyanation step while eliminating the harsh demetallation step and replacing it with a mild Zn(II) demetallation step with near 100% yields

The catalyst is generated *in situ* from tris(dibenzylideneacetone)dipalladium(0) a well studied and highly used palladium catalyst for cyanation reactions. [116,128] Ligands such as triphenylarsine, tri-(o-tolyl)phosphine, or 1,1'-bis(diphenylphosphino)ferrocene (dppf) are commonly used for the cyanation of aromatic bromides,[116,128] and were tested during the development the method. Dppf resulted in the highest yields in our hands, and was used for most of the preparations. This ligand has been found to enhance the yields in other cyanation reactions.[116,126,130]

In addition to finding the right reagents to obtain higher yields for this specific reaction it is important to address various factors that can influence palladium catalyzed cyanation reactions and cause them to give low yields. It was hypothesized that catalyst deactivation [118,122] and a dehalogenation reaction that was occurring during the reaction were some of the major contributors to the initial low yields.

Catalyst deactivation can occur by oxidation of the active palladium (0) species to an inactive palladium (II) species by oxygen[122], and also by the formation of a palladium cyanide complex which is then unable to oxidatively add to an aryl halide.[118,120,125,131] Various reagents have been studied to aid the reduction of catalyst deactivation by oxygen, in addition to carrying out the reaction under an argon atmosphere. Zn dust has been used in palladium coupling reactions to reduce the inactive palladium(II) to the active palladium (0).[122,125,130] In addition to zinc dust, a study by Chidambaram, R. 2004 showed that the addition of 3-4 mol% of zinc acetate in addition to 3-4% mol of zinc acetate increased the conversion rate of aryl bromide to aryl cyanide. The role of the acetate is not fully known but it is thought that in combination with a reducing agent such as zinc dust it aids in keeping the catalyst active during the course of the reaction.[122] The addition of zinc dust as well as the addition of zinc acetate in several test reactions improved the yield in the CyP cyanation reaction in our laboratory.

Studies have shown that excess cyanide affects each step of the catalytic cycle in addition to causing the formation of a palladium cyanide complex which results in catalyst deactivation. [117,118,120,124,131] In order for the palladium catalyzed reaction to give high yields the rate of the reaction must be higher than the rate of the formation of the cyanide complex. The rate of both of these reactions is influenced mainly by the dissolution of the cyanide source and the ionizability of the M-CN bond in the cyanide source, and several studies have been done to obtain conditions that favor the palladium catalyzed cyanation reaction.

The choice of solvent and cyanide source influences these rates as there is a delicate balance between having sufficient cyanide in solution for the desired reaction to occur, limited cyanide in solution to reduce catalyst poisoning, as well as dissolving all compounds in solution. The solvent must dissolve the organic precursor and catalyst, and in addition the cyanide source. If the solvent is too non-polar, sufficient cyanide salt will not dissolve. On the other hand, too much cyanide ion in solution can exacerbate the problem of catalyst cyanation.[117,118,120,123] It was observed that 7,8,17,18 –tetrabromo-5,10,15,20-tetrakis-(4-methylphenyl)porphyrin has limited solubility in several solvents including DMF, DMSO, CH_2Cl_2, $CHCl_3$, and other organic solvents as reported elsewhere[81], therefore several analogues of bromo porphyrins were designed to increase the solubility without changing the redox potentials on any significant levels. This included a 7,8,17,18 -tetrabromo-5,10,15,20-tetrakis-(4-t-butylphenyl)porphyrin, and 7,8,17,18 –tetrabromo-5,10,15,20-tetrakis-(2,4,6-trimethylphenyl)porphyrin, all of which increased the solubility and therefore increased the yield.

There have been studies done using zinc bromide and water to aid in the availability of cyanide in the reaction mixture. In a study done by Buono et al. 2008 it was shown that catalytic amounts of zinc bromide can facilitate the reaction by aiding the dissolution of the zinc cyanide by the formation of a more soluble, non-inhibitory, and more active mixed zinc species.[118,132] Due to these findings a catalytic amount of zinc bromide was used in a trial porphyrin cyanation reaction, which seemed to minimally aid the reaction rate and the yield of the reaction. The study by Buono *et al.* also investigated the effects of water the rate on a cyanation reaction, which showed that a small amount of water in the reaction mixture can also aid the reaction rate but too much will slow the rate.[118] An

older study by Maligres, P. et al. 1999, also determined that using wet DMF over several similar polar solvents gave better results.[126] This was tested in the new method and it was found that dry solvents gave better results. This result indicated that catalyst poisoning may be the major issue. Several tests were done using an excess of zinc cyanide that resulted in a decrease of the yield supporting the hypothesis of catalyst poisoning. A second set of test reactions were done with an excess amount of tris(dibenzylideneacetone)dipalladium(0) which resulted in better yields and no starting material remaining. These results further supported catalyst poisoning being a main problem with the synthetic method.

Several cyanation methods with organic aryl bromide compounds were successful using cyanide sources such an zinc cyanide and potassium ferrocyanide[123] and solvents similar to dimethylformamide. In these reagents the metal-cyanide bond is less ionic than that of the more commonly employed NaCN or KCN, and this reduces the formation of the palladium cyanide complex.[120,133] These salts are also only sparingly soluble in DMF and other similar solvents. Due to zinc cyanide being the second most used cyanide source as of 2011[116] it was used for most of the method development, although potassium ferrocyanide was used in the first few reactions of this study and will be used in future developments of this method due to its lower toxicity, and possible role in stabilizing the active Pd species[123].

Another method of optimizing the amount of cyanide in the reaction is by adding the cyanide source to a preheated reaction mixture.[117] Based on a study for large scale palladium cyanation reactions of an aryl bromide it was found that the most robust

method used was when the zinc cyanide was added to a preheated mixture of the other reactants.[117] This allowed the catalyst to be activated before the cyanide is added to the system allowing for the dissolution rate of the cyanide to be slower than the potential maximum rate of the catalytic reaction.[117] This method was attempted and marginally increased the yield of the reaction.

One of the major problems during the reaction was the significant amount of debromination that was occurring during the reaction, thus synthesizing numerous porphyrin side products. This significantly decreased the yield of the reaction and made purification of the CyP difficult. Although dimethylformamide (DMF) is often used as a solvent for reactions it has been reported that DMF can be a hydride source in palladium catalyzed reactions.[119] A study by Muzart, J. and Zawisza, A., 2007, found that that the thermal and base catalyzed decomposition of DMF gives dimethylamine and carbon monoxide,[24, 37, 39] and that in the presence of secondary acyclic amines, the reduction of aryl bromides occurs under Pd(0) catalysis.[24] It is possible that these reactions also contribute to the debromination. After investigation of several solvent possibilities, *N*,*N*-dimethylacetamide (DMA) purified by distillation from barium oxide was found to give the best yields. The reactions were carried out at 110 °C. Yields are the best when the β-bromoporphyrin component is quite soluble in DMA, and solubility is in general facilitated by substituents on the phenyl rings.

The demetallation of the zinc β-cyanoporphyrins was carried out using a 10% (v/v) solution of trifluoroacetic acid (TFA) in dichloromethane and the free base porphyrins were obtained in nearly quantitative yields. Some of the β-cyanoporphyrins were

prepared bearing methoxycarbonyl groups on *meso*-aryl rings. It was found that to obtain the corresponding carboxylic acid, the ester must be hydrolyzed under base-promoted conditions while the Zn^{2+} is still in the center of the macrocycle in order to prevent hydrolysis/degradation of the cyanide groups. It is hypothesized that the electron donating Zn^{2+} causes the nitriles to be less susceptible to nucleophilic attack.

2.3.4 Future Improvements

It is thought that a high amount of catalyst deactivation is occurring during the reaction due to the high amounts of palladium catalyst that is necessary for a more complete reaction. Theoretically, this problem can be over come by using different reagents to keep the palladium active such as N,N,N',N'-tetramethylethylenediamine, which has been studied as an additive in palladium catalyzed cyanation of aryl bromides and has been found to prevent the deactivation of the palladium(0) complex even in the presence of up to five equivalents of excess cyanide. [125,134] Another method to reduce the amount of palladium deactivation is by controlling the rate at which cyanide is added, which controls the concentration of cyanide ions available in the system throughout the reaction. This allows the reductive coupling to occur continually and efficiently while preventing catalyst deactivation by reducing the amount of cyanide ion available for this process.[125] It is possible to do this by using an organic form of cyanide such as trimethylsilyl cyanide (TMSCN)[125,127], or acetone cyanohydrin[123].This would also allow a wider range of solvents to be used, which may aid in finding the ideal conditions and allow catalytic amounts of catalyst to give high yields of CyP.

2.4 Experimental Synthesis

2.4.1 General Procedures.

Pyrrole was freshly distilled before use. Dichloromethane was distilled from calcium hydride under nitrogen. Tetrahydrofuran was distilled over sodium and benzophenone under argon. *N*-bromosuccinimide was obtained from Sigma Aldrich and recrystallized before use. Compounds 3,*5-di-t-butylphenyldipyrromethane* (21), *5-(4-methoxycarbonylphenyl)-10,15,20-tris-(3,5-di-t-butylphenyl)porphyrin* (22),[40] *5-(4-tert-butylphenyl)dipyrromethane* (23),[41, 42] *5-(4-methoxycarbonylphenyl)-10,15,20-tris-(4-t-butylphenyl)porphyrin* (24)[45], *5-(2,4,6- trimethylphenyl)dipyrromethane* (25)[42], *5,10,15,20-tetrakis-(2,4,6-trimethylphenyl)porphyrin* (26),[46] *5,10,15,20-tetrakis-(4-methylphenyl)porphyrin* (27),[46], and *7,8,17,18–tetrabromo-5,10,15,20-tetrakis-(2,4,6-trimethylphenyl)porphyrin* (28)[47] were prepared following previously reported methods.

All NMR spectra were recorded on a 400 MHz Varian spectrometer. Samples were dissolved in $CDCl_3$ with TMS as an internal reference, unless otherwise stated. Mass spectra were obtained on an Applied Biosystems Voyager-DE STR matrix-assisted laser desorption/ionization time-of-flight spectrometer (MALDI-TOF). *Trans,trans*-1,4-diphenyl-1,3-butadiene was used as a matrix for the MALDI-TOF-MS measurements, with 5,10,15,20-tetrakis-(4-methylphenyl)porphyrin as the internal reference. Ultraviolet-visible absorption spectra were measured on a Shimazu UV2100U spectrometer. Thin-layer chromatography for dipyrromethanes and porphyrins was performed on silica gel GHFL or GHL plates (Analtech). Synthesis, workup and purification were performed in a darkened laboratory.

*2.4.2 5,10,15,20-Tetrakis-(4-t-butylphenyl)porphyrin (**29**)*

Porphyrin **29** was synthesized as a side product from the synthesis of **25** (see below). The product was purified by column chromatography on silica gel using 40% dichloromethane in toluene to yield purple crystals, mp >300 °C, yield, 150 mg (1%). ^{1}H NMR, δ (ppm) 8.86 (s, 8 H, pyrrolic H), 8.14 (d, J=7.9 Hz, 8 H, Ar), 7.75 (d, J=7.9 Hz, 8 H, Ar), 1.60 (s, 36 H, t-butyl H), -2.74 (s, 2 H, -NH); UV-visible, λ_{max} (nm, CH_2Cl_2): 419, 518, 553, 592, 648; MALDI-TOF-MS m/z; calcd for $C_{60}H_{62}N_4$ 839.16 [M^+], obsd 838.65.

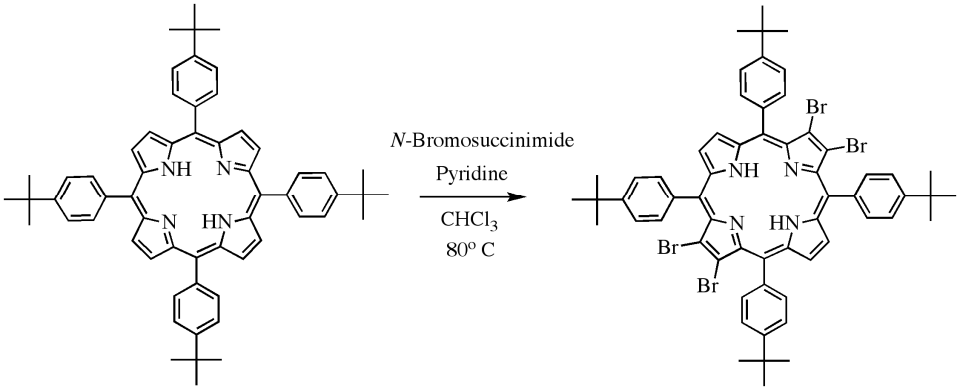

Figure 28. Synthetic scheme for the synthesis of 30

*2.4.3 7,8,17,18-Tetrabromo-5,10,15,20-tetrakis-(4-t-butylphenyl)porphyrin (**30**).*

In an oven-dried round bottomed flask equipped with a reflux condenser and a magnetic stir bar, **29** (150 mg, 0.179 mmol) was dissolved in dry $CHCl_3$ (30 mL) and stirred for 15 min at room temperature. The flask was placed in an oil bath which was brought to 80 °C, and *N*-bromosuccinimide (143 mg, 0.804 mmol) was added to the solution. The solution was allowed to reflux for 4 h after which pyridine (60 μL) was added and the solution was allowed to reflux for an additional 1 h. After a second addition of pyridine (60 μL) the solution was again allowed to reflux for 1 h. *N*-

bromosuccinimide (16 mg, 0.090 mmol) was added and the solution was allowed to reflux for 3 h, followed by a second addition of *N*-bromosuccinimide (16 mg, 0.090 mmol). After 2 h pyridine (120 μL) was added and the solution was allowed to stir for 15 min. The solvent was removed by distillation under reduced pressure and the product was removed by filtration and washed with MeOH (250 mL). The crude product was purified by column chromatography on silica gel using 40% dichloromethane in hexane as the eluent. The final product was recrystallized from $CHCl_3$ and MeOH to yield purple crystals, mp >300 °C, yield 150 mg (72%). ^{1}H NMR, δ (ppm) 8.80 (s, 2 H, pyrrolic H), 8.74 (s, 2 H, pyrrolic H), 8.11 (d, *J*=8.3 Hz, 4 H, Ar), 7.95 (d, *J*=7.9 Hz, 4 H, Ar), 7.79 (d, *J*=7.9 Hz, 4 H, Ar), 7.67 - 7.75 (m, 4 H, Ar), 1.57 (s, 36 H, *t*-butyl H), -2.73 (br s, 2 H, -NH); UV-visible, λ_{max} (nm, CH_2Cl_2): 439, 538, 688; MALDI-TOF-MS m/z; calcd for $C_{60}H_{58}Br_4N_4$ 1154.75 [M^+], obsd 1154.20.

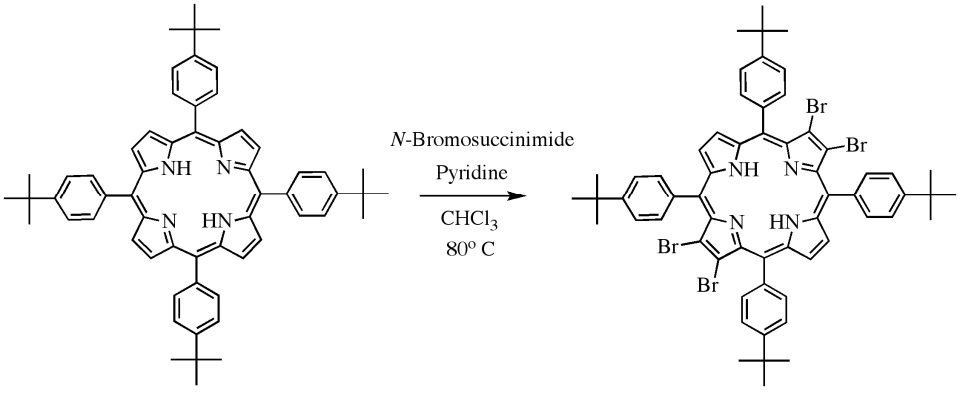

Figure 29. Synthetic scheme for the synthesis of 31

*2.4.4 Zn(II) 2,3,12,13-tetrabromo-5,10,15,20-tetrakis-(4-t-butylphenyl)porphyrin (**31**)*

Porphyrin **30** (150 mg, 0.130 mmol) was dissolved in dichloromethane (120 mL) in a round bottomed flask equipped with a reflux condenser and a magnetic stir bar. The flask was placed in an oil bath which was brought to a temperature of 50 °C. Zinc acetate (427 mg, 1.95 mmol) was dissolved separately in MeOH (4 mL), and the resulting solution was added to the flask containing the porphyrin. The solution was stirred in an oil bath at a temperature of 50 °C for 3.5 h, after which the solvent was distilled under reduced pressure, and the product was purified by recrystallization. The resulting crystals were washed with MeOH (50 mL) to yield pure porphyrin **31** as purple crystals, mp >300 °C, yield 100 mg (63%). ^{1}H NMR, δ (ppm) 8.71 (s, 4 H, pyrrolic H), 7.94 (br d, *J*=1.0 Hz, 8 H, Ar), 7.71 (d, *J*=8 Hz, 8 H, Ar), 1.59 (s, 36 H, *t*-butyl H); UV-visible, λ_{max} (nm, CH_2Cl_2): 452, 561, 601; MALDI-TOF-MS m/z; calcd for $C_{60}H_{56}Br_4N_4Zn$ 1218.14 [M^+], obsd 1218.65.

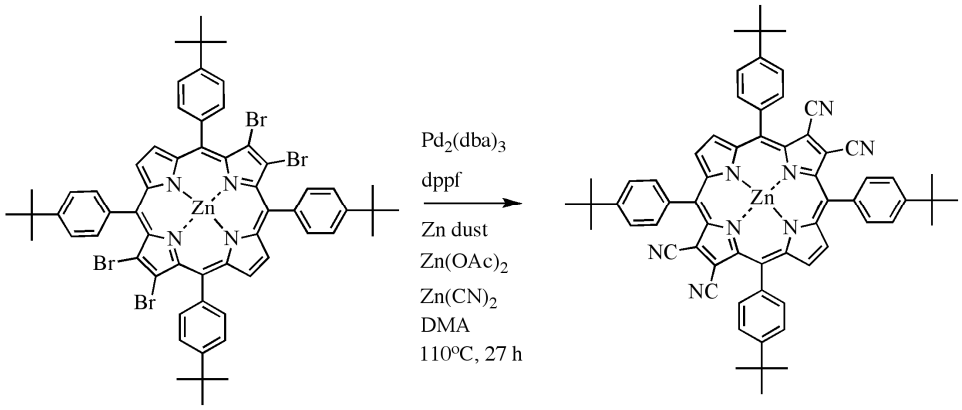

Figure 30. Synthetic scheme for the synthesis of 1

*2.4.5 Zn(II) 2,3,12,13-tetracyano-5,10,15,20-tetrakis-(4-t-butylphenyl)porphyrin (**1**)*

Porphyrin **31**, zinc acetate, 1,1'-bis(diphenylphosphino)ferrocene, and Zn dust were dried under vacuum overnight before use, and all glassware was oven dried. Porphyrin **31** (100 mg, 0.082 mmol), tris-(dibenzylideneacetone)dipalladium(0) (62.6 mg, 0.1 mmol), 1,1'-bis-(diphenylphosphino)ferrocene (75.8 mg, 0.1 mmol), zinc acetate (4.7 mg, 0.02 mmol), Zn dust (2.8 mg, 0.04 mmol), and zinc cyanide (24.1 mg, 0.2 mmol) were dissolved in deoxyxgenated *N*,*N*-dimethylacetamide (10 mL) in a Schlenk flask equipped with a magnetic stir bar. The Schlenk flask was placed in an oil bath which was brought to 115 °C. The solution was allowed to stir under argon for 27 h, after which the solvent was removed by distillation under reduced pressure. The reaction mixture was redissolved in dichloromethane, washed 4 times with 100 mL portions of water, and dried over anhydrous sodium sulfate. The solvent was removed by distillation under reduced pressure. The product was purified by column chromatography on silica gel with 15% EtOAc in toluene as the eluent, and then recrystallized from DCM and hexane to yield porphyrin **1** as purple crystals, mp >300 °C, yield 47.9 mg (56%). ^{1}H NMR, δ (ppm) 8.84 (s, 4 H, pyrrolic H), 7.93 (d, *J*=7.9 Hz, 8 H, Ar), 7.74 (d, *J*=8.4 Hz, 8 H, Ar), 1.58 (s, 36 H, *t*-butyl H); UV-visible, λ_{max} (nm), (CH_2Cl_2): 443, 459, 660, 685; MALDI-TOF-MS m/z; calcd for $C_{64}H_{56}N_8Zn$ 1002.59 [M^+], obsd 1002.44.

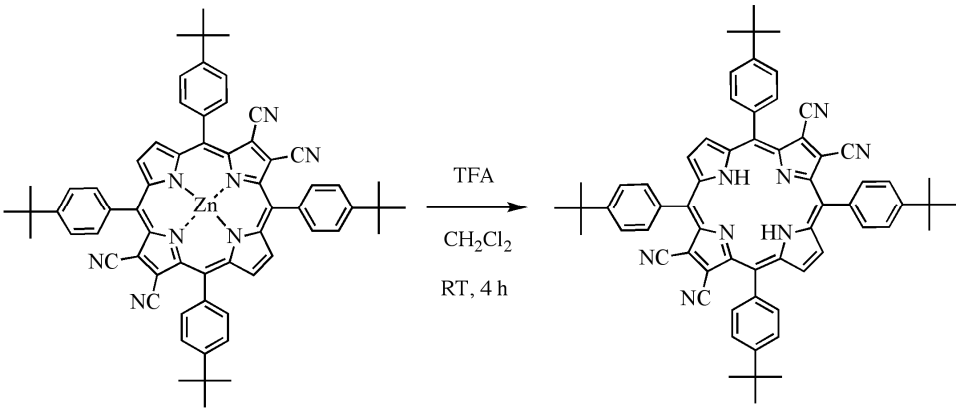

Figure 31. Synthetic scheme for the synthesis of 2

*2.4.6 7,8,17,18-Tetracyano-5,10,15,20-tetrakis-(4-t-butylphenyl)porphyrin (**2**)*

Porphyrin **1** (10 mg, 0.010 mmol) was dissolved in dichloromethane (50 mL) in a round bottomed flask equipped with a magnetic stir bar. Trifluoroacetic acid (7 mL) was added dropwise and the solution was stirred for 4 h at ambient temperature. Triethylamine (0.2 mL) was added and the solution was washed with a saturated solution of $NaHCO_3$ in water (100 mL) and then water (2 × 100 mL). The product was purified by preparative thin layer chromatography with 15% ethyl acetate in toluene as the solvent to give porphyrin **2** as purple crystals, mp >300 °C, yield 7.00 mg (74.6%). ^{1}H NMR, δ (ppm) 8.97 - 9.06 (m, 4 H, pyrrolic H), 8.05 (d, *J*=8.3 Hz, 8 H, Ar), 7.84 (d, *J*=8.3 Hz, 8 H, Ar), 1.61 (s, 36 H, *t*-butyl H), -2.41 (br s, 2 H, -NH); UV-visible, λ_{max} (nm), CH_2Cl_2): 441, 454, 556, 600, 670, 738; MALDI-TOF-MS m/z; calcd for $C_{64}H_{58}N_8$ 939.20 [M^+], obsd 940.08.

*2.4.7 7,8,17,18-Tetrabromo-5-(4-methoxycarbonylphenyl)-10,15,20-tris-(4-t-butyl-phenyl)porphyrin (**32**)*

Porphyrin **24** (500 mg, 0.6 mmol) was dissolved in 100 mL of chloroform stabilized with ethanol (0.75%) in a round bottomed flask equipped with a magnetic stir bar and a reflux condenser. N-bromosuccinimide (476 mg, 2.68 mmol) was added, the flask was placed in an oil bath which was heated to a temperature of 55 ^{o}C, and the solution was stirred for 1h. Pyridine (0.6 mL, 7.7 mmol) was added dropwise, and the solution was stirred for an additional 3.5 h. N-bromosuccinimide (106 mg, 0.596 mmol) was added and after 0.5 h pyridine (0.4 mL, 4.5 mmol) was added and the solution was stirred for an additional 1.5 h. A third portion of N-bromosuccinimide (212 mg, 1.19 mmol) and pyridine (0.4 mL, 4.8 mmol) was added and the solution was stirred for 3 h. The solvent was removed by distillation under reduced pressure and the product was purified by column chromatography on silica gel using 40% hexane in dichloromethane as the eluent. Final purification was done by recrystallization from dichloromethane and hexane, and the resulting purple crystals were washed with methanol to give pure porphyrin **32**, mp >300 °C, yield 377 mg (54.8%); ^{1}H NMR (400 MHz,) δ (ppm) 8.68 - 8.86 (m, 3 H, pyrrolic H), 8.59 (d, J=4.8 Hz, 1 H, pyrrolic H), 8.45 (d, J=7.9 Hz, 2 H, Ar), 8.28 (d, J=7.9 Hz, 2 H, Ar), 8.00 - 8.17 (m, 6 H, Ar), 7.79 (d, J=7.9 Hz, 6 H, Ar), 4.11 (s, 3 H, methoxy H), 1.59 (s, 27 H, t-butyl), -2.75 (br s., 2 H,-NH); UV-visible, λ_{max} (nm, CH_2Cl_2): 440, 538, 613, 690; MALDI-TOF-MS m/z; calcd for $C_{58}H_{52}Br_4N_4O_2$ 1156.68 [M^+], obsd 1156.10.

*2.4.8 Zn(II) 2,3,12,13-tetrabromo-5-(4-methoxycarbonyl)-10,15,20-tris-(4-t-butylphenyl)porphyrin (**33**)*

Porphyrin **32** (370 mg, 0.303 mmol) was dissolved in deaerated dichloromethane (50 mL) in a dry round bottomed flask equipped with a magnetic stir bar. Zinc acetate (1.1 g, 4.8 mmol) was dissolved in methanol (15 mL) in a separate vial and added to the round bottomed flask, and the solution was stirred at room temperature for 1 h. The reaction mixture was washed three times with water and the organic layer was dried over anhydrous sodium sulfate. The product was purified by recrystallization from methanol/hexane to give porphyrin **33** as purple crystals, mp >300 °C, yield 367 mg (94.0%). ^{1}H NMR (400 MHz,) δ (ppm) 8.65 - 8.81 (m, 3 H, pyrrolic H), 8.56 (d, *J*=5.1 Hz, 1 H, pyrrolic H), 8.37 (d, *J*=7 Hz, 2 H, Ar), 8.16 (d, *J*=Hz, 2 H, Ar), 7.94 (d, *J*=7.8 Hz, 6 H, Ar), 7.71 (d, *J*=7.0 Hz, 6 H, Ar), 4.10 (s, 3 H, methoxy H), 1.59 (s, 27 H, *t*-butyl H); UV-visible, λ_{max} (nm, 2% MeOH in CH_2Cl_2): 437, 569, 612; MALDI-TOF-MS m/z; calcd for $C_{58}H_{50}Br_4N_4O_2Zn$ 1220.07 [M^+], obsd 1220.57.

*2.4.9 Zn(II) 2,3,12,13-tetracyano-5-(4-methoxycarbonylphenyl)-10,15,20-tris-(4-t-butylphenyl)porphyrin (**3**)*

Porphyrin **33**, $Zn(OAc)_2$, 1,1'-bis(diphenylphosphino)ferrocene, and Zn dust were dried under vacuum overnight and all glassware was oven dried over night before use. Dimethylacetamide was stirred with BaO for 24 h, refluxed over BaO for 1 h, and distilled under reduced pressure before use. Porphyrin **33** (350 mg 0.287 mmol), tris(dibenzylideneacetone)dipalladium(0) (210 mg, 0.229 mmol), 1,1'-bis(diphenylphosphino)ferrocene (255 mg, 0.460 mmol), zinc acetate (16 mg, 0.09 mmol), Zn dust (9 mg, 0.1 mmol), and zinc cyanide (81 mg, 0.69 mmol) were dissolved

in deaerated *N,N*-dimethylacetamide (40 mL) in a Schlenk flask equipped with a magnetic stir bar. The Schlenk flask was placed in an oil bath which was brought to a temperature of 115 ^{o}C and the reaction mixture was stirred under argon for 20 h. Dichloromethane (60 mL) was added, the solution was washed 5 times with water (100 mL), the organic layer was collected and the solvent was removed by distillation under reduced pressure. The product was purified by column chromatography on silica gel with 20% ethyl acetate in toluene as the eluent. A final purification was done by recrystallization from dichloromethane and hexane to yield porphyrin **3** as purple crystals, mp >300 °C, yield, 115 mg (39.8)%. ^{1}H NMR, δ (ppm) 8.73 - 8.86 (m, 3 H, pyrrolic H), 8.60 (d, *J*=4.8 Hz, 1 H, pyrrolic H), 8.43 (d, *J*=8.3 Hz, 2 H, Ar), 8.17 (d, *J*=8.3 Hz, 2 H, Ar), 7.89 - 8.02 (m, 6 H, Ar), 7.67 - 7.83 (m, 6 H, Ar), 4.09 (s, 3 H, methoxy H), 1.60 (s, 27 H, *t*-butyl H); UV-visible, λ_{max} (nm, 2% MeOH in CH_2Cl_2): 443, 458, 657, 677; MALDI-TOF-MS m/z; calcd for $C_{62}H_{50}N_8O_2Zn$ 1004.5 [M^+], obsd 1002.87.

*2.4.10 Zn(II) 2,3,12,13-tetracyano-5-(4-carboxyphenyl)-10,15,20-tris-(4-t-butylphenyl)porphyrin (**4**)*

Porphyrin **3** (40 mg, 0.04 mmol) was dissolved in a solution of 33% methanol in tetrahydrofuran (17.4 mL) in a round bottomed flask equipped with a magnetic stir bar. A solution of 10% KOH in water (w/w) was added dropwise (3 mL) and the solution was stirred at room temperature for 3 h. Dichloromethane (10 mL) was added and the solution was washed 2 times with water (50 mL) and dried over anhydrous sodium sulfate, and the solvent was distilled under reduced pressure. The product was purified by recrystallization from toluene and ethyl acetate to give porphyrin **4** as purple crystals, mp >300 °C, yield 30 mg (76%). ^{1}H NMR, δ (ppm) 8.73 - 8.87 (m, 3 H, pyrrolic H), 8.63 (d, *J*=4.8 Hz, 1 H,

pyrrolic H), 8.45 (d, *J*=8.3 Hz, 2 H, Ar), 8.17 (d, *J*=7.9 Hz, 2 H, Ar), 7.97 (m, 6 H, Ar), 7.73 - 7.84 (m, 6 H, Ar), 1.53 - 1.69 (m, 27 H, *t*-butyl H); UV-visible, λ_{max} (nm, 2% MeOH in CH_2Cl_2): 443, 458, 659, 681; MALDI-TOF-MS m/z; calcd for $C_{61}H_{48}N_8O_2Zn$ 990.5 [M^+], obsd 988.95.

*2.4.11 7,8,17,18-Tetracyano-5-(4-carboxyphenyl)-10,15,20-tris-(4-t-butylphenyl)porphyrin (**5**)*

Porphyrin **4** (30 mg) was dissolved in a solution of 13.8% ethyl acetate in dichloromethane (58 mL) in a round bottomed flask equipped with a magnetic stir bar. Trifluoroacetic acid (7 mL) was added dropwise and the solution was stirred overnight at ambient temperature. Triethylamine (0.2 mL) was added and the solution was washed with 5% (w/w) $NaHCO_3$ (100 mL) and then water (2 × 100 mL). The product was purified by preparative thin layer chromatography with 20% ethyl acetate in toluene as the solvent to give porphyrin **5** as purple crystals, mp >300 °C, yield, 25 mg (89%). ^{1}H NMR, δ (ppm) 8.98 - 9.10 (m, 3 H, pyrrolic H), 8.83 (d, *J*=4.9 Hz, 1 H, pyrrolic H), 8.53 (d, *J*=7.9 Hz, 2 H, Ar), 8.25 (d, *J*=7.9 Hz, 2 H, Ar), 7.97 - 8.09 (m, 6 H, Ar), 7.76 - 7.88 (m, 6 H, Ar), 1.51 - 1.68 (m, 27 H, *t*-buty), -2.44 (d, *J*=7.9 Hz, 2 H, -NH); UV-visible, λ_{max} (nm, CH_2Cl_2): 445, 459, 555, 602, 672, 738; MALDI-TOF-MS m/z; calcd for $C_{61}H_{48}N_8O_2Zn$ 927.10 [M^+], obsd 927.59.

*2.4.12 5-(3-Methoxycarbonylphenyl)-10,15,20-tris-(4-t-butylphenyl)porphyrin (**34**)*

Dipyrromethane **23** (10 g, 0.04 mol), 4-*t*-butylbenzaldehyde (3 mL, 0.02 mol), and methyl 3-formylbenzoate (3 g, 0.02 mol) were dissolved in dry and deoxygenated dichloromethane (1.8 L) under argon in a round bottomed flask equipped with a magnetic

stirrer. Trifluoroacetic acid (4.9 mL, 0.1 mol) was added dropwise and the solution was stirred for 3 h at room temperature. Next, 2,3-dichloro-5,6-dicyano-1,4-benzoquinone (12.3 g, 0.1 mol) was added and the solution was stirred for 5 h. The solvent was removed by distillation under reduced pressure and the reaction mixture was run through a silica gel pad with dichloromethane as the eluent. The product was purified by column chromatography on silica gel using a solution of 40% dichloromethane in toluene as the eluent to give porphyrin **34** as purple crystals, mp >300 °C, yield, 1.2 mg (7.9%). ^{1}H NMR, δ (ppm) 8.82 - 8.97 (m, 6 H, pyrrolic H), 8.74 (d, *J*=4.9 Hz, 2 H, pyrrolic H), 8.44 - 8.52 (m, 1 H, Ar), 8.41 (dt, *J*=7.7, 1.4 Hz, 1 H, Ar), 8.07 - 8.21 (m, 6 H, Ar), 7.84 (t, *J*=7.7 Hz, 1 H, Ar), 7.71 - 7.80 (m, 6 H, Ar), 3.98 (s, 3 H, methoxy H), 1.57 - 1.65 (m, 27 H, *t*-butyl H), -2.76 (s, 2 H, -NH). UV-visible, λ_{max} (nm, CH_2Cl_2): 419, 517, 553, 591, 647; MALDI-TOF-MS m/z; calcd for $C_{58}H_{56}N_4O_2$ 841.09 [M^+], obsd 840.63.

*2.4.13 7,8,17,18-Tetrabromo-5-(3-methoxycarbonylphenyl)-10,15,20-tris-(4-t-butylphenyl)porphyrin (**35**)*

Porphyrin **34** (300 mg, 0.4 mmol) was dissolved in chloroform (70 mL) stabilized with ethanol in a dry round bottomed flask equipped with a magnetic stir bar and reflux condenser. The round bottomed flask was placed in an oil bath which was brought to a temperature of 80 ^{o}C. *N*-bromosuccinimide (470 mg, 2.5 mmol) was added to the solution which was then allowed to reflux 2 h. An additional amount of *N*-bromosuccinimide (63 mg, 0.4 mmol) was added to the solution, which was refluxed for 1 h. After the reaction was complete as indicated by thin layer chromatography and MALDI mass spectrometry, the solvent was distilled under reduced pressure and the product was purified by column chromatography on silica gel using 0.5% triethylamine in dichloromethane as the eluent.

The final purification was done by column chromatography on silica gel using 50% hexane in dichloromethane as the eluent to yield porphyrin **35** as purple crystals, mp >300 °C, yield, 319 mg (77%). ^{1}H NMR, δ (ppm) 8.83 - 8.91 (m, 1 H, pyrrolic H), 8.72 - 8.81 (m, 3 H, pyrrolic H), 8.59 (d, *J*=5.3 Hz, 1 H, Ar), 8.49 (d, *J*=7.5 Hz, 1 H, Ar), 8.37 (d, *J*=7.5 Hz, 1 H, Ar), 8.11 (dd, *J*=7.9, 3.1 Hz, 6 H, Ar), 7.86 (t, *J*=7.7 Hz, 1 H, Ar), 7.80 (d, *J*=7.5 Hz, 6 H, Ar), 4.03 (s, 3 H, methoxy H), 1.53 - 1.64 (m, 29 H, *t*-butyl H), -2.75 (s, 2 H, -NH); UV-visible, λ_{max} (nm, CH_2Cl_2): 440, 538, 615, 687; MALDI-TOF-MS m/z; calcd for $C_{58}H_{52}Br_4N_4O_2$ 1156.68[M^+], obsd 1156.23.

*2.4.14 Zn(II) 2,3,12,13-tetrabromo-5-(3-methoxycarbonylphenyl)-10,15,20-tris-(4-t-butylphenyl)porphyrin (**36**)*

Porphyrin **35** (156 mg, 0.1 mmol) was dissolved in deaerated dichloromethane (20 mL) in a round bottomed flask equipped with a magnetic stirrer. Zinc acetate (443 mg, 2 mmol) was dissolved in MeOH (2 mL) and the resulting solution was added dropwise to the porphyrin solution, which was then stirred for 1 h at room temperature. The organic layer was washed three times with water (100 mL) and dried over anhydrous sodium sulfate to yield porphyrin **36** as purple crystals, mp >300 °C, yield, 124 mg (75.3%). ^{1}H NMR, δ (ppm) 8.77 - 8.85 (m, 3 H, pyrrolic H), 8.69 (s, 1 H, pyrrolic H), 8.63 (d, *J*=4.7 Hz, 1 H, Ar), 8.42 (d, *J*=7.4 Hz, 1 H, Ar), 8.26 (d, *J*=7.4 Hz, 1 H, Ar), 7.95 (d, *J*=6.7 Hz, 6 H, Ar), 7.80 (t, *J*=7.8 Hz, 1 H, Ar), 7.72 (d, *J*=8.2 Hz, 6 H, Ar), 3.93 (s, 3 H, methoxy H), 1.59 (s, 27 H, *t*-butyl H); UV-visible, λ_{max} (nm, 2% MeOH in CH_2Cl_2): 437, 570, 612; MALDI-TOF-MS m/z; calcd for $C_{58}H_{50}Br_4N_4O_2Zn$ 1220.07 [M^+], obsd 1219.95.

*2.4.15 Zn(II) 2,3,12,13-tetracyano-5-(3-methoxycarbonylphenyl)-10,15,20-tris-(4-t-butylphenyl)porphyrin (**6**)*

Porphyrin **36**, zinc acetate, 1,1'-bis(diphenylphosphino)ferrocene, and Zn dust were dried under vacuum overnight before use, and all glassware was oven dried. Porphyrin **36** (124 mg, 0.1 mmol), tris(dibenzylideneacetone)dipalladium(0) (75 mg, 0.1 mmol), 1,1'-bis(diphenylphosphino)ferrocene (90 mg, 0.2 mmol), zinc acetate (5.6 mg, 0.3 mmol), Zn dust (3 mg, 0.05 mmol), and zinc cyanide (29 mg, 0.2 mmol) were dissolved in deaerated *N,N*-dimethylacetamide (10 mL) in a Schlenk flask equipped with a magnetic stirrer. The Schlenk flask was placed in an oil bath that was heated to 115 ^{o}C and the solution was allowed to stir under argon for 17.5 h, after which the solvent was removed by distillation and the reaction mixture was redissolved in dichloromethane. The solution was washed five times with water (100 mL) and dried over anhydrous sodium sulfate, and the solvent was distilled under vacuum. The product was purified by column chromatography on silica gel with 15% EtOAc in toluene as the eluent, and then recrystallized from dichloromethane and hexane to give porphyrin **6** as purple crystals, mp >300 °C, yield, 30 mg (29%). ^{1}H NMR, δ (ppm) 8.70 - 8.90 (m, 3 H, pyrrolic H), 8.47 (d, *J*=5.3 Hz, 1 H, pyrrolic H), 8.29 (br s, 1 H, Ar), 8.16 (d, *J*=7.5 Hz, 1 H, Ar), 7.99 (br s, 2 H, Ar), 7.57 - 7.91 (m, 11 H, Ar), 3.36 (br s, 3 H, methoxy H), 1.59 (s, 9 H, *t*-butyl H), 1.56 (s, 9 H, *t*-butyl H), 1.53 (s, 9 H, *t*-butyl H); UV-visible, λ_{max} (nm, 2% MeOH in CH_2Cl_2): 443, 459, 661, 685; MALDI-TOF-MS m/z; calcd for $C_{62}H_{50}N_8O_2Zn$ 1004.52 [M^+], obsd 1002.45.

2.4.16 Zn(II) 2,3,12,13-tetracyano-5-(3-carboxyphenyl)-10,15,20-tris-(4-t-butylphenyl)porphyrin (7)

Porphyrin **6** (21 mg, 0.02 mmol) was dissolved in freshly distilled tetrahydrofuran (8 mL) in a dry round bottomed flask equipped with a magnetic stir bar. Methanol (4 mL) was added, followed by the dropwise addition of 17% w/w KOH in water (1.8 mL). The solution was allowed to stir at room temperature for 2 h or until reaction was complete as indicated by thin layer chromatography and mass spectrometry. The most volatile components of the solvent were removed by distillation at reduced pressure and the product was extracted from the remaining aqueous layer with dichloromethane. The organic layer was washed with 0.1 M citric acid followed by water (100 mL), after which the organic layer was dried over anhydrous sodium sulfate. The solvent was distilled under reduced pressure and the product was dried overnight under vacuum. The product was purified by recrystallization from dichloromethane and hexane to yield porphyrin **7** as purple crystals, mp >300 °C, yield, 20 mg (97%). ^{1}H NMR, δ (ppm) 8.72 - 8.84 (m, 3 H, pyrrolic H), 8.68 (s, 1 H, pyrrolic H), 8.62 (d, *J*=5.3 Hz, 1 H, Ar), 8.56 (d, *J*=7.9 Hz, 1 H, Ar), 8.29 (d, *J*=7.5 Hz, 1 H, Ar), 7.95 (d, *J*=6.1 Hz, 6 H, Ar), 7.85 (t, *J*=7.7 Hz, 1 H, Ar), 7.70 - 7.80 (m, 6 H, Ar), 1.55 - 1.66 (m, 27 H, *t*-butyl H); UV-visible, λ_{max} (nm, 2% MeOH in CH_2Cl_2): 443, 460, 662, 689; MALDI-TOF-MS m/z; calcd for $C_{61}H_{48}N_8O_2Zn$ 990.50 [M^+], obsd 988.95.

*2.4.17 7,8,17,18-Tetracyano-5-(3'-carboxyphenyl)-10,15,20-tris-(4-t-butylphenyl)porphyrin (**8**)*

Porphyrin **7** (10 mg, 0.01 mmol) was dissolved in a solution of 15% ethyl acetate in dichloromethane (60 mL) in a round bottomed flask equipped with a magnetic stir bar.

Trifluoroacetic acid (7 mL) was added dropwise and the solution was stirred for 4 h at ambient temperature. Triethylamine (0.2 mL) was added and the solution was washed with a saturated solution of $NaHCO_3$ in water (100 mL) and then water (2 × 100 mL). The product was purified by preparative thin layer chromatography with 20% ethyl acetate in toluene as the solvent to give porphyrin **8** as purple crystals, mp >300 °C, yield, 8 mg (85.4%). ^{1}H NMR, δ (ppm) 8.96 - 9.08 (m, 3 H, pyrrolic H), 8.77 - 8.89 (m, 2 H, pyrrolic H, Ar), 8.67 (d, *J*=7.9 Hz, 1 H, Ar), 8.38 (d, *J*=7.5 Hz, 1 H, Ar), 7.98 - 8.08 (m, 6 H, Ar), 7.94 (t, *J*=7.7 Hz, 1 H, Ar), 7.83 (d, *J*=8.3 Hz, 6 H, Ar), 1.56 - 1.68 (m, 27 H, *t*-butyl-H), -2.45 (br s, 2 H, -NH); UV-visible, λ_{max} (nm, 2% MeOH in CH_2Cl_2): 441, 453, 556, 601, 668, 735; MALDI-TOF-MS m/z; calcd for $C_{61}H_{50}Br_4N_8O_2$ 926.41 [M^+], obsd 927.40.

*2.4.18 5,10,15,20-Tetrakis-(3,5-di-t-butylphenyl)porphyrin (**37**)*

Porphyrin **37** was synthesized as a side product from the synthesis of **28** (see below). The product was purified by column chromatography on silica gel using 30% dichloromethane in toluene to yield purple crystals, mp >300 °C, yield, 375 mg (14.1%); ^{1}H NMR, δ (ppm) 8.89 (s, 8 H, pyrrolic H), 8.08 (d, *J*=1.8 Hz, 8 H, Ar), 7.78 (t, *J*=1.8 Hz, 4 H, Ar), 1.52 (br s, 72 H, *t*-butyl H), -2.68 (s, 2 H, -NH); UV-visible, λ_{max} (nm, CH_2Cl_2): 419, 517, 553, 591, 646; MALDI-TOF-MS m/z; calcd for $C_{76}H_{94}N_4$ 1063.59 [M^+], obsd 1063.25.

*2.4.19 7,8,17,18-Tetrabromo-5,10,15,20-tetrakis-(3,5-di-t-butyl-phenyl)porphyrin (**38**)*

Porphyrin **37** (375 mg, 0.353 mmol) was dissolved in chloroform (50 mL) stabilized with ethanol in a dry round bottomed flask equipped with a magnetic stir bar and reflux

condenser. The flask was placed in an oil bath which was brought to a temperature of 80 ^{o}C. *N*-bromosuccinimide (314 mg, 1.76 mmol) was added to the solution which was then allowed to reflux 1 h, followed by the addition of pyridine (0.142 mL, 1.76 mmol). The solution was allowed to reflux for an additional 5 h. After the reaction was complete as indicated by thin layer chromatography and MALDI mass spectrometry, the solvent was distilled under reduced pressure and the product was purified by column chromatography on silica gel using a solution of 0.5% triethylamine, and 49.5% dichloromethane in hexane as the eluent to yield porphyrin **38** as purple crystals, mp >300 °C, yield, 100 mg (20.7%). ^{1}H NMR, δ (ppm) 8.89 (s, 8 H, pyrrolic H), 8.08 (d, *J*=1.6 Hz, 8 H, Ar), 7.78 (s, 4 H, Ar), 1.52 (br s, 72 H, *t*-butyl H), -2.94 (s, 2 H, -NH); UV-visible, λ_{max} (nm, CH_2Cl_2): 432, 529, 663, 665; MALDI-TOF-MS m/z; calcd for $C_{76}H_{90}Br_4N_4$ 1379.17 [M^+], obsd 1378.44.

*2.4.20 Zn(II) 2,3,12,13-tetrabromo-5,10,15,20-tetrakis-(3,5-di-t-butylphenyl)porphyrin (**39**)*

Porphyrin **38** (100 mg, 0.073 mmol) was dissolved in deaerated chloroform (30 mL) in a round bottomed flask equipped with a magnetic stirrer. Zinc acetate (320 mg, 1.46 mmol) was dissolved in MeOH (3.2 mL) and the resulting solution was added dropwise to the porphyrin solution, which was then stirred for 1 h at room temperature. The organic layer was washed three times with water (100 mL) and dried over anhydrous sodium sulfate to yield porphyrin **39** as purple crystals, mp >300 °C, yield, 60 mg (63.5%). ^{1}H NMR, □ (ppm) 8.76 (s, 4 H, pyrrolic H), 7.85 (s, 8 H, Ar), 7.77 (br s, 4 H, Ar), 1.48 (s, 72 H, *t*-butyl H); UV-visible, λ_{max} (nm, CH_2Cl_2): 429, 557, 597; MALDI-TOF-MS m/z; calcd for $C_{76}H_{88}Br_4N_4Zn$ 1442.56 [M^+], obsd 1442.43.

*2.4.21 Zn(II) 2,3,12,13-tetracyano-5,10,15,20-tetrakis-(3,5-di-t-butyl-phenyl)porphyrin (**9**).*

Porphyrin **39**, zinc acetate, 1,1'-bis(diphenylphosphino)ferrocene, and Zn dust were dried under vacuum overnight before use, and all glassware was oven dried. Porphyrin **39** (20 mg, 0.014 mmol), tris(dibenzylideneacetone)dipalladium(0) (10 mg, 0.011 mmol), 1,1'-bis(diphenylphosphino)ferrocene (12 mg, 0.022 mmol), zinc acetate (1 mg, 0.0035 mmol), Zn dust (1 mg, 0.015 mmol), and zinc cyanide (4 mg, 0.034 mmol) were dissolved in deaerated *N,N*-dimethylacetamide (15 mL) in a Schlenk flask equipped with a magnetic stirrer. The Schlenk flask was placed in an oil bath that was heated to 115 ^{o}C and the solution was allowed to stir under argon for 17.5 h, after which the solvent was removed by distillation and the reaction mixture was redissolved in dichloromethane. The solution was washed five times with water (100 mL) and dried over anhydrous sodium sulfate, and the solvent was distilled under vacuum. The product was purified by column chromatography on silica gel with 15% EtOAc in toluene as the eluent, and then recrystallized from dichloromethane and hexane to give porphyrin **9** as purple crystals, mp >300 °C, yield, 30 mg (29%). ^{1}H NMR, δ (ppm) 8.76 (s, 4 H, pyrrolic H), 7.86 (t, *J*=1.8 Hz, 4 H, Ar), 7.79 (d, *J*=1.8 Hz, 8 H, Ar), 1.41 (s, 72 H, *t*-butyl H); UV-visible, λ_{max} (nm, 2% MeOH in CH_2Cl_2): 443, 458, 655, 677; MALDI-TOF-MS m/z; calcd for $C_{80}H_{88}N_8Zn$ 1227.02 [M^+], obsd 1227.25.

*2.4.22 7,8,17,18-Tetracyano-5,10,15,20-tetrakis-(3,5-di-t-butylphenyl)porphyrin (**10**)*

Porphyrin **9** (5.0 mg, 0.0041 mmol) was dissolved in dichloromethane (26 mL) in a round bottomed flask equipped with a magnetic stir bar. Trifluoroacetic acid (4 mL) was

added dropwise and the solution was stirred for 4 h at ambient temperature. The solution was washed with a saturated solution of $NaHCO_3$ in water (100 mL), followed by water (2 × 100 mL). The organic solution was dried over anhydrous sodium sulfate, and the solvent was removed under reduced pressure. The product was purified by preparative thin layer chromatography with 5% ethyl acetate in toluene as the solvent to give porphyrin **10** as purple crystals, mp >300 °C, yield, 3 mg (60.5%). ^{1}H NMR, δ (ppm) 8.95 (d, *J*=1.3 Hz, 4 H, pyrrolic H), 7.95-7.91 (m, 4 H, Ar), 7.90 (d, *J*=1.3 Hz, 8 H, Ar), 1.48 (s, 72 H, *t*-butyl H), -2.47 (s, 2 H, -NH); UV-visible, λ_{max} (nm, 2% MeOH in CH_2Cl_2); 440, 453, 553, 599, 667, 730; MALDI-TOF-MS m/z; calcd for $C_{80}H_{90}N_8$ 1164.27 [M^+], obsd 1163.62 .

*2.4.23 5-(3-Methoxycarbonylphenyl)-10,15,20-tris-(3,5-di-t-butylphenyl)porphyrin (**40**)*

Methyl 3-formylbenzoate, 3,5-di-*t*-butylbenzaldehyde, and dipyrromethane **21** were dried overnight under vacuum. Compound **21** (3.3 g, 10 mmol), 3,5-di-*t*-butylbenzaldehyde (1.1 g, 5 mmol), and methyl 3-formylbenzoate (0.8 g, 5 mmol) were dissolved in dry and deaerated dichloromethane (600 mL) in a dry round bottomed flask equipped with a magnetic stir bar and stirred for 15 min under argon at room temperature. Trifluoroacetic acid (1.4 mL, 18 mmol) was added dropwise and stirred for 2 h, after which time 2,3-dichloro-5,6-dicyano-1,4-benzoquinone (4.5 g, 20 mmol) was added. The reaction vessel was opened to the atmosphere and stirred for an additional 1.5 h. A portion of 2,3-dichloro-5,6-dicyano-1,4-benzoquinone (0.50 g, 2.2 mmol) was then added and the solution was stirred for an additional 30 min. The solvent was distilled under reduced pressure and the product was redissolved in dichloromethane and run through a short silica gel plug using dichloromethane as the eluent. The first three bands containing

porphyrin were collected and the solvent was removed from each by distillation under reduced pressure. The product, the second band, was further purified by column chromatography on silica gel using 30% dichloromethane in toluene as the eluent. The final purification was done by recrystallization from hexane and dichloromethane to give porphyrin **40** as purple crystals, mp >300 °C, yield, 459 mg (9.1%). ^{1}H NMR, δ (ppm 8.83 - 8.97) (m, 6 H, pyrrolic H), 8.76 (d, *J*=4.9 Hz, 2 H, pyrrolic H), 8.47 (d, *J*=7.9 Hz, 1 H, Ar), 8.42 (d, *J*=7.5 Hz, 1 H, Ar), 8.04 - 8.12 (m, 6 H, Ar), 7.84 (t, *J*=7.7 Hz, 1 H, Ar), 7.77 - 7.81 (m, 3 H, Ar), 3.97 (s, 3 H, methoxy H), 1.52 (s, 54 H, *t*-butyl H), -2.70 (s, 2 H, -NH); UV-visible λ_{max} (nm, CH_2Cl_2): 420, 517, 553, 592, 647; MALDI-TOF-MS m/z; calcd for $C_{70}H_{80}N_4O_2$ 1009.41 [M^+], obsd 1008.85.

*2.4.24 7,8,17,18-Tetrabromo-5-(3-methoxycarbonylphenyl)-10,15,20-tris-(3,5-di-t-butylphenyl)porphyrin (**41**)*

Porphyrin **40** and *N*-bromosuccinimide were dried overnight under vacuum. N-bromosuccinimide (405 mg, 2.3 mmol), and **40** (459 mg, 0.5 mmol) were dissolved in $CHCl_3$ (75 mL) in a dry round bottomed flask equipped with a reflux condenser and a magnetic stirrer. The solution was allowed to reflux for 2 h, after which time additional *N*- bromosuccinimide (162 mg, 0.9 mmol) was added and the solution was allowed to reflux for an additional 2 h. A third portion of *N*-bromosuccinimide (162 mg, 0.910 mmol) was added to the solution, which was then allowed to reflux for 2 h. Pyridine (0.2 mL, 2.5 mol) was added to the solution and the mixture was stirred for 10 min, and then the solvent was distilled under reduced pressure. The product was purified by column chromatography on silica gel using a solution of 40% dichloromethane in hexane as the eluent to give porphyrin **41** as purple crystals, mp >300 °C, yield, 417 mg (69.2%). ^{1}H

NMR, δ (ppm) 8.84 -8.86 (m, 1 H, pyrrolic H), 8.76 – 8.86 (m, 2 H, pyrrolic H), 8.62 (d, J=4 Hz, 1 H, pyrrolic H), 8.49 (d, J=8 Hz, 1 H, Ar), 8.35 (d, J=7.6 Hz, 1 H, Ar), 7.92 – 8.22 (m, 6 H, Ar), 7.852 (t, J=7.6 Hz, 1 H, Ar), 7.84 – 7.62 (m, 3 H, Ar), 4.01 (s, 3 H, methoxy H), 1.46 – 1.60 (m, 54 H, *t*-butyl H), -2.94 (s, 2 H, -NH); UV-visible λ_{max} (nm, CH_2Cl_2): 435, 531, 604, 678; MALDI-TOF-MS m/z; calcd for $C_{70}H_{76}Br_4N_4O_2$ 1324.99 [M^+], obsd 1324.87.

*2.4.25 Zn(II) 2,3,12,13-tetrabromo-5-(3-methoxycarbonylphenyl)-10,15,20-tris-(3,5-di-t-butylphenyl)porphyrin (**42**)*

Porphyrin **41** (417 mg, 0.3 mmol) was dissolved in chloroform (120 mL), in a round bottomed flask equipped with a reflux condenser and a magnetic stirrer. The flask was placed in an oil bath that was heated to 50 ^oC. Zinc acetate (1.4 g, 6.3 mmol) was dissolved in methanol (7 mL), and the resulting solution was added to the round bottom flask containing the porphyrin solution. The solution was allowed to stir for 1 h. The solvent was distilled under reduced pressure, and the product was purified by column chromatography on silica gel using a solution of 50% dichloromethane and in hexane as the eluent to yield porphyrin **42** as purple crystals, mp >300 °C, yield, 304 mg (69.6%). ^1H NMR, δ (ppm) 8.86 - 8.89 (m, 2 H, pyrrolic H), 8.83 (d, J=4.8 Hz, 1 H, pyrrolic H), 8.69 (s, 1 H, Ar), 8.67 (d, J=4.8 Hz, 1 H, Ar), 8.42 (d, J=7.6 Hz, 1 H, Ar), 8.26 (d, J=7.6 Hz, 1 H, Ar), 7.88 – 7.82 (m, 6 H, Ar), 7.82 – 7.77 (m, 4 H, Ar), 3.92 (s, 3 H, methoxy H), 1.51 – 1.47 (m, 54 H, *t*-butyl H); UV-visible λ_{max} (nm, 2% MeOH in CH_2Cl_2): 435, 567, 607; MALDI-TOF-MS m/z; calcd for $C_{70}H_{74}Br_4N_4O_2Zn$ 1388.39[M^+], obsd 1388.66.

*2.4.26 Zn(II) 2,3,12,13-tetracyano-5-(3-methoxycarbonylphenyl)-10,15,20-tris-(3,5-di-t-butylphenyl)porphyrin (**14**)*

Porphyrin **42**, zinc cyanide, zinc dust, and zinc acetate were dried overnight under vacuum. All glassware was oven dried. Porphyrin **42** (135 mg, 0.1 mmol), zinc cyanide (25 mg, 0.2 mmol), zinc dust (2.5 mg, 0.04 mmol), tris-(dibenzylideneacetone)dipalladium(0) (17 mg, 0.02 mmol), tri(o-tolyl)phosphine (11.8, 0.04 mmol), and zinc acetate (2.8 mg, 0.02 mmol) were dissolved in dry and deaerated *N*,*N*- dimethylformamide (10 mL), in a dry Schlenk flask equipped with a magnetic stirrer. The Schlenk flask was immersed in an oil bath, and the temperature of the oil was brought to 110 ^{o}C. The mixture was stirred under argon for 72 h, after which time zinc cyanide (50 mg, 0.4 mmol), zinc dust (5 mg, 0.1 mmol), tris-(dibenzylideneacetone)dipalladium(0) (35 mg, 0.04 mmol), tri(o-tolyl)phosphine (24 mg, 0.08 mmol), and zinc acetate (6 mg, 0.03 mmol) were added and the solution was stirred under argon for an additional 48 h. The solvent was distilled under reduced pressure and the reaction mixture was redissolved in dichloromethane and washed with water (250 mL) 4 times. The organic layer was dried over anhydrous sodium sulfate, and the solvent was distilled under reduced pressure. The crude product was further dried overnight under reduced pressure, and then purified by column chromatography on silica gel using dichloromethane as the eluent. A final purification was done with column chromatography using 5% ethyl acetate in toluene as the eluent to yield porphyrin **14** as purple crystals, mp >300 °C, yield, 15 mg (12.9%). ^{1}H NMR, δ (ppm) 8.83 - 8.90 (m, 2 H), 8.81 (d, *J*=4.9 Hz, 1 H), 8.66 (d, *J*=4.9 Hz, 1 H), 8.55 (br s, 1 H), 8.47 (d, *J*=7.5 Hz, 1 H), 8.26 (d, *J*=7.9 Hz, 1 H), 7.93 (m, *J*=1.8 Hz, 3 H), 7.78 - 7.89 (m, 7 H), 3.84 (s, 3 H),

1.40 - 1.59 (m, 54 H); UV-visible λ_{max} (nm, 2% MeOH in CH_2Cl_2): 445, 459, 659, 681; MALDI-TOF-MS m/z; calcd for $C_{74}H_{74}N_8O_2Zn$ 1172.84 [M^+], obsd 1171.30.

*2.4.27 Zn(II) 2,3,12,13-tetracyano-5-(3-carboxyphenyl)-10,15,20-tris-(3,5-di-t-butylphenyl)porphyrin (**15**)*

Porphyrin **14** (15 mg 0.01 mmol), was allowed to dissolved in tetrahydrofuran (4.6 mL) in a round bottom flask equipped with a magnetic stirrer, and the solution was allowed to stir for 10 min. Methanol (2.3 mL) was added followed by the dropwise addition of 17% w/w KOH in water (1 mL), and the solution was allowed to stir at room temperature for 2 h. The product was extracted with dichloromethane and washed with a solution of 0.1 M citric acid (20 mL) followed by two water washes (20 mL). The organic phase was collected and the solvent was distilled under reduced pressure and the residue was dried under vacuum. The product was purified by preparative thin layer chromatography with toluene containing 5% ethyl acetate as the eluent to give porphyrin **15** as purple crystals, mp >300 °C, yield, 15 mg (98%). ^{1}H NMR (400 MHz, Methanol-d_4) δ (ppm) 8.70 - 8.75 (m, 3 H, pyrrolic H), 8.66 (d, *J*=5.4 Hz, 1 H, pyrrolic H), 8.56 (d, *J*=8.3 Hz, 1 H, Ar), 8.35 (d, *J*=7.8 Hz, 1 H, Ar), 7.84 - 8.02 (m, 10 H, Ar), 7.69 - 7.82 (m, 1 H, Ar), 1.43 - 1.56 (m, 54 H, *t*-butyl H); UV-visible λ_{max} (nm, 2% MeOH in CH_2Cl_2): 445, 460, 661, 685; MALDI-TOF-MS m/z; calcd for $C_{73}H_{72}N_8O_2Zn$ 1158.82 [M^+], obsd 1157.04.

*2.4.28 7,8,17,18-Tetracyano-5-(3-carboxyphenyl)-10,15,20-tris-(3,5-di-t-butylphenyl)porphyrin (**16**)*

Porphyrin **15** (7 mg) was dissolved in a solution of 9% ethyl acetate in dichloromethane (11 mL) in a round bottomed flask equipped with a magnetic stir bar. Trifluoroacetic acid (2.2 mL) was added dropwise and the solution was stirred for 4 h at

ambient temperature. The solution was washed with water (50 mL) follow by wash with a saturated solution of $NaHCO_3$ in water (50 mL) and then a second wash with water (50 mL). The solution was dried over anhydrous sodium sulfate, and the solvent was removed under vacuum. The product was purified by preparative thin layer chromatography with 5% methanol in dichloromethane as the solvent to give porphyrin **16** as purple crystals, mp >300 °C, yield, 5 mg (75.4%).^{1}H NMR, δ (ppm) 8.93 - 9.09 (m, 3 H), 8.86 (d, *J*=4.8 Hz, 1 H), 8.82 (s, 1 H), 8.65 (d, *J*=8.3 Hz, 1 H), 8.36 (d, *J*=7.0 Hz, 1 H), 7.96 (s, 3 H), 7.92 (s, 7 H), 1.51 (s, 54 H), -2.45 (d, *J*=6.6 Hz, 2 H); UV-visible λ_{max} (nm, CH_2Cl_2): 443, 453, 555, 600, 669, 730; MALDI-TOF-MS m/z; calcd for $C_{73}H_{74}N_8O_2$ 1095.42 [M^+], obsd 1096.23.

*2.4.29 7,8,17,18-Tetrabromo-5-(4-methoxycarbonylphenyl)-10,15,20-tris-(3,5-di-t-butylphenyl)porphyrin (**43**)*

Porphyrin **22** and *N*-bromosuccinimide were dried overnight under vacuum. *N*-bromosuccinimide (200 mg, 1.13 mmol), and **22** (350 mg, 0.347 mmol) were dissolved in $CHCl_3$ (60 mL) in a dry round bottomed flask equipped with a reflux condenser and a magnetic stirrer. The solution was allowed to reflux for 2.5 h, after which time pyridine (0.050 mL, 0.621 mmol) was added to the solution, which was then allowed to continue to reflux for an additional 2 h. *N*-bromosuccinimide (115 mg, 0.650 mmol) was added and the solution was allowed to reflux for an additional 0.5 h, after which pyridine (0.250 mL, 4.36 mmol) was added. The reaction mixture was cooled to room temperature and stirred for 3 h, after which a third portion of *N*-bromosuccinimide (50.0 mg, 0.283 mmol) was added to the solution, which was then brought to reflux and allowed to stir for 1 h. The solvent was distilled under reduced pressure, and the product was purified by column

chromatography on silica gel using a solution of 40% DCM in hexane as the eluent to give porphyrin **43** as purple crystals, mp >300 °C, yield, 417 mg (69.2%). ^{1}H NMR, δ (ppm) 8.78 - 8.84 (m, 3 H, pyrrolic H), 8.63 (d, *J*=5.4 Hz, 1 H, pyrrolic H), 8.44 (d, *J*=8.3 Hz, 2 H, Ar), 8.27 (d, *J*=8.3 Hz, 2 H, Ar), 7.93 - 8.00 (m, 6 H, Ar), 7.79 - 7.84 (m, 3 H, Ar), 4.10 (s, 3 H, methoxy H), 1.52 (s, 54 H, *t*-butyl H), -2.91 (s, 2 H, -NH); UV-visible λ_{max} (nm, CH_2Cl_2): 434, 531, 605, 676; MALDI-TOF-MS m/z; calcd for $C_{70}H_{76}Br_4N_4O_2$ 1324.99 [M^+], obsd 1324.67.

*2.4.30 Zn(II) 2,3,12,13-tetrabromo-5-(4-methoxycarbonylphenyl)-10,15,20-tris-(3,5-di-t-butylphenyl)porphyrin (**44**)*

Porphyrin **43** (150 mg, 0.113 mmol) was dissolved in dichloromethane (70 mL), in a round bottomed flask equipped with a reflux condenser and a magnetic stirrer. The round bottomed flask was placed in an oil bath that was heated to 50 ^{o}C. Zinc acetate (500 mg, 2.28 mmol) was dissolved in methanol (4 mL), and the resulting solution was added to the round bottom flask containing the porphyrin. The solution was heated to 45° C allowed to stir for 3 h. The solvent was distilled under reduced pressure, and the product was purified by column chromatography on silica gel using a solution of 50% dichloromethane in hexane as the eluent to yield porphyrin **44** as purple crystals, mp >300 °C, yield, 145 mg (92.2%); ^{1}H NMR, δ (ppm) 8.85 - 8.90 (m, 2 H, pyrrolic H), 8.83 (d, *J*=4.8 Hz, 1 H, pyrrolic H), 8.68 (d, *J*=4.8 Hz, 1 H, Ar), 8.36 (d, *J*=7.9 Hz, 2 H, Ar), 8.15 (d, *J*=7.9 Hz, 2 H, Ar), 7.84 (s, 6 H, Ar), 7.79 (s, 3 H, Ar), 4.07 (s, 3 H, methoxy H), 1.48 (s, 54 H, *t*-butyl H); UV-visible λ_{max} (nm, 2% MeOH in CH_2Cl_2): 430, 558, 596; MALDI-TOF-MS m/z; calcd for $C_{70}H_{74}Br_4N_4O_2Zn$ 1388.39 [M^+], obsd 1388.68.

*2.4.31 Zn(II) 2,3,12,13-tetracyano-5-(4-methoxycarbonylphenyl)-10,15,20-tris-(3,5-di-t-butylphenyl)porphyrin (**11**)*

Porphyrin **44**, zinc cyanide, zinc dust, and zinc acetate were dried overnight under vacuum. All glassware was oven dried. Porphyrin **44** (70 mg, 0.05 mmol), zinc cyanide (14.2 mg, 0.12 mmol), zinc dust (1.65 mg, 0.0504 mmol), tris-(dibenzylideneacetone)dipalladium(0) (36.92 mg, 0.0403 mmol), 1,1'-bis(diphenylphosphino)ferrocene (44.7, 0.08064 mmol), and zinc acetate (2.75 mg, 0.0125 mmol) were dissolved in dry and deaerated *N,N*-dimethylacetamide (10 mL), in a dry Schlenk flask equipped with a magnetic stirrer. The Schlenk flask was immersed in an oil bath, and the temperature of the oil was brought to 110 ^{o}C. The mixture was stirred under argon for 24 h. Once cooled, dichloromethane (20 mL) was added, the mixture was washed with water 5 times (200 ml), and the organic layer was collected and dried over anhydrous sodium sulfate. The crude product was further dried overnight under reduced pressure, and then purified by column chromatography using 5% ethyl acetate in toluene as the eluent to yield porphyrin **11** as purple crystals, mp >300 °C, yield, 18 mg (30%). ^{1}H NMR, δ (ppm) 8.86 (q, *J*=4.9 Hz, 2 H, pyrrolic H), 8.82 (d, *J*=4.9 Hz, 1 H, pyrrolic H), 8.63 (d, *J*=4.9 Hz, 1 H pyrrolic H), 8.05 (d, *J*=8.3 Hz, 2 H, Ar), 7.93 - 8.01 (m, 2 H, Ar), 7.91 (br s, 3 H, Ar), 7.87 (d, *J*=1.0 Hz, 6 H, Ar), 3.65 - 3.77 (m, 3 H, methoxy H), 1.43 - 1.53 (m, 54 H, *t*-butyl H); UV-visible, λ_{max} (nm, 2% MeOH in CH_2Cl_2): 443, 458, 655, 679; MALDI-TOF-MS m/z; calcd for $C_{74}H_{74}N_8O_2Zn$ 1172.84 [M^+], obsd 1172.95.

*2.4.32 Zn(II) 2,3,12,13-tetracyano-5-(4-carboxyphenyl)-10,15,20-tris-(3,5-di-t-butylphenyl)porphyrin (**12**)*

Porphyrin **11** (15 mg 0.01 mmol), was dissolved in tetrahydrofuran (10 mL) in a round bottom flask equipped with a magnetic stirrer, and the solution was stirred for 10 min. Methanol (2 mL) was added, followed by the dropwise addition of 17% w/w KOH in water (1.2 mL), and the solution was stirred at room temperature for 3 h. The product was extracted with dichloromethane and washed with a solution of 0.1 M citric acid (20 mL) followed by two water washes (20 mL). The organic phase was collected and dried over anhydrous sodium sulfate. The solvent was distilled under reduced pressure and the residue was dried under vacuum. The product was purified by preparative thin layer chromatography with toluene containing 5% ethyl acetate as the eluent to give porphyrin **12** as purple crystals, mp >300 °C, yield, 14 mg (98%). ^{1}H NMR (400 MHz, Methanol-d_4) δ (ppm) 8.72 - 8.81 (m, 3 H, pyrrolic H), 8.67 (d, *J*=4.8 Hz, 1 H, pyrrolic H), 8.45 (d, *J*=8.3 Hz, 2 H, Ar), 8.23 (d, *J*=8.3 Hz, 2 H, Ar), 7.87 - 8.00 (m, 9 H, Ar), 1.52 (s, 54 H, *t*-butyl H); UV-visible λ_{max} (nm, 2% MeOH in CH_2Cl_2): 443, 458, 654, 681; MALDI-TOF-MS m/z; calcd for $C_{73}H_{72}N_8O_2Zn$ 1158.82[M^+], obsd 1158.97.

*2.4.33 7,8,17,18-Tetracyano-5-(4-carboxyphenyl)-10,15,20-tris-(3,5-di-t-butylphenyl)porphyrin (**13**)*

Porphyrin **12** (5 mg, 0.004 mmol) was dissolved in a solution of 7% ethyl acetate in dichloromethane (2.2 mL) in a round bottomed flask equipped with a magnetic stir bar. Trifluoroacetic acid (0.4 mL) was added and the solution was stirred for 4 h at ambient temperature. The solution was washed with water (20 mL) followed by washing with a saturated solution of $NaHCO_3$ in water (20 mL) and then a second wash with water (50

mL). The solution was dried over anhydrous sodium sulfate, and the solvent was removed under vacuum. The product was purified by preparative thin layer chromatography with 5% methanol in dichloromethane as the solvent to give porphyrin **13** as purple crystals, mp >300 °C, yield, 4 mg (84.4%). ^{1}H NMR, δ (ppm) 8.97 - 9.09 (m, 3 H, pyrrolic H), 8.89 (d, *J*=3.9 Hz, 1 H, pyrrolic H), 8.59 (d, *J*=7.9 Hz, 2 H, Ar), 8.30 (d, *J*=7.9 Hz, 2 H, Ar), 7.90 - 8.03 (m, 9 H, Ar), 1.50 - 1.58 (m, 54 H, *t*-butyl H), -2.42 (d, *J*=8.3 Hz, 2 H, -NH); UV-visible λ_{max} (nm, CH_2Cl_2): 441, 452, 554, 599, 667, 729; MALDI-TOF-MS m/z; calcd for $C_{73}H_{74}N_8O_2$ 1095.42 [M^+], obsd 1096.08.

*2.4.34 7,8,17,18-Tetrabromo-5,10,15,20-tetrakis-(4-methylphenyl)porphyrin (**45**)*

In an oven-dried round bottomed flask equipped with a reflux condenser and a magnetic stirrer, **27** (1.0 g, 1.5 mmol) was dissolved in dry chloroform (160 mL) and stirred for 15 min at room temperature. *N*-bromosuccinimide (1.2 g, 6.7 mmol) was added, the temperature was brought to 80^o C, and the solution was stirred for 2 h. The solvent was distilled under reduced pressure and the product was collected on a filter paper and washed with methanol (250 mL). The crude product was recrystallized from chloroform and methanol, giving a mixture of **45** and the tribrominated porphyrin, which were not further purified or separated before the next synthetic step. The mixture of porphyrins were obtained as purple crystals; mp >300 °C; yield, 925 mg. MALDI-TOF-MS m/z; calcd for $C_{48}H_{34}Br_4N_4$ 986.43, and $C_{48}H_{35}Br_3N_4$ 907.53 [M^+], obsd 984.5061 and 908.5873.

*2.4.35 Zn(II) 2,3,12,13-tetrabromo-5,10,15,20-tetrakis-(4-methylphenyl)porphyrin (**46**)*

In a round bottomed flask equipped with a reflux condenser and a magnetic stirrer, the mixture above containing **45** (82 mg, 0.083 mmol) was dissolved in a solution of *N*,*N*-dimethylformamide (12 mL) and pyridine (0.5 mL) at room temperature. Zinc acetate (181 mg, 0.825 mmol) was added and the solution was allowed to reflux for 45 min, after which time the reaction was complete as indicated by thin layer chromatography. The solvent was removed by distillation under reduced pressure, and the product was washed with methanol (250 mL). The product was obtained as a mixture of **46** and the tribrominated analog, which was not further separated. The mixture consisted of purple crystals, mp >300 °C, yield, 80 mg. MALDI-TOF-MS m/z; calcd for $C_{48}H_{32}Br_4N_4Zn$ 1049.82, and $C_{48}H_{33}Br_3N_4Zn$ 970.92 [M^+], obsd 1049.72 and 969.82.

*2.4.36 Zn(II) 2,3,12,13-tetracyano-5,10,15,20-tetrakis-(4-methylphenyl)porphyrin (**17**)*

Porphyrin **46** from above containing also the tribrominated analog, Ph_3As, and $K_4[Fe(CN)_6]$ were dried overnight under vacuum and all glassware was oven dried overnight. All reagents; **46** (350 mg), tris-(dibenzylideneacetone)dipalladium(0) (60 mg, 0.066 mmol), triphenylarsine (163 mg, 0.533 mmol), and potassium ferrocyanide (491 mg, 1.33 mmol), were dissolved in dry and deaerated *N*,*N*-dimethylformamide (20 mL) in a round-bottomed flask equipped with a magnetic stir bar, and under argon. The round bottomed flask was put in an oil bath which was brought to 100 ^oC and stirred for 48 h, after which the temperature was increased to 115 ^oC and stirring was continued for 7.5 h. The solution was allowed to cool to room temperature, additional tris-

(dibenzylideneacetone)dipalladium(0) (60 mg, 0.066mmol) and triphenylarsine (163 mg, 0.533mmol) were added, and the solution was allowed to stir for an additional 48 h at 115 ^{o}C. The solvent was removed by distillation under reduced pressure, and the product was purified by column chromatography on silica gel using 30% hexane in dichloromethane as the eluent. Final purification was done by preparative thin layer chromatography with toluene containing 5% ethyl acetate as the eluent. This chromatography yielded **17** (23 mg) and the corresponding tricyanoporphyrin (24 mg). ^{1}H NMR, δ (ppm) 8.76 (s, 4 H, pyrrolic H), 7.92 (d, *J*=7.9 Hz, 8 H, Ar), 7.58 (d, *J*=7.9 Hz, 8 H, Ar), 2.73 (s, 12 H, methyl H); UV-visible λ_{max} (nm, CH_2Cl_2): 443, 458, 658.5, 680; MALDI-TOF-MS m/z; calcd for $C_{52}H_{32}N_8Zn$ 834.27 [M^+], obsd 832.68.

*2.4.37 7,8,17,18-Tetracyano-5,10,15,20-tetrakis-(4-methylphenyl)porphyrin (**18**)*

Porphyrin **17** (12 mg, 0.01 mmol) was dissolved in dichloromethane (7 mL) in a round bottomed flask equipped with a magnetic stir bar. Trifluoroacetic acid (0.5 mL) was added and the solution was allowed to stir for 30 min at room temperature. The solution was washed with water (2 × 50 mL), followed by a saturated aqueous solution of $NaHCO_3$ (50 mL). The product was dried over anhydrous sodium sulfate, and the solvent was distilled under reduced pressure. The product was purified by preparative thin layer chromatography using 10% ethyl acetate in toluene as the solvent to give porphyrin **18** as purple crystals, mp >300 °C, yield, 9.5 mg (84.3%). ^{1}H NMR (400 MHz,) δ (ppm) 8.96 (d, J=2.00, 4 H, pyrrolic H), 8.012 (d, *J*=8 Hz, 8 H, Ar), 7.65 (d, *J*=7.6 Hz, 8 H, Ar), 2.75 (s, 12 H, methyl H); UV-visible λ_{max} (nm, CH_2Cl_2): 441, 453, 556, 601, 677, 736; MALDI-TOF-MS m/z; calcd for $C_{52}H_{34}N_8$ 770.88 [M^+], obsd 770.08.

*2.4.38 Zn(II) 2,3,12,13-tetrabromo-5,10,15,20-tetrakis-(2,4,6-trimethylphenyl)porphyrin (**47**)*

Porphyrin **47** was synthesized from 150 mg (0.137 mmol) of **28** following the method reported for the synthesis of **33**. The product was purified by recrystallization from dichloromethane and methanol to give porphyrin **47**. The product was characterized by thin layer chromatography, no further characterization was done before the next step. The material was obtained as purple crystals, mp >300 °C, yield, 128 mg (80.1%).

*2.4.39 Zn(II) 2,3,12,13-tetracyano-5,10,15,20-tetrakis-(2,4,6-trimethylphenyl)porphyrin (**19**)*

Porphyrin **47**, $Zn(OAc)_2$, and Zn dust were dried under vacuum overnight before use, and all glassware was oven dried. *N*,*N*-dimethylacetamide was stirred with BaO for 24 h, then refluxed over BaO for 1 h and then distilled under reduced pressure. Porphyrin **47** (44 mg, 0.04 mmol), tris(dibenzylideneacetone)dipalladium(0) (27 mg, 0.03 mmol), 1,1'-bis(diphenylphosphino)ferrocene (34 mg, 0.1 mmol), zinc acetate (2 mg, 0.01 mmol), Zn dust (1 mg, 0.02 mmol), and zinc cyanide (11 mg, 0.1 mmol) were dissolved under argon in N,N-dimethylacetamide (20 mL) in a Schlenk flask equipped with a magnetic stir bar. The Schlenk flask was placed in an oil bath that was brought to a temperature of 115 ^{o}C and the solution was stirred under argon for 20 h. Dichloromethane (60 mL) was added to the solution, which was then washed with water (5 × 100 mL). The organic layer was dried over anhydrous sodium sulfate and then the solvent was distilled under reduced pressure. The product was purified by column chromatography on silica gel using a solution of 10% ethyl acetate in toluene as the eluent. The product was further purified by recrystallization from dichloromethane and hexane to yield porphyrin **19** as purple

crystals, mp >300 °C, yield, 7 mg (19.5%). ^{1}H NMR (400 MHz,) δ (ppm) 8.57 (s, 4 H, pyrrolic H), 7.30 (s, 8 H, Ar), 2.63 (s, 12 H, methyl H), 1.84 (s, 25 H, methyl H); UV-visible λ_{max} (nm, 2% MeOH in CH_2Cl_2): 444, 459, 662, 686; MALDI-TOF-MS m/z; calcd for $C_{60}H_{48}N_8Zn$ 946.49 [M^+], obsd 946.94.

*2.4.40 7,8,17,18-Tetracyano-5,10,15,20-tetrakis-(2,4,6-trimethylphenyl)porphyrin (**20**)*

Porphyrin **19** (5.0 mg, 0.0053 mmol) was dissolved in a solution of 3.8% ethyl acetate in dichloromethane (26 mL) in a round bottomed flask equipped with a magnetic stir bar. Trifluoroacetic acid (5 mL) was added and the solution was allowed to stir for 30 min at room temperature. Concentrated HCl (0.5 mL) was added to the solution, which was stirred for an additional 5 min. The solution was washed with water (2 × 50 mL), followed by a saturated aqueous solution of $NaHCO_3$ (50 mL). The product was dried over anhydrous sodium sulfate, and the solvent was distilled under reduced pressure. The product was purified by preparative thin layer chromatography using 10% ethyl acetate in toluene as the solvent to give porphyrin **20** as purple crystals, mp >300 °C, yield, 4 mg (85.8%). ^{1}H NMR, δ (ppm) 8.79 (d, *J*=1.3 Hz, 4 H, pyrrolic H), 7.33 (s, 8 H, Ar), 2.64 (s, 12 H, methyl H), 1.82 (s, 24 H, methyl H), -2.14 (br s, 2 H, -NH); UV-visible λ_{max} (nm, CH_2Cl_2): 439, 451, 552, 599, 673, 733; MALDI-TOF-MS m/z; calcd for $C_{60}H_{50}N_8$ 883.09 [M^+], obsd 883.98.

2.5 Conclusion

This newly developed method for the synthesis of β-cyano substituted porphyrins uses a palladium catalyzed reaction to give yields of up to ca. 50%, while employing milder

conditions than the previous methods used for cyanation of β-tetrabromoporphyrins. This method can be used to synthesize specialized β-cyano substituted porphyrins that have synthetically sensitive functional groups. Like previous methods, this approach still requires the use of more than a catalytic amount of palladium in order to obtain high yields.

The β-tetracyanoporphyrins have absorption maxima at considerably longer wavelengths than do their unsubstituted analogs. For example, as shown in Table 1, the longest-wavelength Q-bands in the free base compounds are found around 740 nm. Absorption in this region is important for solar energy harvesting applications, as there is ample sunlight in this spectral region that is not captured by many other common dyes. In addition, these porphyrins, especially the free base versions, are very good electron acceptors; indeed they are better acceptors than the quinones that are found in natural photosynthesis, and that have often been used in artificial photosynthetic molecules. This means that the cyanoporphyrins can be coupled with excited state electron donors that yield more strongly oxidizing radical cations for water oxidation applications. The β-cyanoporphyrins themselves have radical cations that are more strongly oxidizing than their unsubstituted analogs, also suggesting possible applications in water oxidation or other photocatalytic applications.

2.6 Acknowledgements

This work was supported by the Office of Basic Energy Sciences, Division of Chemical Sciences, Geosciences, and Energy Biosciences, Department of Energy under contract DE-FG02-03ER15393 and the Center for Bio-Inspired Solar Fuel Production, an

Energy Frontier Research Center funded by the U.S. Department of Energy, Office of Science, Office of Basic Energy Sciences under Award Number DE-SC0001016.

Chapter 3 Synthesis and photophysical investigation of a novel electron transfer system where C_{60} acts as an electron transfer bridge

Antaeres Antoniuk-Pablant, Gerdenis Kodis, Ana L. Moore, Thomas A. Moore, Devens Gust

Department of Chemistry and Biochemistry, Arizona State University, Tempe, AZ 85287

3.1 Abstract:

A covalently linked porphyrin-C_{60}-β-cyanoporphyrin (AaP-C_{60}-CyP) molecular triad designed to use C_{60} as an electron transfer mediator in a multi-step photoinduced electron transfer process has been synthesized and studied. The triad features a trimesityl free base porphyrin (AaP) and a high potential β-cyanoporphyrin (CyP) linked through a meso-phenyl group on each of the porphyrins to opposite sides of a pyrrolidine linker functionalizing the C_{60}. The CyP provides sufficient thermodynamic driving force for electron transfer from the C_{60} radical anion to the CyP. The triad and two model porphyrin-C_{60} dyads, AaP-C_{60} and CyP-C_{60}, were studied using electrochemical, as well as steady-state and time-resolved absorption and emission techniques. In benzonitrile, photoexcitation of the AaP moiety resulted in multiple energy and electron transfer reactions both to the C_{60} and the CyP moieties resulting in the final charge-separated state $AaP^{\bullet+}$-C_{60}-$CyP^{\bullet-}$ with an overall quantum yield of 0.85. Two pathways generate $AaP^{\bullet+}$-C_{60}-$CyP^{\bullet-}$ through formation of an intermediate charge-separated state $AaP^{\bullet+}$-$C_{60}^{\bullet-}$-CyP followed by a fast (> 50 ps^{-1}) charge-shift reaction. Another pathway involves energy transfer from AaP to CyP, followed by electron transfer to ^{1}CyP from AaP. The rate of charge recombination of the state $AaP^{\bullet+}$-C_{60}-$CyP^{\bullet-}$, (350 ps)$^-$1, was found to be faster than

the rate for recombination of $AaP^{\bullet+}$-$C_{60}^{\bullet-}$-CyP, $(660\ ps)^{-1}$, which is thought to be due to the charge-separated states being in the Marcus inverted region for charge recombination.

3.2 Introduction

One of the most important steps in the conversion of sunlight into useful energy in molecular artificial photosynthetic systems is the conversion of solar energy to electrochemical potential. The design and investigation of organic molecular constructs that mimic the photoinduced electron transfer process in natural photosynthesis and convert light into electrochemical energy in the form of a charge-separated state is a widely studied area.[1,4,5,13,17] Charge separated states can be generated initially by electron transfer between donor and acceptor molecules following photo-excitation of the donor or acceptor moiety.[5,13,17,37] For high efficiency, the photoinduced electron transfer must kinetically out compete the other processes that deactivate the excited state.[14] The longevity of the charge separated state is also very important as the longer lived the charge separated state, the greater the opportunity to use the stored energy for a useful purpose.[5,14,17,38,64] The molecular design determines the electronic coupling and spatial orientation of the components of the system, which in turn have a significant impact on the rates of electron transfer and competing processes. [22,28,135] In the natural system as well as some artificial systems, a multistep electron transfer process is used to spatially separate the charges. This method uses a series of relatively strongly coupled donor-acceptor species which undergo charge shift reactions that eventually generate the final charge separated state.[135] Each of these electron transfer steps must be exergonic, but it is also important to retain as much of the initial photon energy as possible in the final state.

Molecular constructs have been designed study and optimize this process using Donor-Spacer-Acceptor (D-S-A) systems and have been used to study aspects of photosynthetic electron transfer between the components.[55] These systems are typically designed by covalently bonding chromophores, electron donors, or electron acceptors which are sometimes analogous to those in the natural systems, including porphyrins, carotenes, aromatic imides, quinones, and fullerenes.[103,107] Since the beginnings of artificial photosynthesis research, porphyrins have been used as stable, synthetically available analogs of chlorophylls. They are ideal components for these systems as they generally have small reorganization energies and absorb with in the UV/Vis region, and their high electronic excitation energy allows for preservation of substantial potential energy in the final charge separated state.[29] They have a large π-aromatic system, which gives them an intense Soret (B) band at 400-450 nm, and Q bands at 500–650 nm (generally), which arise from π-π* transitions. [11,82] They can be good electron donors or acceptors, depending upon their substitution pattern. It is also an important feature that the porphyrin singlet and triplet states live long enough that they have a high probability of undergoing energy or electron transfer before deactivation in properly designed molecules.[64] In the construction of artificial photosynthetic reaction centers porphyrins are typically coupled to electron acceptor moieties, where excitation of the porphyrin is followed by electron transfer to the acceptor to yield a charge-separated state. Initially, quinones were favored as acceptor species, but more recently, fullerenes have been found to be more suitable in most applications.

Fullerenes (C_{60}) are well known electron acceptors that can accept up to six electrons [22] with a singlet excitation energy level comparable to other chromophores with large pi

systems such as porphyrins. The singlet excited state of C_{60} undergoes intersystem crossing to its triplet state $^3C_{60}$*. [55,61] The large three-dimensional structure of fullerenes gives them unique properties over smaller electron acceptors. It has been hypothesized that the large size, symmetry, and rigidity of the C_{60} causes the reorganization energy of the C_{60} for electron transfer to be small. The size and symmetry allow the radical anion to be spread over a large area which decreases the solvent reorganization energy, and the internal reorganization energy is lowered by the rigidity.[5,23,29,53,56,59,65] This effect was shown experimentally in a study that compared the electron transfer properties of a porphyrin linked quinone (Q), and a similarly linked porphyrin C_{60}. The porphyrin linked C_{60} had a larger forward electron transfer rate as well as a smaller charge recombination rate than the porphyrin linked quinone.[5,23,56,59] The smaller reorganization energy, leads to a high rate of photoinduced charge separation in the normal region of the Marcus rate constant vs. free energy change curve; concurrently, the charge recombination rate is pushed farther into the inverted region of the Marcus curve, which slows charge recombination.[53,56,59]

Thus, both fullerenes and porphyrins are large, delocalized π-electron systems that have low internal and solvent reorganization energies for electron transfer and relatively small solvent effects on the stability of their radical ions. These make artificial photosynthetic reaction centers with porphyrin donors and fullerene acceptors particularly efficient.

The first example of a porphyrin-fullerene artificial reaction center was reported in 1994.[103] The first example of the C_{60} acting as an electron acceptor in a larger molecular

construct was in a carotene porphyrin fullerene triad by Liddell et al. 1997, which generated a charge separated state with a lifetime of 170 ns, in 2-methyltetrahydrofuran.[5,111] This triad was further elaborated in subsequent studies by utilizing carotenes with lower potential and various porphyrins such as a dimesitylporphyrin (which affects the electronic coupling and thermodynamic driving force).[54] A carotene-porphyrin-fullerene triad synthesized and studied by Gust and cowowrkers,[54] shown in Figure 32, is one example of many such compounds that utilize the multistep electron transfer route. This triad was found to generate the final charge separated state with a quantum yield near unity (0.95), storing about 1 eV of the photon energy as electrochemical potential, with a charge separated state lifetime of 57 ns.[5,54,111]

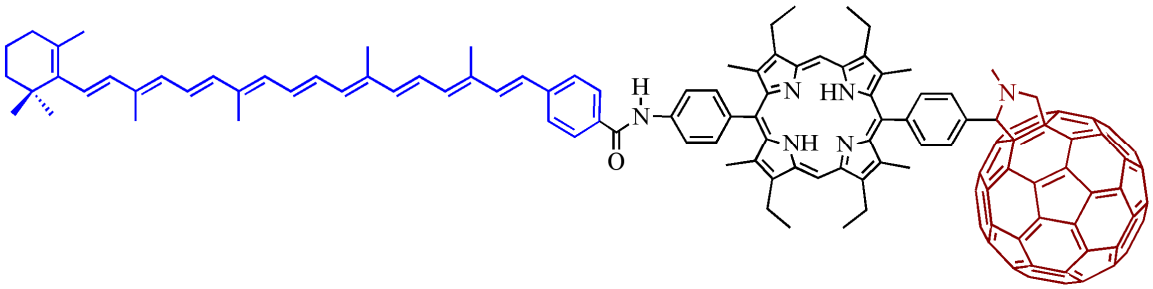

Figure 32. Carotene-porphyrin-fullerene triad synthesized and studied by Gust and coworkers.[54]

As in the carotene-porphyrin-fullerene compound in Figure 32, C_{60} is almost always used as the final electron acceptor in such constructs. In principle, fullerenes could also be used as electron relays that would serve as intermediate acceptors, passing an electron on to another terminal acceptor species. The properties of the C_{60} utilized in this way might produce longer lived intermediate charge separated states, which would allow more time for additional electron transfer steps, and therefore higher yields of final states.

Two examples of fullerenes being used as an electron transfer mediator involve constructs anchored to an electrode in photoelectrochemical cells, where methyl viologen in solution is used as the electron carrier.[23,65] In both of these experiments the C_{60} is linked to a porphyrin sensitizer anchored to an electrode. After excitation, an electron is transferred from the porphyrin to the fullerene, which undergoes a second electron transfer to the methyl viologen in solution. The reduced methyl viologen then donates an electron to the electrode. The results from these experiments indicated that using C_{60} in these electron transfer systems increased the generated photocurrent by allowing forward electron transfer to outcompete charge recombination (CR) to the electrode, when compared to the same systems without C_{60}.

Using a fullerene as an intermediate electron acceptor in a covalently linked system consisting of three or more chemically distinct donor-acceptor moieties has not been explored previously. In order to use the C_{60} as an electron transfer mediator in such a system, an acceptor with a more positive redox potential than that of the fullerene is required. It is known that when substituents are added to the β-positions on the porphyrin macrocycle, both the number and electronic properties of substituents strongly influence both the electronic structure and electrochemical properties of the porphyrin. [87,89,91,95–97] We recently developed a new method for the preparation of tetra-*β*-cyanoporphyrins which increases synthetic versatility of these porphyrins by allowing tetra-*β*-cyanoporphyrins with various functional substituents to be synthesized. These porphyrins are significantly better electron acceptors than fullerenes due to the strong electron

withdrawing effects of the cyano groups and the energy levels are thermodynamically poised to accept an electron from a $C_{60}^{\bullet-}$ with significant driving force.

The synthetic availability of the tetracyanoporphyrins allowed us to design molecular triad AaP-C_{60}-CyP (Figure 2), which consists of a substituted fullerene (C_{60}) bearing both a tetra-arylporphyrin which acts as an electron donor (AaP) and a tetra-β-cyanoporphyrin as a strong electron acceptor (CyP).[136,137]

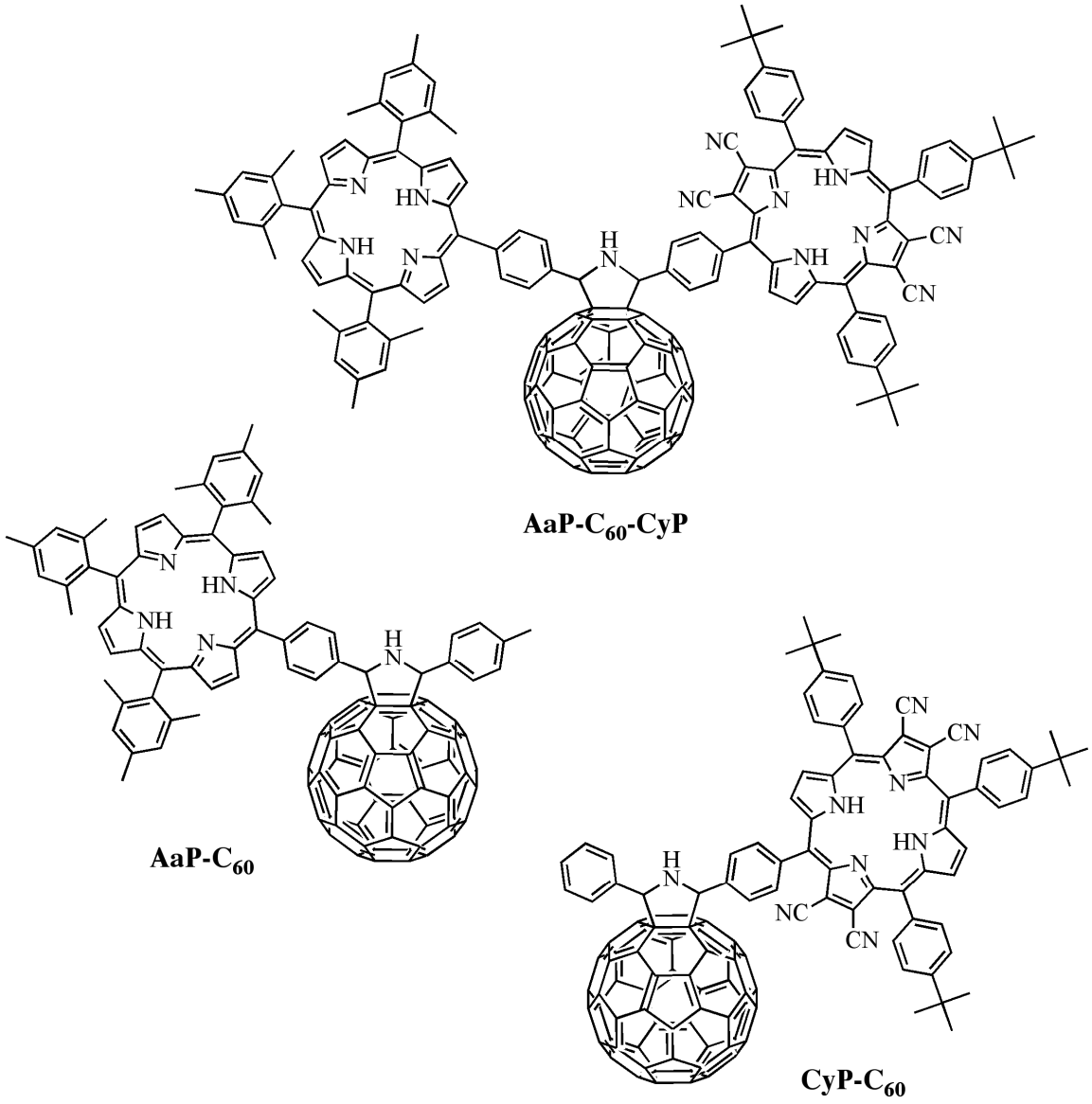

Figure 33. Triad AaP-C_{60}-CyP, and dyads AaP-C_{60} and CyP-C_{60} synthesized and studied.

In principle, excitation of AaP could be followed by photoinduced electron transfer to the fullerene, which could then transfer an electron to CyP to generate a $AaP^{\bullet+}$-C_{60}-$CyP^{\bullet-}$ charge-separated state. From experimental data on model compounds, the lifetime of the charge separated state $AaP^{\bullet+}$-$C_{60}^{\bullet-}$-CyP, is expected to be long enough to allow the second

electron transfer to generate $AaP^{\bullet+}$-C_{60}-$CyP^{\bullet-}$ to occur in good yield. Clearly, other types of photochemical reactions among the three components are also conceivable.

To synthesize AaP-C_{60}-CyP a method was developed to add both porphyrins to the C_{60} through a pyrrolidine functional group in the same synthetic step. The method uses a variation of the Prato reaction[67] that functionalizes C_{60} using azomethine ylides, where the azomethine is generated *in situ* from the condensation of an amino acid and an aldehyde. This approach required methods to be developed for the preparation of a previously unknown porphyrin bearing a suitable amino acid at a *meso*-position and a previously unknown tetra-β-cyanoporphyrin having an aldehyde group on a *meso*-aryl ring. The condensation of these two porphyrins in the presence of C_{60} formed the di-porphyrin azomethine ylide that added to the C_{60} to generate AaP-C_{60}-CyP. These porphyrins were also used successfully to synthesize two model dyads (see Figure 33); using the same method, each porphyrin was condensed with either *p*-tolualdehyde, or the amino acid α-phenylglycine. Below, we discuss the synthesis of this triad and its photochemistry in toluene and in benzonitrile (BzCN).

3.3 Results

*3.3.1 4-[*10,15,20-tris-*(2,4,6-trimethylphenylporphyrin-5-yl]phenylglycine* (**7**)

It was necessary to designed and develop the synthetic method for the synthesis of the porphyrin with the amino acid substituent. Our initial approach for preparation of the amino acid porphyrin began with the well-known and versatile Strecker method for the synthesis of amino acids from various aldehydes.[138] This method goes through an α-amino nitrile intermediate followed by hydrolysis of the nitrile group. The synthesis of

porphyrin with an aldehyde functional group on the meso position has been reported in the literature (change/add references if report actual synthesis) [25,139] and following these synthetic methods 5-(4-formylphenyl)-10,15,20-tris-*(2,4,6-trimethylphenyl)porphyrin* was synthesized. The general method for Strecker synthesis[138] allows an aldehyde to react with a primary amine to form an imine, which reacts with a cyanide to give the corresponding α-amino nitrile. This reaction was first attempted following the general method utilizing the reagents sodium cyanide and ammonium chloride. Through many renditions of the reaction using various reagents the method was optimized and used to synthesize an α-amino nitrile intermediate porphyrin in high yields. This method used a primary amine and a cyanide source that were soluble in organic solvents. 4,4-Dimethoxybenzhydrylamine[140] was used as the primary amine which also protected the amino group. Trimethylsilyl cyanide (TMSCN) was used as the cyanide source. [141] $InCl_3$ was used as a catalyst to activate the carbonyl carbon which resulted in 100% conversion (% by TLC analysis only) of the aldehyde to the alpha amino nitrile intermediate, as verified by mass spectroscopic analysis.

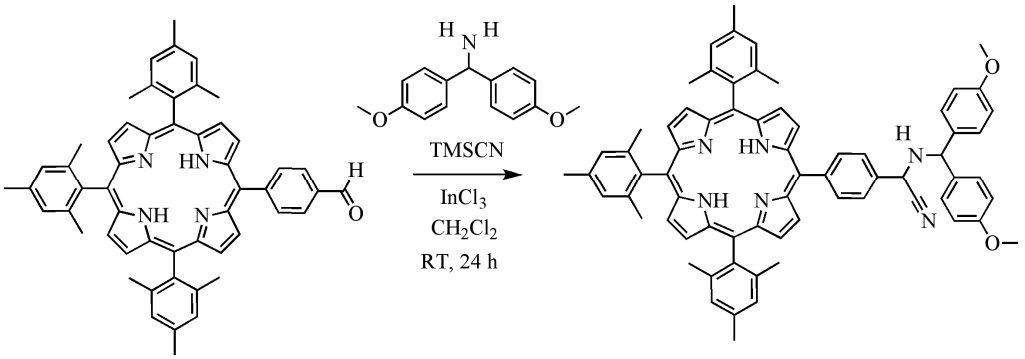

Figure 34. Synthetic scheme for the synthesis of the α-amino nitrile porphyrin.

The hydrolysis of the nitrile was attempted in both basic and acidic conditions at room temperature and with heat, and there was no observed product. The α-amino nitrile starting material was consumed and various side products formed, including the aldehyde starting material. This was hypothesized to be due the occurrence of a reaction similar to a Strecker degradation reaction.[142]

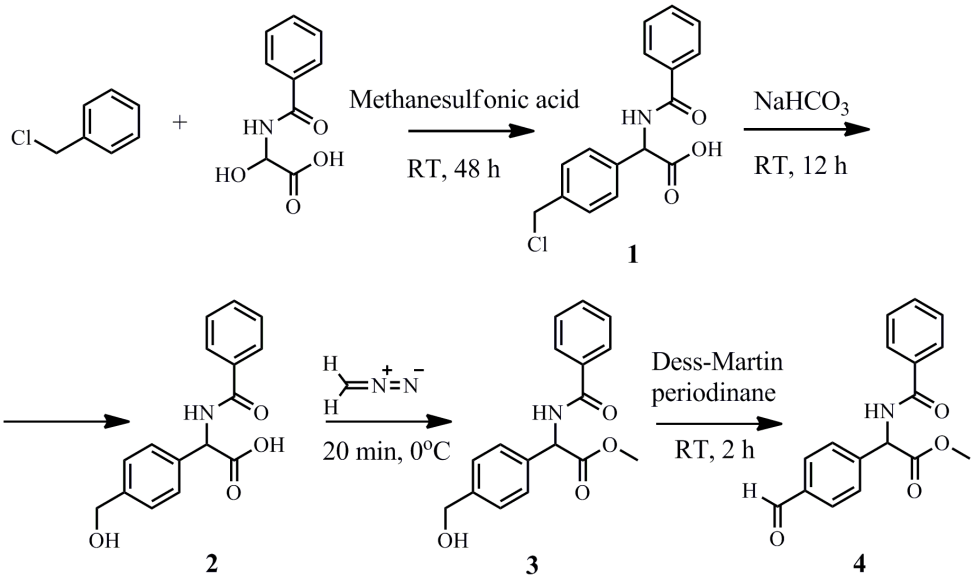

Figure 35. Synthetic scheme for the synthesis of the precursor aldehyde, N-benzoyl-p-formyl-D-L-phenylglycine methyl ester ***4***

A new route was developed with this possibility of sensitivity accounted for, in which an aldehyde that has a protected amino acid substituent could be used directly in the porphyrin condensation reaction to synthesize a porphyrin with the amino acid group at a *meso*-phenyl position (Figure 35). Protection of both the amine and acid moieties was necessary. These protecting groups can be removed under conditions milder than the hydrolysis of a nitrile, and yet remain intact through the porphyrin condensation reaction. The precursor aldehyde **4** was synthesized for this purpose. The synthesis of **2** followed a

method previously reported in the literature.[143] The carboxylic acid group of **2** was methylated using diazomethane to yield compound **3**. This step decreased the polarity of the molecule to avoid possible complications in purification and for ease of use in the porphyrin condensation reaction. General conditions for Dess-Martin oxidation reactions for similar compounds were followed to develop the method for the oxidation reaction that successfully synthesized the final aldehyde **4** from **3**.

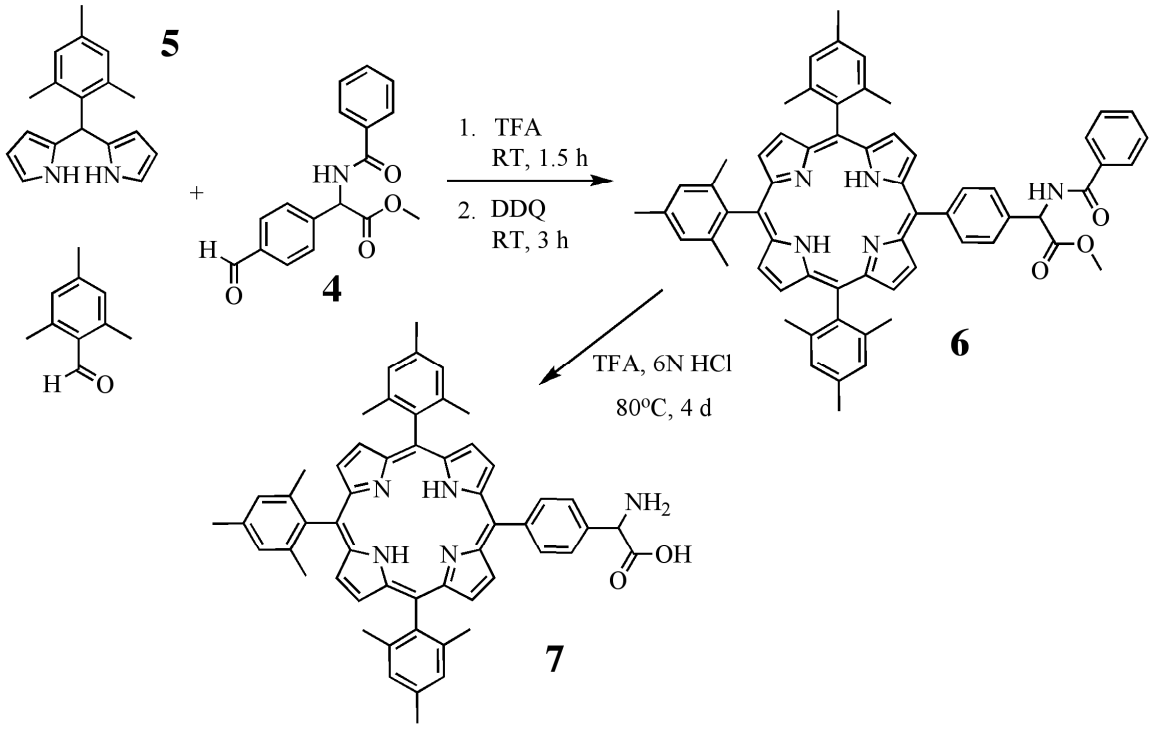

Figure 36. Synthetic scheme for the synthesis of porphyrin **7**

Compound **4** was used in a porphyrin condensation reaction to synthesize a trimesitylporphyrin with the protected amino acid on a meso phenyl position, **6**. Figure 36. The aldehyde **4** was used in excess to ensure that all amino acid aldehyde was consumed as well as to decrease the probability of the formation of di-substituted porphyrin side products. The intermediate porphyrin with the protected amino acid

substituent was found to be relatively stable in for purification in general laboratory conditions. The deprotection of the amino acid proved to be difficult and was attempted under several basic and acidic conditions. It was found that using trifluoroacetic acid to dissolve the porphyrin, together with a solution of 6N HCl, in a sealed pressure tube heated to 80ºC successfully deprotected the amino acid after 4 days, yielding porphyrin **7 (AaP)**. It was noted that in acidic conditions the amino acid remains stable, but in neutral or basic conditions it becomes unstable and degradation is observed. This porphyrin was kept in its protected form until it was used in the Prato reaction to synthesize AaP-C_{60} or AaP-C_{60}-CyP, where it was deprotected, and used without further purification.

*3.3.2 Synthesis of 7,8,17,18–tetracyano-5-(4-formylphenyl)-10,15,20-tris-(4-t-butylphenyl)porphyrin (**15**)*

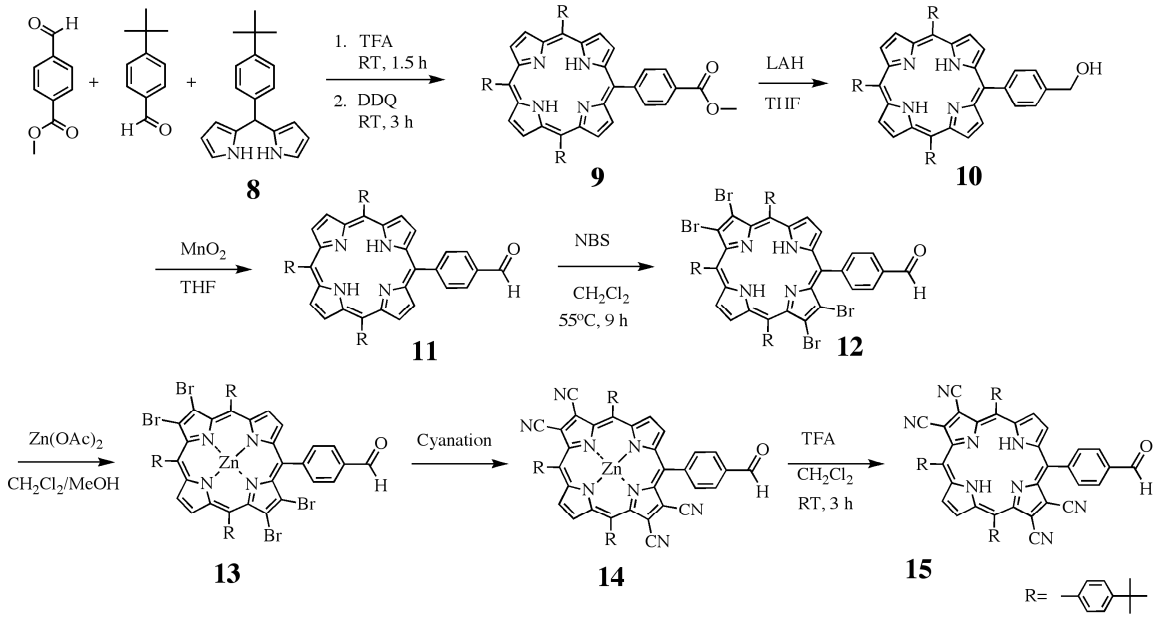

Figure 37. Synthetic scheme for the preparation of **15**

The β-cyano porphyrin with an aldehyde functional group on the *meso*-phenyl position (**15**, Figure 37) was synthesized using the new palladium catalyzed cyanation method developed in our laboratory that has been previously reported.[137] The precursor porphyrin with an aldehyde substituent, **11,** was synthesized following a method previously reported for a similar porphyrin.[25] The porphyrin condensation reaction with the appropriate reagents to synthesize porphyrin **9** with a methyl ester group was done following general porphyrin condensation methods.[137] Hydrolysis and reduction of the ester group of **9**, gave the alcohol porphyrin **10**, which was oxidized to an aldehyde group using manganese dioxide.[25] Following our previously reported procedure for β bromination, a tetra-β-bromo porphyrin with an aldehyde substituent, **12**, was synthesized. After the insertion of Zn(II) in the porphyrin macrocycle to synthesize porphyrin **13**, the developed palladium catalyzed cyanation method was followed to prepare porphyrin **14.** Analysis of the ^{1}H-NMR and mass spectrum revealed that the aldehyde functional group remained intact after both the bromination and cyanation procedures. After removal of zinc, the final porphyrin, *7,8,17,18–tetracyano-5-(4-formylphenyl)-10,15,20-tris-(4-t-butylphenyl)porphyrin,* ***15***, was synthesized.

Porphyrins **7** and **15** were used to synthesize the dyad compounds **AaP-C_{60}**, and **CyP-C_{60}** (Figure 38). Porphyrin **7** was used with *p*-tolualdehyde, and **15** was used with α-phenylglycine following the general reaction method for a 1,3-dipolar cycloaddition of azomethine ylides generated in situ, to a C_{60} to synthesize the dyad models. [67,68] The synthesis of the dyads allowed us to develop the synthetic method using the specialized porphyrins individually with the general conditions used for the Prato reaction.

Photophysical studies of the dyads provided important information on the energy and electron transfer processes among the individual components that also occur in the triad.

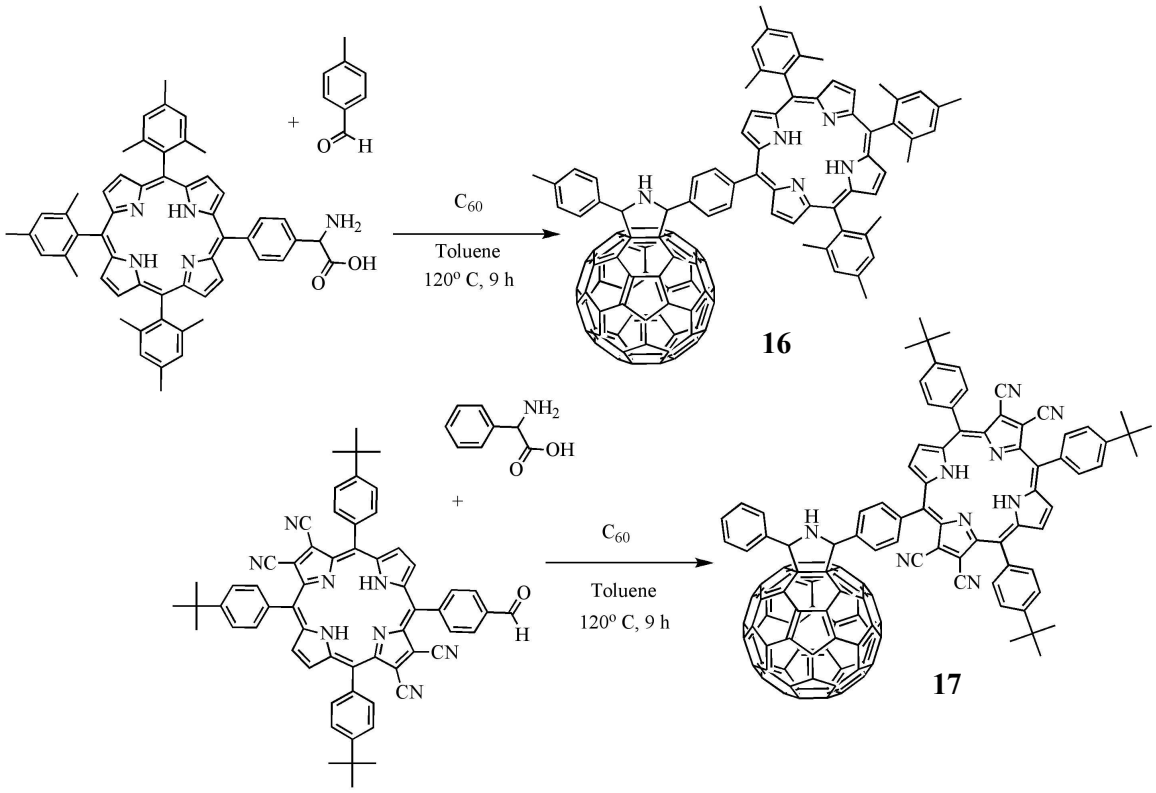

Figure 38. Synthetic scheme for the synthesis of AaP-C_{60} and CyP-C_{60}

The triad was synthesized following the conditions used in the method used for the synthesis of the dyads, using **7** and **14** as the amino acid and aldehyde for the *in situ* formation of the di-porphyrin azomethine, which functionalized the C_{60} with the two porphyrins on the pyrrolidine, giving the final triad, **AaP-C_{60}-CyP** in approximately a 19% yield (Figure 39). The product could in principle be present as a mixture of diastereomers due to the two stereocenters, but NMR and thin layer chromatography

suggest that only one isomer was present. Further analysis of the triad is necessary to confirm this conclusion.

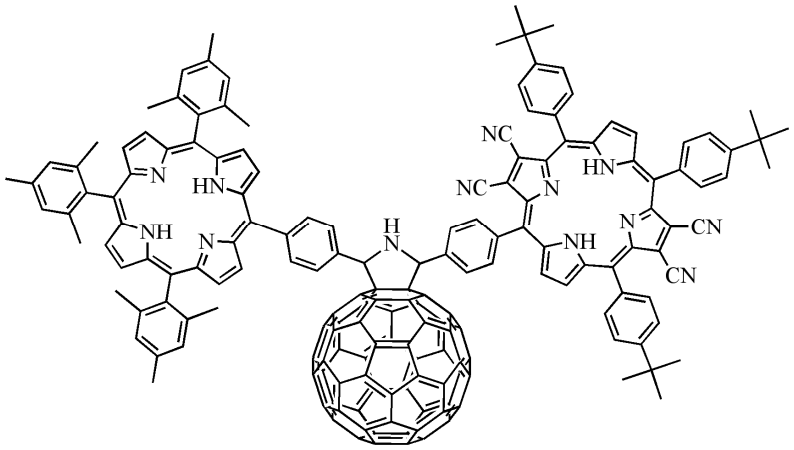

Figure 39. Synthetic scheme for the synthesis of AaP-C_{60}-CyP

3.3.3 Electrochemistry

Table 2. Relevant redox potentials

	Red_2 ($E_{1/2}$, V vs SCE)	**Red_1** ($E_{1/2}$, V vs SCE)	**Ox_1** ($E_{1/2}$, V vs SCE)
7	-1.68	-1.33	1.00
Model CyP[a]	-0.61[a]	-0.31[a]	1.32[a]
C_{60}	-0.932[b]	-0.54[b]	1.78[b]
CyP-C_{60}	-0.65	-0.38	1.34
AaP-C_{60}-CyP	-0.60	-0.32	0.74

[a] Redox values of *7,8,17,18-Tetracyano-5-(4-carboxyphenyl)-10,15,20-tris-(4-t-butylphenyl)porphyrin*, were measured and used instead of porphyrin 15 as the redox values are assumed to be the same.

[b] C_{60} Redox values were taken from those reported by Echegoyen, *et al.*[144]

The redox potentials of the relevant molecules were studied in order to estimate the thermodynamic parameters for the various conceivable electron transfer steps, and the results are reported in Table 2. The electrochemical properties of the compounds were obtained by cyclic votammetry performed under an argon atmosphere in distilled dichloromethane containing 0.1 M tetra-*n*-butylammonium hexafluorophosphate (TBAF) as the supporting electrolyte. The working and counter electrodes were Pt, and an Ag+/Ag quasi-reference electrode was employed. Potentials were determined using a ferrocene internal reference and the results were converted to SCE by referencing peaks to the first oxidation wave of ferrocene, which is 0.46 V vs SCE in this solvent.[43] Cyclic votammograms (CV) of the triad are given in Figures 40a and 40b.

As shown in Figure 40a the anodic wave of the CV reveals numerous reduction peaks. These peaks correspond to the peaks seen in the CVs of the individual model compounds. The first two reduction peaks are reversible, corresponding to the first reduction of the CyP followed by the reduction of C_{60}. In the triad the reduction potentials of the C_{60} are shifted anodically. This anodic shift matches the shift seen in the CyP-C_{60} model dyad (Table 2), and is due to the functionalization of the C_{60}.[22,145] The cathodic wave of the CV of the triad is shown in Figure 40b. The first oxidation peak is corresponds to a reversible first oxidation of the AaP moiety, which corresponds to a wave in the CV of the model compound but is shifted anodically. The first oxidation of the CyP is known to be quasi reversible or irreversible in some analogs, and is represented by the second cathodic wave of the cyclic voltammogram in Figure 40b.

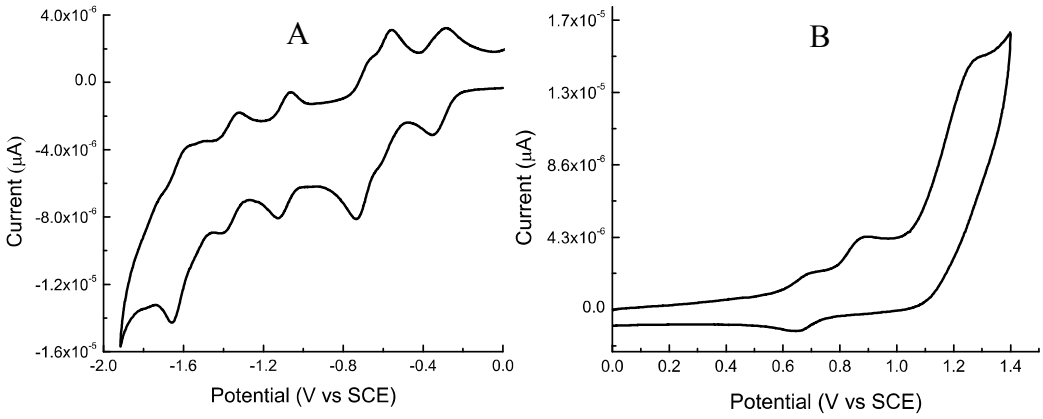

Figure 40. A) Anodic wave of the cyclic votammogram of AaP-C_{60}-CyP. **B**) Cathodic wave of the cyclic voltammogram of AaP-C_{60}-CyP in 0.1 M TBAF in dichloromethane

3.3.4 Absorption Spectra

The absorption spectra of AaP (**7**), CyP (**15)**, AaP-C_{60}, CyP-C_{60}, and AaP-C_{60}-CyP were obtained in both BzCN and toluene. See Figures 41a, 41b, and 42.

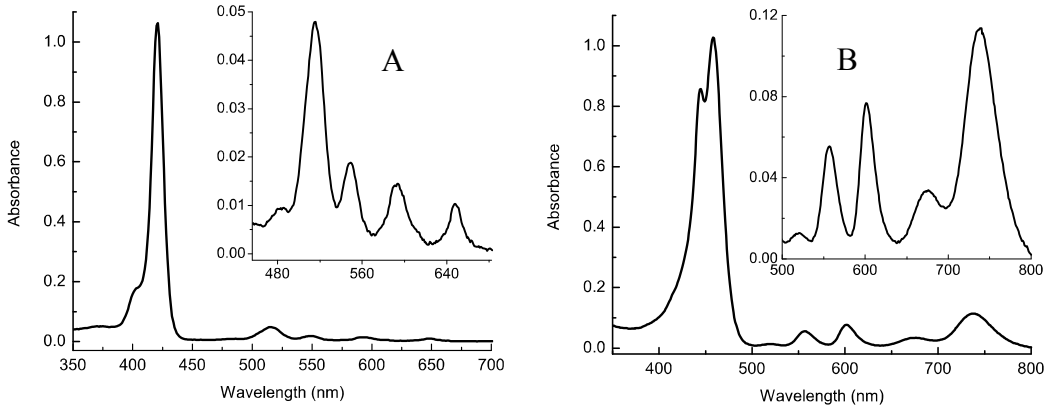

Figure 41. Absorption spectrum of A) AaP (7), and B) CyP (15), in benzonitrile. See table X. for absorption λ_{max} values.

Table 3. Absorption λ_{max} of AaP and CyP in benzonitrile and toluene. Absorption λ_{max} values in BzCN correspond to the absorption spectra in figure 41a and 41b.

	B_x/B_y	$Q_y(1,0)$	$Q_y(0,0)$	$Q_x(1,0)$	$Q_x(0,0)$
AaP (7) BzCN	421/NA	516	548	593	648
CyP (15) BzCN	444/458	556	601	677	737
AaP (7) Toluene	418/NA	513	546	591	646
CyP (15) Toluene	443sh/452	553	597	659	726

In BzCN the triad absorption spectrum (Figure 42) features peaks in the region of 375 to 500 nm that represent the Soret band of the AaP as a sharp peak at 422 nm, and the split and red shifted B-bands of the CyP moiety with maxima at 444 and 460 nm. The multiple peaks from 500 nm to 800 nm are from both the AaP and CyP Q bands. The longest wavelength Q band at 739 nm is from the CyP. The Q bands peaks in the 530 - 660 nm region are the Q bands overlapping from both porphyrins.

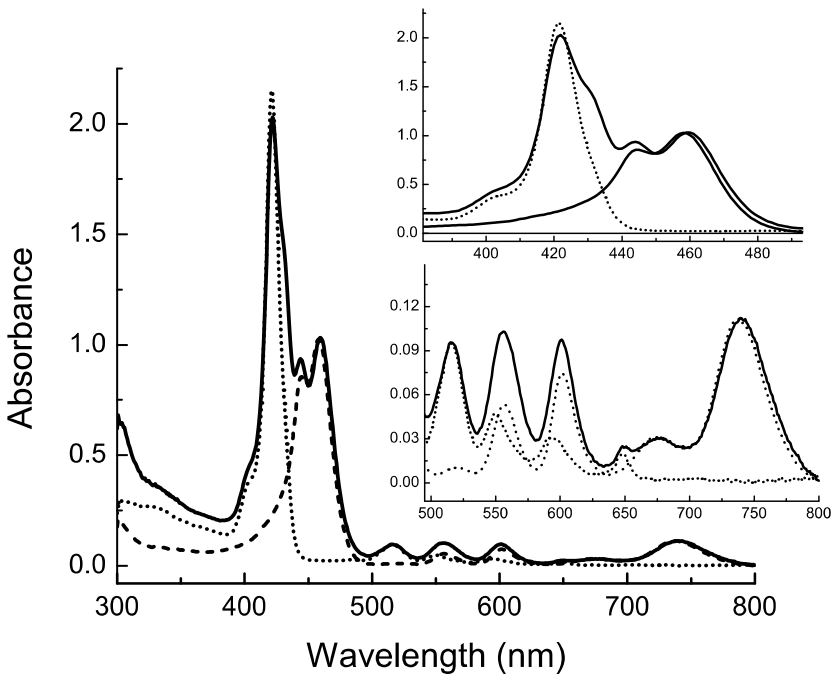

Figure 42. Absorption spectra in benzonitrile of AaP-C_{60}-CyP (soild), AaP-C_{60} (**15)** (dotted), and CyP (dashed) in BzCN. The AaP-C_{60}-CyP spectrum was normalized to the CyP spectrum at 458 nm, and the spectrum of the dyad was normalized to the resulting AaP-C_{60}-CyP spectrum at 515 nm. The inserts are a magnification of select regions of the spectra.

Figure 43 shows that the absorption spectrum of the triad is close to a linear combination of the absorption spectra of the component moieties. The triad spectrum has a small shoulder at around 430 nm that is unique to the triad, and is ascribed to excitonic coupling between the porphyrins. Such splitting has been seen in other multi-porphyrin systems.[83] There are no significant perturbations that are indicative of any very strong ground state interactions among the linked chromophores.

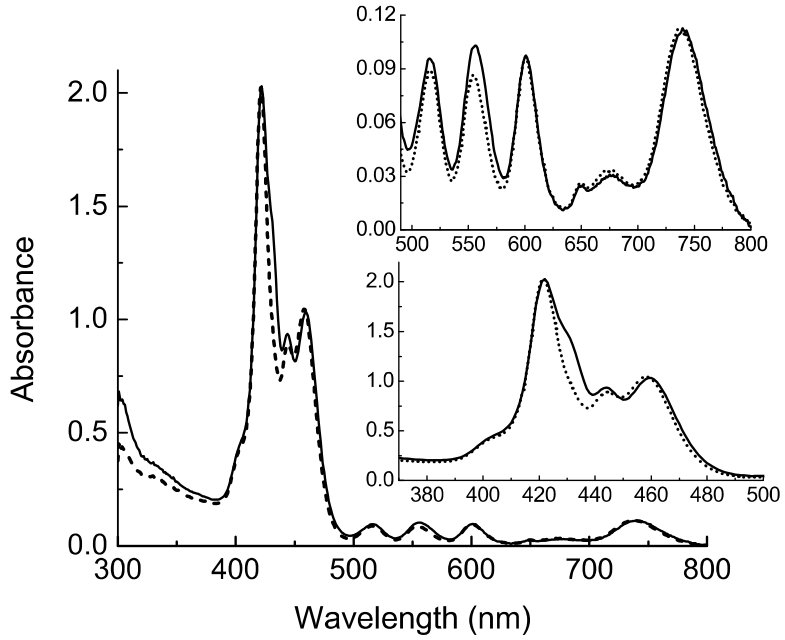

Figure 43. Absorption spectra in benzonitrile of AaP-C_{60}-CyP (solid), AaP-C_{60} + CyP (dashed), the absorption spectra of AaP-C_{60}-CyP has been normalized to the CyP spectrum at 458 nm, the AaP-C_{60} was normalized to the resulting AaP-C_{60}-CyP spectrum at 421 nm, then the CyP was added resulting in the AaP-C_{60} + CyP spectrum.

3.4 Fluorescence Spectra

Figure 44 shows the absorption spectrum of the triad in BzCN (Q-band region) and the emission spectrum of the same sample with excitation at 424 nm. The blue most fluorescence peak at 647 nm and the shoulder at 719 nm correspond to the fluorescence of the AaP moiety, and the peak at 776 nm corresponds to fluorescence from the CyP.

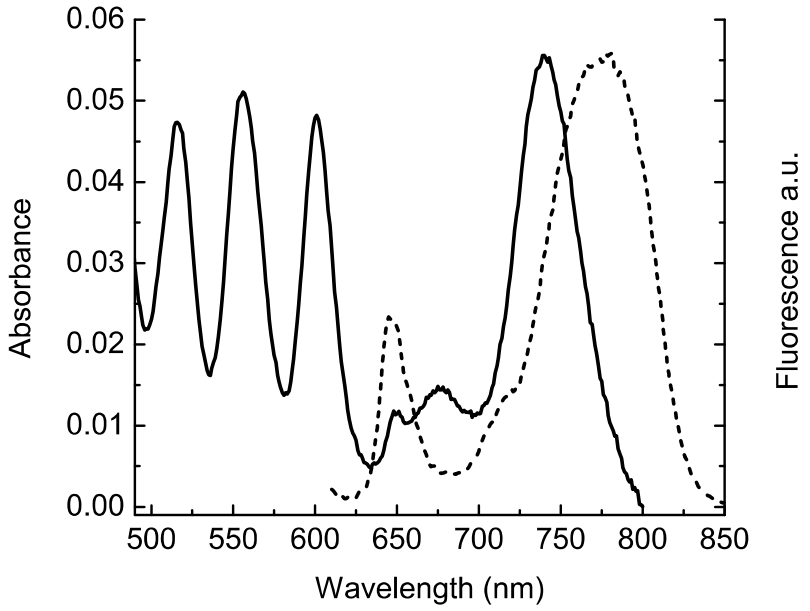

Figure 44. Absorption (solid) and fluorescence (dashed) of AaP-C_{60}-CyP, in BzCN.

Figure 45 shows the emission spectra of the triad and of a solution of AaP-C_{60} with the same absorbance at the excitation wavelength of 510 nm, where most of the absorption in the triad is by the AaP. In the fluorescence spectrum of the triad, the amount of fluorescence from the AaP moiety is strongly decreased, and emission from the CyP around 800 nm is observed. This indicates that in the triad, singlet-singlet energy transfer from AaP to CyP occurs.

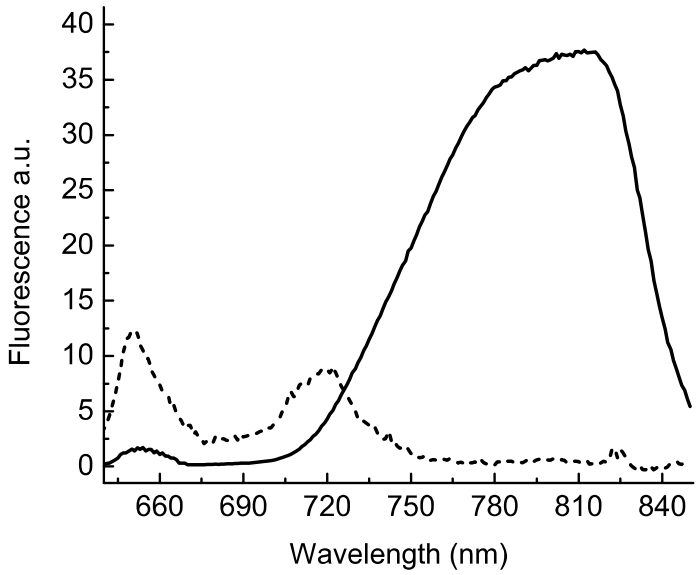

Figure 45. Fluorescence spectra of AaP-C_{60}-CyP (solid), and AaP-C_{60} (dashed), with excitation at 510 nm in MeTHF. The samples have the same absorbance at 510 nm.

Figure 46 shows the fluorescence emission spectra of the triad and CyP model **15** with excitation at 445 nm, where almost all of the light is absorbed by CyP. The samples had the same absorbance at the excitation wavelength. This experiment shows that there is some quenching of the CyP fluorescence by the other components of the triad. Because CyP has the longest-wavelength absorption of any chromophore in the triad, this quenching cannot be due to singlet energy transfer. It is attributed to photoinduced electron transfer from the porphyrin AaP to the ^{1}CyP to give a AaP$^{\bullet+}$-C_{60}-CyP$^{\bullet-}$ charge separated state. This conclusion is in accord with time resolved experiments (*vide infra*).

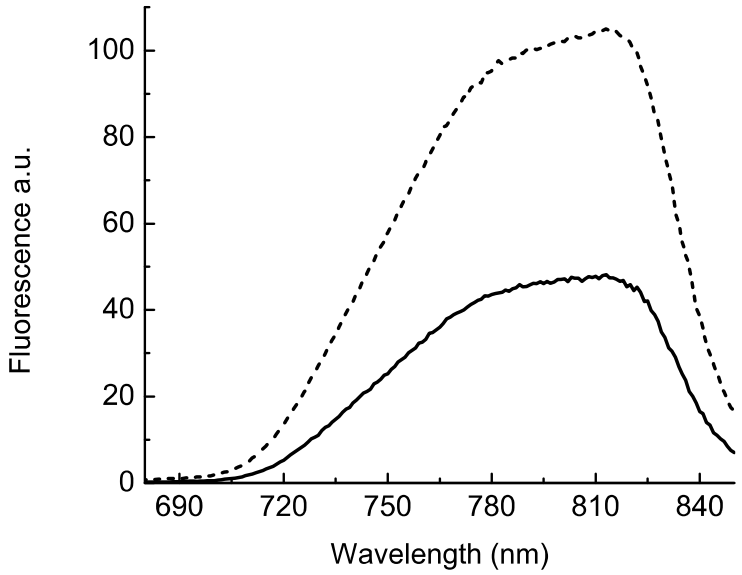

Figure 46. Fluorescence spectra of AaP-C_{60}-CyP (solid) and **15** (dashed), with excitation at 445 nm in MeTHF. The samples have the same absorbance at the excitation wavelength.

3.4.1 Fluorescence Excitation Spectra of the Triad

Figure 47 shows the fluorescence excitation spectra of the triad in both toluene and benzonitrile, normalized at the CyP absorption maximum. In toluene, the excitation spectrum is lower in amplitude than the absorption spectrum in the regions were the AaP absorbs. This shows that energy transfer is not completely efficient, and that some of the AaP excitation is decaying in other ways. In benzonitrile, the effect is more pronounced. Because the absorption spectrum of the triad is nearly the sum of the spectra of the component chromophores (Figure 43), is it possible to roughly estimate the energy transfer efficiencies from the data in Figure 47. In toluene, the efficiency is about 73%. In benzonitrile, the efficiency drops to about 45%, indicating that in this solvent a new pathway for decay of ^{1}AaP-C_{60}-CyP has appeared. As indicated by the time resolved

experiments discussed below, this pathway is formation of the charge separated state $AaP^{\bullet+}$-$C_{60}^{\bullet-}$-CyP.

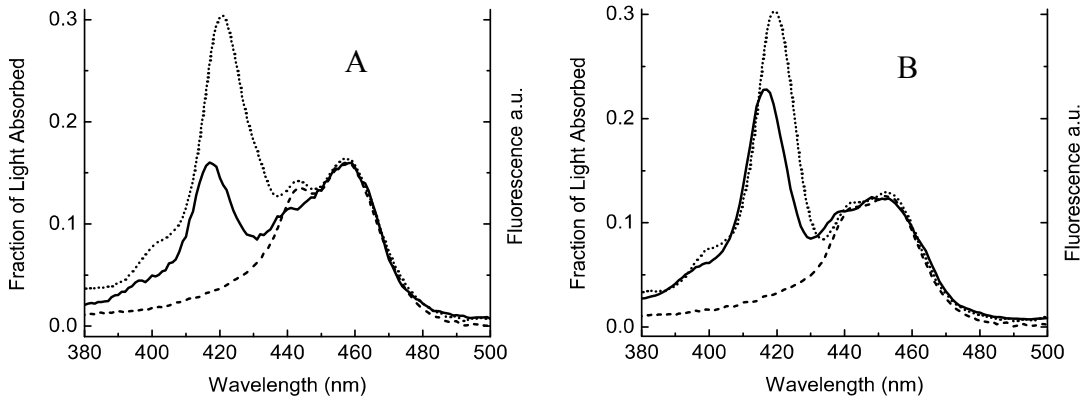

Figure 47. Fluorescence excitation spectrum of AaP-C_{60}-CyP (solid) and absorption spectrum of AaP-C_{60}-CyP (dotted), both normalized to the absorption of the CyP (dashed) at λ_{max} = 456 nm. Experiments were performed in (a) BzCN and (b) toluene.

3.4.2 Time Resolved Fluorescence Studies

Fluorescence quenching yields are difficult to determine accurately using steady-state fluorescence; any small amount of unattached porphyrin impurity can cause inaccurate results.[54] In order to obtain more quantitative information, fluorescence decay measurements were made using the time-correlated single photon counting method. These experiments were done in two solvents; benzonitrile and toluene. Due to the time resolution of the instrument used to obtain these data, time constants of < 30 ps have greater uncertainty than the longer time constants.

Model porphyrin **6** was studied in toluene solution with excitation at 515 nm and emission at 650 nm. A single exponential decay with a time constant of 9.5 ns was

observed, corresponding to decay of ^{1}AaP by the usual photophysical pathways of internal conversion, intersystem crossing and fluorescence. In BzCN, the corresponding lifetime was 10.1 ns.

The time-resolved fluorescence experiments for the CyP model were obtained with excitation at 515 nm in both toluene and BzCN. Experiments in toluene revealed relaxation/solvation process of the excited state of CyP which occur in 21 ps, and that the lowest singlet excited state lifetime is 2.1 ns. In BzCN these values are 45 ps and 1.9 ns. The relaxation/solvation process is slower in BzCN due to an increase of solvent polarity and viscosity going from toluene to BzCN.

In toluene, the time resolved fluorescence experiments on CyP-C_{60} with excitation at 515 nm revealed two lifetimes; 2.02 ns and 50 ps. These are assigned to the singlet excited state lifetime of CyP and the relaxation/solvation process seen in the model CyP, respectively. A similar experiment in BzCN with emission at 5 wavelengths in the 740-820 nm gave similar results, with the lifetime of the singlet excited state being 1.88 ns and a relaxation/solvation lifetime of 135 ps. Thus, attaching the fullerene to CyP does not lead to new photochemistry in the porphyrin excited state.

The time resolved fluorescence measurements on AaP-C_{60} excited at 515 nm in toluene gave two lifetimes; 76 ps, and 1.34 ns. These can be assigned to the decay of the porphyrin singlet excited state by singlet energy transfer to the C_{60}, and the decay of C_{60} singlet excited state via regular relaxation pathways to the triplet excited state and ground state, respectively, as shown by the transient absorption studies below. In BzCN excitation at 515 nm gave one lifetime of 28 ps, which is close to the time resolution of

the instrument and therefore less reliable than the other lifetimes. As discussed below, these are associated with the porphyrin singlet excited state decay by both energy and electron transfer to the C_{60}.

The time resolved fluorescence measurements of the triad in toluene, with excitation at 515 nm and detection of emission at 10 wavelengths in the 650-820 nm region, reveal three decay lifetimes. The 28 ps decay is due to decay of the AaP excited singlet state. The 140 ps decay corresponds to the CyP singlet excited state relaxation/solvation, and the 2.15 ns time constant corresponds to the decay of the singlet excited state of CyP by the usual photophysical processes.

The fluorescence measurements of the triad done in BzCN with excitation at 440 nm and emission at 740 ns (almost exclusively exciting the CyP), gave three decay lifetimes. The shortest lifetime of 52 ps (82% of the decay) can be assigned to the relaxation/solvation of the CyP excited state. As discussed below, a lifetime of 450 ps (17%) is associated with electron transfer to the CyP excited singlet state. The 1.88 ns decay component (1%) is ascribed to small amount of unattached CyP impurity.

3.4.3 Transient Absorption Studies

The time resolved fluorescence experiment only yield information on emissive transient species, and the time resolution available using our instrumentation is not high enough to detect all transient processes in these molecules. Consequently, experiments were carried out using time-resolved absorption techniques. The apparatus is described in the Experimental Section.

3.4.4 Transient Studies of (CyP) Model 15

Figure 48. shows the decay associated spectra (DAS) of **15** in toluene and in BzCN.

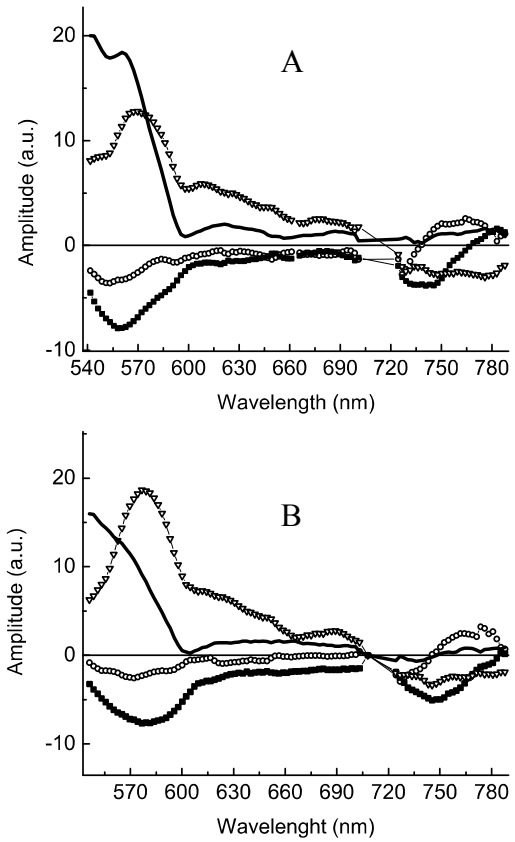

Figure 48. Transient absorption DAS (excitation at 725 nm) for **15** in: (a) Toluene 1.5 ps (circle), 23 ps (square), 2.11 ns (inverted triangle), constant (solid) and (b) BzCN 2.9 ps (circle), 50 ps (square), 1.88 ns (inverted triangle), constant (solid).

A global analysis of the CyP transient absorption data with excitation at the red most Q band of the CyP at 725 nm gives 4 decay components whose decay-associated spectra have similar shapes in both toluene and benzonitrile. The shorter decay components are due to complex relaxation/solvation of the singlet excited state as they show a characteristic stimulated emission band shift to longer wavelengths with a positive

amplitude at longer wavelengths and negative amplitude at shorter wavelengths. In toluene this process occurs with 1.5 ps and 23 ps time constants. Because BzCN is more polar and viscous this process is slower with time constants of 2.9 ps and 50 ps. The 1.88 ns DAS in toluene and 2.11 ns DAS in BzCN show characteristic induced absorption at around 570-580 nm, a ground state bleaching of the Q bands in the region 540 nm to 780 nm and stimulated emission at ~720-790 nm, and are associated with the decay of the lowest singlet excited state of the CyP. The nondecaying DAS show characteristic induced absorption at ~550 nm, bleaching of the Q bands, and no stimulated emission. Therefore these DAS can be associated with the CyP triplet excited state. Thus, the transient absorption and emission data are in agreement, given the longer time limitations in the fluorescence measurement. The time-resolved fluorescence and absorption data of the CyP are in agreement with a previously studied CyP in our laboratory.[146]

3.4.5 Transient Absorption Studies of the CyP-C_{60} Dyad

Figure 49 shows the decay associated spectra from global analysis of the transient absorption data for dyad CyP-C_{60} in toluene and benzene, with excitation at 595 nm.

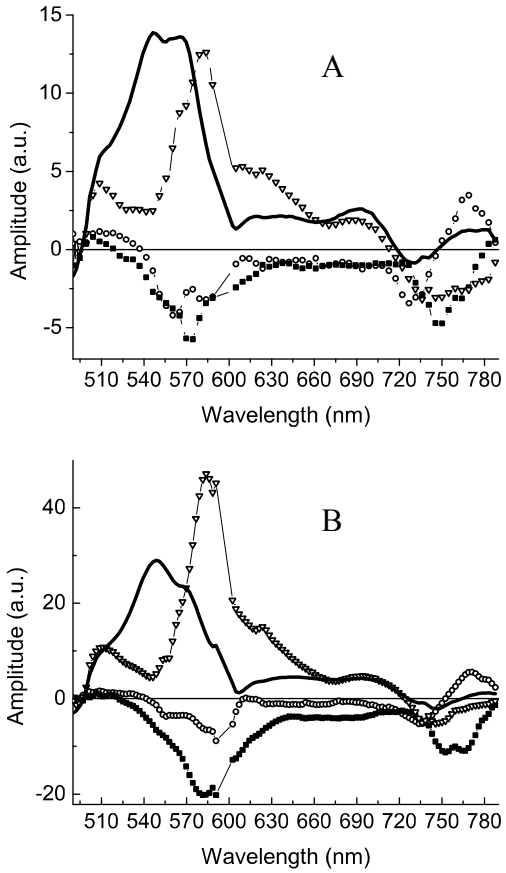

Figure 49. Transient absorption DAS (excitation at 595 nm) for CyP-C_{60} in: (a) Toluene 10 ps (circle), 68 ps (square), 2.16 ns (inverted triangle), constant (solid) and (b) BzCN 8.9 ps (circle), 130 ps (square), 1.88 ns (inverted triangle), constant (solid).

The global analysis of gives 4 components with similar DAS for toluene and BzCN. The two shorter components (10 ps and 68 ps in toluene and 8.9 ps and 130 ps in BzCN) show stimulated emission band shifts in the DAS and are associated with the complex relaxation/solvation of the singlet excited state of CyP as was observed in the CyP model compound. They are slower than observed for the CyP model, which may be due to a lower vibrational freedom along with a lower solvent interaction freedom. The DAS with time constants in BzCN of 1.88 ns and in toluene of 2.2 ns can be assigned to the decay of the singlet excited state of CyP as they show induced absorption at ~570 - 580 nm,

bleaching of the Q bands in the ~540-780 nm region and stimulated emission bands at ~720-780 nm. These features match the DAS from the model CyP (Figure 48). The nondecaying DAS shows characteristic induced absorption at ~550 nm, and no stimulated emission, and therefore can be associated with the decay of CyP triplet excited state, again matching well with the features in the DAS assigned to the CyP triplet state for the model CyP. A transient signal from the C_{60} singlet excited state is not seen in this analysis, which may be explained by the state's low transient extinction in comparison to CyP and its weak absorption at 595 nm. There was no formation of a charge-separated state. No intramolecular energy transfer from the fullerene to the porphyrin was observed in this model dyad with excitation at 595 nm, although such a process is thermodynamically possible and kinetically likely (see below).

3.4.6 Transient Absorption Studies of the AaP-C_{60} Dyad

Transient absorption experiments for the AaP-C_{60} dyad model were carried out in toluene and BzCN with excitation at 590 nm (Figure 50).

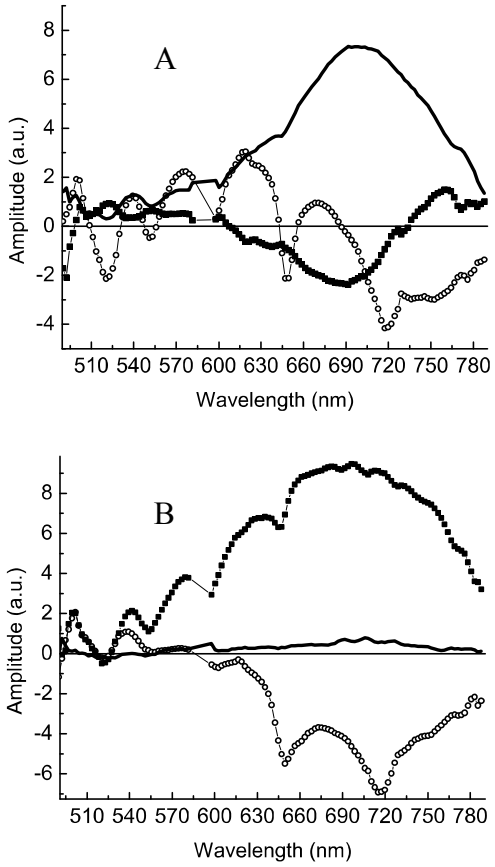

Figure 50. Transient absorption DAS (excitation at 590 nm) for AaP-C_{60} in: (a) Toluene 75 ps (circle), 1.87 ns (square), constant (solid), and (b) BzCN 30 ps (circle), 660 ps (square), constant (solid).

In toluene the 75 ps DAS shows beaching of the Q bands in the region of ~500-650 nm, and stimulated emission at 650 nm and 720 nm. Therefore, this DAS can be associated with the decay of porphyrin singlet excited state. This DAS also has a broad negative amplitude at ~730 -790 nm, showing the formation of induced absorption which is due to the C_{60} singlet excited state. Thus this component can be associated with energy transfer from the AaP singlet excited state to C_{60}. The 1.34 ns DAS shows a signal at ~700 nm with negative amplitude which is characteristic of the formation of the C_{60} triplet state and decay of the excited singlet state. The non-decaying component has a

broad induced absorption at ~700 nm, weak bleaching of the Q bands in the 500-650 nm region, and induced absorption at ~780 nm. The induced absorption at 700 nm is characteristic of a C_{60} triplet excited state decay, the Q-band bleaching and 780 induced absorption can be assigned to the porphyrin triplet excited state. The time constants are consistent with the time resolved emission studies discussed above.

In BzCN the 30 ps DAS shows the formation of a broad induced absorption at ~690 nm (negative amplitude), Q band bleaching in the region of ~500-650 nm, and stimulated emission at ~650nm and 720 nm. These features are assigned to the decay of ^{1}AaP and formation of the AaP$^{\bullet+}$-$C_{60}^{\bullet-}$-CyP charge separated (CS) state with the induced absorption at 690 nm characteristic of AaP$^{\bullet+}$. The CS state decays to the ground state with a lifetime of 660 ps, and the associated DAS shows beaching of the Q bands in 500-650 nm region and induced absorption at ~690 nm due to P$^{\bullet+}$. The nondecaying DAS, with induced absorption around 700 nm, represents a small amount of the C_{60} triplet excited state formed from the C_{60} singlet excited state.

3.4.7 Transient absorption studies of the AaP-C_{60}-CyP triad

Transient absorption DAS of the AaP-C_{60}-CyP were obtained in toluene with the almost exclusive excitation of the AaP at 510 nm (Figure 51a).

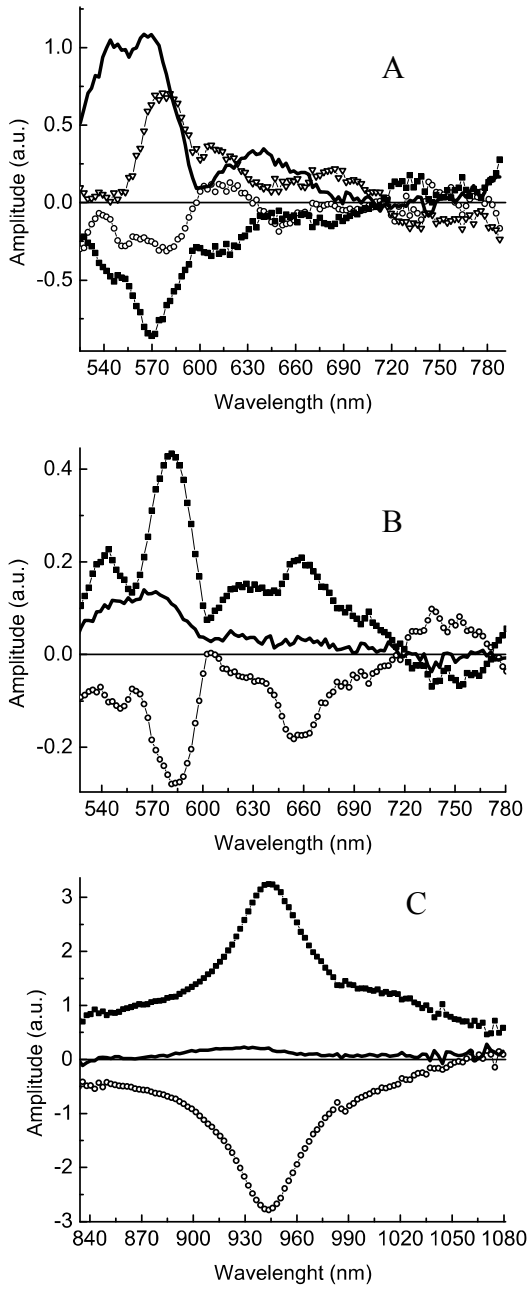

Figure 51. Transient absorption DAS (excitation at 510 nm) for AaP-C_{60}-CyP in: (a) Toluene 29 ps (circle), 143 ps (square), 2.15 ns (inverted triangle), constant (solid) and in BzCN both (b) and (c) 22 ps (circle), 350 ps (square), constant (solid).

Transient absorption DAS of the AaP-C_{60}-CyP were obtained in toluene with the almost exclusive excitation of the AaP at 510 nm (Figure 51a). The global analysis gave

4 components. The 29 ps DAS shows characteristic Q band bleaching in the ~510-650 nm spectral region, and stimulated emission at 660 and 720 nm. This DAS corresponds to the decay of the AaP porphyrin singlet excited state. This component also features a broad negative band at ~580 nm and a positive amplitude signal at ~740-790 nm, indicating the rise of induced absorbance at ~580 nm, and stimulated emission at ~740-790 nm. These features are characteristic of the CyP singlet excited state. Therefore the 29 ps time constant is associated with energy transfer from AaP to CyP. The 143 ps DAS shows the relaxation/solvation of the CyP as seen in the spectra for the model compounds **15** and CyP-C_{60}. The DAS with the lifetime of 2.15 ns can be assigned to the decay of the CyP singlet excited state as it shows characteristic features also seen in the DAS corresponding to the singlet excited state of CyP for the model compounds. The nondecaying DAS has a characteristic induced absorption at ~550 nm with no stimulated emission so it can be assigned to the decay of the CyP triplet excited state.

The global analysis of the transient absorption data with the excitation of the AaP at 510 nm in BzCN (Figure 51b) gave three components. The 22 ps DAS has broad negative bands at 580 nm, 660 nm, and 950 nm. These correspond to the characteristic signals from the formation of induced absorption of $CyP^{\bullet-}$ and $AaP^{\bullet+}$ at ~580 nm, ~950 nm and ~660 nm. Thus, the 22 ps DAS can be assigned to the formation of the $AaP^{\bullet+}$-C_{60}-$CyP^{\bullet-}$ charge separated state. The 350 ps DAS shows decay of the previously mentioned induced absorption, characteristic of $CyP^{\bullet-}$ and $AaP^{\bullet+}$, and can be associated with the decay of the charge-separated state. The nondecaying DAS shows characteristic induced absorption at 550 nm and since there is also no stimulated emission, the DAS is indicative of the CyP triplet excited state.

The global analysis of transient absorption data of the triad in BzCN with exclusive excitation of the CyP at 725 nm gives four components (Figure 52).

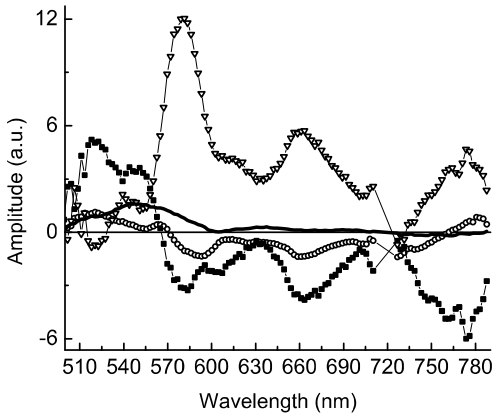

Figure 52. Transient absorption DAS (excitation at 725 nm) for AaP-C_{60}-CyP in: BzCN 14 ps (circle), 350 ps (square), 500 ps (inverted triangle) constant (solid).

The 14 ps DAS shows the stimulated emission band shift observed in decays seen in the model compounds, and can be associated with the complex relaxation/solvation of the singlet excited state of CyP. The 500 ps DAS shows Q band bleaching and induced absorption around 660 nm characteristic of the AaP radical cation, and there is no stimulated emission. The 350 ps DAS has a positive amplitude at ~520 nm and negative amplitude at 660 nm, corresponding to the formation of characteristic Q band bleaching from AaP at ~520 nm and the formation of the induced absorption from $AaP^{\bullet+}$. The 500 ps DAS shows a negative signal in the 520 nm region associated with the Q band bleaching of AaP as well as induced absorption at 660 nm that can be assigned to the $AaP^{\bullet+}$. The 350 and 500 ps DAS indicate a situation of "inverted kinetics," where the 500

ps DAS is characteristic of formation of the $AaP^{\bullet+}$-C60-$CyP^{\bullet-}$ state and the 350 ps DAS represents the decay of that state.

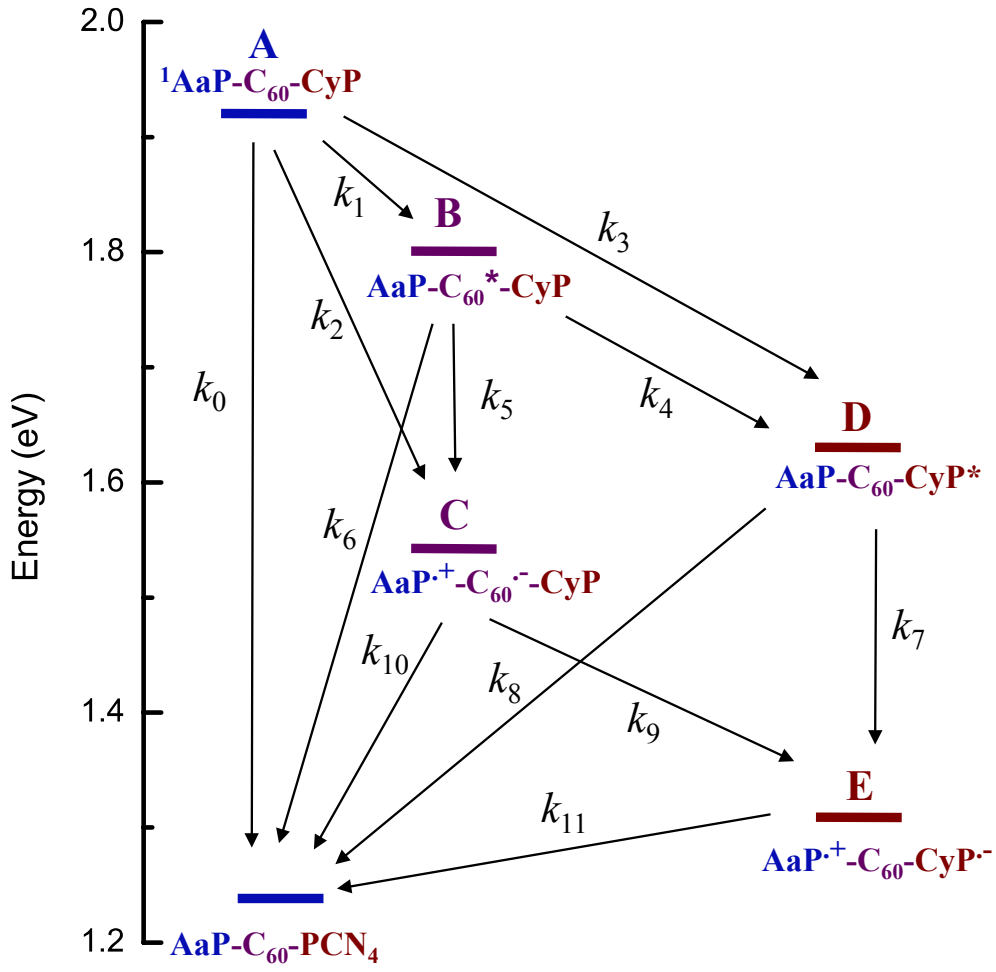

Figure 53. Transient states of AaP-C_{60}-CyP, relevant interconversion pathways and the corresponding rate constants. See Table 4 for energy levels values

Table 4. Energies of the excited and charge separated states of AaP-C_{60}-CyP[a]

	AaP*-C_{60}-CyP (A)	AaP-C_{60}*-CyP[b] (B)	AaP$^{\cdot+}$-$C_{60}^{\cdot-}$-CyP (C)	AaP-C_{60}-CyP* (D)	AaP$^{\cdot+}$-C_{60}-CyP$^{\cdot-}$ [c] (E)
Energy (eV) in BzCN	1.92	1.8[a]	1.54	1.63	1.31

[a] The excited state energy levels were calculated form the absorption and fluorescence of the model compounds, and the energetics of the AaP$^{\bullet+}$-$C_{60}^{\bullet-}$-CyP, AaP$^{\bullet+}$-C_{60}-CyP$^{\bullet-}$ CS states were calculated using the reduction and oxidation potentials of the model compounds **7** and **15** measured by cyclic voltammetry (Table 2).
[b] The excited state energy levels of C_{60} was take from previously reported value.[56]
[c] The previously determined reduction potential of a model β-cyanoporphyrin with an ester functional group in place of the aldehyde group, was used for the energy level calculations.[137]

Table 5. Rate constants in benzonitrile

	k_0 (s^{-1})	k_1 (s^{-1})	k_2 (s^{-1})	k_3 (s^{-1})	k_4 (s^{-1})	k_5 (s^{-1})
Triad BzCN/ Toluene	9.91×10^7/ 1.05×10^8	1.32×10^{10}	2.00×10^{10}	2.12×10^{10}	$\geq k_1$	1.00×10^{10}
Φ of state from process with rate *k*	--	0.24	0.37	0.39	0.13	0.10
	k_6 (s^{-1})	k_7 (s^{-1})	k_8 (s^{-1})	k_9 (s^{-1})	k_{10} (s^{-1})	k_{11} (s^{-1})
Triad BzCN/ Toluene	7.46×10^8	1.47×10^9	5.32×10^8/ 4.74×10^8	$>>k_2$	1.52×10^9	2.86×10^9
Φ of state process with rate *k*	--	0.38	--	0.43	--	--

Table 6. Quantum yields in benzonitrile

	Φ_B	Φ_C (assuming $k_9 >> k_2$)	Φ_D (assuming $k_4 \geq k_1$)	Φ_E (assuming $k_4 \geq k_1$ and $k_9 >> k_2$)
Total Φ	0.24	0.47	0.52	0.85

3.5 Discussion

The various high energy states of the triad and relevant interconversion pathways are shown in figure 53. The energies of the various states have been calculated from the spectroscopic and electrochemical data, and are given in Table 4. Analysis of the time resolved fluorescence and transient absorption results of the model compounds can be used to estimate the rate constants and quantum yields of the relevant energy and electron transfer process that occur in the triad, as reported in Tables 4, 5, and 6. The rate constants were determined in the simpler model systems where a process occurs with the absence of others, and then applied to the more complex triad.

In toluene the charge separated states are destabilized due to the loss of solvent stabilization of the ions.[145] Therefore, in toluene, the only interchromophore processes observed were energy transfer events. No charge-separated states are created or consumed in energy transfer processes, and the rate constants for energy transfer typically show little solvent dependence. In this analysis, we have determined energy transfer rate constants in toluene and used the same values for these processes in BzCN in order to make analysis of the kinetics possible.

The rate of decay via internal conversion, fluorescence and intersystem crossing of the ^{1}AaP moiety, k_0, was obtained from the time resolved fluorescence experiments on **7** in

both toluene, k_0=1.1 × 10^8 s^{-1-1}, and BzCN k_0=9.9 × 10^7 s^{-1}. The results for model compound AaP-C_{60} allow the calculation of the rate constants for energy and electron transfer from the singlet excited state of the porphyrin to form either the C_{60} singlet excited state via step 1, or the charge separated state $AaP^{\bullet+}$-$C_{60}^{\bullet-}$ via step 2. They also allow determination of the rate of charge recombination of $AaP^{\bullet+}$-$C_{60}^{\bullet-}$ via step 10.

The rate constant for energy transfer from ^{1}AaP to the C_{60} moiety was determined from the measured time constant τ=75 ps from the DAS in toluene and k_0 using Equation 9, and found to be 1.3 × 10^{10} s^{-1}.

$$k_1 = \frac{1}{\tau_1} - k_0 \qquad (9)$$

The decay rate constant of the C_{60} singlet excited state by unimolecular processes, k_6=7.5 × 10^8 s^{-1}, was obtained from the transient absorption data for AaP-C_{60} in toluene, and is consistent with other studies.

In BzCN ^{1}AaP-C_{60} decays through three processes; unimolecular decay to the ground state, energy transfer to the fullerene, and also now electron transfer to C_{60}, with rate constant k_2, to form the charge separated state $AaP^{\bullet+}$-$C_{60}^{\bullet-}$. In addition this charge-separated state can be formed from electron transfer from the C_{60} singlet excited state. The rate of this last process, k_5, has been determined previously in similar P-C_{60} systems, and is ~1.0 × $10^{10}$$s^{-1}$.[25] The rate constant for electron transfer from the excited state ^{1}AaP-C_{60} to form $AaP^{\bullet+}$-$C_{60}^{\bullet-}$, k_2, can be calculated using the k_1 from the results obtained in toluene, k_0 measured in BzCN, and the measured time constant τ = 30 ps for the decay

of the AaP singlet excited state in the DAS of AaP-C_{60} in BzCN using Equation 10, and equals 2.0×10^{10} s^{-1}:

$$k_2 = \frac{1}{\tau_2} - k_0 - k_1 \qquad (10)$$

The rate constant for charge recombination to ground state, k_{10}, was measured to be 1.5×10^9 s^{-1} from the DAS of AaP-C_{60} in BzCN as well.

The excited state processes observed in ^{1}CyP and ^{1}CyP-C_{60} consist of only the unimolecular decay processes of the CyP, as the energetics of the system does not allow energy transfer or electron transfer involving the CyP singlet excited state and C_{60}. The singlet excited state lifetimes of the CyP moiety obtained from transient absorption studies and fluorescence SPC experiments of the CyP and the CyP-C_{60} model compounds are equivalent which corroborates the absence of energy transfer between CyP and C_{60}. It is likely that energy transfer from C_{60} to CyP occurs, although the signal to noise available in our experiment did not allow us to detect this process. The rate constant for energy transfer from $^1C_{60}$ to CyP in CyP-C_{60} and the triad, k_4, is expected to be similar to k_1 as the geometric and spectral overlap terms in the Förster equation are expected to be almost the same. Therefore we have taken k_4 to equal 1.3×10^{10} s^{-1}.

The rate constant for the decay of ^{1}CyP was determined by both time resolved fluorescence and transient absorption studies. From these experiments the rate constant for the decay of the CyP singlet excited state is determined in toluene to be k_8=$4.74 \times 10^8 s^{-1}$ and in BzCN to be k_8=$5.3 \times 10^8 s^{-1}$. As explained above, the CyP undergoes a relaxation/solvation process of the singlet excited state, these processes and energy levels

are not shown in the chart, as the processes of interest most likely occur from the relaxed singlet excited state.

The remaining rate constants of the energy and electron transfer processes can be measured and calculated with the data from the time resolved fluorescence and transient absorption of the triad, first in toluene and then in BzCN. In the triad the fluorescence excitation and transient spectroscopy show that the two porphyrins are undergoing an energy transfer processes. This is most likely occurring via a Förster through-space resonant interaction of the transition dipoles of the porphyrins. This process is shown to be occurring between the porphyrins with a relatively fast rate and with a moderate quantum yield. This indicates that the triad must be taking a conformation where the two porphyrins are interacting. This is consistent with the exciplex formation noted in the UV/Vis spectrum of the AaP-C_{60}-CyP, as evidenced by a shoulder peak at around 430 nm.

From the DAS in toluene a time constant of 29 ps was measured, and the rate of energy transfer, k_3, can be calculated to be 2.1×10^{10} s^{-1} using an equation similar to eq. 2.

In BzCN additional electron transfer processes occur in addition to the energy transfer already accounted for in toluene. These are the formation and decay of the intermediate charge separated state, $AaP^{\bullet+}$-$C_{60}^{\bullet-}$-CyP and the final charge separated state $AaP^{\bullet+}$-C_{60}-$CyP^{\bullet-}$. The formation of the final charge separate state occurs through two processes, the excited state of the CyP can undergo electron transfer with a rate k_7, and the charge shift reaction from the intermediate state $AaP^{\bullet+}$-$C_{60}^{\bullet-}$-CyP to the $AaP^{\bullet+}$-C_{60}-$CyP^{\bullet-}$ happens with a rate constant k_9.

The data from transient absorption studies of the triad in BzCN with excitation of only the CyP moiety at 725 nm allows the calculation of the rate constant for the electron transfer process from ^{1}CyP to form AaP$^{\bullet+}$-C$_{60}$-CyP$^{\bullet-}$, k_7. From time resolved fluorescence and transient absorption experiments it was determined that ^{1}CyP decays with the time constant of 500 ps (τ_7), so the rate for the formation of charge separated state state k_7 can be calculated from Equation 11 to be 1.5×10^9 s^{-1}.

$$k_7 = \frac{1}{\tau_7} - k_8 \tag{11}$$

The charge shift reaction from AaP$^{\bullet+}$-C$_{60}$$^{\bullet-}$-CyP to the final charge separated state AaP$^{\bullet+}$-C$_{60}$-CyP$^{\bullet-}$ is not observed in the transient absorption experiments, indicating that the rate constant for the charge shift reaction must be much larger than k_2: $k_9 >> 2.0 \times 10^{10}$ s^{-1}.

Thus, values have been obtained for all of the rate constants in Figure 20. These are listed in Table 3. With these rate constants estimated, the quantum yields for the various species A – E in Figure 20 were calculated (Table 4). The total quantum yield for the formation for the charge-separated state AaP$^{\bullet+}$-C$_{60}$-CyP$^{\bullet-}$ via all known routes based on excitation of AaP was calculated using Equation 12. As mentioned above this calculation was done making the assumptions of $k_4 \geq k_1$ and $k_9 > k_2$.

$$\Phi_E = \Phi_D * \left(\frac{k_7}{k_7 + k_8}\right) + \Phi_C * \left(\frac{k_9}{k_9 + k_{10}}\right) \tag{12}$$

The quantum yields of the two processes that form the charge-separated state AaP$^{\bullet+}$-C$_{60}$-CyP$^{\bullet-}$, indicate that the main pathway of formation is via electron transfer from the

AaP to the fullerene, followed by the charge shift reaction from the fullerene to CyP. In all, 47% of the electron transfer is from the charge shift reaction and 29% is from the direct electron transfer to ^{1}CyP.

The percent of electron transfer is consistent with the previously estimated value from the comparison of the absorption and excitation spectra of the triad, from which it was calculated that about 55% of the energy absorbed by the AaP undergoes electron transfer or decay to ground state in BzCN, see figure 47 and following discussion for the details.

The sum of rate constants $k_0 - k_3$ yield a corresponding lifetime of 18 ps, which is within experimental error of the 22 ps measured for the triad in benzonitrile. This shows that linking the components to form the triad does not introduce any new decay pathways that are not present in the model compounds. For example, there is no evidence for direct electron transfer from ^{1}AaP to CyP to form the final charge separated state. Formation of the final state is stepwise.

It is of interest that the electron transfer between the $C_{60}^{\bullet-}$ and the CyP by step 9 occurs much faster than the electron transfer between the AaP and C_{60} by step 2, even though the driving force is somewhat lower from the $C_{60}^{\bullet-}$ to the CyP. Step 9 is a charge shift reaction, rather than a photoinduced electron transfer, and thus the effect of the various reorganization energy and solvent stabilization processes may be different. Although the electronic coupling between AaP and C_{60} and CyP and C_{60}, should be similar, based on the nature of the chemical linkages, it may be that the CyP is less coupled to the C_{60} due to the CyP having cyano groups at the β-positions. The conjugation of the meso aryl ring with the porphyrin affects the coupling. The conjugation between the aryl ring and the

porphyrin is in turn affected by the angle of the aryl ring with the mean porphyrin plane. With unsubstituted porphyrins the rings make angles ≥ 45° but< 90°. Alkyl groups at the β-pyrrolic positions forces the aryl ring to be at a greater angle with respect to the mean porphyrin plane, reducing π-π overlap.[147] This effect has been shown to be fairly small; in one study, methyl groups on the β-positions flanking the aryl ring were shown to slow down the rate by 1/5.[147]

From the quantum yield calculations the contribution of the formation of the charge separated state $AaP^{\bullet+}$-C_{60}-$CyP^{-\bullet}$ from the CyP excited state is higher than might at first be expected by a cursory comparison of the rate constants for electron transfer steps 2 and 7. The reason for the relatively large contribution from ^{1}CyP is that this state is formed by rapid and relatively efficient energy transfer from ^{1}AaP, and has a long lifetime due to the small value of k_8. The quantum yield of step 7 is high because electron transfer by step 7 is significantly faster than decay by step 8.

It is interesting to note that the rate of the decay of the intermediate CS state $AaP^{\bullet+}$-$C_{60}^{\bullet-}$-CyP is slower than the decay of the final CS state $AaP^{\bullet+}$-C_{60}-$CyP^{\bullet-}$. This shows that recombination of $AaP^{\bullet+}$-C_{60}-$CyP^{\bullet-}$ occurs by a single step 11 rather than stepwise via intermediate *C*. The electronic coupling between the radical ions in $AaP^{\bullet+}$-C_{60}-$CyP^{\bullet-}$ must be significantly smaller than that in $AaP^{\bullet+}$-$C_{60}^{\bullet-}$-CyP due to the increased number of single bonds linking the moieties. Evidently this effect is outweighed by the smaller thermodynamic driving force for step 11 than for step 10. These charge recombination reactions undoubtedly occur in the Marcus inverted region. In this region, a decrease in driving force yields an increase in rate constant.

3.6 Conclusion

The results from these experiments show that multiple photoinduced electron and energy transfer pathways occur in the synthesized triad upon excitation of the AaP moiety. The excitation of AaP results in the formation of the final charge separated state via two pathways, from the ^{1}CyP, and from the intermediate charge separated state $AaP^{\bullet+}$-$C_{60}^{\bullet-}$-CyP. The calculated rates and quantum yields of the major possible processes, which were obtained from the fluorescence lifetime and transient absorption experiments, show that the C_{60} acts as an electron transfer bridge in which the radical anion of C_{60} rapidly transfers an electron to the CyP with a quantum yield with near unity to form the CS state $AaP^{\bullet+}$-C_{60}-$CyP^{\bullet-}$. Singlet energy transfer from ^{1}AaP to CyP is also relatively efficient, and also leads to formation of the final charge separated state via photoinduced electron transfer to ^{1}CyP.

The rapid electron transfer via step 9 easily competes with charge recombination by step 10. This step could be much slower, and still have a quantum yield near unity Future studies of this charge shift reaction between the C_{60} and the CyP, could include decoupling the CyP from the C_{60}, as well as from the donor porphyrin. This in theory would slow down the rate of charge recombination of the final charge separated state, while maintaining forward electron transfer processes that could compete well with recombination steps. Increasing the distance between the two porphyrins would also decrease the rate of energy transfer between the porphyrins, and allow for a higher efficiency of the charge separation reactions.

3.7 Experimental

3.7.1 Instrumental Techniques

All NMR spectra were recorded on 400 MHz Varian spectrometers. Samples were dissolved in $CDCl_3$ with TMS as an internal reference, unless otherwise stated. Mass spectra were obtained on an Applied Biosystems Voyager-DE STR matrix-assisted laser desorption/ionization time-of-flight spectrometer (MALDI-TOF). *Trans, trans*-1,4-diphenyl-1,3-butadiene was used as a matrix for the MALDI-TOF-MS measurements unless otherwise stated. Ultraviolet-visible absorption spectra were measured on a Shimazu UV2100U spectrometer.

Fluorescence

Steady-state fluorescence and fluorescence excitation spectra were measured using a Photon Technology International MP-1 spectrometer and corrected for detection system response and excitation source intensity as a function of wavelength. Excitation was provided by a 75 W xenon-arc lamp and single-grating monochromator. Fluorescence was detected at 90° to the excitation beam via a single-grating monochromator and an R928 photomultiplier tube having S-20 spectral response and operating in the single photon counting mode.

Fluorescence decay measurements were performed on optically dilute (ca. 1×10^{-5} M) samples by the time-correlated single-photon-counting method. Two different excitation systems were employed. The excitation source for the first system was a mode-locked Ti:Sapphire laser (Spectra Physics, Millennia-pumped Tsunami) with a 130-fs pulse

duration operating at 80 MHz. The laser output was sent through a frequency doubler and pulse selector (Spectra Physics Model 3980) to obtain 370-450 nm pulses at 4 MHz. The excitation source for the second system was a fiber supercontinuum laser based on a passive modelocked fiber laser and a high-nonlinearity photonic crystal fiber supercontinuum generator (Fianium SC450). The laser provides 6-ps pulses at a repetition rate variable between 0.1 – 40 MHz. The laser output was sent through an Acousto-Optical Tunable Filter (Fianium AOTF) and the relevant 10 nm interference filter to obtain excitation pulses at a desired wavelength. Fluorescence emission was detected at the magic angle using a double grating monochromator (Jobin Yvon Gemini-180) and a microchannel plate photomultiplier tube (Hamamatsu R3809U-50). The instrument response function was 35-55 ps. The spectrometer was controlled by software based on the LabView programming language and data acquisition was done using a single photon counting card (Becker-Hickl, SPC-830).

Transient absorption

The conventional femtosecond transient absorption apparatus consisted of a kilohertz (adjustable upto subhertz frequencies for EOS applications, *vide infra*) pulsed laser source and a pump-probe optical setup. Laser pulses of 100 fs at 800 nm were generated from an amplified, mode-locked titanium sapphire laser system (Millennia/Tsunami/Spitfire, Spectra Physics). Part of the laser pulse was sent through an optical delay line and focused on to a 3 mm sapphire plate to generate a white light continuum for the probe beam. The remainder of the pulse energy was used to pump an optical parametric amplifier (Spectra Physics) to generate excitation pulses, which were

selected using a mechanical chopper. The white light generated was then compressed by prism pairs (CVI) before passing through the sample. The polarization of pump beam was set to the magic angle (54.7°) relative to the probe beam and its intensity adjusted using a continuously variable neutral density filter. The white light probe was dispersed by a spectrograph (300 line grating) onto a charge-coupled device (CCD) camera (DU420, Andor Tech.). The final spectral resolution was about 2.3 nm for over a nearly 300 nm spectral region. The instrument response function (IRF) was ca. 150 fs.

Transient absorption spectra and kinetics on the ps-ms time scale were obtined using EOS spectrometer from Ultrafast Systems (IRF ~800 ps); excitation was from the same optical parametric amplifier as descibed above.

Data analysis was carried out using locally written software (ASUFIT) developed under a MATLAB environment (Mathworks Inc.). Decay-associated spectra (DAS) were obtained by fitting the transient absorption or fluorescence change curves over a selected wavelength region simultaneously as described by Equation 13 (parallel kinetic model),

$$\Delta A(\lambda,t)=\sum_{i=1}^{n} A_i(\lambda)\exp(-t/\tau_i) \qquad (13)$$

where $\Delta A(\lambda,t)$ is the observed absorption (or fluorescence) change at a given wavelength at time delay t and n is the number of kinetic components used in the fitting. A plot of $A_i(\lambda)$ versus wavelength is called a decay-associated spectrum, and represents the amplitude spectrum of the i^{th} kinetic component, which has a lifetime of τ_i. The global analysis procedures described here have been extensively reviewed in literature.[148]

Random errors associated with the reported lifetimes obtained from fluorescence and transient absorption measurements were typically ≤ 5%.

3.7.2 Synthesis General Procedures.

Thin-layer chromatography for dipyrromethanes and porphyrins was performed on silica gel GHFL or GHL plates (Analtech). Synthesis, workup and purification were performed in a darkened laboratory. *5-(4-tert-butylphenyl)dipyrromethane* (**8**)[149] *5-(4-methoxycarbonylphenyl)-10,15,20-tris-(4-t-butylphenyl)porphyrin* (**9**)[150], and *5-(2,4,6-trimethylphenyl)dipyrromethane* (**5**)[151] were prepared following previously reported methods.

*3.7.3 N-Benzoyl-p-chloromethyl-D,L-phenylglycine (**1**)*

Compound **1** was prepared by modifying previously reported methods.[143] Benzyl chloride (5.3 g, 41.7 mmol) and α-hydroxyhippuric acid (1.95 g, 1.00 mmol) were added to a round bottomed flask under argon, equipped with a magnetic stir bar. Methane sulfonic acid (99.5 %) (10 mL) was added and the solution was allowed to stir for 48 h at room temperature under argon. The reaction mixture was poured into ice water and was extracted with EtOAc. The organic layer was washed with water (3 x 50 mL), then dried over anhydrous sodium sulfate. The solvent was removed and the oil was dissolved in dichloromethane, and the compound was purified by column chromatography on silica gel using 50% ethyl acetate in dichloromethane as the solvent, after the first band was removed the eluent was switched to 50% ethyl acetate 8% MeOH in dichloromethane. The solvent was distilled under reduced pressure and the product was purified by recrystallization from dichloromethane/hexane to yield compound 3 as white crystals. ^{1}H

NMR, (CD_3OD) δ (ppm) 7.81 - 7.90 (m, 2 H), 7.31 - 7.62 (m, 7 H), 5.70 (br s, 1 H), 4.65 (s, 2 H).

*3.7.4 N-benzyloxycarbonyl-p-hydroxymethyl-D,L-phenylglycine (**2**)*

Compound **2** was prepared following the previously reported method with modifications.[143] Compound **1** (1.4 g, 4.6 mmol) and K_2CO_3 (400 mg, 2.90 mmol) were dissolved in 70 mL of water in a round bottomed flask equipped with a magnetic stir bar. The solution was stirred at room temperature for 48 h, after which concentrated HCl was added dropwise until the solution was pH 3, upon which a white precipitate formed. The solution was then extracted with EtOAc and the organic layer was washed with water (3 x 100 mL), the organic layer was collected, dried over anhydrous sodium sulfate, and the solvent was removed by distillation under reduced pressure. The product was dried under reduced pressure yielding compound **2** as white crystals. Yield (46%, 1 g) The product contained a trace of the hydrochloride form. ^{1}H NMR, (CD_3OD) δ (ppm) 7.82 - 7.88 (m, 2 H), 7.34 - 7.58 (m, 7 H), 5.67 (s, 1 H), 4.61 (s, 2 H).

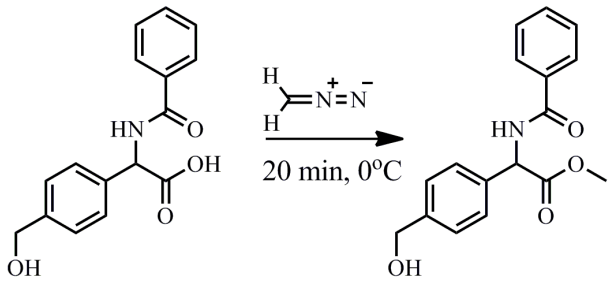

Figure 54. Synthetic scheme for the synthesis of 3

*3.7.5 N-benzoyl-p-hydroxymethyl-D-L-phenylglycine methyl ester (**3**)*

All glassware used had no ground glass joints. Compound **2** (500 mg, 1.75 mmol) was dissolved in ethyl acetate (100 mL) in an Erlenmeyer flask equipped with a magnetic stir bar, and the flask was placed in an ice bath. In a separate two neck round bottomed flask, equipped with a condenser in one neck which was positioned to condense into the Erlenmeyer flask, and a separatory funnel in the other, KOH (2g, 0.04mol) was dissolved in a solution of EtOH (20 mL) and water (8 mL). A solution of diazald (1.29 mg, 6.00 mmol) dissolved in diethyl ether (15 mL) was added to the separatory funnel. The round bottomed flask was placed in an oil bath heated at 70^{o}C, and the solution in the separatory funnel was added dropwise to the round bottomed flask generating diazomethane which then condensed along with diethyl ether into the Erlenmeyer flask. After 15 min the reaction was complete as indicated by thin layer chromatography, and acetic acid (1 mL) was added to the solution. The solvent was removed by distillation under reduced pressure, and the product was dissolved in dichloromethane and washed with an aqueous solution of $NaHCO_3$ followed by water (2 x 100 mL). The solvent was removed was removed by distillation under reduced pressure and the product was dried under vacuum, and purified by column chromatography on silica gel using 50% ethyl acetate in dichloromethane. The second band was collected and the solvent was removed by distillation under reduced pressure yielding pure product **3** as white crystals, yield, (76.2%, 400mg). ^{1}H NMR, δ (ppm) 7.79 - 7.85 (m, 2 H), 7.35 - 7.56 (m, 7 H), 7.17 (d, J=6.2 Hz, 1 H, -NH), 5.78 (d, J=6.6 Hz, 1 H), 4.70 (d, J=6.2 Hz, 2 H), 3.77 (s, 3 H)

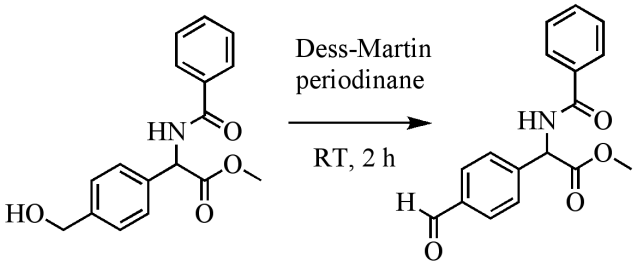

Figure 55. Synthetic scheme for the synthesis of 4

*3.7.6 N-benzoyl-p-formyl-D-L-phenylglycine methyl ester (**4**)*

Compound **3** (200 mg, 0.670 mmol) was dissolved in distilled tetrahydrofuran (10 mL) in a round bottomed flask equipped with a magnetic stir bar. Dess-Martin periodinane (595 mg, 1.40 mmol) was added and the solution was stirred for 2.5 h. $Na_2S_2O_3$ (1.83 g, 7.37 mmol) was dissolved in a solution of 80% Na_2HCO_3 (30 mL) and this solution was added to the reaction mixture stirred for an additional 20 min. The solution was extracted with EtOAc, and the organic layer collected and washed with water (3 x 50 mL). The water washes were extracted with dichloromethane and the organic layers combined and the solvent was removed by distillation under reduced pressure. The product was dried under reduced pressure and purified by column chromatography on silica gel with 30% dichloromethane in EtOAc as the solvent to give pure **6**. Yield (100 mg, 40.3%). ^{1}H NMR, δ (ppm) 10.01 (s, 1 H), 7.89 (d, J=8.2 Hz, 2 H), 7.84 (d, J=7.8 Hz, 2 H), 7.63 (d, J=7.8 Hz, 2 H), 7.50 - 7.58 (m, 1 H), 7.43 - 7.50 (m, 2 H), 7.36 (d, J=6.3 Hz, 1 H, -NH), 5.86 (d, J=6.7 Hz, 1 H), 3.80 (s, 3 H).

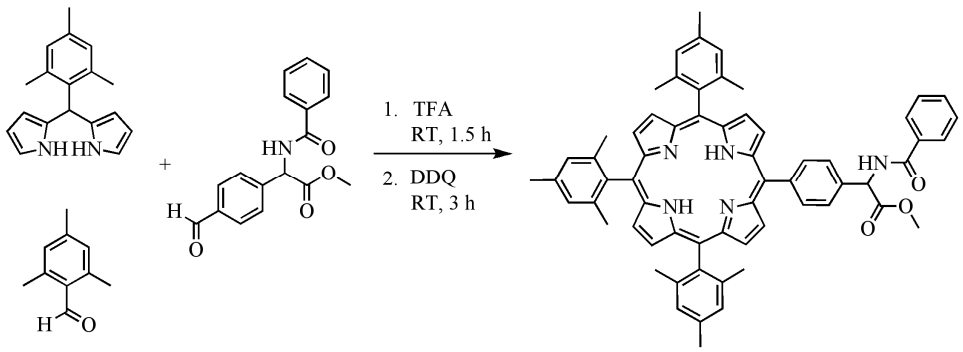

Figure 56. Synthetic scheme for the synthesis of 6

3.7.7 *N*-benzoyl- *4-[*10,15,20-tris-*(2,4,6-trimethylphenylporphyrin-5-yl]phenylglycine,* methyl ester ***(6)***

Compound **4** (427 mg, 1.44 mmol), dipyrromethane **5** (1.5g, 5.7 mmol), and mesitaldehyde (427 mL, 2.90 mmol), were dissolved in dry and deoxygenated dichloromethane (300 mL) under argon in a round bottomed flask equipped with a magnetic stir bar. Trifluoroacetic acid (0.41 mL, 5.3 mmol) was added dropwise and the solution was stirred for 2 h at room temperature. 2,3-dichloro-5,6-dicyano-1,4-benzoquinone (653 mg, 2.88 mmol) was added and the solution was stirred for 3 h, then triethylamine (0.3 mL, 2.2 mmol) was added and the solution was stirred for 10 min. The solvent was removed by distillation under reduced pressure and the product was purified by column chromatography on silica gel with a solution of 35% hexanes in dichloromethane, after the first band was removed dichloromethane was used as the solvent, and after the second band was removed a solution of 5% EtOAc in dichloromethane was used to give pure product 6 as purple crystals, mp >300 °C, yield, 20 mg (1.5%). ^{1}H NMR, δ (ppm) 8.77 (d, J=4.8 Hz, 2 H), 8.67 (d, J=4.8 Hz, 2 H), 8.62 (s, 4 H), 8.21 (d, J=8.3 Hz, 2 H), 7.99 (d, J=7.0 Hz, 2 H), 7.82 (d, J=7.9 Hz, 2 H), 7.48 - 7.63 (m, 3 H), 7.43 (d, J=7.0 Hz, 1 H), 7.27 (br s, 6 H), 6.17 (d, J=7.0 Hz, 1 H), 3.97 (s, 3

H), 2.55 - 2.68 (m, 9 H), 1.84 (d, J=3.9 Hz, 18 H), -2.57 (s, 2 H). MALDI-TOF-MS m/z; calcd for 932.16 [M+], obsd 931.98.

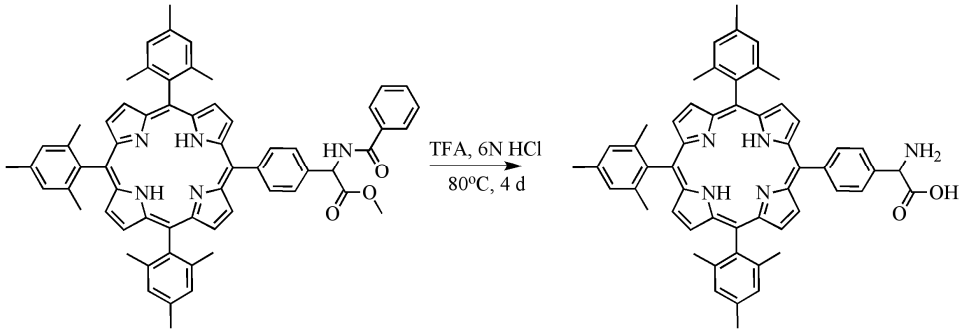

Figure 57. Synthetic scheme for the synthesis of 7

*3.7.8 4-[*10,15,20-tris-*(2,4,6-trimethylphenylporphyrin-5-yl]phenylglycine* ***(AaP)***

Porphyrin **6** (10 mg, 0.011 mmol) was dissolved in trifluoroacetic acid (2 mL), in a glass pressure tube equipped with a magnetic stir bar. 6N HCl (5mL) was added to the solution and the pressure tube was placed in an oil bath at a temperature of 80°C, and the solution was stirred for 4 days at 80°C. The solution was allowed to cool to room temperature was extracted with 10 mL of dichloromethane. The organic layer was washed with a solution of sat. $NaHCO_3$ (100 mL), followed by a wash with water (100 mL), and finally washed with 0.1 M citric acid (100 mL). The organic layer was collected and dried over anhydrous sodium sulfate and dried under reduced pressure for 4 h giving porphyrin **7** as purple crystals. The mass spectrum of the compound was analyzed and no further characterization was done due to the possible instability of porphyrin 7 and the next synthetic step was carried out immediately. Yield (N/A). MALDI-TOF-MS m/z; calcd for 814.03 [M+], obsd 813.46.

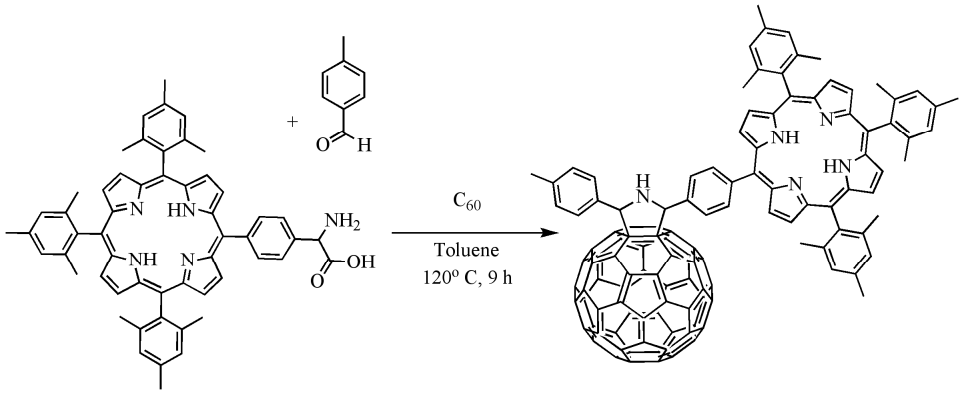

Figure 58. Synthetic scheme for the synthesis of 16

*3.7.9 Porphyrin **AaP-C60** Dyad (**16**)*

Dyad 16 was synthesized using a general procedure for the functionalization of a C_{60} as a guide. [66] Porphyrin **7** (6.00 mg, 0.009 mmol) was dissolved in distilled toluene (15 mL) in a round bottomed flask equipped with a magnetic stir bar and a reflux condenser. p-Tolualdehyde (2.0 mg, 0.02 mmol), and C_{60} (6.00 mg, 0.008 mmol) was added to the solution, and the reaction flask was placed in an oil bath which was slowly brought to a temperature of 120°C. The solution was to refluxed for 16 h, after which it was cooled to room temperature, and solvent was removed by distillation under reduced pressure. The product was purified by preparative thin layer chromatography with 30% dichloromethane in hexane as the solvent to give **AaP-C60** as a yellow/brown solid. ^{1}H NMR δ (ppm) 8.56 - 8.75 (m, 8 H), 8.38 (d, J=7.9 Hz, 2 H), 8.23 - 8.31 (m, 2 H), 8.00 (d, J=8.3 Hz, 2 H), 7.31 (d, J=7.9 Hz, 2 H), 7.25 (s, 6 H), 6.33 (s, 1 H), 6.15 (s, 1 H), 2.60 (s, 9 H), 2.40 (s, 3 H), 1.77 - 1.87 (m, 18 H), -2.58 (s, 2 H); MALDI-TOF-MS m/z; calcd for 871.46 [M+ - C_{60}], obsd 871.91; calcd for 720 [M- - AaP +pyrrolidine fragment], obsd 720.

5-[(4-(Hydroxymethyl)phenyl]- 10,15,20-tris-(4-t-butylphenyl)porphyrin (**10**)

Porphyrin **9** (500 mg, 0.59 mmol) was dissolved in anhydrous THF (60 mL), degassed with argon, in a round bottomed flask equipped with a magnetic stir bar. $LiAlH_4$ (90 mg, 2.4 mmol) was added to the reaction flask, and the solution was stirred under argon at room temperature for 15 min. The reaction was quenched with MeOH drop wise until no further reaction was observed. The solvent was removed by distillation under reduced pressure and the products were dissolved in DCM, and washed with 1N HCl (100 mL), followed by a wash with a sat. aqueous solution of $NaHCO_3$ (100 mL), then water (100 mL) yielding pure porphyrin **10** as purple crystals, mp >300 °C, yield 450 mg (93%). ^{1}H NMR δ ppm 8.82 - 9.01 (m, 6 H), 8.66 - 8.79 (m, 2 H), 8.20 - 8.33 (m, 2 H), 8.06 - 8.18 (m, 6 H), 7.67 - 7.84 (m, 8 H), 5.64 (s, 2 H), 1.60 (s, 27 H), -2.76 (br s, 2 H); MALDI-TOF-MS m/z; calcd for 813.08 [M+], obsd 812.98

*3.7.10 5-(4-Formylphenyl)-10,15,20-tris-(4-t-butylphenyl)porphyrin (**11**)*

Porphyrin **10** (450 mg, 0.55 mmol) was dissolved in anhydrous THF (100 mL) in a round bottomed flask equipped with a magnetic stir bar. MnO_2 (480 mg, 5.53 mmol) was added in small portions over a period of 30 min. After which the reaction mixture was filtered through Celite, and then the product was purified by column chromatography on silica with 0.2 % acetone in dichloromethane to give pure porphyrin **11** as purple crystals, mp >300 °C, yield x mg (x%). ^{1}H NMR δ ppm 10.37 (s, 1 H), 8.83 - 8.95 (m, 6 H), 8.75 (d, *J*=4.8 Hz, 2 H), 8.40 (d, *J*=7.9 Hz, 2 H), 8.26 (d, *J*=7.9 Hz, 2 H), 8.08 - 8.20 (m, 6 H), 7.76 (d, *J*=8.3 Hz, 6 H), 1.61 (s, 27 H), -2.74 (s, 2 H). MALDI-TOF-MS m/z; calcd for 811.06 [M+], obsd 810.98

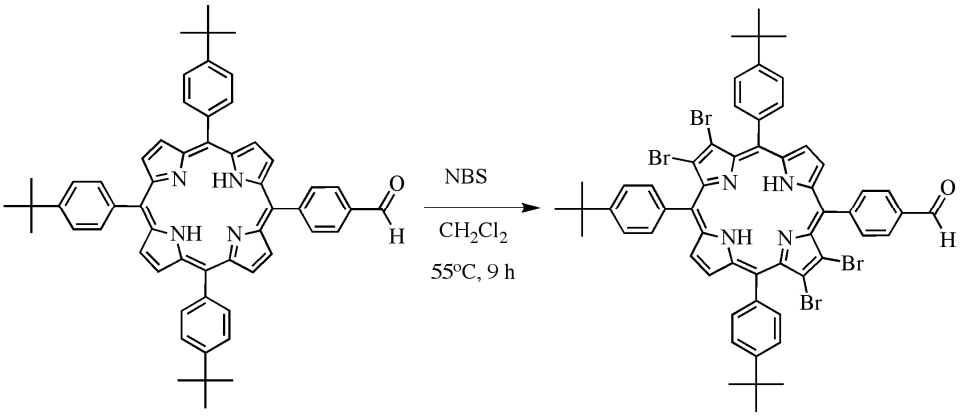

Figure 59. Synthetic scheme for the synthesis of 12

*3.7.11 7,8,17,18–tetrabromo-5-(4-formylphenyl)-10,15,20-tris-(4-t-butylphenyl)porphyrin (**12**)*

Compound **11** (260 mg, 0.32 mmol) was dissolved in dichloromethane (100 mL) in a round bottomed flask equipped with a magnetic stir bar and a reflux condenser. Recrystallized *N*-bromosuccinimide (256 mg, 1.44 mmol) was added to the solution, and the flask was placed in an oil bath heated to 55°C, stirred for 45 min under argon and in the dark. Pyridine (65 μL, 0.81 mmol) was added to the reaction mixture and it was allowed to stir for 2 h. *N*-bromosuccinimide (150 mg, 0.843 mmol), followed by pyridine (65 μL, 0.81 mmol) was again added and the solution was stirred for an additional 2 h. A second additional amount of *N*-bromosuccinimide (150 mg, 0.843 mmol) followed by pyridine (65 μL, 0.81 mmol) was added to the reaction mixture and allowed to stir for another 3 h. A final addition of *N*-bromosuccinimide (150 mg, 0.843 mmol) and pyridine (65 μL, 0.81 mmol) was added and after 1 h the solution was allowed to cool to room temperature. The solvent was removed by distillation under reduced pressure and the

product was purified by column chromatography on silica gel using 30% toluene in dichloromethane as the solvent to give pure **12** as purple crystals, mp >300 °C, yield 90 mg (25%). ^{1}H NMR δ (ppm) 10.38 (s, 1 H), 8.79 (d, J=4.8 Hz, 1 H), 8.75 (s, 2 H), 8.59 (d, J=2.6 Hz, 1 H), 8.39 (d, J=7.9 Hz, 2 H), 8.29 (d, J=8.3 Hz, 2 H), 8.06 - 8.14 (m, 6 H), 7.79 (d, J=7.9 Hz, 6 H), 1.59 (s, 27 H), -2.72 (d, J=8.3 Hz, 2 H, -NH); MALDI-TOF-MS m/z; calcd for 1126.65 [M+], obsd 1127.02

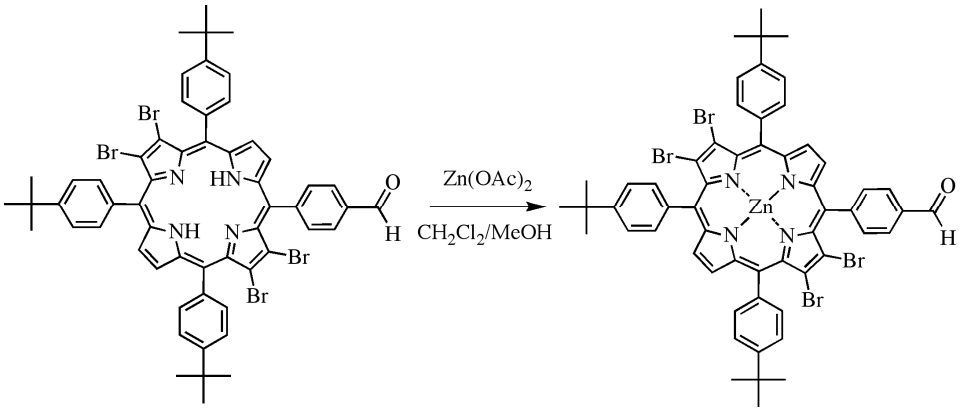

Figure 60. Synthetic scheme for the synthesis of 13

*3.7.12 Zn(II) 2,3,12,13–tetrabromo-5-(4-formylphenyl)-10,15,20-tris-(4-t-butylphenyl) porphyrin (**13**)*

Porphyrin **12** (87 mg, 0.77 mmol) was dissolved in dichloromethane in a round bottomed flask equipped with a magnetic stir bar. Zinc acetate (285 mg, 1.55 mmol) and MeOH (6 mL) was added to the solution, which was then stirred at room temperature for 6 h. The solution was washed with water (2 x 100 mL) and the organic layer was collected and dried over anhydrous sodium sulfate. The solvent was removed by distillation under reduced pressure and the product was purified by column chromatography on silica gel using dichloromethane as the solvent giving pure **13** as purple crystals, mp >300 °C, yield 80 mg (94.0%); ^{1}H NMR CD_3Cl with 2% CD_3OD) δ

(ppm) 10.35 (s, 1 H), 8.72 - 8.78 (m, 3 H), 8.59 (d, J=4.8 Hz, 1 H), 8.17 - 8.31 (m, 4 H), 7.89 - 7.99 (m, 6 H), 7.68 - 7.78 (m, 6 H), 1.59 (br s, 27 H); MALDI-TOF-MS m/z; calcd for 1190.04 [M+], obsd 1190.41

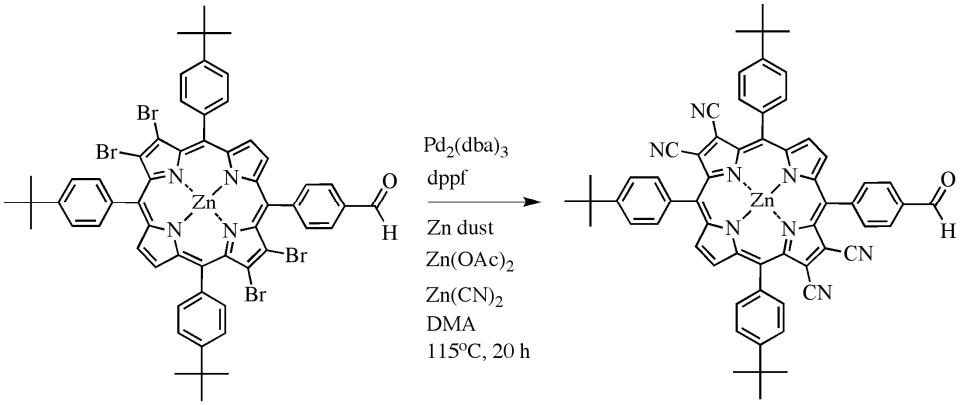

Figure 61. Synthetic scheme for the synthesis of 14

*3.7.13 Zn(II) 2,3,12,13–tetracyano-5-(4-formylphenyl)-10,15,20-tris-(4-t-butylphenyl) porphyrin (**14**)*

Porphyrin **13**, $Zn(OAc)_2$, 1,1'-bis(diphenylphosphino)ferrocene, and Zn dust were dried under reduced pressure overnight and all glassware was oven dried before use. *N,N*-Dimethylacetamide was stirred with BaO for 24 h, then refluxed over BaO for 1 h, and distilled under reduced pressure before use. Porphyrin **13** (65 mg 0.06 mmol), tris(dibenzylideneacetone)dipalladium(0) (40 mg, 0.04 mmol), 1,1'-bis(diphenylphosphino)ferrocene (49 mg, 0.09 mmol), $Zn(OAc)_2$ (3.0 mg, 0.01 mmol), Zn dust (1.80 mg, 0.028 mmol), and $Zn(CN)_2$ (15.5 mg, 0.130 mmol) were dissolved in deaerated dimethylacetamide (10 mL) in a Schlenk flask equipped with a magnetic stir bar. The Schlenk flask was placed in an oil bath which was brought to a temperature of 115°C and the reaction mixture was stirred under argon for 20 h. Dichloromethane (60

mL) was added, the solution was washed 5 times with water (100 mL), the organic layer was collected, and the solvent distilled under reduced pressure. The product was purified by column chromatography on silica gel with 20% EtOAc in toluene as the solvent. A final purification was done by recrystallization from dichloromethane and hexane to yield pure porphyrin **14** as purple crystals, mp >300 °C, yield, 10 mg (18.6%); 1H NMR δ ppm 10.33 (s, 1 H), 8.75 (br s, 2 H), 8.59 (br s, 1 H), 8.01 - 8.29 (m, 3 H), 7.86 (br s, 3 H), 7.57 - 7.77 (m, 6 H), 7.26 (t, J=7.7 Hz, 2 H), 6.81 - 6.97 (m, 3 H), 1.58 (br s, 27 H); MALDI-TOF-MS m/z; calcd for 974.49 [M+], obsd 972.78

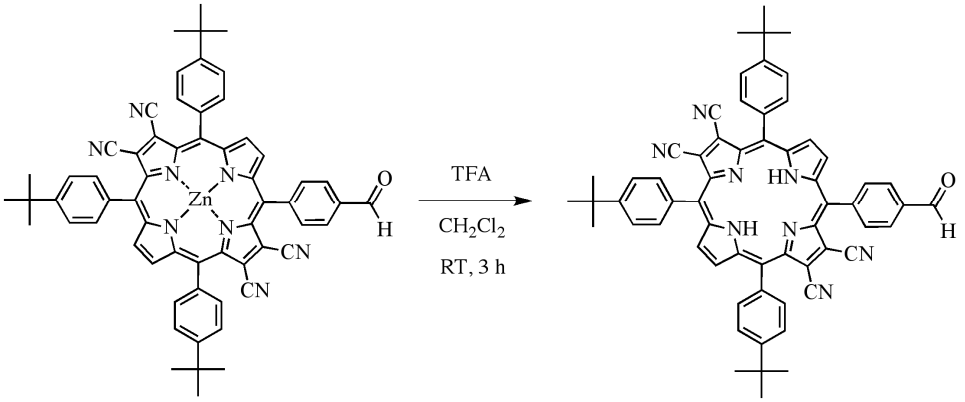

Figure 62. Synthetic scheme for the synthesis of 15

*3.7.14 7,8,17,18–tetracyano-5-(4-formylphenyl)-10,15,20-tris-(4-t-butylphenyl) porphyrin (CyP) (**15**)*

Compound **14** (7.0 mg, 0.01 mmol), was dissolved in dichloromethane (10 mL) in a round bottomed flask equipped with a magnetic stir bar. Trifluoroacetic acid (1.6 mL) was added to the solution and the reaction was stirred at room temperature for 3 h. The reaction mixture was washed with a saturated solution of aqueous $NaHCO_3$ (3 x 50 mL) followed by a wash with water (2 x 50 mL). The organic layer was collected and dried

over anhydrous sodium sulfate, and the solvent was removed by distillation under reduced pressure and the product was dried under reduced pressure, yielding pure porphyrin **15** as a purple precipitate, mp >300 °C, yield, 6 mg (94%); ^{1}H NMR δ ppm 10.42 (s, 1 H), 8.99 - 9.10 (m, 3 H), 8.87 (dd, *J*=5.3, 1.3 Hz, 1 H), 8.27 - 8.41 (m, 4 H), 8.04 - 8.12 (m, 6 H), 7.79 - 7.92 (m, 6 H), 1.55 - 1.68 (m, 27 H), -2.42 (d, J=7.5 Hz, 2 H); MALDI-TOF-MS m/z; calcd for 911.10 [M+], obsd 910.97

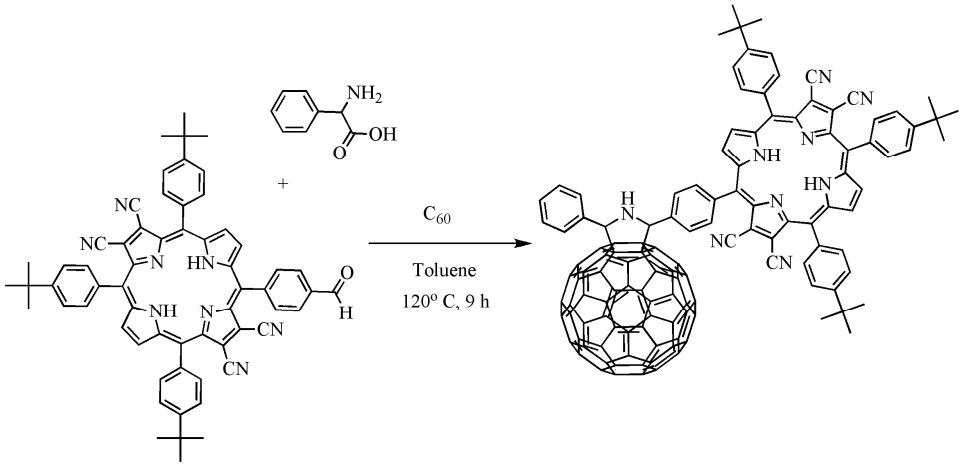

Figure 63. Synthetic scheme for the synthesis of 17

*3.7.15 CyP-C60 Dyad (**17**)*

Porphyrin **15,** C_{60}, and α-phenylglycine were dried under vacuum for 6 h. Porphyrin **15** (60 mg, 0.07 mmol), α-phenylglycine (99.5 mg, 0.66 mmol), and C_{60} (100 mg, 0.14 mmol) were dissolved in distilled toluene, under argon in a round bottomed flask equipped with a magnetic stir bar and a reflux condenser. The reaction flask was placed in an oil bath heated to 120^{o}C, and solution was refluxed for 9 h. The reaction was allowed to cool to room temperature and then the solvent was removed by distillation

under reduced pressure. The product was purified by column chromatography on silica gel using dichloromethane as the solvent, giving pure dyad **16** as a brown precipitate.

$_1$H NMR δ ppm 8.58 - 8.73 (m, 8 H), 8.38 (d, J=8.3 Hz, 2 H), 8.29 (s, 1 H, -NH pyrrolidine), 8.26 (d, J=8.3 Hz, 2 H), 8.00 (d, J=8.3 Hz, 2 H), 7.31 (d, J=8.3 Hz, 2 H), 7.25 (s, 6 H), 6.33 (s, 1 H), 6.15 (s, 1 H), 2.60 (s, 9 H), 2.40 (s, 3 H), 1.76 - 1.89 (m, 18 H), -2.58 (s, 2 H); MALDI-TOF-MS m/z; calcd for 999.47 [M+ -C_{60}], obsd 999.39; calcd for 720 [M- loss of C60] 719.98.

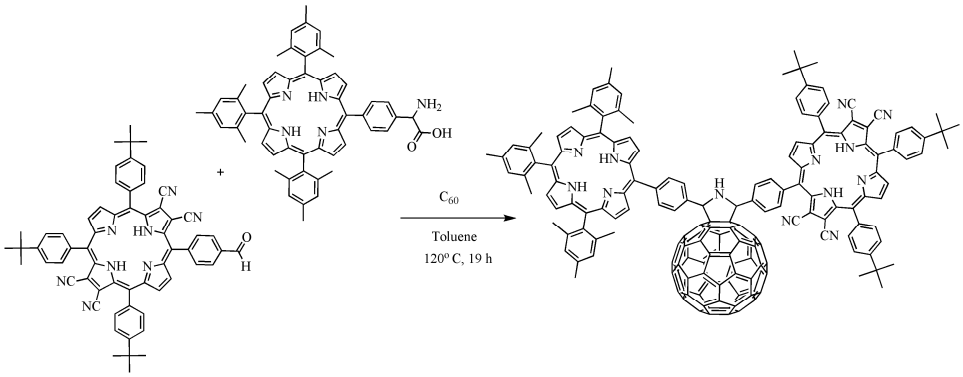

Figure 64. Synthetic scheme for the synthesis of 18

*3.7.16 AaP-C_{60}-CyP (**18**)*

Porphyrin **15**, porphyrin **7**, and C_{60} were dried for 4 h before. Porphyrin **15** (10 mg, 0.01 mmol), porphyrin **7** (10 mg, 0.01 mmol), and C_{60} (16 mg, 0.02 mmol) were dissolved in distilled toluene in a round bottomed flask equipped with a magnetic stir bar and a reflux condenser. The flask was placed in an oil bath that was brought to a temperature of 120°C, and the reaction was allowed to reflux for 19 h. The reaction was

cooled to room temperature and the solvent was removed by distillation under reduced pressure. The product was purified by column chromatography on silica gel using 20% hexane in dichloromethane as the solvent, giving pure **18** as a brown precipitate, mp>300 °C, yield 5 mg (19.1%); MALDI-TOF-MS m/z; calcd for 1661.8 [M+ -C_{60}], obsd 1662.4; calcd for 720 [M- -loss of C_{60}], obsd 720.

3.8 Acknowledgements

This work was supported by the Office of Basic Energy Sciences, Division of Chemical Sciences, Geosciences, and Energy Biosciences, Department of Energy under contract DE-FG02-03ER15393 and the Center for Bio-Inspired Solar Fuel Production, an Energy Frontier Research Center funded by the U.S. Department of Energy, Office of Science, Office of Basic Energy Sciences under Award Number DE-SC0001016.

Chapter 4 Mimicking the electron transfer chain in Photosystem II with a molecular triad thermodynamically capable of water oxidation

Jackson D. Megiatto Jr.[a], Antaeres Antoniuk-Pablant[a], Benjamin D. Sherman[a], Gerdenis Kodis[a], Miguel Gervaldo[b], Thomas A. Moore[a1], Ana L. Moore[a1] and Devens Gust[a1]
[a]Center for Bio-Inspired Solar Fuel Production, Department of Chemistry and Biochemistry, Arizona State University, Tempe, AZ 85287.
[b]Departamento de Química, Universidad Nacional de Río Cuarto, Agencia Postal 3 (5800), Río Cuarto, Argentina

Author contributions: J.D.M, A.A.-P., B.D.S., G.K. and M.G. designed and performed research and analyzed data; J.D.M., T.A.M, A.L.M. and D.G. designed research, analyzed data and wrote the paper.

4.1 Abstract

In the photosynthetic photosystem II, electrons are transferred from the manganese-containing oxygen evolving complex (OEC) to the oxidized primary electron donor chlorophyll $P680^{\bullet+}$ by a proton coupled electron transfer process involving a tyrosine-histidine pair. Proton transfer from the tyrosine phenolic group to a histidine nitrogen tunes the redox potential of the tyrosine to locate it between those of $P680^{\bullet+}$ and the OEC. We report the synthesis and time resolved spectroscopic study of a molecular triad that models this electron transfer. The triad consists of a high-potential porphyrin bearing two pentafluorophenyl groups (PF_{10}), a tetracyanoporphyrin electron acceptor (TCNP), and a benzimidazole-phenol secondary electron donor (Bi–PhOH). Excitation of PF_{10} in benzonitrile is followed by singlet energy transfer to TCNP (τ = 41 ps), whose excited state decays by photoinduced electron transfer (τ = 830 ps) to yield Bi-PhOH-$PF_{10}^{\bullet+}$-$TCNP^{\bullet-}$. A second electron transfer reaction follows (τ < 12 ps), giving a final state postulated as BiH^{+}–$PhO^{\bullet}$–PF_{10}–$TCNP^{\bullet-}$, in which the phenolic proton now resides on

benzimidazole. This final state decays with a time constant of 3.8 μs. The triad thus functionally mimics the electron transfers involving the tyrosine-histidine pair in PSII. The final charge-separated state is thermodynamically capable of water oxidation, and its long lifetime suggests the possibility of coupling systems such as this to water oxidation catalysts for use in artificial photosynthetic fuel production.

4.2 Introduction

The machinery of photosynthesis is an elaborate nanosystem composed of organic and inorganic cofactors assembled in large organized protein arrays that cooperatively perform the specific tasks needed to convert sunlight into biofuel. Through eons of evolution, nature has developed specialized enzymes able to oxidize water molecules and use the resulting electrons to reduce carbon dioxide to carbohydrate. The central component in the water oxidation process is the protein complex known as Photosystem II (PSII), which uses sunlight to split water into molecular oxygen, protons and reducing equivalents.[21]

Essential to the function of PSII is its ability to combine single-photon excitation with the multi-electron process of water oxidation. To perform this thermodynamically challenging reaction, PSII is equipped with the oxygen evolving complex (OEC), an inorganic complex featuring one calcium and four manganese ions.[152–154] Functionally, the OEC is a charge accumulator able to store the four oxidizing equivalents needed for water oxidation. The OEC is electronically coupled to the chlorophyll complex P680 through a redox-active tyrosine-hystidine pair (Tyr_Z-D_1His190). This pair acts as an

electron relay between P680 and the OEC components through proton-coupled electron transfer (PCET).[155–158]

In PSII, the oxidizing equivalents are produced through photo-excitation of the chlorophyll molecules in the P680 complex, which decay by electron transfer to the quinone cofactors Q_A and Q_B *via* a pheophytin primary electron acceptor. The highly oxidizing $P680^{\bullet+}$ is reduced by the Tyr_Z residue on the nanosecond time scale. In this process, Tyr_Z loses its phenolic proton, likely to the nearby D_1His190 group, to generate the neutral tyrosine radical Tyr_Z-O$^{\bullet}$ (E^0 = 0.9−1.0 V *vs.* SCE). The radical Tyr_Z-O$^{\bullet}$ then removes one electron from the OEC on the microsecond time scale, increasing its oxidation state.[156,159–161] After four light-induced charge separations, the OEC oxidizes two water molecules, releases molecular oxygen and returns to its initial oxidation state .

The functional principles of PSII can be used to guide the design of artificial photosynthetic devices. The highly efficient initial light-induced charge separation is a particularly attractive biomimetic target because the resulting electron/hole pair can in principle be used for conversion to electrical power or to generate a redox gradient to drive chemical reactions for fuel production. Therefore, development of synthetic systems able to produce useful forms of energy from abundant sunlight and water require a better understanding of the thermodynamic and kinetic parameters of the primary processes of PSII.

In this context, we report the preparation and photophysical investigation of a bio-inspired molecular triad engineered to functionally mimic the initial charge separation events of PSII. The three units are designed and covalently assembled to simulate the

specific interactions between P680, pheophytin and the Tyr_Z-D_1His190 pair of PSII. The energetics of the model are designed so that the final charge separated state is thermodynamically capable of oxidizing water. A detailed spectroscopic investigation highlights the importance of electron transfer reactions associated with proton translocation in stabilizing the photo-induced charge separated state and provides new insight into how electron and proton motion can be used to bridge the gap between light and chemistry.

4.3 Synthesis

Porphyrins are useful artificial alternatives to synthetically demanding and relatively unstable chlorophylls found in natural systems. In the case of PSII, the photogenerated $P680^{\bullet+}$ must be an extremely strong oxidant in order to provide the overpotential required for efficient water oxidation. Chlorophyll *a* in solution is incapable of carrying out such photo-oxidations, and the potential of chlorophyll in PSII is tuned by the protein environment in order to achieve the necessary redox power.[162–164] Molecular triad **1** (Figure 65) was engineered with the redox potentials of the porphyrin components designed to fulfill thermodynamic requirements similar to those found in P680 by adjusting the substituents on the macrocycles.

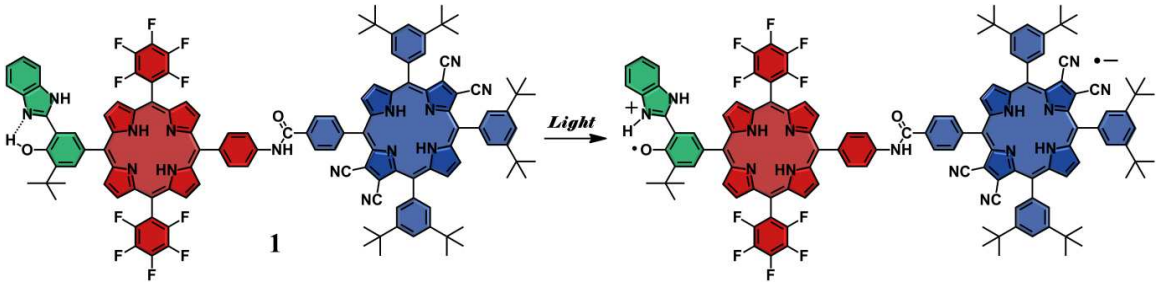

Figure 65. Molecular structure of triad **1**, which is composed of three covalently-linked subunits that mimic the redox processes in PS II. Upon irradiation, sequential electron transfer (ET) and proton-coupled electron transfer (PCET) reactions eventually yield the final charge separated state BiH^{+}–$PhO^{\bullet}$–PF_{10}–$TCNP^{\bullet-}$.

In the design of **1**, the tetracyanoporphyrin (TCNP) unit (in blue, Figure 65) acts as a powerful electron acceptor due to the electron withdrawing effects of the four cyano groups at the *β*-positions of the tetrapyrrolic core. The two pentafluorophenyl groups provide the primary electron donor porphyrin (PF_{10}) (in red, Figure 65) with the right redox balance to transfer one electron to the TCNP acceptor after irradiation of the complex, resulting in the $PF_{10}^{\bullet+}$ cation, which is thermodynamically competent to oxidize the benzimidazole-phenol (Bi–PhOH) secondary electron donor component (in green, Fig. 1). The Bi–PhOH unit features an intramolecular hydrogen bond between the phenolic proton and the lone pair of the nitrogen atom in the benzimidazole moiety. In the course of oxidation of Bi-PhOH by the photo-generated $PF_{10}^{\bullet+}$, the phenol is designed to transfer its proton to the benzimidazole group by a PCET mechanism to produce a neutral phenoxyl radical (E = 1.06 V *vs.* SCE in the case of **1**) suitably poised for water oxidation (E^{0} = +0.58 V *vs* SCE, pH 7), thus mimicking the role of the Tyr_{Z}-D_{1}His190 in PSII.

To assemble the three active units of **1**, we developed the synthetic strategy depicted in Figure 66.

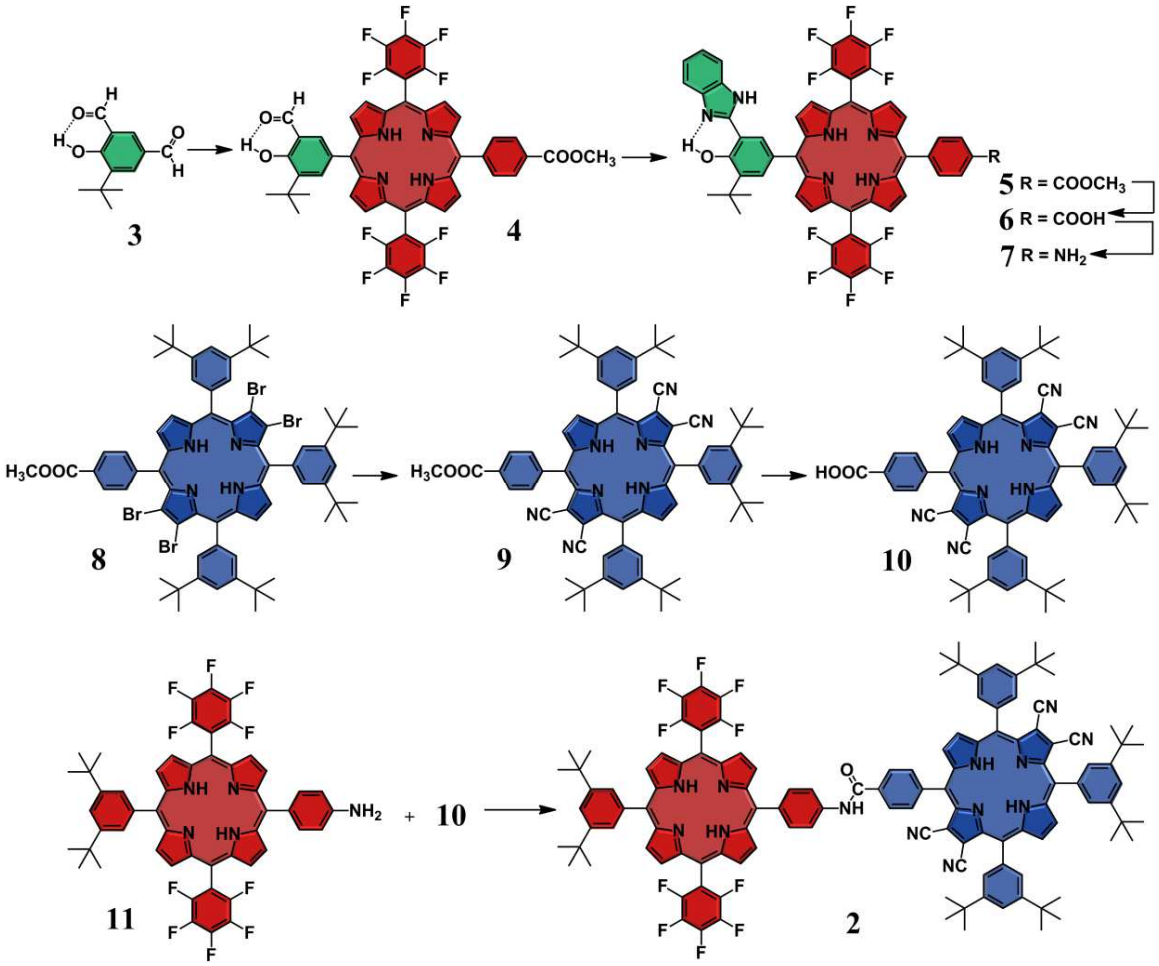

Figure 66. Synthetic strategy and building blocks used to construct triad **1** and dyad **2**.

The synthesis begins with the preparation of porphyrin **4**, which relies on an approach based on the selective condensation of the *para*-formyl group of compound **3**. This selectivity is grounded in the reduced chemical reactivity of the formyl group involved in the intramolecular O–H---O=C hydrogen bond, which efficiently discourages its activation by acid catalysts. The benzimidazole moiety is then formed upon cyclization of the formyl group in **4** with *ortho*-phenylenediamine to afford **5**, which is in turn

hydrolyzed under acid conditions to yield **6**. The resulting carboxylic acid in **6** is transformed into an amine group by a Curtius reaction to afford dyad **7**. The TCNP **10** is efficiently prepared from tetrabromo derivative **8** [165] using a new cyanation procedure developed in our laboratory. Finally, triad **1** is afforded through an amide-coupling reaction between **7** and **10**. The dyad PF_{10}–TCNP model compound **2** (Figure 66) is prepared from the required precursors following similar procedures (see SI for experimental details).

4.4 Results and Discussion

Photophysical Investigation. Spectroscopic investigations were carried out with triad 1, PF_{10}–TCNP dyad 2 and Bi−PhOH−PF_{10} model compound 5 as well as with porphyrin references TCNP 9 and PF_{10} 11 to gain insight into the photophysical properties of the photoactive units.

4.4.1 Steady State Spectroscopic Investigations and Electrochemical Studies.

The absorption spectrum of PF_{10} **11** in cyclohexane solution (Figure 67, black line) exhibits characteristic electronic transitions of free base porphyrins (Soret absorption at 419 nm and Q-bands at 512, 547, 592 and 648 nm). The TCNP **9** (Figure 67, solid red line) features a split in the Soret region with maxima at 440 and 444 nm, and broader Q-bands that appear at 543, 588, 654 and 711 nm (Figure 67).

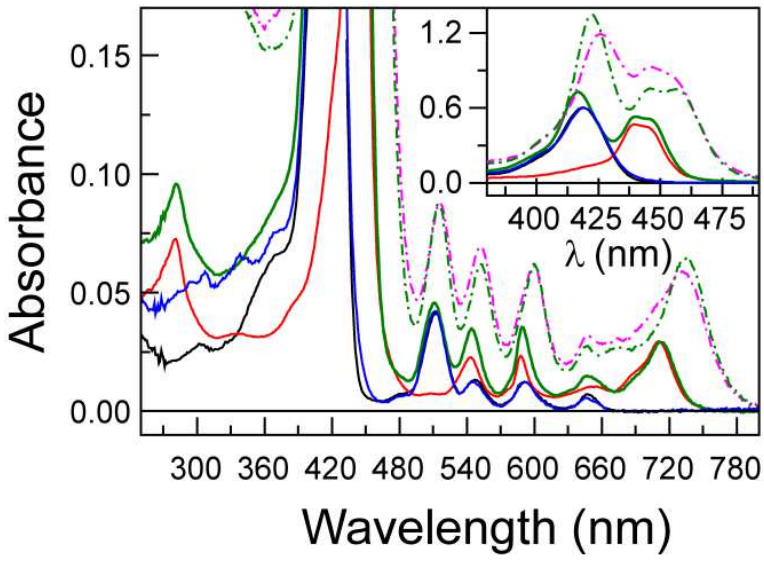

Figure 67. Ground state absorption spectra in cyclohexane (solid lines) and benzonitrile (broken lines) In cyclohexane: PF_{10} reference **11** (black solid), TCNP **9** (red solid), Bi−PhOH−PF_{10} model compound **5** (blue solid)) and PF_{10}–TCNP dyad **2** (green solid). In benzonitrile: PF_{10}–TCNP dyad **2** (green broken) and triad **1** (magenta broken).

These spectroscopic features are characteristic of a nonplanar porphyrin.[166–172] Steric repulsion between the *β*-cyano groups and the *meso*-phenyl substituents leads to deformation of the tetrapyrrolic ring from its original planar geometry. The red shift is explained by two different phenomena which operate cooperatively to reduce the HOMO−LUMO gap. The strong electron withdrawing effect induced by the four cyano groups is known to stabilize the LUMO orbital, while distortion of the porphyrin macrocycle destabilizes the HOMO orbital.[172]

The absorption spectrum of Bi−PhOH−PF_{10} model compound **5** (Figure 67, solid blue line) shows a slight broadening of the Soret band compared to that of **11**, suggesting some electronic interaction between the Bi−PhOH and PF_{10} components in the ground state. On the other hand, the spectrum of PF_{10}−TCNP dyad **2** (solid green line) is similar to a linear combination of the absorption spectra of its components, indicating no strong

electronic interactions between the photoactive units when covalently-linked to each other. Triad **1** is not sufficiently soluble in cyclohexane to obtain a useful absorption spectrum, but the spectrum in benzonitrile (Fig. 67, magenta broken line) resembles that of **2** in the same solvent (green broken line).

Steady-state fluorescence investigations in cyclohexane with excitation in the corresponding Soret region (SI Appendix, Fig. S2) disclose that PF_{10} reference **11** emits at 657 and 723 nm, while TCNP **9** fluoresces at 727 and 815 nm. From the absorption and emission data, the energies of the first singlet excited states (E_{00}) are estimated as 1.90 eV for **11** and 1.72 eV for **9**.

Estimation of the energies of the charge separated states was afforded from electrochemical studies (SI Appendix, Figs. S6 and S7, Table S1). The first redox potentials (*vs.* SCE) of a PF_{10} model (SI Appendix, Fig. S8) are at E_{ox} = + 1.29 V and E_{red} = − 0.96 V, while the Bi−PhOH first oxidation in model compound **5** occurs at E_{ox} = + 1.04 V. The first reduction of TCNP reference **9** takes place at E_{red} = − 0.30 V. Therefore, the intermediate Bi−PhOH−$PF_{10}^{\bullet+}$–$TCNP^{\bullet-}$ and final BiH^{+}−$PhO^{\bullet}$−PF_{10}–$TCNP^{\bullet-}$ charge separated states are roughly 1.59 eV and 1.34 eV above the ground state in triad **1.**

4.5 Time Resolved Spectroscopic Investigations.

Time resolved emission experiments in cyclohexane with excitation in the corresponding Soret regions yielded lifetimes of 8.89 ns (χ^2 = 1.17) for the first singlet excited state of PF_{10} **11** and 9.00 ns (χ^2 = 1.03) for that of Bi−PhOH−PF_{10} model compound **5**. The decay of reference TCNP **9** requires three components to satisfactorily fit the decay data (χ^2 = 1.07): 102 ps, 2.47 ns and 4.87 ns. A preliminary investigation of

the photophysical properties of **9** revealed that the singlet excited state dynamics significantly depend on the solvent polarity and viscosity, which signals a complex excited state manifold and the possibility of different conformations in the excited state. We postulate that the ^{1}TCNP state formed immediately after excitation undergoes a rather slow, solvent dependent (102 ps in cyclohexane) structural reorganization process that yields a relaxed singlet excited state, which then decays via ordinary relaxation pathways with a fluorescence lifetime of 2.47 ns. The 4.87 ns component may represent the decay of an additional minor conformation, or in principle a minor impurity, although no other evidence for impurities was found.

Global analysis (χ^2 = 1.07) of transient fluorescence experiments on dyad **2** in cyclohexane with excitation at 400 nm yielded five decay components, which are depicted in the form of decay-associated spectra (DAS) in Figure 68.

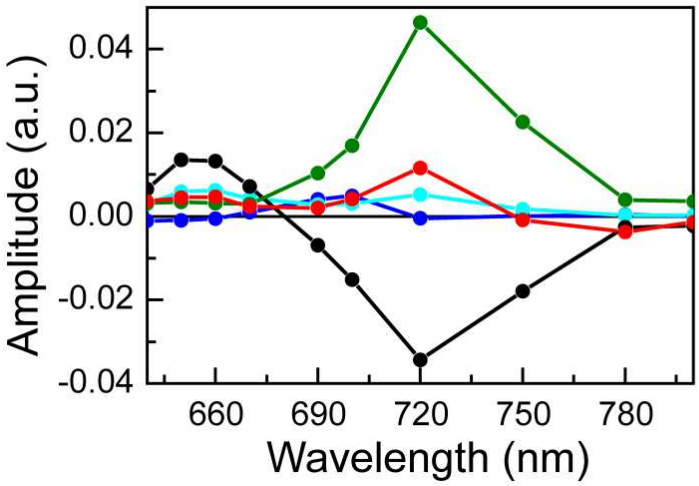

Figure 68. Fluorescence decay-associated spectra (DAS) in cyclohexane of dyad 2 following ~100 fs laser pulse excitation at 400 nm. Global analysis (□□□1.07) yields five exponential components with lifetimes of 41 ps (black), 136 ps (red), 2.41 ns (green), 4.15 ns (blue) and 7.94 ns (turquoise).

The 41 ps DAS spectrum shows positive amplitude at ~650 nm, where most of the fluorescence comes from the PF_{10} subunit, and negative amplitude between 700-800 nm, where the fluorescence is primarily due to the TCNP moiety (SI Appendix, Fig. S2). This spectrum reflects singlet-singlet energy transfer from PF_{10} to TCNP. Thus, the lifetime of $^1PF_{10}$ in dyad **2** is reduced from the 8.89 ns found for PF_{10} model **11** to 41 ps by the addition of the energy transfer decay pathway. From these numbers, we calculate a rate constant of $k_{EnT} = 2.4 \times 10^{10}$ s^{-1} and a quantum yield of 98% for the energy transfer process in **2**.

The 136 ps, 2.4 ns and 4.15 ns DAS spectra have very similar lifetimes to those obtained for the TCNP model **9** in cyclohexane. The 136 ps spectrum shows band-shift-like character with positive amplitude at the blue side and negative amplitude at the red side of the TCNP fluorescence emission bands and can be attributed to the relaxation of the singlet excited state in the complex excited state manifold to form a relaxed singlet excited state which lives for 2.4 ns (see red and green lines in Figure 68). The two minor components (4.15 and 7.94 ns) required in the global analysis may reflect conformational heterogeneity, minor impurities and/or fitting artifacts. The fact that the decay time constants observed for ^{1}TCNP in **2** are essentially identical to those observed for model **9** show that no charge separated states are formed by decay of $^1PF_{10}$ or ^{1}TCNP in cyclohexane. Therefore, spectroscopic investigations of **2** were carried out in a more polar medium, benzonitrile, in order to facilitate charge transfer processes through driving force and reorganization energy effects.

Time-resolved emission experiments with **2** in benzonitrile reveal a different scenario. Global analysis of the fluorescence decays ($\chi^2 = 1.16$) reveals time constants of 41 ps, 129 ps, 536 ps, 1.8 ns and 9.3 ns. The first two decays represent energy transfer from $^1PF_{10}$ to TCNP and relaxation of ^{1}TCNP, respectively, as was observed in cyclohexane. The 536 ps component indicates a new decay pathway for ^{1}TCNP that was not present in **9** or in **2** in cyclohexane. The most likely mechanism is photoinduced electron transfer to form $PF_{10}^{\bullet+}$-$TCNP^{\bullet-}$. This interpretation is consistent with the strong solvent dependence of the time constant and the spectroscopic and electrochemical results discussed above. Photoinduced electron transfer between porphyrins joined by similar linkages has been reported. [173,174] The fact that the shortest decay component in benzonitrile has a time constant that is essentially identical to the corresponding component in cyclohexane is consistent with an absence of significant photoinduced electron transfer from $^1PF_{10}$-TCNP in both solvents. The 1.8 ns and 9.3 ns DAS are attributed to minor impurities or conformations, or fitting artifacts.

Transient absorption techniques were used to gain further insights into the spectral evolution of dyad **2**. In order to identify the transient spectroscopic changes that are indicative of the formation of charge separated states upon excitation, we first determined the spectroscopic absorption signatures of each possible cation and anion by spectroelectrochemical investigation of reference compounds **4** and **9**. The results (see SI) reveal that the $PF_{10}^{\bullet+}$ cation is characterized by a broad absorption in the 650-780 nm region, while the $TCNP^{\bullet-}$ anion has maximum absorptions at 660 and 940 nm. The redox processes are reversible in both cases, reflecting the redox stability of the porphyrins.

Excitation at 740 nm of an air saturated benzonitrile solution of TCNP model porphyrin **9** yielded evolution associated difference spectra (EADS) with time constants of 116 ps, 1.9 ns, and a component with a lifetime too long to resolve on the time scale of the experiment (SI Appendix, Fig. S3). The 116 ps component is assigned to relaxation of the initially formed ^{1}TCNP to a more stable species (spectral evolution shows band shift character), which decays in 1.9 ns. One of the products of this 1.9 ns decay is ^{3}TCNP, which decays very slowly in the absence of oxygen (last, non-decaying EADS).

The results of a similar experiment with **2**, excited at 740 nm in benzonitrile, where only TCNP absorbs, are presented in Figure 69a.

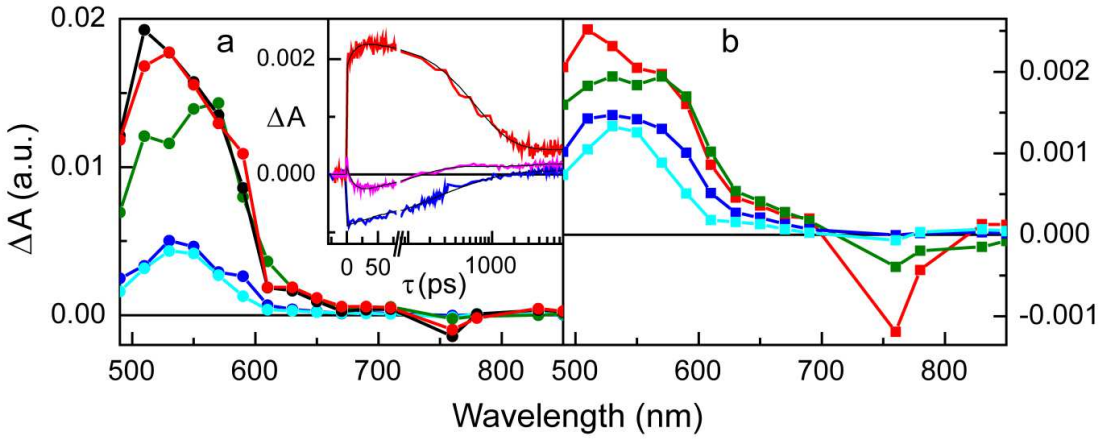

Figure 69. Transient absorption of dyad **2** (Fig. 69a) and triad **1** (Fig. 69b) in benzonitrile upon femtosecond excitation at 740 nm presented in the form of evolution associated difference spectra (EADS). For dyad **2** (69a) global analysis yielded five components: 12 ps (black), 120 ps (red), 590 ps (green), 1.8 ns (blue), and non-decaying (turquoise). For triad **1** (69b), global analysis afforded four components: 120 ps (red), 610 ps (green), 2.1 ns (blue), and non-decaying (turquoise). Inset in 69a: transient absorption kinetic traces in benzonitrile for dyad **2** at 650 nm (red) and 780 nm (pink) and for triad **1** at 780 nm (blue).

Five EADS with time constants of 12 ps, 120 ps, 590 ps, 1.8 ns (very minor EADS) and a component that did not decay on the <10 ns time scale were obtained. Based on the EADS shapes, the time resolved fluorescence results for **2** and **9** and the transient absorption data for **9**, we interpret the 120 ps process as relaxation of the initially formed ^{1}TCNP, which has a strong induced absorption with a maximum at ~520 nm. The 590 ps component, with strong induced absorption at ~570 nm, is due to decay of the resulting relaxed excited state by photoinduced electron transfer to yield $PF_{10}^{\bullet+}$-$TCNP^{\bullet-}$. The non-decaying component is assigned to porphyrin triplet states having induced absorption maxima at ~540 nm; consistent with this interpretation, the lifetime is reduced in the presence of oxygen. This triplet is formed in part by intersystem crossing of ^{1}TCNP, and potentially in part by decay of the charge-separated state. Consistent with the fluorescence results discussed above, the 1.8 ns EADS is attributed to minor impurities, conformations, or fitting artifacts. The EADS with the 12 ps lifetime can be attributed to charge recombination of $PF_{10}^{\bullet+}$-$TCNP^{\bullet-}$, at least in part to the ground state. The kinetic traces depicted in the inset of Figure 69 clearly show a rise/formation of stimulated emission at 780 nm and characteristic induced absorption due to the $PF_{10}^{\bullet+}$ radical cation at 650 nm. The combined transient absorption and fluorescence results therefore reveal that the formation (590 ps) of the $PF_{10}^{\bullet+}$-$TCNP^{\bullet-}$ state is slower than its decay (12 ps). This is an example of inverted kinetics, where the rate constant for recombination is larger than that for charge separation, and transient signals can be inverted in amplitude relative to their usual appearance.[174,175] A quantum yield of 77 % is calculated for

formation of $PF_{10}^{\bullet+}$-$TCNP^{\bullet-}$ in **2**. This yield is independent of which porphyrin is excited, as the quantum yield of PF_{10}-^{1}TCNP from $^1PF_{10}$-TCNP is essentially unity.

Turning now to triad **1**, incorporation of Bi–PhOH into the structure creates a redox gradient that provides sufficient driving force for secondary electron transfer from the Bi–PhOH to the $PF_{10}^{\bullet+}$ cation. The resulting oxidation of the Bi–PhOH unit dramatically enhances the acidity of the phenolic proton (Δ pKa ~ 12),[175,176] which creates the chemical potential required for proton transfer to the hydrogen bonded benzimidazole moiety.[177–180] Therefore, excitation of triad **1** is expected to lead to eventual formation of a charge separated state characterized by cationic benzimidazole, a phenoxyl radical, a neutral PF_{10} and a reduced TCNP porphyrin (BiH^+–$PhO^{\bullet}$–PF_{10}–$TCNP^{\bullet-}$). Transient absorption techniques were employed to investigate this possibility. Based on the observation that excitation of the PF_{10} unit leads to a fast and nearly quantitative energy transfer to the TCNP moiety, the transient absorption experiments with **1** were carried out with exclusive excitation of the TCNP component at 740 nm.

Global analysis of the femtosecond excitation data for **1** in the form of EADS (Figure 69b) gives four time constants of 120 ps, 610 ps, 2.1 ns and a long-lived non-decaying component. As with the model compounds, the 120 ps component is assigned to decay of the initially formed ^{1}TCNP to a relaxed first excited singlet state. The 610 ps EADS is ascribed to decay mainly by photoinduced electron transfer to give BiH–PhO–$PF_{10}^{\bullet+}$–$TCNP^{\bullet-}$ ($k_{ET} = 1.2 \times 10^9$ s^{-1}). An important observation from these experiments is the absence of the 12 ps component in the triad dynamics (see blue line, inset of Figure 69a). According to our interpretation of the dyad spectral evolution, this 12 ps component

represents charge recombination of the $PF_{10}^{\bullet+}$–$TCNP^{\bullet-}$ radical ion pair. Therefore, the Bi–PhOH–$PF_{10}^{\bullet+}$–$TCNP^{\bullet-}$ intermediate charge separated state is rapidly quenched due to a new decay channel, which we interpret as charge shift to yield the BiH^{+}–$PhO^{\bullet}$–PF_{10}–$TCNP^{\bullet-}$ state.

Complementary nanosecond transient absorption experiments on triad **1** dissolved in air-saturated benzonitrile solutions were carried out to investigate the relatively long-lived transient species. Global analysis of data for **1** in benzonitrile excited at 735 nm is presented in the form of DAS in Figure 70.

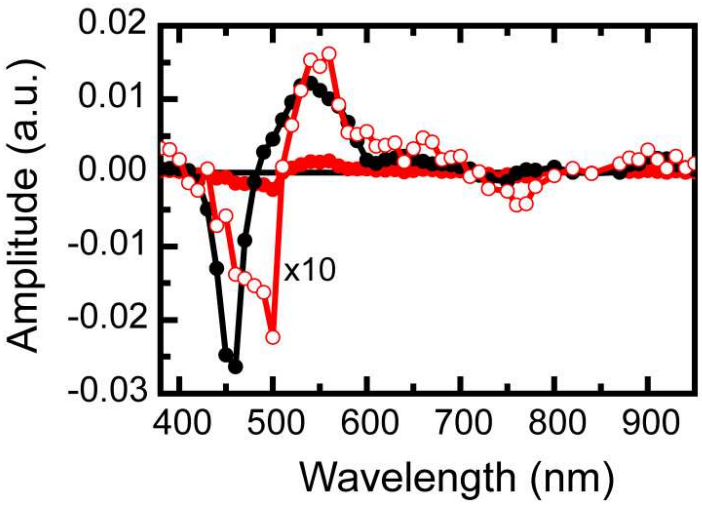

Figure 70. Transient absorption of triad **1** in air-saturated benzonitrile upon nanosecond excitation at 735 nm presented in the form of decay-associated spectra (DAS). The time constants associated with the spectra are 0.8 μs (black line and symbols) and 3.8 μs (red line and symbols). The 3.8 μs spectrum is also shown as a ×10 expansion (hollow symbols).

The first DAS (0.8 μs, black line) clearly shows TCNP ground state bleaching at 450 nm and ^{3}TCNP excited state absorption at 540 nm. This DAS corresponds to the TCNP triplet excited state quenched by molecular oxygen. This lifetime increases when oxygen

is removed from the sample. The 3.8 μs DAS (red line in Figure 70), whose amplitude is also shown magnified ten times for better visualization (open symbols), shows ground state bleaching at 450 and 740 nm as well as induced absorptions in the 560-700 nm and > 800 nm regions. A closer inspection of the spectrum < 490 nm clearly reveals competition between the TCNP ground state bleaching at 450 nm and an induced absorption with a maximum at ~400 nm. Based on the spectroelectrochemistry results (SI Appendix, Figs. S9 and S10), the induced absorption at 400-500 nm and >800 nm is assigned to formation of BiH^{+}–$PhO^{\bullet}$, while those at 660 and 940 nm are due to $TCNP^{\bullet-}$. Therefore, the 3.8 μs DAS contains the spectroscopic signature of the BiH^{+}–$PhO^{\bullet}$–PF_{10}–$TCNP^{\bullet-}$ final charge separated state, providing compelling evidence that such state is indeed produced upon excitation of triad **1** in benzonitrile. From comparison of triad and dyad kinetic traces at 940 nm, where the $TCNP^{\bullet-}$ radical anion has a transient signature, the quantum yield of the final charge separated state is estimated as ~ 52 % (SI Appendix, Fig. S5).

These spectroscopic observations together with the electrochemical data allow elaboration of the energy diagram depicted in Figure 71, which highlights the photophysical decay pathways for **1** in benzonitrile.

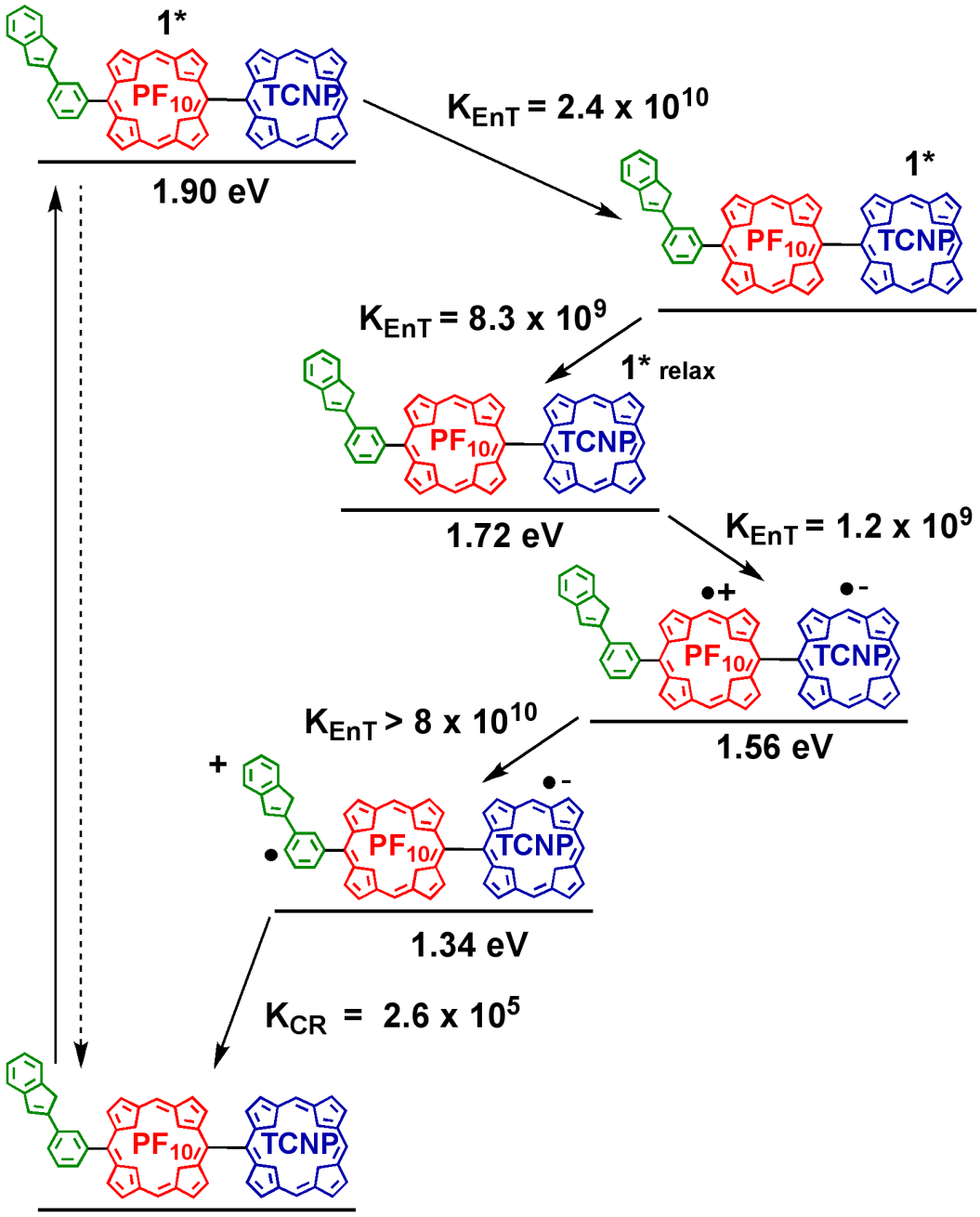

Figure 71. Energy level diagram, proposed decay pathways, and rate constants in s^{-1} for triad **1** following excitation of the PF_{10} unit in benzonitrile. The energy levels were derived from steady state absorption, fluorescence and electrochemical measurements. The rate constants were obtained from transient absorption and fluorescence measurements. k_{EnT} = rate constant for energy transfer; k_{ET} = rate constant for photoinduced electron transfer; k_{PCET} = rate constant for the proton-coupled electron transfer and k_{CR} = rate constant for charge recombination.

The first singlet excited state $^1PF_{10}$ decays quantitatively through energy transfer to the TCNP unit with a time constant $k_{EnT} = 2.4 \times 10^{10}$ s^{-1}. The ^{1}TCNP excited state undergoes an excited state relaxation/structural reorganization ($k = 8.3 \times 10^9$ s^{-1}) to yield a relaxed first excited singlet state that decays through electron transfer to form the Bi–PhOH–$PF_{10}^{\bullet+}$–$TCNP^{\bullet-}$ radical ion pair ($k_{ET} = 1.2 \times 10^9$ s^{-1}). Favorably competing with charge recombination of BiH–PhO–$PF_{10}^{\bullet+}$–$TCNP^{\bullet-}$ is the extremely fast charge shift reaction that oxidizes the phenol ($k_{PCET} > 8 \times 10^{10}$ s^{-1}). This proton coupled electron transfer reaction involves both electron transfer from the phenol to $PF_{10}^{\bullet+}$ and transfer of the phenolic proton to the appended benzimidazole group to afford the BiH^+–$PhO^{\bullet}$–PF_{10}–$TCNP^{\bullet-}$ final charge separated state. The final state undergoes charge recombination with $k_{CR} = 2.6 \times 10^5$ s^{-1}.

Previous studies of benzimidazole-phenol systems with internal hydrogen bonds have suggested that oxidation of the phenol is accompanied by transfer of a proton to the hydrogen-bonded imidazole, thereby lowering the oxidation potential of the phenol unit.[79,181] The ultra-fast secondary charge shift (< 12 ps) observed for **1** is consistent with such a PCET mechanism. The PCET avoids formation of a Bi–$PhOH^{\bullet+}$–PF_{10}–$TCNP^{\bullet-}$ intermediate. Electrochemical studies of a model phenol that lacks the internal hydrogen bond, 2,4,6-tri-*tert*-butylphenol, show that the oxidation potential of the phenol is ~1.36 V *vs.* SCE.[181,182] Using this number, we estimate the energy of Bi–$PhOH^{\bullet+}$–PF_{10}–$TCNP^{\bullet-}$ to be ~1.66 eV. Thus, formation of this state from Bi–PhOH–$PF_{10}^{\bullet+}$–$TCNP^{\bullet-}$ at 1.56 eV would be endergonic, and would be expected to occur slowly or not at all. As mentioned

above, electron transfer in the photosynthetic OEC is thought to occur by a similar pathway.

The final charge separated state, proposed to be BiH^{+}–$PhO^{\bullet}$–PF_{10}–$TCNP^{\bullet-}$, is relatively long lived (~4 □s). In related triads of the carotenoid-porphyrin-porphyrin (C–P–P) type, where the carotenoid is the secondary electron donor and no proton transfer is involved in the charge separation or recombination processes, the final charge separated states $C^{\bullet+}$–P–$P^{\bullet-}$ typically live only hundreds of nanoseconds at room temperature.[173,174] The systems are not strictly comparable to **1**, as the thermodynamic driving forces and solvents differ in the various systems. However, it is possible that nuclear rearrangements resulting from the PCET process may increase the energy barrier for charge recombination. Such a possibility has been suggested for the natural photosynthetic system[175] and we are in the process of investigating this hypothesis by femtosecond infra-red spectroscopy using molecules related to the one described in this work.

4.6 Conclusion

The results for triad **1** demonstrate that structural and mechanistic motifs involving proton coupled electron transfer in the Tyr_Z-D_1His190 couple that are found in natural PSII can also be realized in a synthetic model system. Excitation of either porphyrin moiety of the triad powers a sequence of rapid electron transfer reactions that generate a long lived charge separated state in good yield. The results are consistent with the involvement of PCET in the second step of the charge-separation, a charge shift reaction. Furthermore, the design of the triad incorporates both a high-potential electron-donor porphyrin and a low-potential electron accepting porphyrin, leading to a final charge

separated state that is thermodynamically capable of water oxidation. Such constructs may be of value in the development of synthetic fuel production systems that draw their energy from sunlight.[183]

4.7 Synthesis.

All chemicals were purchased from Aldrich, Alfa Aesar, and Acros and were used without further purification. Solvents were obtained from EM Science and were used as received unless otherwise noted. Thin layer chromatography (TLC) was performed with silica gel coated glass plates from Analtech. Column chromatography was carried out using Silicycle silica gel 60 with 230-400 mesh. All new compounds were characterized by ^{1}H-NMR spectroscopy and MALDI-TOF mass spectrometry. Details of the synthesis and characterization are given in the SI Appendix.

Spectroscopy.

Steady-state absorption spectra were measured on a Shimadzu UV2100U UV-vis and/or UV-3101PC UV-vis-NIR spectrometer. Steady-state fluorescence spectra were measured using a Photon Technology International MP-1 spectrometer and corrected for detection system response. All time resolved spectroscopic studies were carried out with laboratory-build instrumentation. This instrumentation is described in the SI Appendix.

4.8 Electrochemical and Spectroelectrochemical Studies.

All electrochemical and spectroelectrochemical studies were carried out using a CH Instruments 760D potentiostat. Spectroelectrochemical experiments were performed with an indium doped tin oxide (ITO) working electrode having a glass cover slip attached

over the conductive face of the ITO with heat-shrink plastic. The spectroelectrochemical setup was contained in a 1 cm quartz cuvette under a constant Ar flow, and a Shimadzu UV-3101PC spectrophotometer was used for all experiments. Details and spectra are presented in the SI Appendix.

Chapter 5 Carotenoids as electron or excited-state energy donors in artificial photosynthesis: an ultrafast investigation of a caroteno-porphyrin and a caroteno-fullerene dyad

Smitha Pillai[x], Janneke Ravensbergen[x], Antaeres Antoniuk-Pablant, Benjamin D. Sherman, Rienk van Grondelle, Raoul N. Frese, Thomas A. Moore, Devens Gust, Ana L. Moore* and John T.M. Kennis*.
[x]*These two authors made equal contributions*

5.1 Abstract

Photophysical investigations of molecular donor-acceptor systems have helped elucidate many details of natural photosynthesis and revealed design principles for artificial photosynthetic systems. To obtain insights into the factors that govern the partition between excited-state energy transfer (EET) and electron transfer (ET) processes among carotenoids and tetrapyrroles, we have designed artificial photosynthetic dyads that are thermodynamically poised to favor ET over EET processes. The dyads were studied using transient absorption spectroscopy with ~100 femtosecond time resolution. For dyad **1**, a caroteno-porphyrin, excitation to the carotenoid S_2 state induces ultrafast ET, competing with internal conversion (IC) to the carotenoid S_1 state. In addition, the carotenoid S_1 state gives rise to ET. In contrast with biological photosynthesis and many artificial photosynthetic systems, no EET at all was detected for this dyad upon carotenoid S_2 excitation. Recombination of the charge separated state takes place in hundreds of picoseconds and yields a triplet state, which is interpreted as a triplet delocalized between the porphyrin and carotenoid moieties. In dyad **2**, a caroteno-fullerene, excitation of the carotenoid in the S_2 band results in internal conversion to the S_1 state, ET and probably EET to fullerene on ultrafast timescales. From the carotenoid

S_1 state EET to fullerene occurs. Subsequently, the excited-state fullerene gives rise to ET from the carotenoid to the fullerene. Again, the charge separated state recombines in hundreds of picoseconds. The results illustrate that for a given rate of EET, the ratio of ET to EET can be controlled by adjusting the driving force for electron transfer.

5.2 Introduction

Oxygenic photosynthesis utilizes a small set of cofactors, primarily chlorophylls and carotenoids, to carry out light harvesting and photochemical energy conversion tasks. Chlorophylls are tetrapyrroles that are found in the antenna and reaction center complexes of Photosystem I and II. In the antenna, chlorophylls absorb sunlight and the resulting excitation energy is transferred to the reaction center, where redox-active chlorophylls gives rise to charge separation. In Photosystem II, a proton-coupled-electron-transfer process transfers the hole on the oxidized primary electron donor $P680^+$ to the manganese cluster, where it drives the splitting of water. [1] Carotenoids are polyene derivatives that fulfill various roles in biological photosynthesis. They act as light harvesting pigments for sunlight in the 400-550 nm region. They regulate and protect the photosynthetic system by quenching triplet chlorophyll and excessive excited singlet chlorophyll. In addition, they are known to be good electron donors. [2-5] The versatile properties of carotenoids arise from their extraordinary excited-state manifold. The three absorption bands in the 400-550 nm region reflect the $S_0 - S_2$ vibronic transitions. The optically forbidden S_1 state, which lies below the S_2 cannot be directly accessed from the ground state by a single photon, but can be populated by internal conversion (IC) from S_2. The energy levels of S_1 and S_2 are determined by the length of the conjugated chain

and by the nature of groups attached. [3,6] Even though this basic two-level scheme of the carotenoid excited-state manifold showed itself useful in the interpretation of a wide range of carotenoid-involving phenomena, [6,7] the results of recent experiments call for more extended models. [3,8-19]

The issues in regulated light harvesting and photoprotection in photosynthesis condense to a molecular understanding of controlled energy and electron transfer processes in confined Chl – carotenoid geometries. A key question concerns the prevalence of electron transfer (ET) versus excited-state energy transfer (EET) between carotenoids and chlorophylls in various types of LH and RC complexes under a range of physiological conditions. In the majority of the cases, EET is the dominant process and energy flows from the carotenoid S_2 and S_1 states to Chl [20-22]. Under high-light conditions, in plant PSII LHCs and some other photosystems the flow direction is reversed and EET occurs from Chl to carotenoids, after which excess energy is dissipated as heat.[23-26] On the other hand, in the thylakoid membrane, ET processes between Chl and carotenoids have been observed under quenching conditions.[27,28] In addition, in the PSII reaction center, □-carotene acts as an 'emergency' electron donor to $P680^+$ under photoinhibitory conditions.[29] These observations raise questions as of which molecular geometries, pigment-protein interactions and thermodynamic conditions control the excited-state energy and energy transfer rates among Chls and carotenoids in oxygenic photosynthesis.

Photophysical investigations of molecular donor-acceptor systems have elucidated many details of natural photosynthesis and revealed design principles for artificial

photosynthetic systems.[30-34] In a series of newly synthesized covalently linked carotenoid-tetrapyrrole dyads and triads, energy and ET processes have been investigated by means of time-resolved spectroscopy. Invariably, carotenoid excitation in the optically allowed S_2 band lead to rapid EET to the tetrapyrrole moiety in these systems in competition with IC to lower-lying optically forbidden carotenoid states,[31,34-37] a situation that is experimentally found in basically every natural photosynthetic systems as well.[9,10,21,22,38,39]

To obtain insights into the factors that govern the partition between excited-state energy and electron transfer processes among carotenoids and tetrapyrroles, we have designed artificial photosynthetic dyads that are thermodynamically poised to favor ET over EET processes. Two biomimetic artificial photosynthetic constructs were synthesized and investigated: a caroteno-porphyrin dyad (Dyad **1**) and a caroteno-fullerene dyad (Dyad **2**), as depicted in Figure 72.

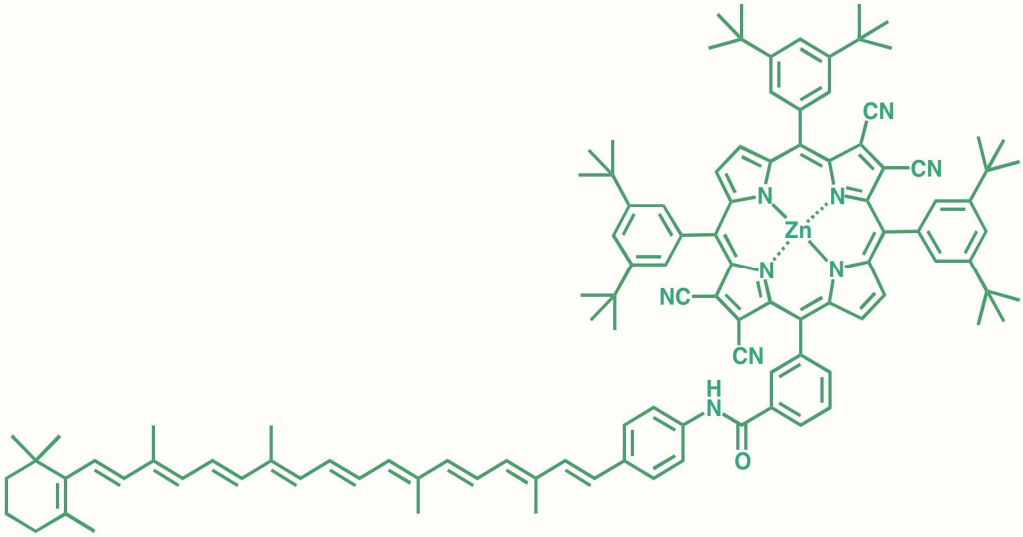

Dyad 1

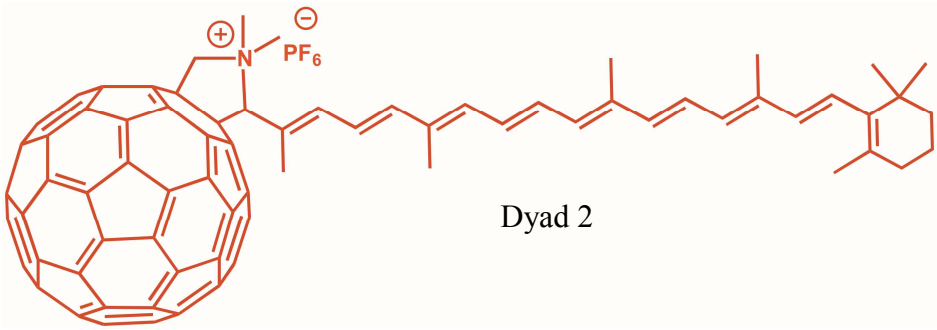

Dyad 2

Figure 72. Structure of the dyads: carotenoporphyrin (dyad 1) and carotenofullerene (dyad 2)

Dyad **1** consists of a carotenoid covalently attached to a porphyrin moiety, substituted with electron withdrawing CN groups to enhance its electron accepting properties. The carotenoid has 9 double bonds in the polyene chain, an additional double bond in the □-ionone ring and an elongation of the conjugated system into the linker moiety by a phenyl group. The effective conjugation length of this carotenoid is estimated at ~11 double bonds (considering the phenyl group as 1.5 conjugation length and the cyclohexene-like □-ionone ring 0.5 conjugation length, because it is rotated out of the plane of the polyene). The bulky substituted phenyl groups are oriented at steep angles to the

porphyrin plane are added to prevent the dyad from stacking. The two pigments are linked through two phenyl rings and a peptide bond.

Dyad **2** has a carotenoid with 8 double bonds in the polyene chain and one in the adjacent □-ionone ring, which gives an effective conjugation length of ~8.5 double bonds. It is coupled to a C_{60} fullerene by a positively charged methylated pyrrolidine linker. Fullerenes are not found in biological systems, but are promising components for artificial photosynthesis. [40,41] They have a small reorganization energy in electron transfer reactions, which can help place the ET reaction at the peak of the Marcus curve, facilitating fast photoinduced ET and slow recombination. [42,43]

We present transient absorption spectroscopy studies to derive EET and ET pathways that follow after excitation of the carotenoid and determine ensuing EET and ET rates. Remarkably, for dyad 1 we find that ET from the carotenoid S_2 state to the porphyrin completely outcompetes any EET process. In dyad 2, ET from carotenoid to the fullerene is the dominant process, but an EET process from the optically forbidden carotenoid S_1 state to the lowest fullerene singlet excited state is observed as well. We discuss that for a given electronic coupling, the ratio of ET and EET is governed by the driving force for charge separation. This thermodynamic switching is an important design principle for natural photosynthesis and illustrates a pathway for photosynthetic carotenoids to act both as ET quenchers and light harvesters.

5.3 Synthesis

The synthesis of 5,10,15-*tris*(3,5-di-*tert*-butylphenyl)-20-(4-carboxyphenyl)-7,8,17,18-tetracyanozinc(II)porphyrin (TCNP) and 7'-apo-7'-(4-aminophenyl)-β-carotene has been

reported previously. [44,45] Dyad **1** was prepared by coupling the amino group of the carotenoid with the carboxylic acid moiety of TCNP with N-(3-dimethylaminopropyl)-N'-ethylcarbodiimide (EDC) as a coupling reagent with a yield of 43%. Dyad **2** consists of a carotenoid moiety covalently attached to C_{60} through a pyrrolidine ring. Methylation with iodomethane yielded N,N-dimethylpyrrolidinium iodide derivative.[46] Metathesis of the salt was achieved by treatment with potassium hexafluorophosphate to give the dyad **2** in 80% yield.[47]

5.4 Results and Discussion

The dyads were studied in the nonpolar solvent toluene (dielectric constant 2.4) and the moderately polar tetrahydrofuran (THF) (dielectric constant 7.5). The absorption spectra of dyad **1** in these solvents are shown in Figure 73 in black and red respectively. The double band around 450 nm corresponds to the porphyrin Soret band, the bands around 660 nm and 680 nm to the porphyrin Q-band absorption. The carotenoid absorption bands overlap with the porphyrin Soret band, except for the lowest vibronic S_2 transition, which is found at 515 nm in toluene and at 506 nm in THF.

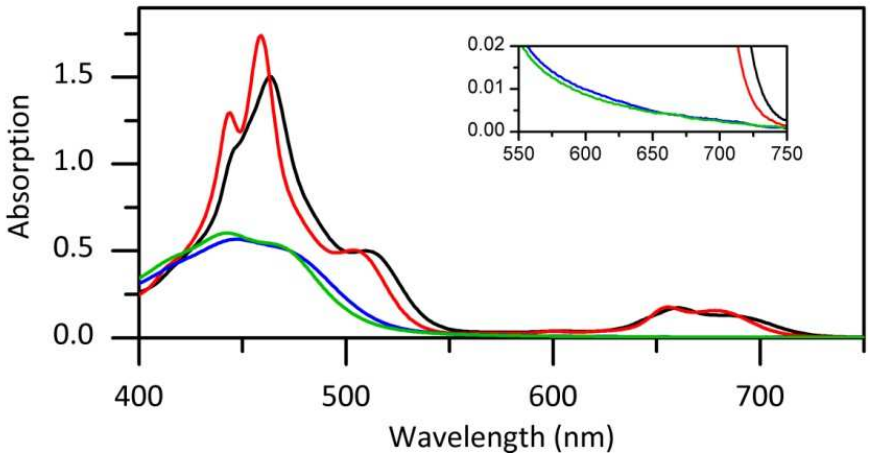

Figure 73. Absorption spectra. Black: dyad **1** in toluene. Red: dyad **1** in THF. Blue: dyad **2** in toluene. Green: dyad **2** in THF. All spectra were measured in a 1 mm path length quartz cuvette.

The absorption spectra for dyad **2** in toluene and THF are shown in blue and green. The carotenoid absorption is shifted to the blue with respect to dyad **1**, as expected from the shorter conjugation length of the molecule, leading to a larger energy gap between the ground and excited states.[3] Fullerene has an absorption band around 300 nm [52] (not shown) and an absorption tail with very small amplitude that extends throughout the visible range (see inset).

5.4.1 Dyad 1

The data from transient absorption measurements was globally analyzed using a simultaneous analysis for measurements in the visible and near-IR. In Figure 74a, we present the Evolution Associated Difference Spectra (EADS) for dyad **1** in toluene. The Decay Associated Difference Spectra (DADS) and time traces are shown in Figures S3 and S7 of the Supporting Information. Six time constants were needed for a sufficient fit

of the data. The first EADS (gray) shows a negative ΔA band in the visible and a positive band in the near-IR region. This is the typical absorbance difference spectrum due to population of the carotenoid S_2 state, and is characterized by ground state bleach and stimulated emission (negative ΔA signals) in the visible and excited state absorption (positive ΔA signal) in the near-IR. [3,53] This EADS decays into the second EADS with a time constant of about 100 fs. This time constant has been fixed in the analysis because it is around the limit of our temporal resolution.

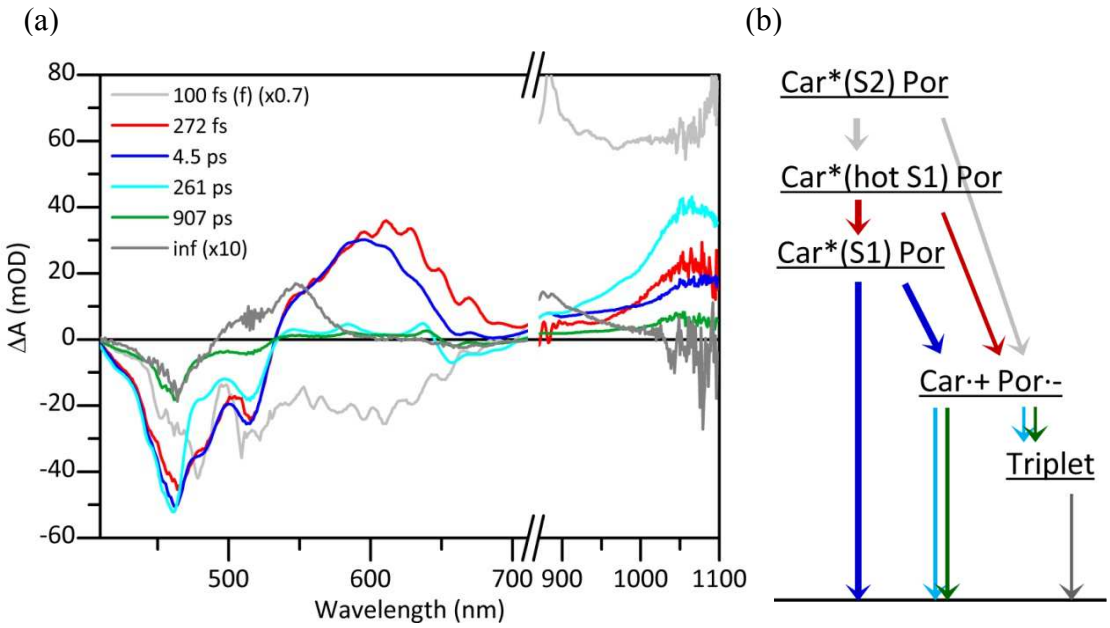

Figure 74. (a) EADS of dyad 1 in toluene. (b) Proposed excitation pathway for dyad 1; the colors of the arrows are matched with the corresponding EADS in (a)

Both the second (red, 272 fs) and third (blue, 4.5 ps) EADS show a positive band between 530 and 700 nm, originating from carotenoid S_1 excited state absorption. [3,53] The excited state absorption of the third EADS is blue-shifted with respect to the second, which corresponds to a transition from vibrationally hot to relaxed S_1. [3,53] Both the 272 fs

EADS and the 4.5 ps EADS show a negative signal below 530 nm, which can be assigned as a mix of carotenoid and porphyrin Soret bleaching. In the near-IR, these EADS show a band at 1060 nm that can be assigned to the carotenoid cation radical. [31,54] This, together with the presence of porphyrin bleaching, indicates that charge separation has taken place. Hence we can attribute these two spectra to a mix of (hot) carotenoid S_1 and the charge-separated Car $^{\bullet +}$ Por$^{\bullet -}$ state.

The fourth (cyan, 261 ps) EADS show bleaching signatures around 650 nm originating from porphyrin and around 450 and 500 nm originating from both porphyrin and carotenoid. Furthermore, the spectrum show an increased absorption of the carotenoid cation radical in the near-IR. The cation absorption band has increased with respect to the third spectrum (blue 4.5 ps), while the carotenoid S_1 absorption band has disappeared. This observation shows that charge separation has taken place from the S_1 state in 4.5 ps. The 907 ps EADS (green line) has a spectral shape that is virtually identical to that of the 261 ps EADS, but with significantly reduced amplitude, and hence the 261 and 907 ps time constants are assigned to radical-pair recombination. The need for two recombination time constants is probably related to heterogeneity in the sample. Structural heterogeneity has been demonstrated previously in axially linked caroteno-phthalocyanine triads by NMR spectroscopy. [55] The observation that the majority of the population recombines with the faster time scale can be seen from the larger amplitude of the 261 ps EADS.

The last EADS (brown) is non-decaying on the time scale of this experiment. The spectrum has been expanded 10 × for clarity. It shows an excited state absorption band at

550 nm. This band is characteristic of the long-lived carotenoid triplet state. [3,53,56] Usually, this band is only accompanied by carotenoid bleaching. Here, we also see porphyrin bleaching at both the Q and Soret wavelengths. The presence of porphyrin features in the final state is surprising, as the charge-separated state has recombined in the previous processes and porphyrin triplet states are in general energetically higher than those of carotenoids. As observed previously in several natural and artificial light-harvesting systems, this observation suggests that the triplet state is delocalized on the carotenoid and the porphyrin, which leads to a ground state bleach signal of both moieties. [18,19,57,58]

For dyad **1** in THF similar results are found. The EADS, DADS and time traces are presented in Figure S1, S4 and S8 of the Supporting Information.

Our interpretation of the transient absorption data is given in Figure 74b, the colors of the arrows are matched with the corresponding processes in the EADS. The carotenoid is excited to the S_2 state, where internal conversion to the S_1 state competes with ET to the porphyrin. The populated S_1 state gives rise to additional ET to the porphyrin on a picosecond time scale. In addition, the carotenoid can decay to the ground state by internal conversion. The model carotenoid has been measured by Berera et al. [56] who reported an S_1 decay rate of $(7.7\ \text{ps})^{-1}$ in toluene, ascribed to IC to the ground state. For dyad **1** we found an S_1 lifetime of 4.5 ps,. We therefore estimate the ET rate to be $(11\ \text{ps})^{-1}$, which suggests that around 40% of the S_1 state results in charge separation and 60% decays to the ground state. Caution should be exercised here in quantitatively addressing this issue, as the environment may affect the intrinsic S_1 lifetime of carotenoids.[59] Finally,

the charge-separated state recombines to the ground or the triplet state. Based on the area under the DADS, we estimate that 80% of the molecules recombine on a 261 ps time scale and 20% on a 907 ps time scale.

Surprisingly, the transient absorption data show no indication of EET from carotenoid to porphyrin. To investigate whether EET from the carotenoid to porphyrin occurs, we performed fluorescence excitation experiments. Figure 75 shows in blue the excitation spectrum of dyad **1** in toluene; the detection wavelength was chosen in the porphyrin Q-band fluorescence (750 nm). The 1-transmission spectrum of the dyad is shown in red for comparison. It can be seen that the excitation spectrum has the features of porphyrin, but shows no contribution at all from carotenoid. At the excitation wavelength that was used for transient absorption experiments (512 nm) the fluorescence excitation spectrum is substantially zero. This shows that EET from carotenoid to porphyrin is indeed absent.

The time-resolved data on dyad **1** thus reveal two remarkable phenomena (i) efficient ET from both the carotenoid S_2 and S_1 states to porphyrin in a nonpolar as well as a polar solvent. ET upon carotenoid excitation is typically not observed in natural photosynthetic LH systems, with the notable exception of low-yield radical formation in bacterial LH2.[60-62]; (ii) a total absence of EET upon carotenoid excitation. Again, this observation does not have a counterpart in natural photosynthesis, where substantial EET is invariably found from carotenoid S_2 to (B)Chl in oxygenic and anoxygenic photosynthesis.[3,20-22,38,39,63]

The branching between internal conversion to S_1, ET to porphyrin and EET to porphyrin is governed by the individual rates of these processes. Apparently the EET rate

is too small to contribute to S_2 decay. From the amplitudes of the carotenoid radical cation band in the EADS in Figure 74, we estimate that 2/3rd of the generated radical pairs originates from S_1, and 1/3rd from S_2. With an S_2 lifetime of 100 fs, this would correspond to an IC rate of $(150\ fs)^{-1}$ and an ET rate of $(300\ fs)^{-1}$, assuming that the EET rate is negligible. For the carotenoid S_2 state, the energy level lies around 19,400 cm^{-1} or 2.4 eV (Figure 75). The driving force for ultrafast charge separation in dyad **1** can be found from thermodynamic considerations. From the redox potentials of 0.47 V and -0.40 V (vs, SCE) for the carotenoid[64] and the porphyrin, respectively, and the S_2 energy of the carotenoid, we calculate a driving force of ~1.53 eV to form $Car^{\bullet +}\ Por^{\bullet -}$ from the carotenoid S_2. This exceptionally large driving force results in the observed ultrafast photoinduced ET rate that can compete with the S_2-S_1 IC process. From the carotenoid S_1 state, rapid ET to the porphyrin occurs with a rate constant of $(11\ ps)^{-1}$. Assuming an S_1 energy of 13,000 cm^{-1} (1.6 eV), we calculate a driving force of 0.74 V.

The absence of EET from carotenoid S_2 shows that the EET rate is much smaller than those of IC and ET, despite the fact that EET to porphyrin is thermodynamically feasible. From the fluorescence excitation spectrum (Figure 75) we derive that the EET quantum yield is less than 5 %. With a decay rate of S_2 of $(100\ fs)^{-1}$, we estimate the upper limit of the EET rate to be $(2\ ps)^{-1}$. This result is very different from the efficient EET that is invariably found from carotenoid S_2 to chlorophyll in oxygenic photosynthesis.[20-22,38,39,63] or artificial systems where the covalently bound tetrapyrrole was either a pyropheophorbide or phthalocyanine. [31,34,35,37]. The decreased EET rate in the present dyads very likely follows from the low dipole strength of the Q-band in porphyrins,

which is an order of magnitude smaller than in chlorophylls, pyropheophorbides or phtalocyanines. In a coulombic EET mechanism, this leads to an equally diminished EET rate.

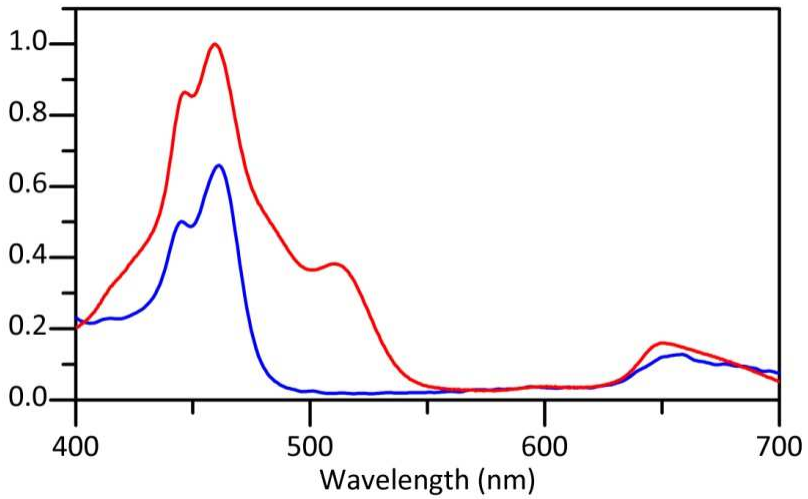

Figure 75. Fluorescence excitation spectrum (blue, detection at 750 nm) and 1-transmission spectrum (red) of dyad **1** in toluene.

The absence of EET from the carotenoid S_1 state can be explained from the energy-levels of the states involved. The S_1 state of a carotenoid with a conjugation length of 11 double bonds lies around 13,000 cm^{-1}. [3] The porphyrin Q-bands are located at 660 and 680 nm, which corresponds to 15,152 and 14,706 cm^{-1}, making EET from carotenoid S_1 to porphyrin energetically unfavorable.

We conclude that the dominance of ET over EET upon carotenoid excitation in dyad **1** finds its origin in two separate causes: (i) a large driving force that speeds up the ET rate to $(300\ fs)^{-1}$ from S_2 and $(11\ ps)^{-1}$ from S_1 and (ii) a slow EET rate of $< (2\ ps)^{-1}$ from carotenoid S_2 that is probably caused by the low dipole strength of the porphyrin acceptor.

5.4.2 Dyad 2

Dyad **2** (Figure 76), was excited in toluene solution in its carotenoid moiety at 473 nm. The EADS are presented in Figure 76a, for the DADS and time traces we refer to Figure S5 and S9 of the supporting information. The first EADS in global analysis corresponds to the carotenoid S_2 spectrum, of which the lifetime was fixed at 100 fs (Figure 76a, gray). The second EADS (red, 545 fs) consists of carotenoid ground state bleach, S_1 excited state absorption at 550 nm and carotenoid cation absorption at 900 nm. The presence of the signature of both S_1 and the charge-separated state in the second EADS implies that the S_2 state decays via at least two pathways, IC to S_1 and ET to the fullerene. EET from S_2 to the fullerene could also take place, but cannot be identified because spectral signature of singlet-excited state fullerene is spectrally silent in the probed spectral window. Due to the shorter conjugation length of this carotenoid compared to the one in dyad **1**, the carotenoid signals are shifted to the higher energy side of the spectrum. The anion of pyrollidinofullerene that was previously reported around 1010 nm ($\varepsilon = 8 \times 10^3$ M^{-1} cm^{-1}) [52] was not detected and is probably obscured by the large signal of the carotenoid ion ($\varepsilon = 10^5$ M^{-1} cm^{-1}). [54]

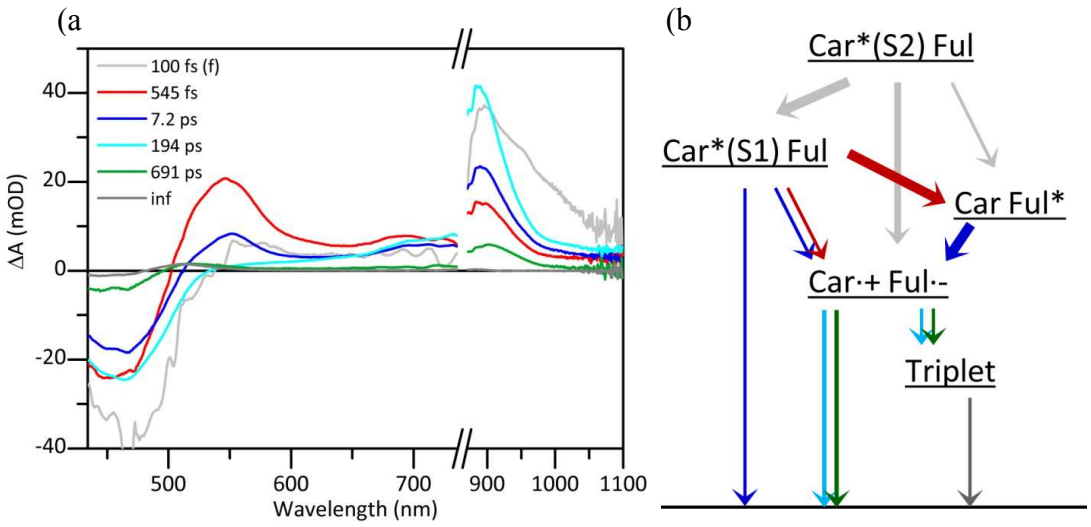

Figure 76. (a) EADS of dyad **2** in toluene. (b) Proposed excitation pathway for dyad **2**; the colors of the arrows are matched with the corresponding processes in (a).

The second EADS (red) evolves in 545 fs into the third EADS (blue). This evolution includes a large decay of the S_1 excited state absorption, an increase of the cation band and a decrease of the carotenoid ground state bleach. The growth of the cation band shows that ET takes place from the carotenoid S_1 state to the fullerene. This event is accompanied by a decrease of the carotenoid ground state bleach, which is unexpected because ET would preserve this signal. We may exclude the possibility that significant carotenoid S_1 state decays to the ground state not only because the 545 fs time constant is too short for such a process[3], but also because in the next EADS (cyan line) the carotenoid bleach is fully restored. Most likely, then, the decrease in ground state bleach in 545 fs results from EET from the carotenoid S_1 to the fullerene moiety.

The transition from the third (blue, 7.2 ps) to the fourth (cyan, 194 ps) EADS shows the recovery of the carotenoid ground state bleach and a further growth of the carotenoid

radical cation band. This can be interpreted as a charge separation process from the lowest fullerene excited state, whose energy level is estimated at 14,000 cm^{-1} from the absorption spectrum. In this charge-separated state the carotenoid moiety is involved again, which explains the increase of carotenoid ground state bleach. The growth and decay of the carotenoid ground state bleach - indicating the role of singlet excited fullerene - is shown in the 450 nm time trace (Figure 77). Decay of fullerene to the ground state can be neglected, as the lifetime of fullerene and derivatives is reported to be more than a nanosecond. [65] The 7.2 ps transition also includes the decay of the residual carotenoid S_1 band at 550 nm. This S_1 population can give rise to further charge separation or decay to the ground state. The fourth (cyan, 194 ps) and smaller fifth (green, 691 ps) EADS show carotenoid bleach and carotenoid radical cation absorption and are assigned to the charge-separated state which is recombining with these rates. The fifth EADS also shows carotenoid triplet absorption. The sixth EADS (brown) shows carotenoid ground state bleach and carotenoid triplet absorption at 517 nm and does not decay on the time scale of the experiment.

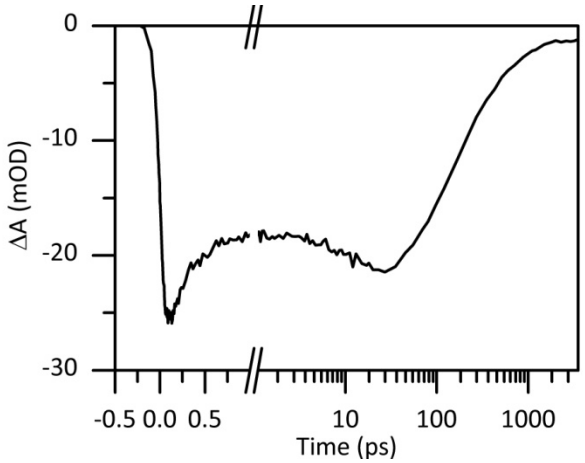

Figure 77. Time trace of dyad **2** in toluene at 433 nm.

The interpretation of these processes is shown in Figure 76b. The carotenoid S_2 state, which decays on a 100 fs time scale, partly gives rise to charge separation and partly decays to S_1. Probably this decay is again via the hot S_1 state, but this process is not resolved independently. From the S_1 state, excitation energy is transferred to the fullerene moiety on a time scale of 545 fs. In this case the driving force for ET is also large, ~0.9 eV from the S_1 state of the carotenoid, (assuming the S_1 state of the carotenoid at 700 nm and the redox potential for the carotenoid moiety as 0.7 V vs. SCE and that of the C_{60}-*N,N*-dimethylpyrrolidinium moiety as -0.17 vs. SCE, measured values in model compounds). In dyad **2** EET from the carotenoid S_1 to C_{60} appears to be able to compete with the ET process. The next step is ET from carotenoid to the excited fullerene moiety on a picosecond time scale. This charge-separated state subsequently decays with lifetimes of 194 and 691 ps, leading to a small population of the long-lived carotenoid triplet state which forms via charge recombination of the triplet biradical. The triplet biradical is derived from the initially formed singlet biradical charge separated state.[66-71] For dyad **2** in THF similar results are found. The EADS, DADS and time traces are presented in Figure S2, S6 and S10 of the supporting information.

5.5 Conclusion

Taken together, our transient absorption data show that for dyad **1,** excitation to the carotenoid S_2 state induces efficient electron transfer. Driven by the large driving force, this charge separation occurs at a rate of $(300\ fs)^{-1}$ from S_2 and in about $(11\ ps)^{-1}$ from S_1. In fluorescence excitation measurements EET from carotenoid to porphyrin is not

observed. This is remarkable when compared with natural systems where EET usually is faster than ET. In this artificial system, because of a large driving force for ET (~ 1.5 V) and low dipole strength of the energy acceptor, the ET outcompetes EET. These results illustrate that for a given rate of EET, determined by the overlap integral and the electronic coupling of the chromophores, the ratio of ET to EET can be controlled by adjusting the thermodynamic term. This is an important design principle for artificial photosynthesis and is almost certainly at play in photosynthesis where carotenoids participate in both ET quenching and light harvesting.

The charge-separated state recombines with two characteristic lifetimes. In toluene these were found to be 261 and 907 ps. Recombination yields a triplet signal that is accompanied by porphyrin bleaching. This was interpreted as a delocalized triplet, located on both the carotenoid and the porphyrin moiety. Similar features are seen in preparations of pigment protein complexes from photosynthetic membranes.

Upon excitation of the carotenoid of dyad **2**, EET to fullerene takes place, as well as charge separation from the S_1 and probably the S_2 states of the carotenoid. Subsequently, the excited fullerene gives rise to charge separation. Here, the lifetimes of the charge-separated state in toluene were found to be 194 and 691 ps.

Finding ultrafast ET from the carotenoid S_2 state in these two dyads opens a new time window for exploring carotenoid photophysics in artificial photosynthetic systems. Moreover, important questions such as the role if any of coherent charge separation and the dynamics of disorder have emerged. Raman results in progress will give us information on the instantaneous interactions in dyads and in natural systems (ref Bruno).

Pump probe techniques such as used here cover the time domain greater than about 100 fs. This frames the challenge of understanding the dynamics and electronic coupling at times less than 100 fs, the nature of which probably define and set in motion all subsequent physical and chemical processes of converting light into chemical potential. It is anticipated that artificial systems such as these dyads will be useful in this regard.

5.6 Experimental

The ^{1}HNMR spectra were recorded on the Varian spectrometer at 400 MHz. Mass spectra were recorded on a matrix-assisted laser desorption/ionization time-of-flight spectrometer (MALDI-TOF). Ultraviolet-visible ground state absorption spectra were measured on a Shimadzu UV2100U spectrometer. The reagent 8'-apo-□-carotene-8'-al (Hoffmann-La Roche) was purified by flash chromatography with 100% dichloromethane before use. Thin layer chromatography (TLC) was performed with silica gel coated glass plates from Analtech. Column chromatography was carried using Silicycle silica gel 60 of 230-400 mesh. All the reactions were carried out under an argon atmosphere.

5.6.1 Carotenoporphyrin (Dyad 1)

Porphyrin (14 mg, 0.01 mmol) and 7'-apo-7'-(4-aminophenyl)-β□-carotene (6.72 mg, 0.01 mmol) were dissolved in 10 mL dichloromethane. N-(3-dimethylaminoprpyl)-N'-ethylcarbodiimide hydrochloride (3.47 mg, 0.018 mmol) and 4-(dimethylamino)pyridine (2.95 mg, 0.03 mmol) were added and the reaction mixture was stirred for 5.5 h at room temperature. The reaction mixture was washed with water and brine. The organic layer was then dried over anhydrous sodium sulfate. The solvent was removed with a rotary

evaporator. The crude product was then purified by column chromatography on silica gel using 20% ethyl acetate and hexane. Yield: 8.5 mg (43%). ^{1}HNMR (400MHz, $CDCl_3$): δ 1.02 (6H, s, CH_3-16C and CH_3-17C), 1.41 (11H, bs), 1.46 (12H, bs), 1.5 (14H, bs), 1.58(12H, bs), 1.7 (12H, bs), 1.93-2.02(14H, m), 6.1-6.84 (14H, m), 6.96(1H, bs), 7.09 (1H, bs), 7.29(1H, s), 7.33(1H, bs), 7.63(1H, s),7.72-8.09(11H, m), 8.16(1H, s), 8.82-9(4H, m). MALDI-TOF-MS *m/z:* calcd. for $C_{110}H_{117}N_9OZn$ 1646.55, obsd. 1646.57; UV-vis (CH_2Cl_2): 353, 373, 445, 454, 506, 597, and 649 nm.

5.6.2 CarotenoC$_{60}$

A portion of 8'-apo-β-caroten-8'-al (50 mg, 0.12 mmol), C_{60} (179 mg, 0.25 mmol) and sarcosine (108.2 mg, 1.2 mmol) were refluxed in 50 mL chlorobenzene for 24 h. The reaction mixture was cooled and the solvent was removed under vacuum. The crude reaction mixture was purified by column chromatography on silica gel using 5% carbon disulfide, 5% ethyl acetate with 90% hexanes. Yield: 105 mg (75%). ^{1}HNMR (400MHz, $CDCl_3/CS_2$): δ 1.02 (6H, s, CH_3-16C and CH_3-17C), 1.43-1.5 (2H, m, CH_2-2C), 1.57-1.64 (2H, m, CH_2-3C), 1.7(3H, s, CH_3-19C), 1.91-2 (11H, m, CH_3-18C, CH_3-20C, CH_3-20'C, CH_2-4C), 2.26(3H, s, CH_3-19'C), 2.82(3H, s, CH_3), 4.16(1H, d, *J*=12Hz), 4.48(1H, bs), 4.93(1H, bs), 5.98-6.84 (12H, m vinyl H). MALDI-TOF-MS *m/z*: calcd. for $C_{92}H_{45}N$ 1163.35, obsd. 1163.39; UV-vis (CH_2Cl_2) 328, 417, 439, 466, and 698 nm.

5.6.3 CarotenoC$_{60}$-N,N-dimethylpyrrolidinium iodide

CarotenoC$_{60}$ (25 mg, 0.02 mmol) was suspended in a mixture of 1 mL dimethyl sulfoxide and 3 mL iodomethane in a screw cap vial. The reaction mixture was stirred at room temperature for 36 h. Most of the iodomethane was removed under a nitrogen

stream to give a wet brown colored compound. The compound was then dissolved in 10 mL of dichloromethane and filtered. The filtrate was washed with water and then the organic solvent was concentrated under reduced pressure. The crude product was purified by column chromatography on silica gel using 5% methanol 15% carbon disulfide with 80% dichloromethane. Yield: 17 mg (60%). ^{1}HNMR [(400MHz, $CDCl_3/CS_2$(1:1)]: δ 0.01 (6H, s, CH_3-16C and CH_3-17C), 1.42-1.48 (2H, m, CH_2-2C), 1.58-1.64 (2H, m, CH_2-3C), 1.69(3H, s, CH_3-19C), 1.91-2.04(11H, m, CH_3-18C, CH_3-20C, CH_3-20'C, CH_2-4C), 2.43(3H, s, CH_3-19'C), 4.32(6H, s, -CH_3), 5.9(1H, d, *J*=12Hz), 6.02-6.83(12H, m vinyl H), 7.21(1H, s), 7.34(1H, bs). ^{1}HNMR [(400MHz, $CDCl_3/CS_2$/MeOD(1:1:0.2)]: δ 0.95 (6H, s, CH_3-16C and CH_3-17C), 1.37-1.42 (2H, m, CH_2-2C), 1.5-1.58 (2H, m, CH_2-3C), 1.63(3H, s, CH_3-19C), 1.85-1.97 (11H, m, CH_3-18C, CH_3-20C, CH_3-20'C, CH_2-4C), 2.37(3H, s, CH_3-19'C), 4.01(3H, s, -CH_3), 4.21(3H, s, -CH_3), 5.75(1H, d, *J* =13Hz), 5.98-6.66 (12H, m vinyl H), 6.78(1H, s), 7.15(1H, s). MALDI-TOF-MS *m/z*: calcd. for $C_{93}H_{48}N$ 1178.58, obsd. 1178.62; UV-vis (CH_2Cl_2) 325, 423, 445, 465, and 690 nm.

5.6.4 CarotenoC$_{60}$-N,N-dimethylpyrrolidinium hexafluorophosphate (Dyad 2)

CarotenoC$_{60}$-N,N-dimethylpyrrolidinium iodide (10 mg, 0.009 mmol) was dissolved in 5 mL tetrahydrofuran, potassium hexafluorophosphate (6.24 mg, 0.034 mmol) was added in 2 mL of water and the reaction mixture was stirred at room temperature for 3 h. The product was then extracted in dichloromethane and washed with water several times. The solvent was evaporated under reduced pressure. Yield: 8.6 mg (80%). ^{19}FNMR [(400MHz, $CDCl_3/CS_2$ (1:1)]: δ -67.67(d, 6F).

5.7 Spectroscopy

Each dyad was dissolved in nitrogen-flushed toluene or THF and transferred to a 1 mm path length quartz cuvette. The concentration was set to produce an absorbance of 0.5 at the excitation wavelength.

Room-temperature absorption spectra were recorded on a Perkin Elmer Lambda 40 UV/VIS spectrometer. Room-temperature fluorescence excitation spectra were measured with a commercial spectrophotometer (Jobin Yvon, Fluorolog) with detection at 750 nm.

Ultrafast transient absorption spectroscopy was performed on a set-up described earlier. [48] In short, the output of an 800 nm, 1 kHz amplified Ti:Sapphire laser system was used to drive an optical parametric amplifier to produce the excitation pulses. The excitation wavelength was set at 515 nm for dyad **1** in toluene, 506 nm for dyad **1** in THF and 473 nm for dyad **2** in both toluene and THF, in all cases exciting the carotenoid at the lowest-energy vibronic band. The pulse energy was set to 80 nJ per pulse and focused to a size of 200 μm. The probe pulse was created by focusing part of the 800 nm beam on a CaF_2 crystal for probing in the visible or sapphire plate for probing in the near-IR. The pump and probe were focused on the sample and the polarization was set to the magic angle of 54.7˚. Absorption difference spectra (ΔA) are calculated by $\Delta A(\lambda) = -\log(I_{pumped})/\log(I_{unpumped})$ for delays up to 3.5 ns.

Global analysis of the transient absorption data was performed using the program Glotaran. [49,50] In global analysis all wavelengths are analyzed simultaneously using a sequentially interconverting model $1 \rightarrow 2 \rightarrow 3 \rightarrow \ldots$ Here the numbers indicate evolution associated difference spectra (EADS) that interconvert with successive monoexponential

decay rates, each of which can be regarded as the lifetime of each EADS. Data from experiments in the visible and near-IR were fitted simultaneously. The EADS that follow from the sequential analysis are visualizations of the evolution of the (excited) states of the system and usually represent a mixture of molecular species. This sequential analysis is mathematically equivalent to a parallel (sum-of-exponentials) analysis and the time constants that follow from the analysis apply to both. [51] The parallel decay scheme produces decay associated difference spectra (DADS), which are shown in the Supporting Information. For a more detailed description of global analysis we refer to Van Stokkum et al. 2004. [49]

Chapter 6 2.2 β-Cyano Substituted Porphyrins as Sensitizers in Photoelectrochemical Devices

Antaeres Antoniuk-Pablant,[†] Bradley J. Brennan,[‡] Benjamin D. Sherman,[†] Gary W. Brudvig,[‡] Ana L. Moore,[†*] Thomas A. Moore,[†*] Devens Gust[†][1]
[†]***Department of Chemistry and Biochemistry, Arizona State University, Tempe, AZ 85287***
[‡]***Energy Sciences Institute and Department of Chemistry, Yale University, P. O. Box 208107, New Haven, CT 06520***

6.1 Abstract

β-Cyanoporphyrins have very positive oxidation potentials and absorb light at longer wavelengths than most porphyrins, making them potential candidates for sensitizers in photoelectrosynthetic cells for water oxidation. In order to begin to evaluate this potential, two tetra-β-cyanoporphyrins were synthesized and evaluated as sensitizers in dye sensitized solar cells using I^-/I_3^- as the redox mediator. The porphyrins produced no photocurrents in nanoparticulate TiO_2-based cells as their excited stated are not energetic enough to inject electrons into the TiO_2 conduction band. However, both molecules produced photocurrents in SnO_2-based cells. The cells performed comparably, producing short circuit photocurrent densities of about 2 mA cm^{-2} and open circuit photovoltages of about 120 mV, and both had fill factors of 0.31. The sensitizer linked to the SnO_2 via a carboxylate at the *para* position of a *meso* phenyl ring gave a slightly higher packing density on the electrode, but the corresponding porphyrin linked via a carboxylate at the *meta* position showed better performance on a per molecule basis. Electrochemical studies indicate that the radical cations of these porphyrins that are produced upon

electron injection into the semiconductor have sufficient electrochemical potential to oxidize water.

6.2 Introduction

The pioneering report[184] by O'Regan and Grätzel in 1991 has generated a huge number of investigations of approaches to dye sensitized solar cells (DSSC) for electricity production with a view toward improving performance.[37,185–187] The concept of a dye-sensitized nanoparticulate wide band gap semiconductor electrode can be extended to the design of photoelectrosynthetic cells for water splitting or other forms of solar powered fuel production by the addition of suitable catalysts for water oxidation.[19,31–33] In either application, the choice of dye is critical, as the excited state of the dye must inject electrons into the conduction band (CB) of the semiconductor, which is a function of the redox potential and the absorption spectrum of the material. Other important properties of system need to be considered such as the linkage joining the dye to the semiconductor particles, and the nature of the semiconductor. In DSSC, the oxidized form of the dye must be able to accept electrons from the mediator in solution, but must not readily accept electrons from the semiconductor. Stability and surface packing effects are also important. Of the many types of sensitizers for DSSC that have been investigated,[13,15,65,77,188–198] porphyrins have recently been found to be particularly promising. Porphyrins have long been used as light absorbers and electron donors in artificial photosynthetic molecules,[2,11,17,73,76] and have given some of the highest efficiencies yet observed for DSSC.[14,15] However, porphyrins have several shortcomings as ideal dyes. For example, the most common porphyrins do not absorb light in the far

red and infrared spectral regions, and sunlight at these wavelengths is wasted, thus reducing efficiency. From the point of view of water splitting, the radical cations of most common porphyrins are not oxidizing enough to drive catalysts for water oxidation efficiently.

Porphyrins bearing cyano groups at β-positions of the macrocyclic ring might in principle overcome some of these problems. The substituents lead to a shift of the absorption spectrum toward longer wavelengths, and thus could permit better usage of the solar spectrum by a DSSC. The electron withdrawing nature of the cyano groups increases the oxidation potential of the molecule, which could make such porphyrins useful for water oxidation. Also, the location of the cyano groups at β-sites, rather than on aryl rings at the *meso*-positions, adds flexibility for the placement of anchoring groups to attach the sensitizer to the semiconductor surface. In spite of these potential advantages, cyanoporphyrins have not been investigated as sensitizers in DSSC. This is due mainly to the fact that their synthesis has been difficult, and the synthetic methods available have limited the selection of substituents to serve as anchoring groups.

Recently, we reported a new synthetic approach to β-cyanoporphyrins that is considerably more convenient than past routes, and that allows the incorporation of a wide variety of other substituents.[137] Here, we report the investigation of the use of these porphyrins in DSSC applications. First, we investigated the spectroscopic and electrochemical properties of model porphyrins bearing either three or four β-cyano groups, **1**, **2** and their zinc analogs in Figure 78, in order to determine which were most

suitable for DSSC applications. Based upon these results, we selected porphyrins **3**$_{Zn}$ and **4**$_{Zn}$ (Figure 78) as sensitizers for DSSC.

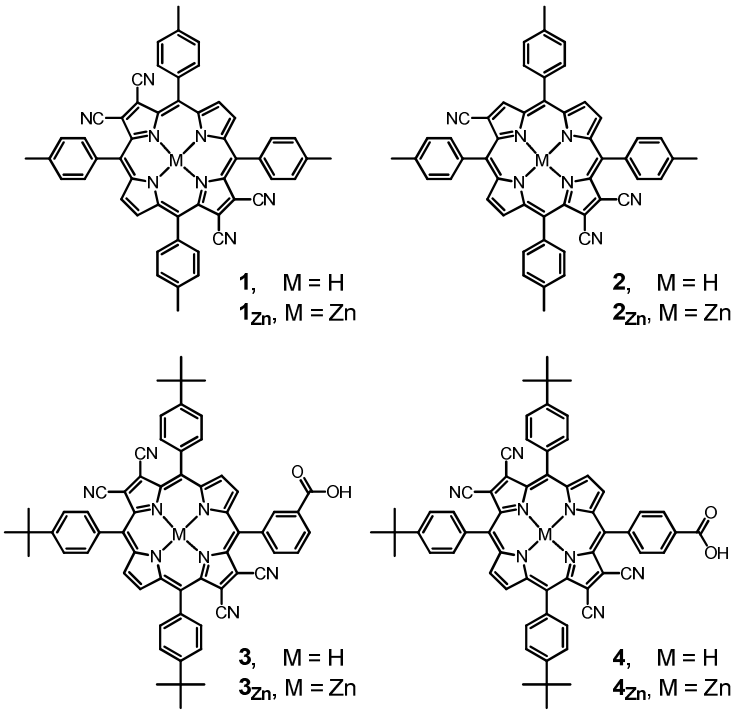

Figure 78. The β-cyanoporphyrins used in this work.

These two compounds differ in the position of the carboxylic acid group that serves to link the porphyrin to the semiconductor oxide. It has been hypothesized that having the anchoring group at a *meta* position to the macrocycle on a benzene ring can allow for more efficient net electron injection into the semiconductor by causing the orientation of the porphyrin to lie flat and therefore closer to the surface, which increases the electron injection into the semiconductor.[13,199,200] Finally, we prepared and tested several cell types in order to determine whether or not β-cyanoporphyrins might be useful in DSSC.

6.3 Results and Discussion

6.3.1 Synthesis

Compounds **2** and $\mathbf{2_{Zn}}$ were synthesized using methods we have previously reported.[137] The details are given in the Experimental Section. The preparation of the other porphyrins has been reported.[137]

6.3.2 Cyclic Voltammetry

The first oxidation and reduction potentials for the porphyrins were obtained by cyclic voltammetry as discussed in the Experimental Section, and the results are shown in Figure 79 and values in V vs. NHE in Table 1.

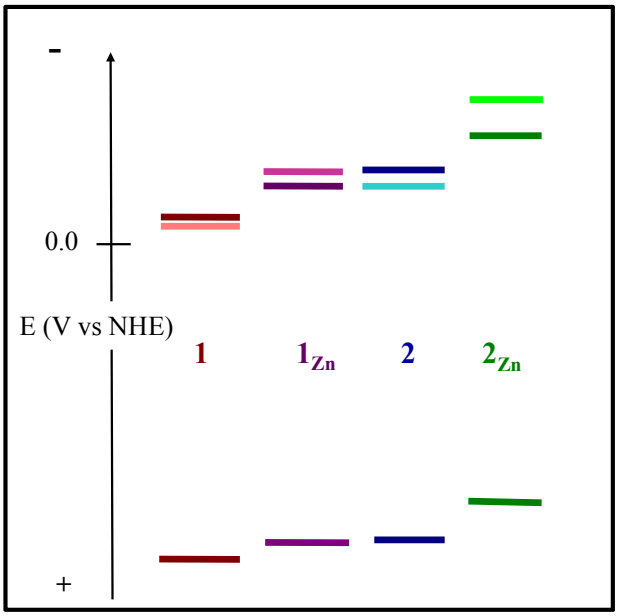

Figure 79. Diagram of reduction and oxidation potentials (dark colored bars) and excited state oxidation potentials (light colored bars) of porphyrins 1, 1_{Zn}, 2, and 2_{Zn}. Corresponding values are given in table 7.

Table 7. Longest wavelength absorption maximum in dichloromethane (^{1}P (nm)), energy of the first excited singlet state (^{1}P (eV)), first oxidation potential vs. NHE (Ox_1), first reduction potential vs. NHE (Red_1), excited state oxidation potentials vs NHE (*Ox), and free energy changes (ΔG° (eV)) for injection into the conduction bands of TiO_2 and SnO_2 for selected porphyrins.

cmpd	^{1}P (nm)	^{1}P (eV)[a]	Ox_1	Red_1	*Ox[b]	ΔG° TiO_2[c]	ΔG° SnO_2[d]
1	737	1.59	1.52	-0.06	-0.07	+0.56	-0.12
1$_{Zn}$	680	1.75	1.44[f]	-0.23	-0.31	+0.32	-0.36
2	708	1.70	1.43	-0.29	-0.27	+0.36	-0.32
2$_{Zn}$	632	1.87	1.26	-0.45	-0.61	+0.02	-0.66
3$_{Zn}$	685	1.75	1.42	-0.16	-0.33	+0.30	-0.38
4$_{Zn}$	677	1.75	1.43[e]	-0.14	-0.32	+0.31	-0.37
PF$_{10}$	641	1.93	1.57	-0.73	-0.36	+0.27	-0.41
PF$_{10Zn}$	578	2.12	1.35	-0.91	-0.77	-0.14	-0.82

[a]Calculated from the wavenumber average of the longest wavelength absorption maximum and shortest wavelength emission maximum.
[b]The excited state oxidation potentials were estimated by subtracting the energy of the first excited singlet state from Ox_1.
[c]Calculated using the literature value of -0.63 V vs. NHE for the CB of nanoparticulate TiO_2 at pH 8.[201]
[d]Calculated using the literature value of 0.05 V vs. NHE for the CB of SnO_2 at pH 8.[98]
[e]Oxidation is quasi-reversible
[f]Oxidation is irreversible

Most of the cyanoporphyrins demonstrated reversible first and second reduction waves and quasi-reversible first oxidation waves. The potentials show the anticipated [80,89,90,95] anodic shift due to the electron withdrawing cyano groups. For example, the first oxidation potential of 5, 10, 15, 20-tetrakis-(4-methylphenyl)porphyrin is 1.18 V vs NHE and the first reduction potential is -1.03 V. [202] The corresponding numbers for **2**, with three cyano groups, are 1.43 V and -0.29 V vs. SCE. Thus addition of the three cyano groups has a very large effect on the stabilization of a negative charge on the porphyrin

during reduction, and a smaller but still substantial effect on oxidation. Addition of the fourth cyano group in **1** increases the effect by about 230 mV in reduction and about 100 mV in oxidation, relative to **2**. Addition of zinc to the porphyrin makes the macrocycle somewhat easier to oxidize and more difficult to reduce, as can be seen in Table 1 by comparing **1** and **2** with their zinc analogs. Addition of an electron withdrawing carboxyl group to one of the *meso*-aryl rings as in $\mathbf{3_{Zn}}$ and $\mathbf{4_{Zn}}$ has little effect on oxidation potentials and makes the reduction potentials more negative by less than 100 mV.

Table 7 also shows data for 5-(4-methoxycarbonylphenyl)-15-(4-carboxyphenyl)-10,20-bis(pentafluorophenyl)porphyrin, $\mathbf{PF_{10}}$, and its zinc analog $\mathbf{PF_{10Zn}}$ which have been explored for use in light-driven water oxidation due to their strong oxidizing ability.[98,203] The tetracyanoporphyrins are roughly comparable to the PF_{10} compounds in terms of oxidation, whereas reduction of the cyanoporphyrins is considerably more facile. This last fact suggests that cyanoporphyrins may be useful as electron acceptors in molecular artificial photosynthetic reaction centers and related compounds in place of the more usually employed quinones or fullerenes. Such applications have been recently demonstrated.[146,183,204]

6.3.3 Absorption Spectra

The absorption spectra of **1** and $\mathbf{1_{Zn}}$ in dichloromethane are shown in Figure 80.

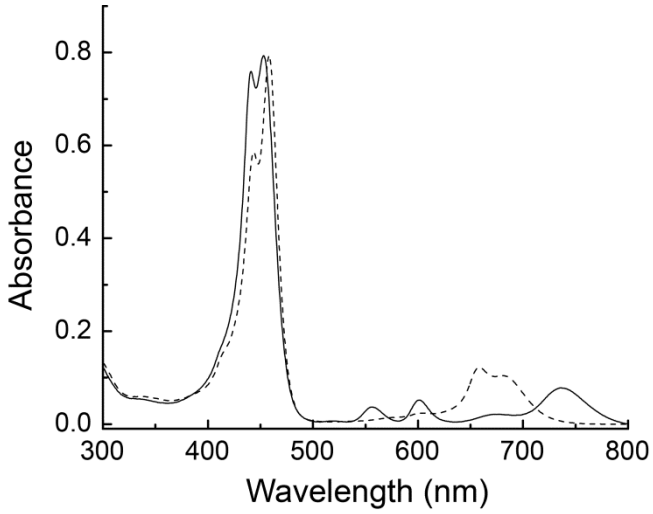

Figure 80. Absorption spectra of β-cyanoporphyrin **1** (solid) and its zinc analog $\mathbf{1}_{\mathbf{Zn}}$ (dashed) in a 1% MeOH in dichloromethane solution. The spectra have been normalized at the Soret band with the largest extinction coefficient.

The B band, which appears as a single peak around 420 nm in the spectra of typical free base *meso*-tetra-arylporphyrins, is split into two peaks with comparable extinction coefficients in the tetra-β-cyanoporphyrins, and these appear at 441 and 453 nm in **1**. In terms of the Gouterman four orbital theory,[82] the Soret band (B) is due to electronic transitions from the b_2 orbital (HOMO) to the c_1 and c_2 LUMO orbitals. These transitions consists of two transition dipole moments in directions along a set of axes on the porphyrin which pass through the two sets of opposing pyrrole rings. Due to the electronic effects of the four cyano substituents on the antipodal β-pyrrole positions on only one axis, the energies of the c_1 and c_2 orbitals are no longer degenerate in these compounds, and this in turn leads to the observed split in the Soret band. Due to the electron withdrawing β-substituents, the longest wavelength Q-band of **1** has a maximum at 737 nm, whereas typical free base *meso*-tetra-arylporphyrins have this maximum around 650 nm. In $\mathbf{1}_{\mathbf{Zn}}$ the B bands appear in the same spectral region as those of **1**, but

the longest-wavelength Q-band absorption is at 680 nm. The spectra of the other tetra-β-cyanoporphyrins are similar to those of **1** and **1Zn**, whereas those of the cyanoporphyrins with only three cyano groups do not show the splitting of the B bands, and have less pronounced shifts of the Q-bands to longer wavelengths (see literature[137] Experimental Section). The wavelengths of the maxima of the longest-wavelength Q-bands for the porphyrins examined in this study are shown in Table 7. The energies of the first excited singlet states were calculated from the wavenumber average of the longest-wavelength absorption maxima and the shortest-wavelength emission maxima, and are also given in Table 7. It will be noted that the cyanoporphyrins absorb at significantly longer wavelengths than the fluorinated porphyrins shown in Table 7, and thus have lower-energy excited states.

6.3.4 Photoelectrochemical Cells

Both DSSC and photoelectrosynthetic cells for water splitting share the concept of a dye-sensitized nanoparticulate wide band gap semiconductor as a photoanode. Thus, we have evaluated the cyanoporphyrins as sensitizers for DSSC as a step toward their use in water splitting cells. The redox potential for water oxidation at pH 0 is 1.23 V vs NHE, and at pH 8 it is 0.76 V. Thus, from Table 7 it is clear that from a thermodynamic point of view, any of the tetra-β-cyanoporphyrins investigated can oxidize water, and that they have significant excess oxidizing power to supply reasonable overpotentials to drive the reaction. The sensitizer must also be able to inject an electron into the CB of the semiconductor. This ability is a function of both the first oxidation potential and the excited state energy. Table 7 shows the excited state oxidation potentials for the various

porphyrins. It also shows the thermodynamic driving force values for electron injection into the conduction bands of TiO_2 and SnO_2 based on the CB potentials of the nanoparticulate semiconductors. These data show that with the possible exception of **2Zn**, none of the porphyrins are expected to be able to sensitize TiO_2. With the exception of **1**, all of the porphyrins have some driving force for electron injection into the CB of SnO_2. On the other hand, the tri-β-cyanoporphyrins, especially **2Zn**, do not absorb at especially long wavelengths compared to other tetra-arylporphyrins, and thus do not have the advantage of absorbing more of the solar spectrum. We decided to evaluate the zinc tetra-β-cyanoporphyrins as potential sensitizers for DSSC. We also decided to examine both the commonly used TiO_2 and the less common SnO_2 as semiconductors. Although the table suggests that TiO_2 would not be suitable, the values for ΔG° in the table are based on CB data for the bulk semiconductors, and the nanoparticulate materials will have somewhat different conduction band energies. In addition, the CB values will be a function of the solvent in the cell. We therefore decided to study sensitization of both semiconductors.

The sensitizer dye in a DSSC must bear some substituent that serves to bind the sensitizer to the semiconductor nanoparticle. Although various choices are possible,[13] we chose to use carboxylic acid moieties, as these have been extensively employed in the DSSC literature.[13,87,199,205] The effect of the position of the anchoring group on the macrocycle has been studied and it has been hypothesized that having the anchoring group at the *meta* position on a *meso*-phenyl group allows the porphyrin to lie flatter on the semiconductor surface than does a substituent at the para position, and that this

increases the efficiency of electron injection.[199,200] Thus, we have studied both **3**$_{Zn}$ and **4**$_{Zn}$ as sensitizers.

For construction of the cells, the photoanode featured nanoparticulate TiO_2 or SnO_2 deposited on glass substrates bearing a coating of conductive fluorine-doped tin oxide (FTO). The sensitizer was deposited on the electrode from solution. The cathode was platinized FTO, the electrolyte was acetonitrile or a mixture of acetonitrile and valeronitrile, the redox mediator was I^-/I_3^-, and the solutions contained Li^+. The cells were prepared using one of two slightly different protocols. Details of cell construction are given in the Experimental Section.

The absorption maxima of the sensitizers on both TiO_2 and SnO_2 were slightly shifted to longer wavelengths relative to the spectra in solution (Table 7). Figure 81a shows the light harvesting efficiency for electrodes sensitized with **3**$_{Zn}$ and **4**$_{Zn}$. The absorption spectra from which these plots were derived were corrected for scatter and absorbance by the unsensitized electrode. The electrodes for the two sensitizers were prepared under identical conditions, but electrodes bearing **4**$_{Zn}$ consistently showed slightly stronger absorption than those sensitized with **3**$_{Zn}$. This is likely because the *para* carboxylate linkage group on **4**$_{Zn}$ allows the molecules to attach to the semiconductor oxide with the macrocycle plane more perpendicular to the local semiconductor surface than does the *meta*-carboxylate linkage in **3**$_{Zn}$, and thus **4**$_{Zn}$ achieves a greater packing density.

Figure 82 shows the current-voltage plots for DSSC with a TiO_2 photoanode sensitized with **3**$_{Zn}$ and two cells with SnO_2 electrodes sensitized with either **3**$_{Zn}$ or **4**$_{Zn}$ and prepared using the electrodes characterized in Figure 81. The TiO_2 cell was prepared according to

protocol 1 (see Experimental Section) and the SnO_2 cells were prepared according to protocol 2. Illumination was with simulated AM 1.5 G sunlight. The TiO_2-based cell produced no significant photocurrent. This is consistent with the positive free energy change for injection of an electron into the conduction band of the semiconductor shown in Table 7.

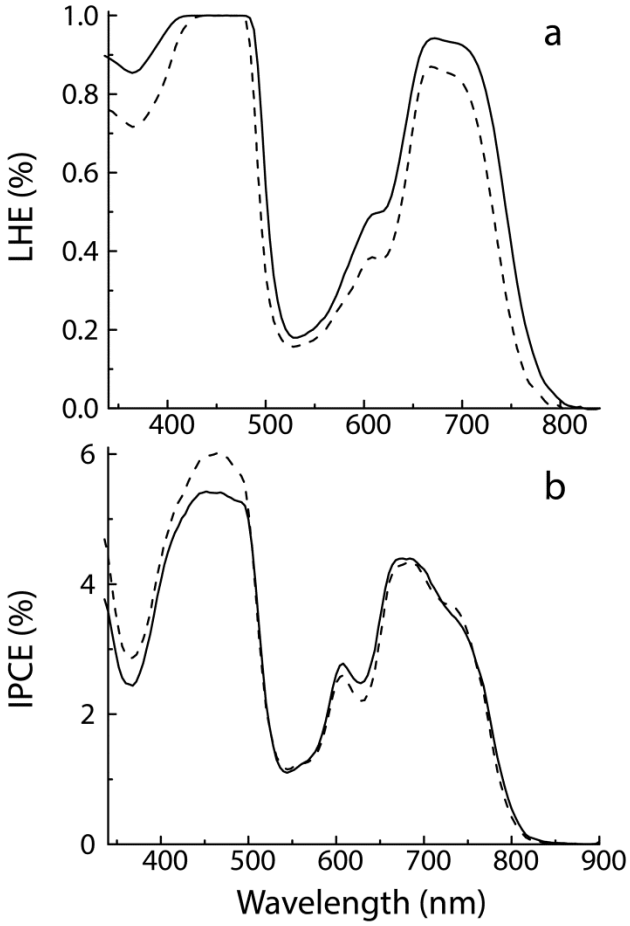

Figure 81. (a) Light harvesting efficiency (LHE) of SnO_2 electrodes bearing $\mathbf{3_{Zn}}$ (dashed) and $\mathbf{4_{Zn}}$ (solid). The absorption spectra were corrected by subtraction of the spectra of the corresponding unsensitized electrodes. (b) Incident photon to current efficiency (IPCE) as a function of wavelength for DSSC constructed using the electrodes whose LHE is shown in (a). The curves are from electrodes bearing $\mathbf{3_{Zn}}$ (dashed) and $\mathbf{4_{Zn}}$ (solid).

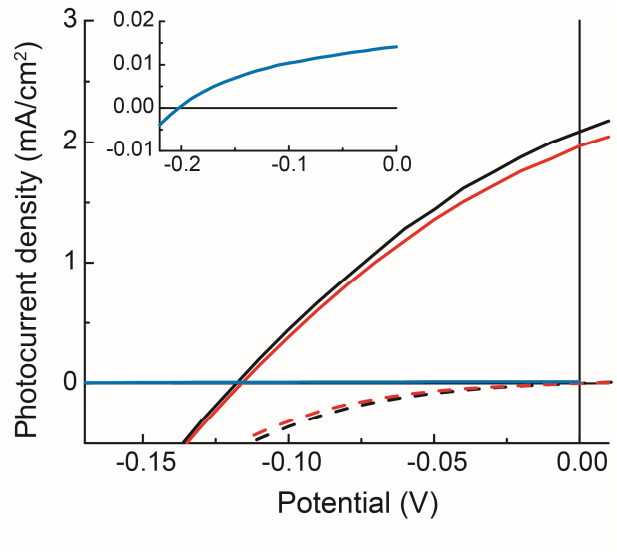

Figure 82. Current density-voltage plots for DSSC with SnO_2 photoanodes sensitized by **3**$_{Zn}$ (red) and **4**$_{Zn}$ (black). The solid lines show performance under illumination (simulated AM 1.5 G solar irradiation) and the dotted lines show behavior in the dark. The blue curves show the behavior of a DSSC using **3**$_{Zn}$ deposited on a TiO_2 electrode. The inset is an expansion of the vertical axis for **3**$_{Zn}$ on TiO_2.

The SnO_2 electrodes, on the other hand, both produced photocurrents. The *para*-linked compound **4**$_{Zn}$ produced slightly more photocurrent than the *meta*-linked **3**$_{Zn}$. For **4**$_{Zn}$, the short-circuit photocurrent density J_{sc} was 2.09 mA cm^{-2} whereas for **3**$_{Zn}$ J_{sc} was 1.97 mA cm^{-2}. The open-circuit voltages V_{oc} for the cells were nearly identical at 0.118 V for **4**$_{Zn}$ and 0.116 V for **3**$_{Zn}$, and the fill factor (FF) was 0.31 for both cells. These values give a slightly higher efficiency η for **4**$_{Zn}$ (0.08 %) than for **3**$_{Zn}$ (0.07 %).

More detailed information concerning performance comes from the incident photon to current efficiency vs. wavelength plots shown in Figure 3b. In the B-band region around 430 nm where both electrodes absorb essentially all of the available photons, *meta* sensitizer **3**$_{Zn}$ performs slightly better than the *para* isomer **4**$_{Zn}$. This increase is consistent with the findings of other workers for other porphyrins sensitizing TiO_2, as

mentioned above.[13,199,200] On the other hand, the *para* isomer **4**$_{Zn}$ has efficiencies comparable to or greater than those of **3**$_{Zn}$ in the region from ca. 550 – 800 nm due to the increased LHE in this spectral region shown in Figure 3a. Thus, in all spectral regions **3**$_{Zn}$ molecules are more efficient than **4**$_{Zn}$ molecules in net electron injection into the cell circuit, but **4**$_{Zn}$ achieves higher packing density on the electrode.

6.4 Conclusions

The purpose of this study was to determine whether porphyrins bearing β-cyano groups could act as sensitizers in DSSC, with a view toward their eventual use in photoelectrosynthetic cells for water splitting or other solar fuel production. The results show that the tetra-β-cyanoporphyrins can inject electrons into the conduction band of nanoparticulate SnO_2, but are not thermodynamically competent to inject into TiO_2. This is due to a combination of the relatively long wavelength absorption of the porphyrin Q-bands, which decreases the energy of the first excited singlet state relative to many other porphyrins, and the high oxidation potentials of these molecules, which is due to the electron withdrawing properties of the cyano groups. These same properties – long wavelength absorption and strong oxidizing power – make the cyanoporphyrins good candidates for use in photoelectrosynthetic cells for solar fuel production. Their redox potentials ensure that their radical cations possess significant overpotential for water oxidation via suitable catalysts. The long wavelength absorption ensures that they can absorb significant amounts of light at longer wavelengths than can most porphyrin sensitizers. These two properties are especially promising for the application of these porphyrins in tandem photoelectrosynthetic cells for solar fuel production.

The performance of the DSSC prepared here is much inferior to that of optimized TiO_2 based cells. The results are similar to those obtained in similarly constructed DSSC with Zn(II) 5-(4-carbomethoxyphenyl)-15-(4-carboxyphenyl)-10,20-bis(pentafluorophenyl)porphyrin.[98] No attempt was made to optimize the cells reported here, but in general, cells made with SnO_2 electrodes perform more poorly than those that use TiO_2.[206,207] Losses in efficiency relative to TiO_2 cells could be related to inefficient injection of electrons into the semiconductor, enhanced recombination between the semiconductor conduction band and the oxidized porphyrin, or enhanced recombination reactions involving the I^-/I_3^- mediator. The use of cobalt complexes as mediators would be expected to increase V_{oc} in such cells.[208]

Future work includes the continuation of the development of a synthetic method to synthesize a CyP with a phosphonate and a malonate group on *meso*-phenyl positions, see Figure 83. These functional groups allow for the anchoring of the porphyrin to both a SnO_2 semiconductor and a water oxidation catalyst such as IrO_2 nH_2O.[209] In order to synthesize this porphyrin it is necessary to develop the synthetic method where addition of the functional groups are interwoven with the steps for the addition of the nitrile substituents so there are few if any side reactions. The beginning steps of the synthetic method has been recently developed, and was guided by previous work on the synthesis of porphyrins with malonate and phosphonate groups by Dr. Jesse Bergkamp, and Dr. Smitha Pillai.

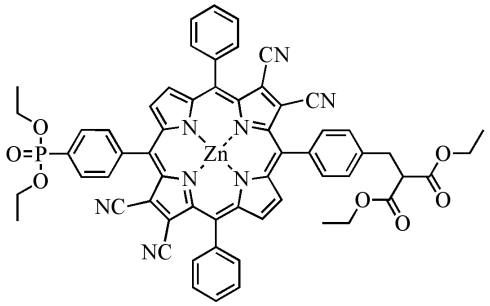

Figure 83. CyP with both a phosphonate and a malonate group.

6.5 Synthesis

6.5.1 General Procedures.

Pyrrole was freshly distilled before use. Dichloromethane was distilled from calcium hydride under nitrogen. Tetrahydrofuran was distilled over sodium and benzophenone under argon. *N*-Bromosuccinimide was obtained from Sigma Aldrich and recrystallized before use. All NMR spectra were recorded on a 400 MHz Varian spectrometer. Samples were dissolved in $CDCl_3$ with TMS as an internal reference, unless otherwise stated. Mass spectra were obtained on an Applied Biosystems Voyager-DE STR matrix-assisted laser desorption/ionization time-of-flight spectrometer (MALDI-TOF). *Trans, trans*-1,4-diphenyl-1,3-butadiene was used as a matrix for the MALDI-TOF-MS measurements, with 5,10,15,20-tetrakis-(4-methylphenyl)porphyrin as the internal reference. Ultraviolet-visible absorption spectra were measured on a Shimazu UV2100U spectrometer. Thin-layer chromatography for dipyrromethanes and porphyrins was performed on silica gel GHFL or GHL plates (Analtech). Synthesis, workup and purification were performed in a darkened laboratory. The preparation of **1**, **1**$_{Zn}$, **3**, **3**$_{Zn}$, **4** and **4**$_{Zn}$ has been reported previously.[137] The preparation of 2,3,11,12-tetrabromo-5,10,15,20-tetrakis-(4-

methylphenyl)porphyrin and 2,3,12-tetrabromo-5,10,15,20-tetrakis-(4-methylphenyl)porphyrin, as an inseparable mixture, has been reported previously.[137]

*6.5.2 Zn(II) 2,3,12–tricyano-5,10,15,20-tetrakis-(4-methylphenyl)porphyrin (**2**$_{Zn}$)*

A inseparable mixture of porphyrin 2,3,11,12-Tetrabromo-5,10,15,20-tetrakis-(4-methylphenyl)porphyrin and 2,3,12-tribromo-5,10,15,20-tetrakis-(4-methylphenyl)porphyrin analog was synthesized as reported previously Ph_3As, and $K_4[Fe(CN)_6]$ were dried overnight under vacuum and all glassware was oven dried overnight. All reagents; the mixture of the two β-brominated porphyrins (350 mg), tris-(dibenzylideneacetone)dipalladium(0) (60mg, 0.066 mmol), triphenylarsine (163 mg, 0.533 mmol), and potassium ferrocyanide (491 mg, 1.33 mmol) were dissolved in dry and deaerated dimethylformamide (20 mL) in a round-bottomed flask equipped with a magnetic stir bar, and under argon. The round bottomed flask was put in an oil bath which was brought to 100 ^{o}C and stirred for 48 h, after which the temperature was increased to 115 ^{o}C and stirring was continued for 7.5 h. The solution was allowed to cool to room temperature, additional tris-(dibenzylideneacetone)dipalladium(0) (60 mg, 0.066mmol) and triphenylarsine (163 mg, 0.533mmol) were added, and the solution was allowed to stir for an additional 48 h at 115 ^{o}C. The solvent was removed by distillation under reduced pressure, and the product was purified by column chromatography on silica gel using 30% hexane in dichloromethane as the eluent. Final purification was done by preparative thin layer chromatography with toluene containing 5% ethyl acetate as the eluent. This chromatography yielded pure **2**$_{Zn}$. mp >300 °C, yield, 23.64 mg (N/A). ^{1}H NMR □ (ppm) 9.39 (s, 1 H), 8.81 - 8.90 (m, 2 H), 8.75 - 8.80 (m, 2 H), 7.98 (d, *J*=7.5

Hz, 2 H), 7.85 - 7.95 (m, 6 H), 7.50 - 7.61 (m, 8 H), 2.68 - 2.74 (m, 12 H); UV-visible λ_{max} (nm, CH_2Cl_2): 444, 632; MALDI-TOF-MS m/z; calcd for $C_{51}H_{33}N_7Zn$ 809.26 [M^+], obsd 807.14.

*6.5.3 2,3,12,–Tricyano-5,10,15,20-tetrakis-(4-methylphenyl)porphyrin (**2**)*

Porphyrin **2Zn** (12 mg, 0.01 mmol) was dissolved in dichloromethane (7 mL) in a round bottomed flask equipped with a magnetic stir bar. Trifluoroacetic acid (0.5 mL) was added and the solution was allowed to stir for 30 min at room temperature. The solution was washed with water (2 × 50 mL), followed by a saturated aqueous solution of $NaHCO_3$ (50 mL). The product was dried over anhydrous sodium sulfate, and the solvent was distilled under reduced pressure. The product was purified by preparative thin layer chromatography using 10% ethyl acetate in toluene as the solvent to give porphyrin **2** as purple crystals, mp >300 °C, yield, 9.5 mg (44%). ^{1}H NMR δ (ppm) 9.293 (s, 1 H, pyrrolic H), 8.969-8.91 (m, 2 H, pyrrolic), 8.861 (d, *J*=2.4 Hz, 1 H, pyrrolic), 8.01-7.97 (m, 8 H, Ar), 7.621-7.565 (m, 8 H, Ar), 2.716-2.687 (m, 12 H, methyl H); UV-visible λ_{max} (nm, CH_2Cl_2): 444, 545, 586, 648, 707; MALDI-TOF-MS m/z; calcd for $C_{51}H_{35}N_7$ 745.87 [M^+], obsd 745.31.

6.6 Electrochemical Experiments

All materials used for electrochemical and photoelectrochemical experiments were obtained from Sigma Aldrich, unless otherwise stipulated. Solvents were distilled prior to use for electrochemical investigations. Tetrabutylammonium hexafluorophosphate was doubly recrystallized from ethanol, and then dried under vacuum at elevated temperature

prior to use as supporting electrolyte. Electrochemical investigations were carried out in distilled dichloromethane with tetrabutylammonium hexafluorophosphate (100 mM) as supporting electrolyte. A platinum disc working electrode in combination with a platinum counter electrode and an Ag^+/Ag quasi-reference was used for all cyclic voltammetry experiments. A CH Instruments 760D potentiostat with included software was used. Prior to taking a voltammogram, the solution was bubbled with argon and then an argon atmosphere was maintained over the cell head space during the measurement. The potentials were derived using the ferrocenium/ferrocene couple as an internal reference, with $E_{Fc+/Fc}$ taken as 0.45 V vs. SCE.[210]

6.6.1 DSSC Preparation and Testing

Two related protocols were used to prepare and evaluate the cells.

Protocol 1. A titanium dioxide based electrode was used for constructing DSSC. Transparent conductive fluorine-doped tin oxide (FTO) glass electrodes (Hartford Glass) were coated with a TiO_2 paste[211] and sintered at 450 °C for 45 min. After sintering, the FTO-semiconductor electrode was allowed to cool in air, and was then immersed in a porphyrin solution in ethyl acetate while still warm. Electrodes were soaked for at least 18 h.

A DSSC was constructed using the TiO_2 electrode in combination with a platinum-coated FTO counter electrode. Heat shrink film (Solaronix) was used to seal the electrodes together. Electrolyte was introduced to the internal volume of the cell via holes drilled in the FTO-Pt counter electrode. The electrolyte consisted of an acetonitrile:valeronitrile (1:1 by volume) mixture containing 0.2 M lithium iodide, 0.05

M iodine, 0.2 M tetrabutylammonium iodide, and 0.5 M 4-*t*-butyl pyridine. A mask with a 0.2 cm^2 opening placed over the solar cell defined the illuminated area used for photo-based measurements. A 350 W Xenon arc lamp (Osram) light source with a 400 nm cutoff filter (Thor Labs) and an AM 1.5 solar spectrum filter (Oriel) was used to provide 100 mW cm^{-2} illumination. The 400 nm cutoff filter was used to avoid direct bandgap excitation of the semiconducting layer. A Keithley sourcemeter was used for photocurrent and photovoltage experiments. A monochromator (Jobin-Yvon) was placed between the Xe lamp and solar cell to provide monochromatic light for incident photon to current (IPCE) measurements. Light intensity at each wavelength used in the IPCE measurements was determined using a silicon photodiode (Newport).

Protocol 2. Conductive FTO-coated glass (TEC 7, Hartford Glass) was cleaned by sonication in acetone and then water, and rinsed with ethanol. Using tape (Scotch® magic tape) as a mask and spacer to outline a defined area on the FTO, a film of SnO_2 paste was spread using a glass rod. The film was dried at 80 ^oC for 9 min, and the process was repeated to produce a double layer. This layer was sintered (temperature ramped from 180 ^oC to 370^oC, held for 10 min, ramped from 180 ^oC to 470 ^oC, held for 30 min, and slowly cooled). An additional SnO_2 layer was added as described above, and the sintering step repeated. The thickness of the nanoparticulate porous SnO_2 films was ~ 12 μm as determined using profilometry (Tencor Alpha-step 200). The colloidal SnO_2 paste used in this experiment was prepared using a modification of the procedure of Ito and co-workers.[48] Acetic acid (200 μL) and water (1 mL) were added to 1.2 g of Sn(IV) oxide nanoparticles (Nanoarc - Alfa Aesar, 13-19 nm). Once the particles were hydrated, 10 mL

of ethanol was added and the mixture was sonicated using a sonic horn (Branson 450 with ¼" tip; 30 s × 3, 50% duty cycle, power level 4). α-Terpineol (4 mL, Alfa Aesar) was added, and the mixture was sonicated using the sonic horn (30 s × 3, 50% duty cycle, power level 4). In 20 mL ethanol was dissolved 300 mg of ethylcellulose (Acros Organics, 22 cps) and 300 mg of ethylcellulose (Acros Organics, 10 cps), and the resulting solution was added to the colloid. The colloid was sonicated using the sonic horn (30 s × 3, 50% duty cycle, power level 4). Under reduced pressure, the volatile ethanol was removed from the colloid by evaporation to yield a viscous paste. The SnO_2 electrodes were sensitized in 0.150 mM solutions of porphyrin in ethyl acetate overnight, rinsed, and dried under a nitrogen atmosphere in the absence of light. A defined electrode area was formed by removal of the undesired SnO_2 film using a plastic razor blade. Platinized FTO was prepared by adding a drop of 20 mM H_2PtCl_6 in ethanol to FTO coated glass (TEC 7, Hartford Glass), drying the glass in air, and then heating it at 450 ^oC for 30 min. A hole was drilled in the FTO to allow for incorporation of electrolyte.

DSSC devices were prepared by sandwiching a 25 μm thermoplastic spacer (Surlyn, Solaronix) between the dye-sensitized electrode and the counter electrode and sealing at 115 ^oC for 45 s. Electrolyte (600 mM LiI, 50 mM I_2, 10 mM *tert*-butylpyridine in acetonitrile) was introduced into the device by vacuum-assisted addition, and the Pt/FTO hole was sealed using Surlyn®.

Incident photon to current efficiency (IPCE) was measured by illumination using monochromatic light from a xenon lamp and single-grating monochromator. Power density was determined using a calibrated silicon diode (Newport 818-UV). Current-

voltage (I-V) curves were obtained under simulated sunlight at 100 mW cm^{-2} at the electrode by filtering light from a xenon arc lamp with an AM 1.5 G filter (Newport Corp). The power density was determined using a calibrated silicon diode (ASTM E948-09 / ASTM E1021-06). The IPCE and I-V data were obtained using a Keithley 2400 sourcemeter and LabView software.

6.7 Acknowledgements

This work was supported by the Office of Basic Energy Sciences, Division of Chemical Sciences, Geosciences, and Energy Biosciences, Department of Energy under contract DE-FG02-03ER15393 and the Center for Bio-Inspired Solar Fuel Production, an Energy Frontier Research Center funded by the U.S. Department of Energy, Office of Science, Office of Basic Energy Sciences under Award Number DE-SC0001016.

CONCLUSION

The research reported in this dissertation primarily expands our knowledge of the synthetic chemistry, electrochemistry, and photochemistry of β-cyanoporphyrins. The results include a new route for the synthesis of CyP that allows for a wider variety of CyP to be synthesized, enabling them to be used in systems for studying several energy and electron transfer processes. The studies are geared toward the conversion of light into electrochemical potential. It was found that CyPs have the potential to be used in photoelectrochemical cells for water oxidation, as determined through a study that used them as sensitizers in a dye sensitized solar cell. One of the distinguishing properties of CyPs is their ability to act as strong electron acceptors, more so than that of fullerenes. Therefore, they can provide a strong driving force in electron transfer systems. This driving force has been used in several studies including in a carotene-CyP dyad synthesized to study electron transfer from a carotene, as well as in a proton-coupled electron transfer system to study light driven water oxidation. The CyPs' high reduction potential led to the design and synthesis of a molecular triad, which enabled the study of a unique electron transfer process from a radical anion of C_{60} to a CyP. The results of these studies show that the CyP can be used as a sensitizer in DSSCs, and potentially for light driven water oxidation. They can also be used as powerful electron acceptors in molecular systems as they can provide a stronger driving force for electron transfer than fullerenes.

REFERENCES

(1) Armaroli, N., and Balzani, V. (2007) The future of energy supply: Challenges and opportunities. *Angew. Chemie - Int. Ed. 46*, 52–66.

(2) Gust, D., Moore, T. A., and Moore, A. L. (2009) Solar fuels via artificial photosynthesis. *Acc. Chem. Res. 42*, 1890–8.

(3) Rockström, J., Steffen, W., Noone, K., Persson, Å., Chapin, F. Stuart, I., Lambin, E. F., Lenton, T. M., Scheffer, M., Folke, C., Schellnhuber, H. J., Nykvist, B., Wit, C. A. de, Hughes, T., Leeuw, S. van der, Rodhe, H., Sverker, S., Snyder, P. K., Costanza, R., Svedin, U., Falkenmark, M., Karlberg, L., Corell, R. W., Fabry, V. J., Hansen, J., Walker, B., Liverman, D., Richardson, K., Crutzen, P., and Foley, J. A. (2009) A safe operating space for humanity. *Nature 461*.

(4) Hambourger, M., Moore, G. F., Kramer, D. M., Gust, D., Moore, A. L., and Moore, T. A. (2009) Biology and Technology for Photochemical Fuel Production. *Chem. Soc. Rev. 38*, 25–35.

(5) Sherman, B. D., Vaughn, M. D., Bergkamp, J. J., Gust, D., Moore, A. L., and Moore, T. A. (2014) Evolution of reaction center mimics to systems capable of generating solar fuel. *Photosynth. Res. 120*, 59–70.

(6) Hansen, J., Sato, M., Kharecha, P., Beerling, D., Berner, R., Masson-Delmotte, V., Pagani, M., Raymo, M., Royer, D. L., and Zachos, J. C. (2008) Target atmospheric CO2: Where should humanity aim? *Open Atmos. Sci. J. 2*, 217–231.

(7) Hansen, J., Nazarenko, L., Ruedy, R., Sato, M., Willis, J., Del Genio, A., Koch, D., Lacis, A., Lo, K., Menon, S., Novakov, T., Perlwitz, J., Russell, G., Schmidt, G. a, and Tausnev, N. (2005) Earth's energy imbalance: confirmation and implications. *Science 308*, 1431–1435.

(8) Antoniuk Pablant, N. (2010) Development of the B-Stark motional Stark effect diagnostic for measurements of the internal magnetic field in the DIII-D tokamak.

(9) Shah, A., Torres, P., Tscharner, R., Wyrsch, N., and Keppner, H. (1999) Photovoltaic Technology: The Case for Thin-Film Solar Cells. *Science (80-.). 285*, 692–698.

(10) Grätzel, M. (2001) Photoelectrochemical cells. *Nature 414*, 338–344.

(11) Imahori, H., Umeyama, T., and Ito, S. (2009) Large pi-aromatic molecules as potential sensitizers for highly efficient dye-sensitized solar cells. *Acc. Chem. Res. 42*, 1809–18.

(12) Halme, J., Vahermaa, P., Miettunen, K., and Lund, P. (2010) Device physics of dye solar cells. *Adv. Mater. 22*, E210–34.

(13) Campbell, W. M., Burrell, A. K., Officer, D. L., and Jolley, K. W. (2004) Porphyrins as light harvesters in the dye-sensitised TiO2 solar cell. *Coord. Chem. Rev. 248*, 1363–1379.

(14) Higashino, T., and Imahori, H. (2015) Porphyrins as excellent dyes for dye-sensitized solar cells: recent developments and insights. *Dalt. Trans. 44*, 448–463.

(15) Mathew, S., Yella, A., Gao, P., Humphry-Baker, R., Curchod, B. F. E., Ashari-Astani, N., Tavernelli, I., Rothlisberger, U., Nazeeruddin, M. K., and Grätzel, M. (2014) Dye-sensitized solar cells with 13% efficiency achieved through the molecular engineering of porphyrin sensitizers. *Nat. Chem. 6*, 242–7.

(16) Pagliaro, M., Konstandopoulos, A. G., Ciriminna, R., and Palmisano, G. (2010) Solar hydrogen: fuels of the near future. *Energy Environ. Sci. 3*, 279.

(17) Gust, D., Moore, T. A., and Moore, A. L. (2012) Realizing artificial photosynthesis. *Faraday Discuss. 155*, 9–26.

(18) Dau, H., and Zaharieva, I. (2009) Principles, efficiency, and blueprint character of solar-energy conversion in photosynthetic water oxidation. *Acc. Chem. Res. 42*, 1861–70.

(19) Youngblood, W. J., Lee, S.-H. A., Maeda, K., and Mallouk, T. E. (2009) Visible light water splitting using dye-sensitized oxide semiconductors. *Acc. Chem. Res. 42*, 1966–73.

(20) Song, W., Chen, Z., Glasson, C. R. K., Hanson, K., Luo, H., Norris, M. R., Ashford, D. L., Concepcion, J. J., Brennaman, M. K., and Meyer, T. J. (2012) Interfacial dynamics and solar fuel formation in dye-sensitized photoelectrosynthesis cells. *ChemPhysChem 13*, 2882–2890.

(21) Blankenship, R. E. (2001) Molecular Mechanisms of Photosynthesis. Oxford: Blackwell Science Ltd.

(22) Ohkubo, K., and Fukuzumi, S. (2008) Long-lived charge-separated states of simple electron donor-acceptor dyads using porphyrins and phthalocyanines. *J. Porphyr. Phthalocyanines 12*, 993–1004.

(23) Imahori, H., and Sakata, Y. (1999) Fullerenes as Novel Acceptors in Photosynthetic Electron Transfer Hiroshi Imahori and Yoshiteru Sakata. *European J. Org. Chem.* 2445–2457.

(24) Palacios, R. E., Gould, S. L., Herrero, C., Hambourger, M., Brune, A., Kodis, G., Liddell, P. a., Kennis, J., Macpherson, A. N., Gust, D., Moore, T. a., and Moore, A. L. (2005) Bioinspired energy conversion. *Pure Appl. Chem. 77*, 1001–1008.

(25) Kuciauskas, D., Liddell, P. a., Lin, S., Johnson, T. E., Weghorn, S. J., Lindsey, J. S., Moore, A. L., Moore, T. a., and Gust, D. (1999) An artificial photosynthetic antenna-reaction center complex. *J. Am. Chem. Soc. 121*, 8604–8614.

(26) Gust, D., Moore, T. A., and Moore, A. L. (2001) Mimicking photosynthetic solar energy transduction. *Acc. Chem. Res. 34*, 40–48.

(27) Petke, J. D., and Maggiora, G. M. (1986) Nature and location of excited charge-transfer states in porphyrin dimers: Development of preliminary design characteristics for biomimetic solar energy conversion systems. *J. Chem. Phys. 84*, 1640.

(28) Imahori, H. (2004) Porphyrin – fullerene linked systems as artificial photosynthetic mimics. *Org. Biomol. Chem. 2*, 1425–1433.

(29) Guldi, D. M. (2002) Fullerene-porphyrin architectures; photosynthetic antenna and reaction center models. *Chem. Soc. Rev. 31*, 22–36.

(30) Gust, D., and Moore, T. A. (1989) Mimicking Photosynthesis. *Science (80-.). 244*, 35–41.

(31) Youngblood, W. J., Lee, S.-H. A., Kobayashi, Y., Hernandez-Pagan, E. A., Hoertz, P. G., Moore, T. A., Moore, A. L., Gust, D., and Mallouk, T. E. (2009) Photoassisted overall water splitting in a visible light-absorbing dye-sensitized photoelectrochemical cell. *J. Am. Chem. Soc. 131*, 926–7.

(32) Alibabaei, L., Brennaman, M. K., Norris, M. R., Kalanyan, B., Song, W., Losego, M. D., Concepcion, J. J., Binstead, R. a., Parsons, G. N., and Meyer, T. J. (2013) Solar Water Splitting in a Molecular Photoelectrochemical Cell. *Proc. Nat. Acad. Sci. USA 110*, 20008–20013.

(33) Li, L.-L., and Diau, E. W.-G. (2013) Porphyrin-sensitized solar cells. *Chem. Soc. Rev.* 291–304.

(34) Maeda, K., Teramura, K., Lu, D., Takata, T., Saito, N., Inoue, Y., and Domen, K. (2006) Photocatalyst releasing hydrogen from water. *Nature 440*, 295.

(35) Loewe, R. S., Lammi, R. K., Diers, J. R., Kirmaier, C., Bocian, D. F., Holten, D., and Lindsey, J. S. (2002) Design and synthesis of light-harvesting rods for intrinsic rectification of the migration of excited-state energy and ground-state holes. *J. Mater. Chem. 12*, 1530–1552.

(36) Walter, M. G., Rudine, A. B., and Wamser, C. C. (2010) Porphyrins and phthalocyanines in solar photovoltaic cells. *J. Porphyr. Phthalocyanines 14*, 759–792.

(37) Grätzel, M. (2003) Dye-sensitized solar cells. *J. Photochem. Photobiol. C Photochem. Rev. 4*, 145–153.

(38) Snaith, H. J. (2010) Estimating the Maximum Attainable Efficiency in Dye-Sensitized Solar Cells. *Adv. Funct. Mater. 20*, 13–19.

(39) Anslyn, E. V., and Dougherty, D. A. (2006) Modern Physical Organic Chemistry. University Science Books.

(40) Jablonski, A. (1933) Efficiency of Anti-Stokes Fluorescence in Dyes. *Nature 131*, 839–840.

(41) Kasha. (1999) From Jablonski to femtoseconds. Evolution of Molecular Photophysics. *Acta Phys. Pol. A 95*, 15.

(42) Closs, G. L., and Miller, J. R. (1988) Intramolecular Long-Distance Electron Transfer in Organic Molecules. *Science (80-.). 240*, 440–447.

(43) Gilbert, M., and Albinsson, B. (2015) Photoinduced charge and energy transfer in molecular wires. *Chem. Soc. Rev. 44*, 845–862.

(44) Marcus, R. A., and Sutin, N. (1985) Electron transfers in chemistry and biology. *Biochim. Biophys. Acta 811*.

(45) Marcus, R. A. (1959) On the theory of electrochemical and chemical electron transfer processes. *Can. J. Chem. 37*.

(46) Hush, N. S. (1961) Adiabatic Theory of Outer Sphere Electron-Transfer Reactions in solution. *Trans. Faraday Soc. 57*.

(47) Levich, V. (1966) Present state of the theory of oxidation-reduction in solution (bulk and electrode reactions). *Adv. Electrochem. Electrochem. Eng. 4*, 249.

(48) Marcus, R. A. (1993) Electron Transfer Reactions in Chemistry. Theory and Experiment. *Angew. Chemie Int. Ed. 32*, 1111–1121.

(49) Lemmetyinen, H., Tkachenko, N., Efimov, A., and Niemi, M. (2009) Transient states in photoinduced electron transfer reactions of porphyrin- and phthalocyanine-fullerene dyads. *J. Porphyr. Phthalocyanines 13*, 1090–1097.

(50) Bard, A. J., and Faulkner, L. R. (2001) Electrochemical Methods Fundamentals and Applications 2nd ed. John Wiley and Sons, Inc.

(51) Rizzi, A. C., Gastel, M. Van, Liddell, P. a, Palacios, R. E., Moore, G. F., Kodis, G., Moore, A. L., Moore, T. a, Gust, D., and Braslavsky, S. E. (2008) Entropic changes control the charge separation process in triads mimicking photosynthetic charge separation. *J. Phys. Chem. A 112*, 4215–23.

(52) Gust, D. (1997) Very small arrays. *Nature 386*.

(53) El-Khouly, M. E., Han, K.-J., Kay, K.-Y., and Fukuzumi, S. (2010) Stabilization of the charge-separated States of covalently linked zinc porphyrin-triphenylamine-[60]fullerene. *Chemphyschem 11*, 1726–1734.

(54) Kodis, G., Liddell, P. a., Moore, A. L., Moore, T. a., and Gust, D. (2004) Synthesis and photochemistry of a carotene-porphyrin-fullerene model photosynthetic reaction center. *J. Phys. Org. Chem. 17*, 724–734.

(55) Imahori, H., Hagiwara, K., Aoki, M., Akiyama, T., Taniguchi, S., Okada, T., Shirakawa, M., and Sakata, Y. (1996) Linkage and Solvent Dependence of Photoinduced Electron Transfer in Zincporphyrin-C60 Dyads. *J. Am. Chem. Soc. 118*, 11771–11782.

(56) Imahori, H., and Sakata, Y. (1997) Donor-Linked Fullerenes: Photoinduced electron transfer and its potential application. *Adv. Mater. 9*, 537–546.

(57) Hauke, F., Atalick, S., Guldi, D. M., and Hirsch, A. (2006) Covalently linked heterofullerene-porphyrin conjugates; new model systems for long-lived intramolecular charge separation. *Tetrahedron 62*, 1923–1927.

(58) Di Valentin, M., Bisol, A., Agostini, G., and Carbonera, D. (2005) Electronic coupling effects on photoinduced electron transfer in carotene-porphyrin-fullerene triads detected by time-resolved EPR. *J. Chem. Inf. Model. 45*, 1580–1588.

(59) Hiroshi, I., Kiyoshi, H., Tsuyoshi, A., Masanori, A., Seiji, T., Tadashi, O., Masahiro, S., and Yoshiteru, S. (1996) The small reorganization energy of C60 in electron transfer. *Chem. Phys. Lett. 263*, 545–550.

(60) Fukuzumi, S., Hasobe, T., Ohkubo, K., Crossley, M. J., Kamat, P. V., and Imahori, H. (2004) π-Complex formation in electron-transfer reactions of porphyrins. *J. Porphyr. Phthalocyanines 08*, 191–200.

(61) Accorsi, G., and Armaroli, N. (2010) Taking Advantage of the Electronic Excited States of [60] -Fullerenes. *J. Phys. Chem. C 114*, 1385–1403.

(62) Arbogast, J. W., Darmanyan, A. P., Foote, C. S., Rubin, Y., Diederich, F. N., Alvarez, M. M., Anz, S. J., and Whetten, R. L. (1991) Photophysical Properties of C60. *J. Phys. Chem.* 11–12.

(63) Lin, S.-K., Shiu, L.-L., Chien, K.-M., Luh, T.-Y., and Lin, T.-I. (1995) Fluorescence of fullerene derivatives at room temperature. *J. Phys. Chem. 99*, 105–111.

(64) El-Khouly, M. E., Ito, O., Smith, P. M., and D'Souza, F. (2004) Intermolecular and supramolecular photoinduced electron transfer processes of fullerene-porphyrin/phthalocyanine systems. *J. Photochem. Photobiol. C Photochem. Rev. 5*, 79–104.

(65) Cho, Y., Ahn, T. K., Song, H., Kim, K. S., Lee, C. Y., Seo, W. S., Lee, K., Kim, S. K., Kim, D., and Park, J. T. (2005) Unusually High Performance Photovoltaic Cell Based on a [60] Fullerene Metal Cluster - Porphyrin Dyad SAM on an ITO Electrode. *J. Am. Chem. Soc. 127*, 2380–2381.

(66) Prato, M., Maggini, M., Giacometti, C., Scorrano, G., Sandonà, G., and Farnia, G. (1996) Synthesis and electrochemical properties of substituted fulleropyrrolidines. *Tetrahedron 52*, 5221–5234.

(67) Maggini, M., Scorrano, G., and Prato, M. (1993) Addition of Azomethine Ylides to C60: Synthesis, Characterization, and Functionalization of Fullerene Pyrrolidines *115*, 9798–9799.

(68) Prato, M., and Maggini, M. (1998) Fulleropyrrolidines: A Family of Full-Fledged Fullerene Derivatives. *Acc. Chem. Res. 31*, 519–526.

(69) Burrell, A. K., Officer, D. L., Plieger, P. G., and Reid, D. C. W. (2001) Synthetic Routes to Multiporphyrin Arrays. *Chem. Rev. 101*, 2751–2796.

(70) D'Souza, F., and Ito, O. (2009) Supramolecular donor-acceptor hybrids of porphyrins/phthalocyanines with fullerenes/carbon nanotubes: electron transfer, sensing, switching, and catalytic applications. *Chem. Commun. 0*, 4913–4928.

(71) Fukuzumi, S. (2000) Electron Transfer Chemistry of Porphyrins and Metalloporphyrins. *Porphyr. Handb. 8*, 115–151.

(72) Guldi, D. M., and Fukuzumi, S. (2002) Electron transfer in electron donor-acceptor ensembles containing porphyrins and metalloporphyrins. *J. Porphyr. Phthalocyanines 06*, 289–295.

(73) Gust, D. (2000) Intramolecular photoinduced electron-transfer reactions of porphyrins. *Porphyr. Handb. 8*, 154–190.

(74) Sakata, Y., Imahori, H., and Sugiura, K.-I. (2001) Molecule-Based Artificial Photosynthesis. *J. Incl. Phenom. Macrocycl. Chem. 41*, 31–36.

(75) Schuster, D. I. (2000) Synthesis and photophysics of new types of fullerene–porphyrin dyads. *Carbon N. Y. 38*, 1607–1614.

(76) Wasielewski, M. R. (1992) Photoinduced electron transfer in supramolecular systems for artificial photosynthesis. *Chem. Rev. 92*, 435–461.

(77) Robertson, N. (2006) Optimizing dyes for dye-sensitized solar cells. *Angew. Chem. Int. Ed. Engl. 45*, 2338–45.

(78) Littler, J., Ciringh, Y., and Lindsey, J. S. (1999) Investigation of conditions giving minimal scrambling in the synthesis of trans-porphyrins from dipyrromethanes and aldehydes. *J. Org. Chem 64*, 2864–2872.

(79) Moore, G. F., Hambourger, M., Gervaldo, M., Poluektov, O. G., Rajh, T., Gust, D., Moore, T. A., and Moore, A. L. (2008) A Bioinspired Construct that Mimics the Proton Coupled Electron Transfer Between P680*+ and the Tyr(Z)-His190 Pair of Photosystem II. *J. Am. Chem. Soc. 130*, 10466–7.

(80) Crossley, M., Burn, P., Chew, S., Cuttance, B., and Newsom, I. (1991) Regiospecific introduction of four substituents to porphyrin systems at antipodal pyrrolenic positions. *J. Chem. Soc. Chem. Commun.* 1564.

(81) Bhyrappa, P., Velkannan, V., Karunanithi, K., Varghese, B., and Harikrishna. (2008) Regioselective Synthesis of Antipodal beta-tetrabrominated meso-tetraarylporphyrins. *Bull. Chem. Soc. Jpn. 81*, 995–1001.

(82) Gouterman, M. (1961) Spectra of porphyrins. *J. Mol. Spectrosc. 6*, 138–163.

(83) Kadish, K. M., Smith, K. M., and Guilard, R. (2003) The Porphyrin Handbook: Multiporphyrins, multiphthalocyanines, and arrays.

(84) Spellane, P. J., Gouterman, M., Antipas, a, Kim, S., and Liu, Y. C. (1980) Porphyrins. 40. Electronic spectra and four-orbital energies of free-base, zinc, copper, and palladium tetrakis(perfluorophenyl)porphyrins. *Inorg. Chem. 19*, 386–391.

(85) Gouterman, M. (1959) Study of the Effects of Substitution on the Absorption Spectra of Porphin. *J. Chem. Phys. 30*, 1139.

(86) Nemykin, V. N., and Hadt, R. G. (2010) Interpretation of the UV - Vis spectra of the meso (ferrocenyl)-containing porphyrins using a TDDFT approach: Is Gouterman's classic four-orbital model still in play? *J. Phys. Chem. A 114*, 12062–12066.

(87) Ma, R., Guo, P., Cui, H., Zhang, X., Nazeeruddin, M. K., and Grätzel, M. (2009) Substituent Effect on the meso-substituted Porphyrins: Theoretical Screening of Sensitizer Candidates for Dye-sensitized Solar Cells. *J. Phys. Chem. A 113*, 10119–24.

(88) Uttamlal, M., and Sheila Holmes-Smith, a. (2008) The excitation wavelength dependent fluorescence of porphyrins. *Chem. Phys. Lett. 454*, 223–228.

(89) Kadish, K. M., and Caemelbecke, E. Van. (2003) Electrochemistry of porphyrins and related macrocycles. *J. Solid State Electrochem. 7*, 254–258.

(90) D'Souza, F., Zandler, M. E., Tagliatesta, P., Ou, Z., Shao, J., Van Caemelbecke, E., and Kadish, K. M. (1998) Electronic, Spectral, and Electrochemical Properties of (TPPBr(x)())Zn Where TPPBr(x)() Is the Dianion of beta-Brominated-Pyrrole Tetraphenylporphyrin and x Varies from 0 to 8. *Inorg. Chem. 37*, 4567–4572.

(91) Ou, Z., Shao, J., D'Souza, F., Tagliatesta, P., and Kadish, K. M. (2004) Beta-pyrrole brominated meso-Tetraphenylporphyrins: Synthesis, Spectral and Electrochemical Properties. *J. Porphyr. Phthalocyanines 08*, 201–214.

(92) Lindsey, J. S. (2010) Synthetic Routes to meso -Patterned Porphyrins. *Acc. Chem. Res. 43*.

(93) Hsieh, C.-P., Lu, H.-P., Chiu, C.-L., Lee, C.-W., Chuang, S.-H., Mai, C.-L., Yen, W.-N., Hsu, S.-J., Diau, E. W.-G., and Yeh, C.-Y. (2010) Synthesis and characterization of porphyrin sensitizers with various electron-donating substituents for highly efficient dye-sensitized solar cells. *J. Mater. Chem. 20*, 1127.

(94) Santos, T. Dos, Morandeira, A., Koops, S., Mozer, A. J., Tsekouras, G., Dong, Y., Wagner, P., Wallace, G., Earles, J. C., Gordon, K. C., Officer, D., and Durrant, J. R. (2010) Injection limitations in a series of porphyrin dye-sensitized solar cells. *J. Phys. Chem. C 114*, 3276–3279.

(95) Giraudeau, A., Callot, H. J., and Gross, M. (1979) Effects of Electron-Withdrawing Substituents on the Electrochemical Oxidation of Porphyrins. *Inorg. Chem. 18*, 201–206.

(96) Bhyrappa, P., Sankar, M., and Varghese, B. (2006) Mixed substituted porphyrins: structural and electrochemical redox properties. *Inorg. Chem. 45*, 4136–49.

(97) Bhyrappa, P., and Krishnan, V. (1991) Octabromotetraphenylporphyrin and its metal derivatives: Electronic structure and electrochemical properties. *Inorg. Chem. 30*, 239–245.

(98) Moore, G. F., Konezny, S. J., Song, H., Milot, R. L., Blakemore, J. D., Lee, M. L., Batista, V. S., Schmuttenmaer, C. a., Crabtree, R. H., and Brudvig, G. W. (2012) Bioinspired High-Potential Porphyrin Photoanodes. *J. Phys. Chem. C 116*, 4892–4902.

(99) Tagliatesta, P., Li, J., Autret, M., Caemelbecke, V. E., Villard, A., D'Souza, F., and Kadish, K. M. (1996) Electrochemistry and Spectral Characterization of Oxidized and

Reduced (TPPBr(x)())FeCl Where TPPBr(x)() Is the Dianion of beta-Brominated-Pyrrole Tetraphenylporphyrin and x Varies from 0 to 8. *Inorg. Chem. 35*, 5570–5576.

(100) Ochsenbein, P., Ayougou, K., Mandon, D., Fischer, J., Weiss, R., Austin, R. N., Jayaraj, K., Gold, A., Terner, J., and Fajer, J. (1994) Conformational Effects on the Redox Potentials of Tetraarylporphyrins Halogenated at the beta-Pyrrole Positions. *Angew. Chem. Int. Ed. Engl. 33*, 348–350.

(101) Kadish, K. M., Li, J., Caemelbecke, E. Van, Ou, Z., Guo, N., Autret, M., Souza, F. D., and Tagliatesta, P. (1997) Electrooxidation of Cobalt (II) -Brominated-Pyrrole Tetraphenylporphyrins in CH 2 Cl 2 under an N 2 or a CO Atmosphere. *Inorg. Chem. 36*, 6292–6298.

(102) Giraudeau, A., Callot, H. J., Jordan, J., Ezhar, I., and Gross, M. (1979) Substituent Effects in the Electroreduction of Porphyrins and Metalloporphyrins. *J. Am. Chem. Soc.* 3857–3862.

(103) Liddell, P. A., Sumida, J. P., Macpherson, A. N., Noss, L., Seely, G. R., Clark, K. N., Moore, A. L., Moore, T. A., and Gust, D. (1994) Preparation and photophysical studies of porphyrin-C60 dyads. *Photochem. Photobiol. 60*, 537–541.

(104) Drovetskaya, T., Reed, C. A., and Boyd, P. (1995) A Fullerene Porphyrin Conjugate. *Tetrahedron Lett. 36*, 7971–7974.

(105) Kuciauskas, D., Lin, S., Seely, G. R., Moore, A. L., Moore, T. A., Gust, D., Drovetskaya, T., Reed, C. A., and Boyd, P. D. W. (1996) Energy and Photoinduced Electron Transfer in Porphyrin−Fullerene Dyads. *J. Phys. Chem. 100*, 15926–15932.

(106) Imahori, H. (1996) Synthesis of Closely spaced Porphyrin-Fullerene. *Chem. Lett.* 199.

(107) Kuciauskas, D., Liddell, P. A., Lin, S., Stone, S. G., Moore, A. L., Moore, T. A., and Gust, D. (2000) Photoinduced Electron Transfer in Carotenoporphyrin−Fullerene Triads: Temperature and Solvent Effects. *J. Phys. Chem. B 104*, 4307–4321.

(108) Moore, T. A., Gust, D., Mathis, P., Mialocq, J.-C., Chachate, C., Bensasson, R. V., Land, E. J., Doizi, D., Liddell, Paul, A., Lehman, W., Nemeth, G. A., and Moore, A. L. (1984) Photodriven charge separation in a carotenoporphyrin-quinone triad. *Nature 307*.

(109) Kong, J. L. Y., and Loach, P. A. (1978) Covalently-linked porphyrin quinone complexes as RC models. *Front. Biol. Energ. 1*, 73–82.

(110) Tabushi, I., Koga, N., and Yanagita, M. (1979) Efficient intramolecular quenching and electron transfer in tetraphenylporphyrin attached with benzoquinone or hydroquinone as a photosystem model. *Tetrahedron Lett. 3*, 257–260.

(111) Liddell, P. A., Kuciauskas, D., Sumida, J. P., Nash, B., Nguyen, D., Moore, A. L., Moore, T. A., and Gust, D. (1997) Photoinduced charge separation and charge recombination to a triplet state in a carotene-porphyrin-fullerene triad. *J. Am. Chem. Soc. 119*, 1400–1405.

(112) Marcus, R. A. (1964) Chemical and electrochemical electron transfer theory. *Annu. Rev. Phys. Chem. 15*, 155.

(113) Ou, Z., Shao, J., D'Souza, F., Tagliatesta, P., and Kadish, K. (2004) No Title. *J. Porphyr. Phthalocyanines 8*, 201.

(114) Liu, C., and Chen, Q.-Y. (2005) Fluoroalkylation of Porphyrins: A Facile Synthesis of Trifluoromethylated Porphyrins by a Palladium-Catalyzed Cross-Coupling Reaction. *European J. Org. Chem.* 3680–3686.

(115) Hioki, H., Nakaoka, R., Maruyama, A., and Kodama, M. (2001) Palladium-catalyzed cyanation of bromocalix[4]arenes at the upper rim. *J. Chem. Soc. Perkin Trans. 1* 3265–3268.

(116) Anbarasan, P., Schareina, T., and Beller, M. (2011) Recent developments and perspectives in palladium-catalyzed cyanation of aryl halides: synthesis of benzonitriles. *Chem. Soc. Rev. 40*, 5049–67.

(117) Ryberg, P. (2008) Development of a Mild and Robust Method for Large-Scale Palladium-Catalysed Cyanation of Aryl Bromides: Importance of the Order of Addition. *Org. Process Res. Dev. 12*, 540–543.

(118) Buono, F. G., Chidambaram, R., Mueller, R. H., and Waltermire, R. E. (2008) Insights into palladium-catalyzed cyanation of bromobenzene: additive effects on the rate-limiting step. *Org. Lett. 10*, 5325–8.

(119) Zawisza, A. M., and Muzart, J. (2007) Pd-catalyzed reduction of aryl halides using dimethylformamide as the hydride source. *Tetrahedron Lett. 48*, 6738–6742.

(120) Dobbs, K. D., Marshall, W. J., and Grushin, V. V. (2007) Why excess cyanide can be detrimental to Pd-catalyzed cyanation of haloarenes. Facile formation and characterization of [Pd(CN)(3)(H)](2-) and [Pd(CN)(3)(Ph)](2-). *J. Am. Chem. Soc. 129*, 30–1.

(121) Schareina, T., Zapf, A., Mägerlein, W., Müller, N., and Beller, M. (2007) A State-of-the-art Cyanation of Aryl Bromides: a Novel and Versatile Copper Catalyst System Inspired by Nature. *Chem. Eur. J. 13*, 6249–54.

(122) Chidambaram, R. (2004) A robust palladium-catalyzed cyanation procedure: beneficial effect of zinc acetate. *Tetrahedron Lett. 45*, 1441–1444.

(123) Schareina, T., Zapf, A., and Beller, M. (2004) Improving palladium-catalyzed cyanation of aryl halides: development of a state-of-the-art methodology using potassium hexacyanoferrate(II) as cyanating agent. *J. Organomet. Chem. 689*, 4576–4583.

(124) Sundermeier, M., Mutyala, S., Zapf, A., Spannenberg, A., and Beller, M. (2003) A convenient and efficient procedure for the palladium-catalyzed cyanation of aryl halides using trimethylsilylcyanide. *J. Organomet. Chem. 684*, 50–55.

(125) Sundermeier, M., Zapf, A., and Beller, M. (2003) Palladium-Catalyzed Cyanation of Aryl Halides: Recent Developments and Perspectives. *Eur. J. Inorg. Chem.* 3513–3526.

(126) Maligres, P. E., Waters, M. S., Fleitz, F., and Askin, D. (1999) A highly catalytic robust palladium catalyzed cyanation of aryl bromides. *Tetrahedron Lett. 40*, 8193–8195.

(127) Chatani, N., and Hanafusa, T. (1986) Palladium-Catalyzed Cyanation of Aryl Halides by Trimethylsilyl Cyanide *51*, 4714–4716.

(128) Ellis, G. P., and Romney-Alexander, T. M. (1987) Cyanation of Aromatic Halides. *Chem. Rev. 87*, 779–794.

(129) Kubota, H., and Rice, K. C. (1998) Palladium-catalyzed cyanation of hindered, electron-rich aryl triflates by zinc cyanide. *Tetrahedron Lett. 39*, 2907–2910.

(130) Jin, F., and Confalone, P. N. (2000) Palladium-catalyzed cyanation reactions of aryl chlorides. *Tetrahedron Lett. 41*, 3271–3273.

(131) Marcantonio, K. M., Frey, L. F., Liu, Y., Chen, Y., Strine, J., Phenix, B., Wallace, D. J., and Chen, C. (2004) An investigation into causes and effects of high cyanide levels in the palladium-catalyzed cyanation reaction. *Org. Lett. 6*, 3723–5.

(132) Hatsuda, M., and Seki, M. (2005) A practical synthesis of highly functionalized aryl nitriles through cyanation of aryl bromides employing heterogeneous Pd/C: in quest of an industrially viable process. *Tetrahedron 61*, 9908–9917.

(133) Tschaen, D. M., Desmond, R., King, A. O., Fortin, M. C., Pipik, B., King, S., and Verhoeven, T. R. (1994) An Improved Procedure for Aromatic Cyanation. *Synth. Commun. 24*, 887–890.

(134) Sundermeier, M., Zapf, A., Mutyala, S., Baumann, W., Sans, J., Weiss, S., and Beller, M. (2003) Progress in the palladium-catalyzed cyanation of aryl chlorides. *Chemistry 9*, 1828–36.

(135) Imahori, H., Tamaki, K., Guldi, D. M., Luo, C., Fujitsuka, M., Ito, O., Sakata, Y., and Fukuzumi, S. (2001) Modulating Charge Separation and Charge Recombination

Dynamics in Porphyrin-Fullerene Linked Dyads and Triads: Marcus-Normal versus Inverted Region. *J. Am. Chem. Soc. 123*, 2607–2617.

(136) Antoniuk-Pablant, A., Brennan, B. J., Sherman, B. D., Brudvig, G. W., Moore, A. L., Moore, T. A., and Gust, D. (2015) β-Cyano substituted porphyrins as sensitizers in photoelectrochemical devices. *In Print*.

(137) Antoniuk-Pablant, A., Terazono, Y., Megiatto, J. D., Sherman, B. D., Moore, A. L., Moore, T. A., and Gust, D. (2015) New Synthetic Method for beta-Cyano Substituted Porphyrins. *Tetrahedron*.

(138) Strecker, A. (1850) Ueber die künstliche Bildung der Milchsäure und einen neuen, dem Glycocoll homologen Körper. *Justus Liebigs Ann. Chem. 75*, 27–45.

(139) Liu, G., Khlobystov, A. N., Charalambidis, G., Coutsolelos, A. G., Briggs, G. A. D., and Porfyrakis, K. (2012) N@C 60-porphyrin: A dyad of two radical centers. *J. Am. Chem. Soc. 134*, 1938–1941.

(140) Greenlee, W. J. (1984) Synthesis of beta, gamma-unsaturated amino acids by the strecker reaction. *J. Org. Chem 49*, 2632–2634.

(141) Bandyopadhyay, D., Velazquez, J. M., and Banik, B. K. (2011) A truly green synthesis of α-aminonitriles via Strecker reaction. *Org. Med. Chem. Lett. 1*, 11.

(142) Schonberg, A., and Moubacher, R. (1951) The Strecker Degradation of alpha-Amino Acids. *Chem. Rev. 50*, 261–277.

(143) Ben-Ishai, D., Altman, J., and Peled, N. (1977) The synthesis of p-substituted D,L-Phenylglycines by the Amidoalkylation of Benzylchloride and N-Benzylbenzamide. *Tetrahedron 33*, 2715–2717.

(144) Echegoyen, L., Diederich, F. N., and Echegoyen, L. E. (2000) Electrochemistry of Fullerenes. *Fullerenes Chem. physics, Technol. 1*.

(145) Bahr, J., Kuciauskas, D., Liddell, P., Moore, A., Moore, T., and Gust, D. (2000) Driving force and electronic coupling effects on photoinduced electron transfer in a fullerene-based molecular triad. *J. Photochem. Photobiol. 72*, 598–611.

(146) Megiatto, J. D., Antoniuk-Pablant, A., Sherman, B. D., Kodis, G., Gervaldo, M., Moore, T. A., Moore, A. L., and Gust, D. (2012) Mimicking the electron transfer chain in photosystem II with a molecular triad thermodynamically capable of water oxidation. *Proc. Natl. Acad. Sci. U. S. A.* 1–6.

(147) Kuciauskas, D., Liddell, P. a, Hung, S. C., Lin, S., Stone, S., Seely, G. R., Moore, a L., Moore, T. a, and Gust, D. (1997) Structural effects on photoinduced electron transfer in carotenoid-porphyrin-quinone triads. *J. Phys. Chem. B 101*, 429–440.

(148) Van Stokkum, I. H. M., Larsen, D. S., and Van Grondelle, R. (2004) Global and target analysis of time-resolved spectra. *Biochim. Biophys. Acta - Bioenerg. 1657*, 82–104.

(149) Dogutan, D. K., Zaidi, S. H. H., Thamyongkit, P., and Lindsey, J. S. (2007) New route to ABCD-porphyrins via bilanes. *J. Org. Chem. 72*, 7701–14.

(150) Wessendorf, F., Gnichwitz, J.-F., Sarova, G. H., Hager, K., Hartnagel, U., Guldi, D. M., and Hirsch, A. (2007) Implementation of a Hamiliton-receptor-based hydrogen-bonding motif toward a new electron donor-acceptor prototype: electron versus energy transfer. *J. Am. Chem. Soc. 129*, 16057–71.

(151) Rohand, T., Dolusic, E., Ngo, T. H., Maes, W., and Dehaen, W. (2007) Efficient synthesis of aryldipyrromethanes in water and their application in the synthesis of corroles and dipyrromethenes. *Arkivoc 2007*, 307–324.

(152) Ferreira, K. N. ., Iverson, T. M. ., Maghlaoui, K., Barber, J., and Iwata, S. (2004) Architecture of the Photosynthetic Oxygen-Evolving Center : Kristina N . Ferreira , Tina M . Iverson , Karim Maghlaoui , James Barber and So Iwata. *Science (80-.). 303*, 1831–1838.

(153) Umena, Y., Kawakami, K., Shen, J.-R., and Kamiya, N. (2011) Crystal structure of oxygen-evolving photosystem II at a resolution of 1.9 Å. *Nature 473*, 55–60.

(154) Loll, B., Kern, J., Saenger, W., Zouni, A., and Biesiadka, J. (2005) Towards complete cofactor arrangement in the 3.0 A resolution structure of photosystem II. *Nature 438*, 1040–1044.

(155) Limburg, J., Vrettos, J. S., Liable-Sands, L. M., Rheingold, a L., Crabtree, R. H., and Brudvig, G. W. (1999) A functional model for O-O bond formation by the O2-evolving complex in photosystem II. *Science 283*, 1524–1527.

(156) Debus, R. J., Barry, B. a, Babcock, G. T., and McIntosh, L. (1988) Site-directed mutagenesis identifies a tyrosine radical involved in the photosynthetic oxygen-evolving system. *Proc. Natl. Acad. Sci. U. S. A. 85*, 427–430.

(157) Tommos, C., and Babcock, G. T. (1998) Oxygen Production in Nature: A Light-Driven Metalloradical Enzyme Process. *Acc. Chem. Res. 31*, 18–25.

(158) Hammarström, L., and Styring, S. (2011) Proton-coupled electron transfer of tyrosines in Photosystem II and model systems for artificial photosynthesis: the role of a redox-active link between catalyst and photosensitizer. *Energy Environ. Sci. 4*, 2379.

(159) Groot, M. L., Pawlowicz, N. P., van Wilderen, L. J. G. W., Breton, J., van Stokkum, I. H. M., and van Grondelle, R. (2005) Initial electron donor and acceptor in isolated Photosystem II reaction centers identified with femtosecond mid-IR spectroscopy. *Proc. Natl. Acad. Sci. U. S. A. 102*, 13087–13092.

(160) Rappaport, F., Guergova-Kuras, M., Nixon, P. J., Diner, B. A., and Lavergne, J. (2002) Kinetics and Pathways of Charge Recombination in Photosystem II. *Biochemistry 41*.

(161) Barry, B. a, and Babcock, G. T. (1987) Tyrosine radicals are involved in the photosynthetic oxygen-evolving system. *Proc. Natl. Acad. Sci. U. S. A. 84*, 7099–7103.

(162) Lin, X., Murchison, H. a, Nagarajan, V., Parson, W. W., Allen, J. P., and Williams, J. C. (1994) Specific alteration of the oxidation potential of the electron donor in reaction centers from Rhodobacter sphaeroides. *Proc. Natl. Acad. Sci. U. S. A. 91*, 10265–10269.

(163) Kalman, L., LoBrutto, R., Allen, J. P., and Williams, J. C. (1999) Modified reaction centres oxidize tyrosine in reactions that mirror photosystem II. *Nature 402*, 696–699.

(164) Dutton, P. L., and Mosser, C. C. (1994) Quantum biomechanics of long-range electron transfer in protein: hydrogen bonds and reorganization energies. *Proc. Natl. Acad. Sci. U. S. A. 91*, 10247–10250.

(165) Chumakov, D. E., Khoroshutin, A. V, Anisimov, A. V, and Kobrakov, K. I. (2009) BROMINATION OF PORPHYRINS (REVIEW). *Chem. Heterocycl. Compd. 45*, 259–283.

(166) Birnbaum, E. R., Hodge, J. a., Grinstaff, M. W., Schaefer, W. P., Henling, L., Labinger, J. a., Bercaw, J. E., and Gray, H. B. (1995) 19F NMR Spectra and Structures of Halogenated Porphyrins. *Inorg. Chem. 34*, 3625–3632.

(167) Drain, C. M., Kirmaier, C., Medforth, C. J., Nurco, D. J., Smith, K. M., and Holten, D. (1996) Dynamic Photophysical Properties of Conformationally Distorted Nickel Porphyrins. 1. Nickel(II) Dodecaphenylporphyrin. *J. Phys. Chem. 100*, 11984–11993.

(168) Jentzen, W., Simpson, M. C., Hobbs, J. D., Song, X., Ema, T., Nelson, N. Y., Medforth, C. J., Smith, K. M., and Veyrat, M. (1995) Ruffling in a Series of Nickel(II) meso-Tetrasubstituted Porphyrins as a Model for the Conserved Ruffling of the Heme of Cytochromes c. *J. Am. Chem. Soc. 117*, 11085–11097.

(169) Kadish, K. M., Van Caemelbecke, E., D'Souza, F., Lin, M., Nurco, D. J., Medforth, C. J., Forsyth, T. P., Krattinger, B., Smith, K. M., Fukuzumi, S., Nakanishi, I., and Shelnutt, J. a. (1999) Synthesis and Electrochemical Studies of a Series of Fluorinated Dodecaphenylporphyrins. *Inorg. Chem. 38*, 2188–2198.

(170) Nurco, D. J., Medforth, C. J., Forsyth, T. P., Olmstead, M. M., and Smith, K. M. (1996) Conformational flexibility in dodecasubstituted porphyrins. *J. Am. Chem. Soc. 118*, 10918–10919.

(171) Sazanovich, I. V., Galievsky, V. a., Van Hoek, A., Schaafsma, T. J., Malinovskii, V. L., Holten, D., and Chirvony, V. S. (2001) Photophysical and structural properties of saddle-shaped free base porphyrins: Evidence for an "orthogonal" dipole moment. *J. Phys. Chem. B 105*, 7818–7829.

(172) A. Shelnutt, J., Song, X.-Z., Ma, J.-G., Jia, S.-L., Jentzen, W., J. Medforth, C., and J. Medforth, C. (1998) Nonplanar porphyrins and their significance in proteins. *Chem. Soc. Rev. 27*, 31.

(173) Gust, D., Moore, T. a, Moore, a L., Gao, F., Luttrull, D., Degraziano, J. M., Ma, X. C. C., Makings, L. R., Lee, S. J., Trier, T. T., Bittersmann, E., Seely, G. R., Woodward, S., Bensasson, R. V, Rougee, M., Deschryver, F. C., and Vanderauweraer, M. (1991) Long-lived Photoinitiated Charge Separation In Carotene Diporphyrin Triad Molecules. *J. Am. Chem. Soc. 113*, 3638–3649.

(174) Gust, D., Moore, T. a., and Moore, A. L. (1993) Molecular mimicry of photosynthetic energy and electron transfer. *Acc. Chem. Res. 26*, 198–205.

(175) Faller, P., Goussias, C., Rutherford, a W., and Un, S. (2003) Resolving intermediates in biological proton-coupled electron transfer: a tyrosyl radical prior to proton movement. *Proc. Natl. Acad. Sci. U. S. A. 100*, 8732–8735.

(176) Harriman, A. (1987) Further Comments on the Redox Potentials of Tryptophan and Tyrosine. *J. Phys. Chem. 91*, 6102–6104.

(177) Costentin, C., Robert, M., and Savéant, J.-M. (2010) Concerted proton-electron transfers in the oxidation of phenols. *Phys. Chem. Chem. Phys. 12*, 11179–11190.

(178) Markle, T. F., Markle, T. F., Rhile, I. J., Rhile, I. J., Dipasquale, A. G., Dipasquale, A. G., Mayer, J. M., and Mayer, J. M. (2007) Probing concerted proton– electron transfer in phenol–imidazoles. *Sci. York 2007*.

(179) Westlake, B. C., Brennaman, M. K., Concepcion, J. J., Paul, J. J., Bettis, S. E., Hampton, S. D., Miller, S. a, Lebedeva, N. V, Forbes, M. D. E., Moran, A. M., Meyer, T. J., and Papanikolas, J. M. (2011) Concerted electron-proton transfer in the optical excitation of hydrogen-bonded dyes. *Proc. Natl. Acad. Sci. U. S. A. 108*, 8554–8558.

(180) Zhang, M., Irebo, T., Johansson, O., Hammarstrom, L., and Hammarström, L. (2011) Proton-Coupled Electron Transfer from Tyrosine : A Strong Rate. *J. Am. Chem. Soc. 133*, 13224–13227.

(181) Moore, G. F., Hambourger, M., Kodis, G., Michl, W., Gust, D., Moore, T. a., and Moore, A. L. (2010) Effects of protonation state on a tyrosine-histidine bioinspired redox mediator. *J. Phys. Chem. B 114*, 14450–14457.

(182) Richards, J. A. A. (1975) Electrochemical Oxidation of 2,4,6-tri-tert-butylphenol. *J. Electroanal. Chem. Interfacial Electrochem. 63*, 311–327.

(183) Zhao, Y., Swierk, J. R., Megiatto, J. D., Sherman, B., Youngblood, W. J., and Qin, D. (2012) Improving the efficiency of water splitting in dye-sensitized solar cells by using a biomimetic electron transfer mediator *109*, 15612–15616.

(184) O'Regan, B., and Grätzel, M. (1991) A low-cost, high-efficiency solar cell based on dye-sensitized colloidal TiO2 films. *Nature 353*, 737–740.

(185) Hagfeldt, A., Boschloo, G., Sun, L., Kloo, L., and Pettersson, H. (2010) Dye-sensitized solar cells. *Chem. Rev. 110*, 6595–6663.

(186) Cahen, D., Hodes, G., and Gra, M. (2000) Nature of Photovoltaic Action in Dye-Sensitized Solar Cells. *J. Phys. Chem. B 9*, 2053–2059.

(187) Ardo, S., and Meyer, G. J. (2009) Photodriven heterogeneous charge transfer with transition-metal compounds anchored to TiO2 semiconductor surfaces. *Chem. Soc. Rev. 38*, 115–164.

(188) Grätzel, M. (2009) Recent advances in sensitized mesoscopic solar cells. *Acc. Chem. Res. 42*, 1788–1798.

(189) Horiuchi, T., Miura, H., Sumioka, K., and Uchida, S. (2004) High efficiency of dye-sensitized solar cells based on metal-free indoline dyes. *J. Am. Chem. Soc. 126*, 12218–12219.

(190) Mishra, A., Fischer, M. K. R., and Büuerle, P. (2009) Metal-Free organic dyes for dye-Sensitized solar cells: From structure: Property relationships to design rules. *Angew. Chemie - Int. Ed. 48*, 2474–2499.

(191) Gao, F., Wang, Y., Shi, D., Zhang, J., Wang, M., Jing, X., Humphry-baker, R., Wang, P., Zakeeruddin, S. M., and Gra, M. (2008) Enhance the Optical Absorptivity of Nanocrystalline TiO Film with High Molar Extinction Coefficient Ruthenium Sensitizers for High Performance Dye-Sensitized Solar Cells Enhance the Optical Absorptivity of Nanocrystalline TiO 2 Film with High Molar Extinc. *J. Am. Chem. Soc.* 10720–10728.

(192) Hara, K., Sato, T., and Katoh, R. (2003) Molecular design of coumarin dyes for efficient dye-sensitized solar cells. *J. Chem. Phys. B 107*, 597–606.

(193) Kitamura, T., Ikeda, M., Shigaki, K., Inoue, T., Anderson, N. a, Ai, X., Lian, T., and Yanagida, S. (2004) Phenyl-Conjugated Oligoene Sensitizers for TiO_2 Solar Cells. *Chem. Mater. 16*, 1806–1812.

(194) Hagberg, D. P., Yum, J.-H., Lee, H., De Angelis, F., Marinado, T., Karlsson, K. M., Humphry-Baker, R., Sun, L., Hagfeldt, A., Grätzel, M., and Nazeeruddin, M. K. (2008) Molecular engineering of organic sensitizers for dye-sensitized solar cell applications. *J. Am. Chem. Soc. 130*, 6259–6266.

(195) Zeng, W., Cao, Y., Bai, Y., Wang, Y., Shi, Y., Zhang, M., Wang, F., Pan, C., and Wang, P. (2010) Efficient dye-sensitized solar cells with an organic photosensitizer featuring orderly conjugated ethylenedioxythiophene and dithienosilole blocks. *Chem. Mater. 22*, 1915–1925.

(196) Campbell, W. M., Jolley, K. W., Wagner, P., Wagner, K., Walsh, P. J., Gordon, K. C., Schmidt-mende, L., Nazeeruddin, M. K., Wang, Q., Grtzel, M., and Officer, D. L. (2007) Highly Efficient Porphyrin Sensitizers for Dye-Sensitized Solar Cells Highly Efficient Porphyrin Sensitizers for Dye-Sensitized Solar Cells. *J. Phys. Chem. Lett. 36*, 11760–11762.

(197) Imahori, H., Hayashi, S., Hayashi, H., Oguro, A., Eu, S., Umeyama, T., and Matano, Y. (2009) Effects of porphyrin substituents and adsorption conditions on photovoltaic properties of porphyrin-sensitized TiO2 Cells. *J. Phys. Chem. C 113*, 18406–18413.

(198) Lee, C.-W., Lu, H.-P., Lan, C.-M., Huang, Y.-L., Liang, Y.-R., Yen, W.-N., Liu, Y.-C., Lin, Y.-S., Diau, E. W.-G., and Yeh, C.-Y. (2009) Novel zinc porphyrin sensitizers for dye-sensitized solar cells: synthesis and spectral, electrochemical, and photovoltaic properties. *Chemistry 15*, 1403–1412.

(199) Odobel, F., Blart, E., Lagrée, M., Villieras, M., Boujtita, H., El Murr, N., Caramori, S., and Alberto Bignozzi, C. (2003) Porphyrin dyes for TiO2 sensitization. *J. Mater. Chem. 13*, 502–510.

(200) Rochford, J., Chu, D., Hagfeldt, A., and Galoppini, E. (2007) Tetrachelate porphyrin chromophores for metal oxide semiconductor sensitization: effect of the spacer length and anchoring group position. *J. Am. Chem. Soc. 129*, 4655–65.

(201) Hambourger, M., Brune, A., Gust, D., Moore, A. L., and Moore, T. a. (2005) Enzyme-assisted reforming of glucose to hydrogen in a photoelectrochemical cell. *Photochem. Photobiol. 81*, 1015–1020.

(202) Hariprasad, G., Dahal, S., and Maiya, B. G. (1996) meso-Substituted octabromoporphyrins: synthsis, spectroscopy, electrochemistry and electronic structure. *J. Chem. Soc. Dalt. Trans.* 3429–3436.

(203) Moore, G. F., Blakemore, J. D., Milot, R. L., Hull, J. F., Song, H., Cai, L., Schmuttenmaer, C. a., Crabtree, R. H., and Brudvig, G. W. (2011) A visible light water-splitting cell with a photoanode formed by codeposition of a high-potential porphyrin and an iridium water-oxidation catalyst. *Energy Environ. Sci. 4*, 2389.

(204) Megiatto Jr., J. D., Mendez-Hernandez, D. D., Tejeda-Ferrari, M. E., Teillout, a L., Llansola-Portoles, M. J., Kodis, G., Poluektov, O. G., Rajh, T., Mujica, V., Groy, T. L., Gust, D., Moore, T. a, and Moore, a L. (2014) A bioinspired redox relay that mimics radical interactions of the Tyr-His pairs of photosystem II. *Nat Chem 6*, 423–428.

(205) Listorti, A., O'Regan, B., and Durrant, J. R. (2011) Electron Transfer Dynamics in Dye-Sensitized Solar Cells. *Chem. Mater. 23*, 3381–3399.

(206) Kay, A., and Grätzel, M. (2002) Dye-sensitized core-shell nanocrystals: Improved efficiency of mesoporous tin oxide electrodes coated with a thin layer of an insulating oxide. *Chem. Mater. 14*, 2930–2935.

(207) Green, a N. M., Palomares, E., Haque, S. a, Kroon, J. M., and Durrant, J. R. (2005) Charge transport versus recombination in dye-sensitized solar cells employing nanocrystalline TiO2 and SnO2 films. *J. Phys. Chem. B 109*, 12525–12533.

(208) Sapp, S. a., Elliott, C. M., Contado, C., Caramori, S., and Bignozzi, C. a. (2002) Substituted polypyridine complexes of cobalt(II/III) as efficient electron-transfer mediators in dye-sensitized solar cells. *J. Am. Chem. Soc. 124*, 11215–11222.

(209) Young, K. J., Martini, L. a., Milot, R. L., Snoeberger, R. C., Batista, V. S., Schmuttenmaer, C. a., Crabtree, R. H., and Brudvig, G. W. (2012) Light-driven water oxidation for solar fuels. *Coord. Chem. Rev. 256*, 2503–2520.

(210) Kang, M. G., Park, N. G., Park, Y. J., Ryu, K. S., and Chang, S. H. (2003) Manufacturing method for transparent electric windows using dye-sensitized TiO2 solar cells. *Sol. Energy Mater. Sol. Cells 75*, 475–479.

(211) Ito, S., Chen, P., Comte, P., Nazeeruddin, M. K., Liska, P., Pechy, P., and Gratzel, M. (2007) Fabrication of Screen-Printing Pastes From TiO2 Powders for Dye-Sensitized Solar Cells. *Prog. Photovoltaics Res. Appl. 20*, 603.

APPENDIX A

NMR SPECTRA

1. 400 MHz ^{1}H NMR spectrum recorded in chloroform-d, 7,8,17,18-Tetracyano-5-(4-carboxyphenyl)-10,15,20-tris-(4-t-butylphenyl)porphyrin

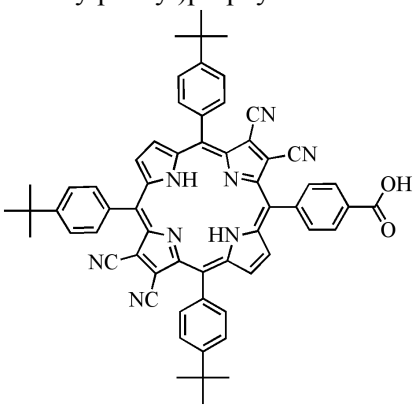

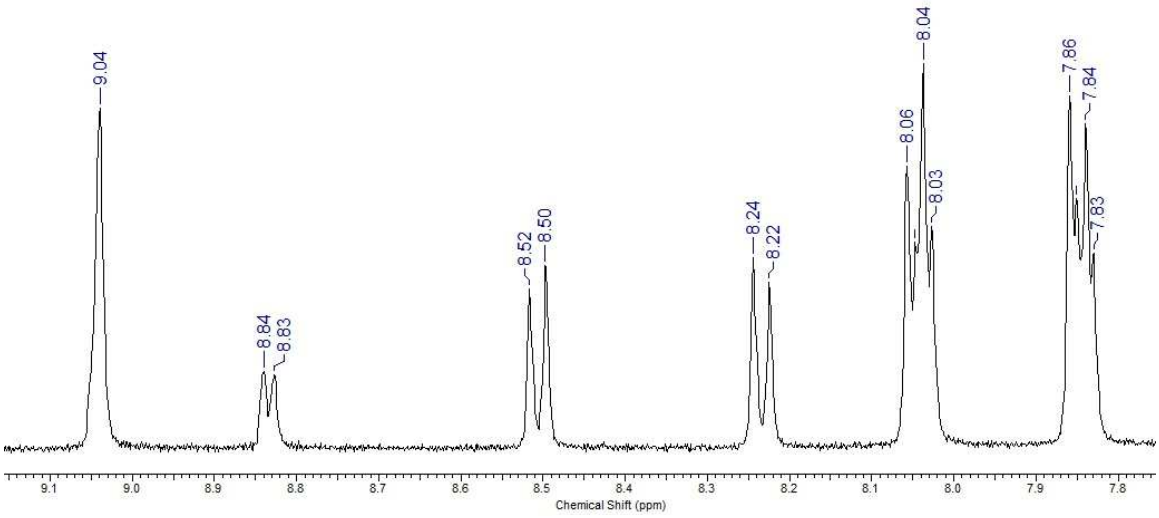

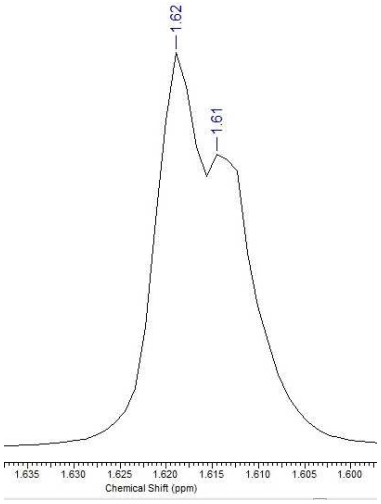

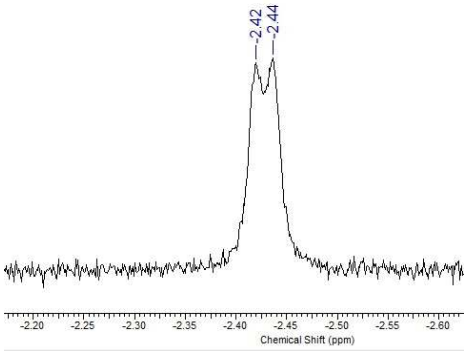

2. 400 MHz ^{1}H NMR spectrum recorded in chloroform-d, Zn(II) 2,3,12,13-tetrabromo-5,10,15,20-tetrakis-(4-t-butylphenyl)porphyrin (**31**)

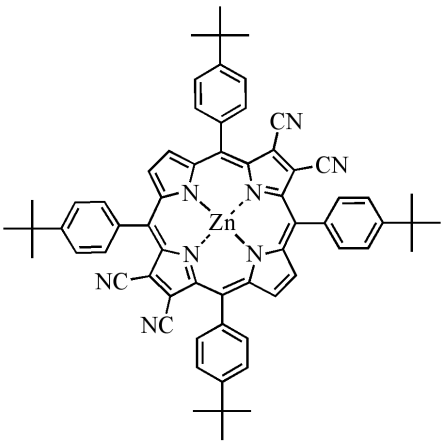

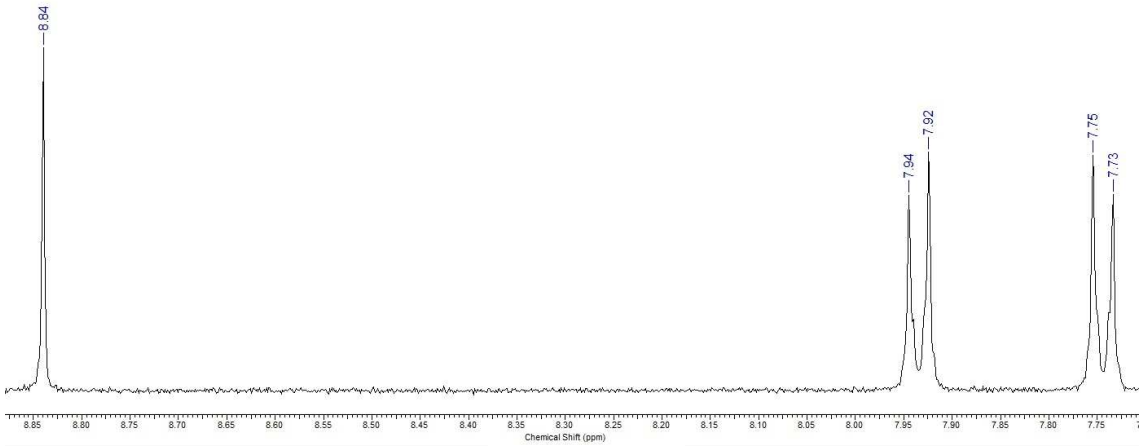

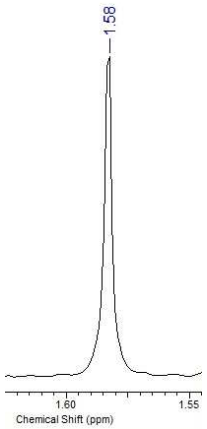

3. 400 MHz ^{1}H NMR spectrum recorded in chloroform-d, N-benzoyl-p-hydroxymethyl-D-L-phenylglycine methyl ester (3)

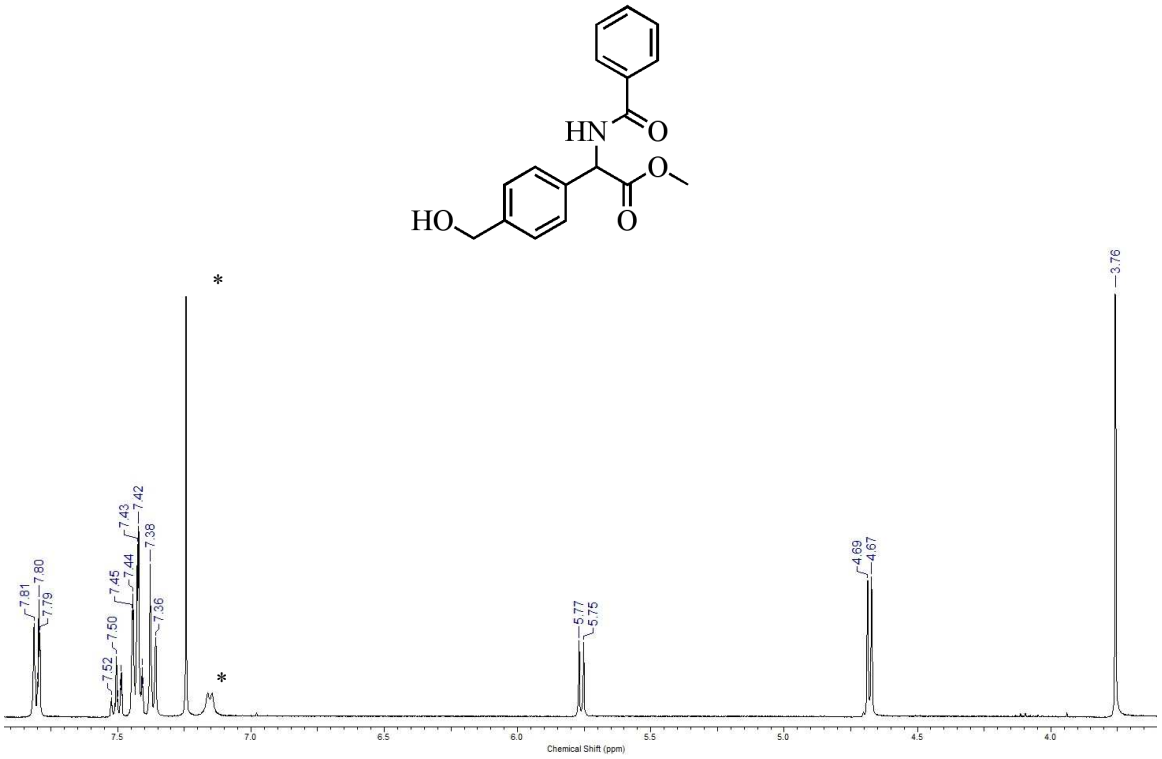

4. 400 MHz ^{1}H NMR spectrum recorded in chloroform-*d*, N-benzoyl-p-formyl-D-L-phenylglycine methyl ester (**4**)

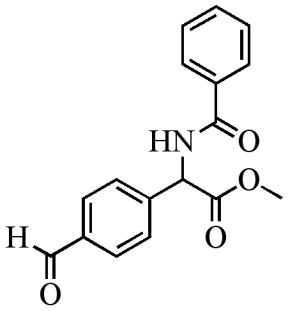

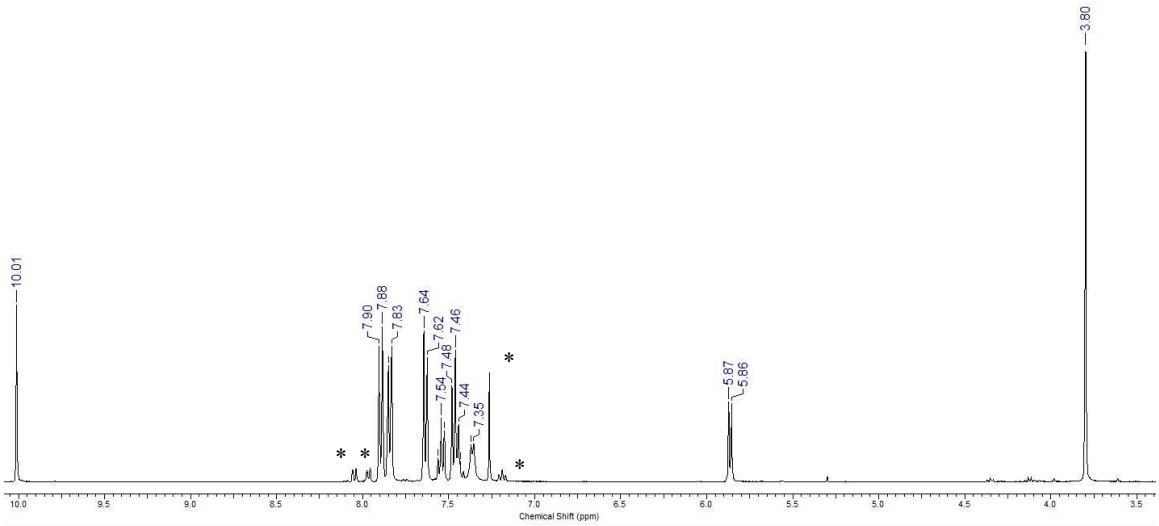

5. 400 MHz [1]H NMR spectrum recorded in chloroform-d, N-benzoyl- *4-[*10,15,20-tris-*(2,4,6-trimethylphenylporphyrin-5-yl]phenylglycine,* methyl ester ***(6)***

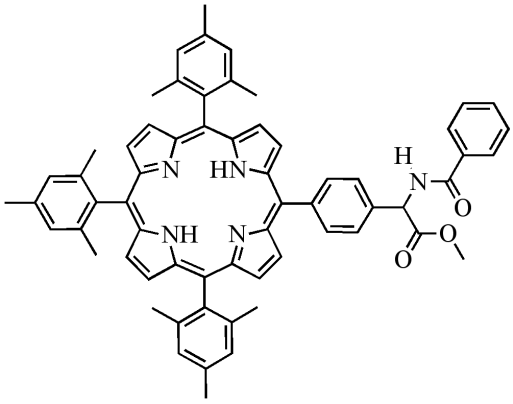

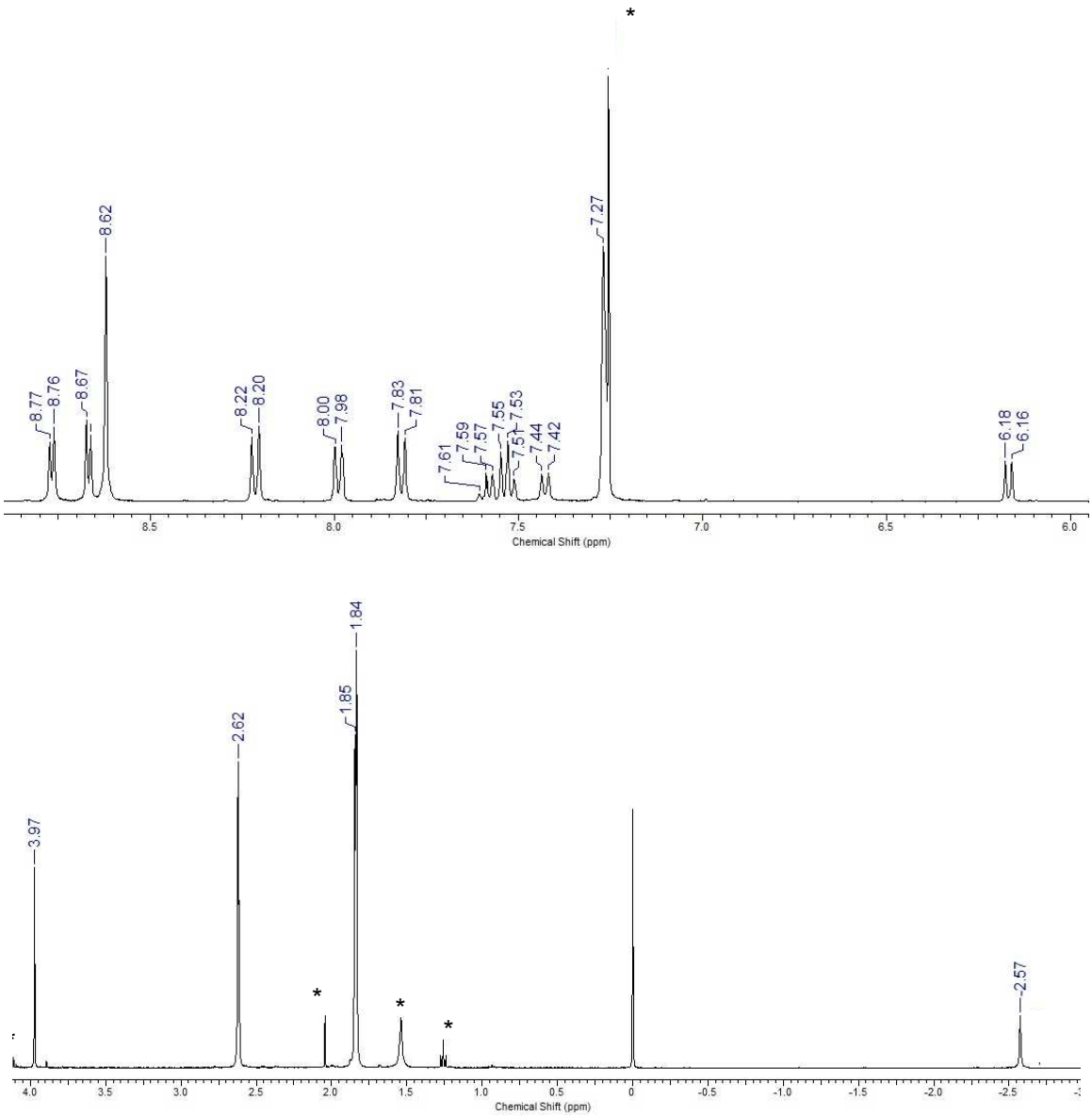

6. 400 MHz ^{1}H NMR spectrum recorded in chloroform-*d,* 7,8,17,18–tetracyano-5-(4-formylphenyl)-10,15,20-tris-(4-t-butylphenyl) porphyrin (CyP) (**15)**

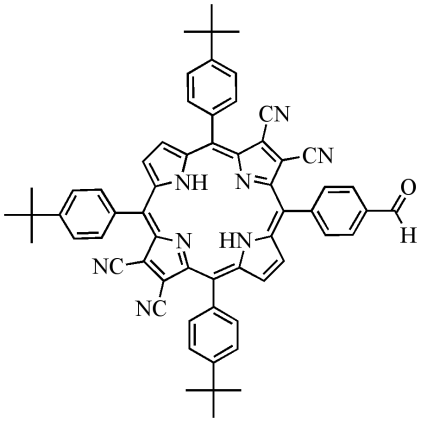

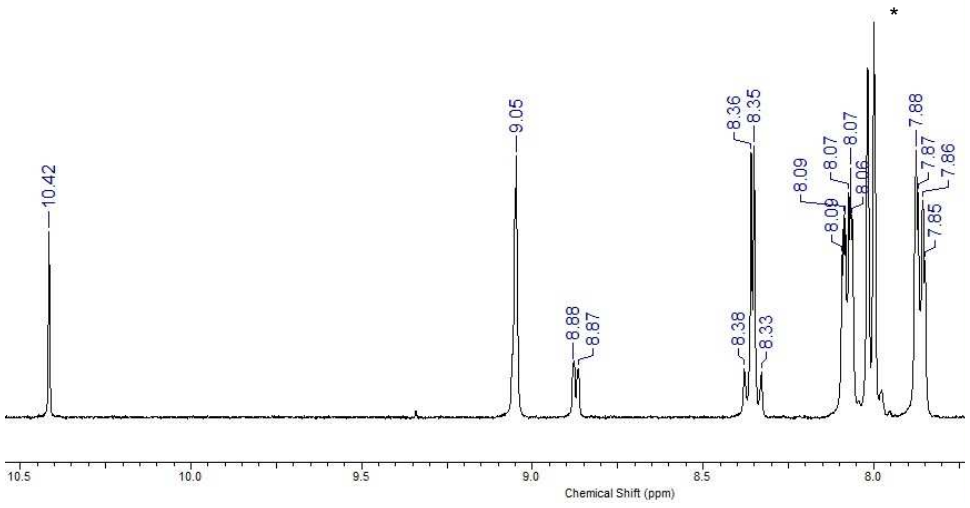

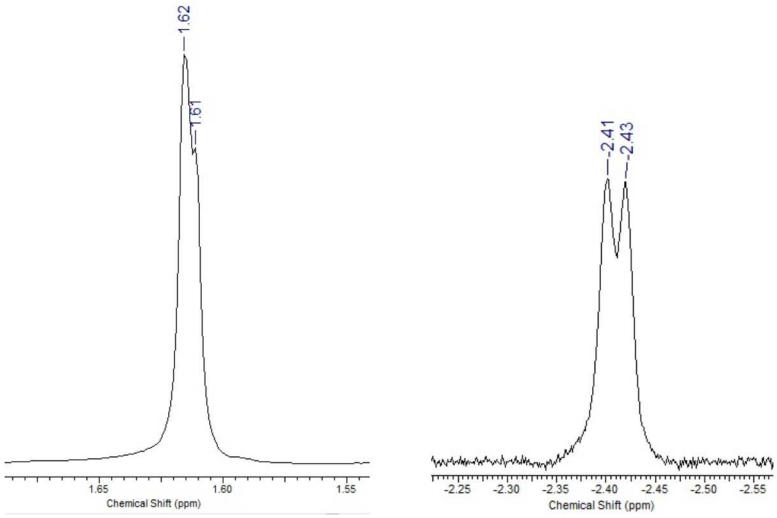

7. 400 MHz ^{1}H NMR spectrum recorded in chloroform-*d,* **AaP-C_{60} (16)**

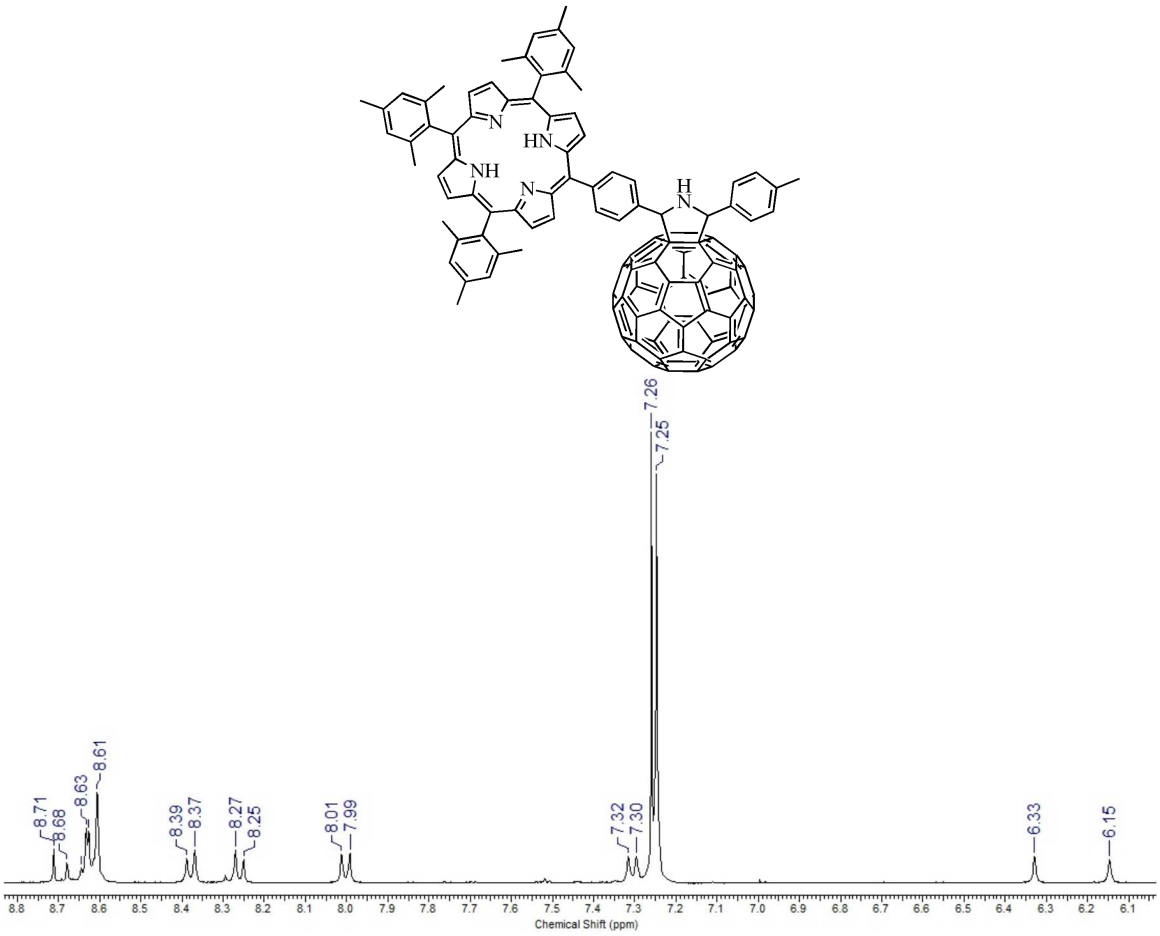
HN
NH
N
N
H
N
8.71
8.68
8.63
8.61
8.39
8.37
8.27
8.25
8.01
7.99
7.32
7.30
7.26
7.25
6.33
6.15
Chemical Shift (ppm)

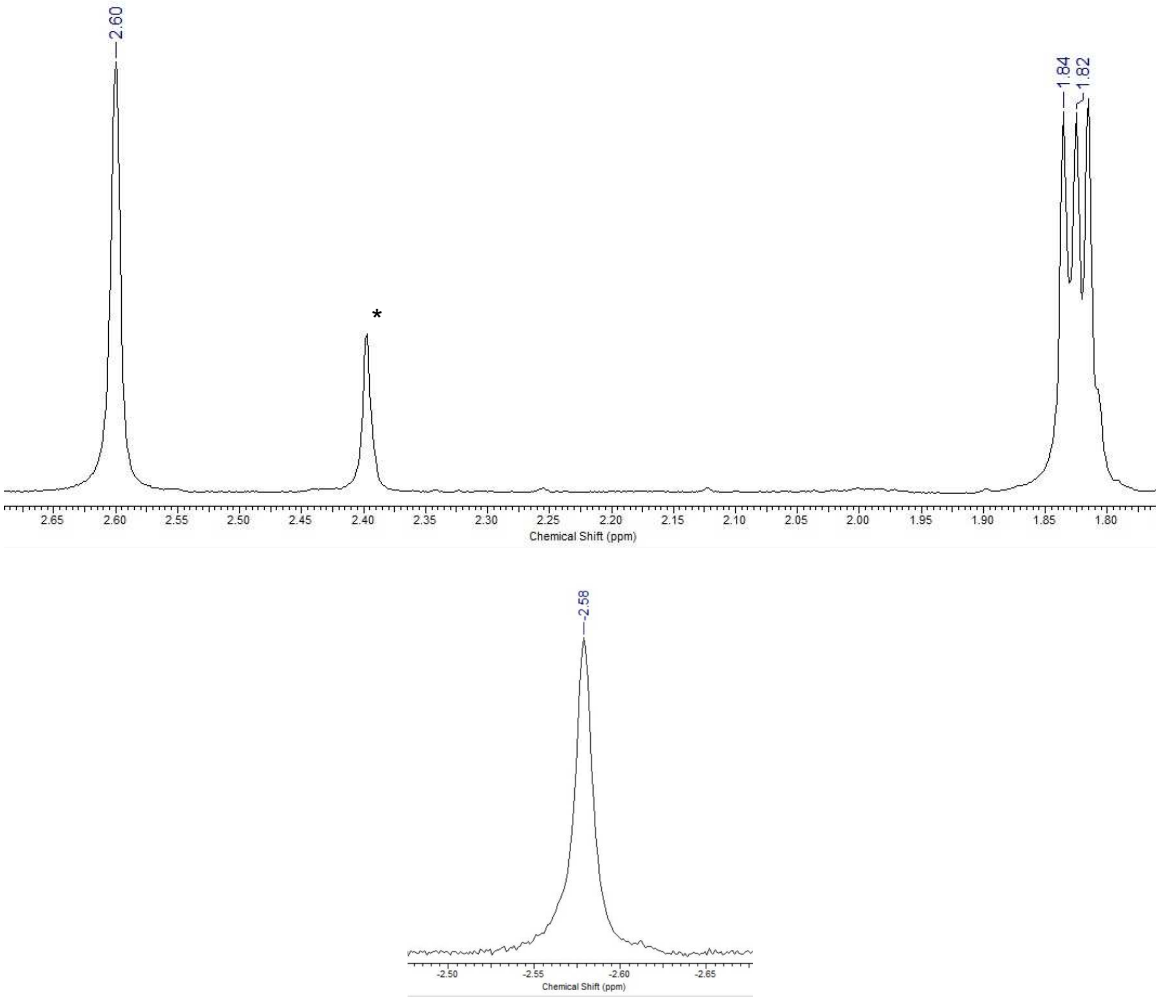

8. 400 MHz ^{1}H NMR spectrum recorded in chloroform-*d* **CyP-C$_{60}$ (17)**

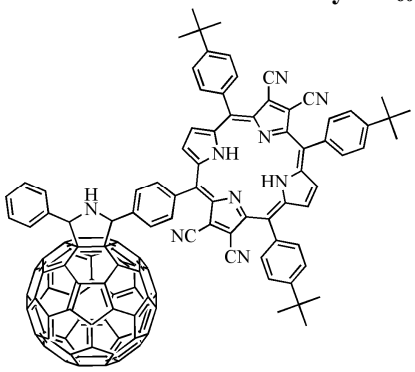

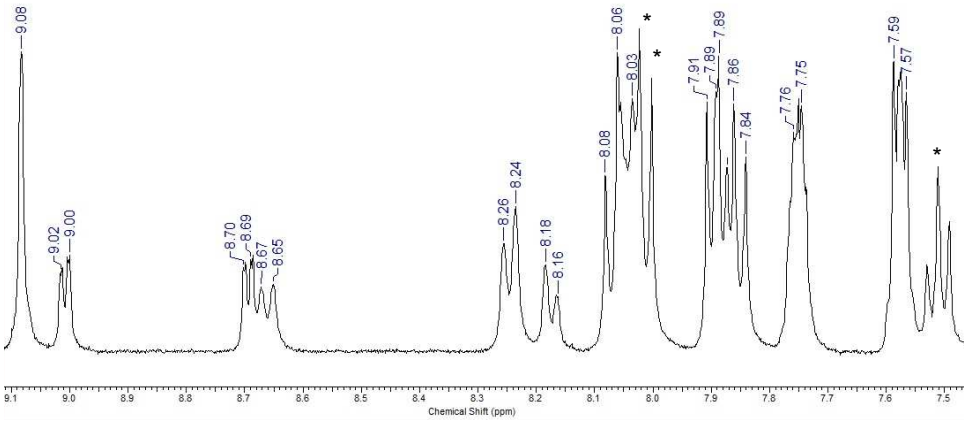
9.08
9.02
9.00
8.70
8.69
8.67
8.65
8.26
8.24
8.18
8.16
8.08
8.06
8.03
*
*
7.91
7.89
7.89
7.86
7.84
7.76
7.75
7.59
7.57
*
Chemical Shift (ppm)

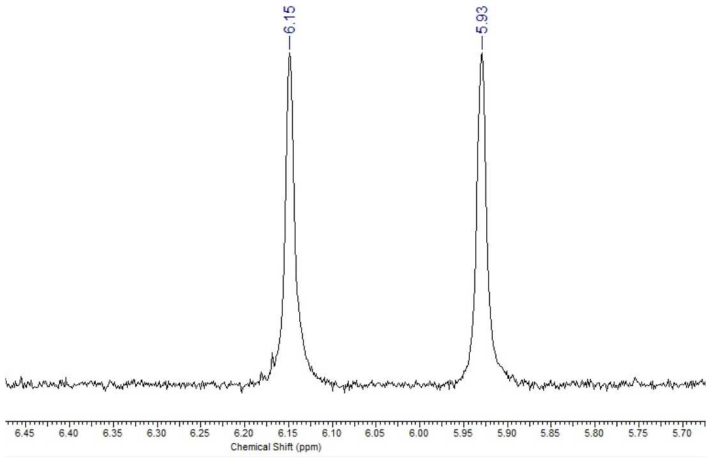
6.15
5.93
Chemical Shift (ppm)

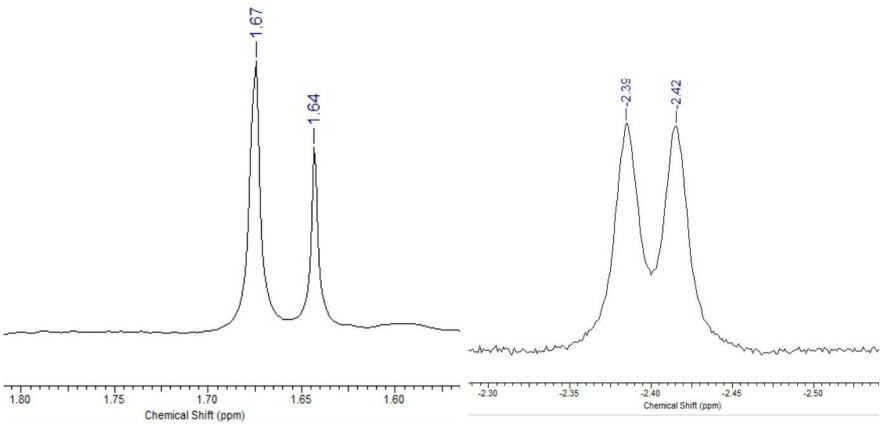
1.67
1.64
Chemical Shift (ppm)
-2.39
-2.42
Chemical Shift (ppm)